INVESTIGATION OF THE DYNAMIC CHARACTERISTICS AND DECAYING BEHAVIOUR OF SF_6 ARCS IN SWITCHING APPLICATIONS

A THESIS
SUBMITTED TO THE UNIVERSITY OF LIVERPOOL

BY

WEIZONG WANG

IN PARTIAL FULFILLMENT OF THE REQUIREMENTS
FOR THE DEGREE OF
DOCTOR OF PHILOSOPHY

JUNE 2013

DEPARTMENT OF ELECTRICAL ENGINEERING AND ELECTRONICS,
THE UNIVERSITY OF LIVERPOOL

ABSTRACT

Investigation into the dynamic characteristics and decaying behaviour of SF_6 arcs during the current-zero period is of great significance to improving the interruption performance of high voltage circuit breakers and ensuring their reliable operation. The present research was conducted by means of modeling and experiment to provide a better knowledge of the switching process to help the design and optimization of high voltage SF_6 circuit breakers.

The first part of the work concerns the determination of thermophysical properties of SF_6 plasmas under local thermodynamic equilibrium state (LTE). A systematic comparison with transport coefficients obtained using an old data set and experimental test has been performed to check the reliability of the proposed phenomenological approach in evaluating transport cross sections. Properties especially transport coefficients become sensitive to the choice of Debye length definition predominantly due to the different collision integrals affected by the different screening distance. Pressures increase can also influence thermophysical properties due to the inhibited chemical reactions.

Moreover, the thermophysical properties under non-equilibrium conditions have been investigated using a two-temperature model. It was noted that the special case with equal electrons and heavy species temperatures produces results agreeing excellently with those obtained by the LTE model. The forms of mass action laws as well as the choice of reaction excitation temperature for molecular ionization used in the calculation can significantly modify the species composition and plasma properties. This model lays the micro-theoretical foundation for a deeper understanding of SF_6 plasma formation and evolution mechanism and provides a reliable properties input for non-equilibrium arc behaviour simulation.

Following a traditional approach of arc modelling assuming LTE, considerable effort has been devoted to study the arc-shock interaction and its influence on the dynamic characteristics and current zero behaviour of SF_6 arcs in a supersonic nozzle with a hollow contact. It was found that the close coupling between the shock region and its surrounding gas flow greatly influences the aerodynamic and electrical behaviour of a nozzle arc and hence the thermal recovery process. In addition, deceleration of gas flow caused by the shocks and

enhanced turbulent cooling brought by the sucked gas interacting with the arc both play a significant role in the determination of the thermal interruption capability.

Possible departure from LTE in a decaying SF_6 arc was studied using a two-temperature hydrodynamic model in a supersonic nozzle under well-controlled conditions. The predicted radial temperature variation presents quite good agreement with test result using emission spectroscopy. It is demonstrated that the electron and heavy-particle temperature diverge in cases where the collision energy exchange is ineffective. For the arc decay phase, the two-temperature model gives a lower cooling rate than the LTE model, and hence a higher conductance of the discharge passage at current zero showing the necessity of using a two-temperature model to accurately predict the current interruption capability of SF_6 gas-blast circuit breakers.

For thermal recovery phase, considering the chemically non-equilibrium effect, a global kinetic model of decaying SF_6 arcs was established to study the electrons elimination mechanisms around current zero. For dielectric recovery phase, the critical dielectric strength of hot SF_6 are investigated based on a two-term Boltzmann equation solution of electrons energy distribution function. It is noted that the main mechanisms of electrons elimination are the dissociative attachment from 3500K to 7500K, electron-molecular ion recombination in the temperature lower than 3500K. The temperature increase, pressure decrease and departure from chemically non-equilibrium can all contribute to the dielectric strength reduction. The entrainment of PTFE ablation vapour can enhance the dielectric strengh of SF_6 above 2500K.

Finally, this research manufactures a model SF_6 gas blast interrupter and investigates the dynamic characteristics of electrical, light radiation, pressure along together with electrode movement. Arc dynamic characteristics and decaying behaviour of CO_2 and N_2 is compared with that of SF_6 arcs in order to obtain the dominant properties influencing arc quenching. It is noted that the extinction voltage, which decreases with increase in the interrupting current, is related to the conductance decay during current zero period and can be considered as an evaluation of interruption capability. Gas blast can bring a much more rapid variation of arc resistance and a much higher cut-off current before its extinction. SF_6 has a superior interruption capability possibly due to its high thermal conductivity and specific heat.

ACKNOWLEDGEMENTS

To begin with, I would like to acknowledge and extend my heartfelt gratitude to my supervisors—Professor M. Z. Rong, Professor J. W. Spencer and Dr. J. D. Yan for their support and continuous encouragement throughout my study, for their vital encouragement and patient guidance, generous assistance and invaluable advice, all of which have been of inestimable worth to the completion of my thesis. Specially, I am grateful to Professor M. T. C. Fang and Dr. A. B. Murphy for their stimulating suggestions and discussions during my study and for their helpful comments concerning my thesis via e-mail or face-to-face discussions. All these scholars with stringent realistic attitude in their scholarly work, great generousness and kindness to people, a high degree of professionalism, dedication and assiduous work style and bold innovation and entrepreneurial spirit to me has an important impact and will encourage me to continue the journey of research and service to others.

I also wish to thank other members of the Arc Research Group in Xi'an Jiaotong University and the University of Liverpool, especially Professor Y. Wu, Dr. H. M. Looe, and Mr. J. E. Humphries for their insightful guidance, valuable discussions and tremendous help, which will leave me a cheerful memory. Additionally, I would like to take this opportunity to express my gratitude to the Dual Collaborative PhD Degree Program between Xi'an Jiaotong University and the University of Liverpool and the Chinese Government Scholarship Program for Postgraduates. This thesis would not have been possible without their financial support. Thanks also go to Professor Q. L. Chao and my friends & classmates for making my time at the University of Liverpool and Xi'an Jiaotong University a great experience.

The last but not least, to my mother, my fiancee Mary and my family, I wish to express my greatest thanks for their love, endless support and encouragement which give me confidence, wisdom, strength, and endurance to pursue my dreams throughout all my study. My endless yearning goes to my father who passed away during my study and will live in my heart and encourage me to continuously progress for ever.

TABLE OF CONTENTS

List of Figures

List of Tables

CHAPTER 1 INTRODUCTION

1.1 Background

The electric power industry as a pillar of the national economy in China has been developing rapidly in the past ten years. It is of great significance to increase the transmission capacity, enhance the network reliability, and maintain operational stability to meet the demand for power consumption and security of electricity supply, and make better use of remote energy resources, especially renewable energy sources. Circuit breaker is one of the most complex and important switching equipment in the electric power system. A circuit breaker needs to switch on or off the load in normal operation; when a short circuit fault in the network takes place, it is called upon by the protection system to interrupt the fault current and restore network connection if possible. It also provides insulation under certain circumstances to allow network maintenance. The basic requirements of the electric power system on a circuit breaker is that it can reliably and rapidly disconnect the faulty lines before the short-circuit current destroys the electric equipment or damage the local grid severely.

As soon as the contacts depart from each other in the operation of a circuit breaker, an electric arc is formed between the contacts. Through the arc, the current continues to pass without getting interrupted. The electric current causes strong Joule heating and results in high arc temperature (>20,000 K) during the high current phase. Such a high temperature arc is usually considered to be in local thermodynamic equilibrium state (**LTE**) where electrons and heavy species posses a common temperature. High current switching arcs are thermal plasma that is a good conductor (high electrical conductivity) until shortly before a natural current zero of an alternative current.

Towards current-zero, Joule heating gradually decreases towards zero. As a result, the arc loses energy and its temperature declines until the gap regains its dielectric strength. There exist two types of current interruption failure. One is thermal failure, and the other is dielectric failure. After current zero, there remains hot gas between the contacts, which is referred to as the post arc channel with finite electrical conductivity. Under the imposed

transient recovery voltage, a current of a few amperes flows through the post-arc channel, referred to as the post-arc current. If the post-arc current gradually increases and the post arc channel regains its high conductivity, thermal failure will occur because of Ohmic heating overtaking energy loss in the first several microseconds immediately after current zero. After a successful thermal recovery, the transient recovery voltage continuously increases. A dielectric failure may occur if the recovery voltage reaches such a value that electron avalanches take place in strong electric field and the contact gap breaks down,

Sulfur hexafluoride (SF_6) is widely adopted in gas-blast circuit breakers because of its excellent arc quenching ability and dielectric strength which can sustain a higher critical breakdown field. Therefore, higher requirements are put forward for its reliability and stability. Whether a high voltage SF_6 circuit breaker can interrupt the fault current successfully is closely related to the dynamic characteristics and decaying behaviour of SF_6 arcs during the current-zero period where the gas in the contact gap changes from conduction to insulation. Research on the dynamic characteristics and decaying behaviour of SF_6 arcs during the current-zero period is therefore of great significance to improve the interrupting performance of high voltage circuit breakers and ensure its reliable operation as well as the security and stability of the whole network.

1.2 Brief Review of the Applications of Plasmas

It is commonly known that over 99% of the matter in the universe is in plasma state. However, plasma on earth has to be man-made. The earliest scientific investigation related to plasmas is perhaps that of Faraday, who observed glow discharges in the 1830's [1]. The studies by Sir William Crooks on the gas in his discharge tube suggest the existence of a new state of matter in 1879 [2]. J. J. Thomson discovered electrons in the 1890's [3] and Townsend investigated the phenomena of ionisation [4]. Both these marked the birth of a new scientific discipline, the ionised gases. Tonks and Langmuir firstly introduced the term plasma in 1929 [5] to describe the collective behaviour of the ionised gases, for which the Debye length is much smaller than the characteristic length of the system.

The discovery of arc discharges at the turn of 19th century signals the beginning of the application of plasmas. The most common type of arc discharges is a plasma sustained by a current between two electrodes. Arcs are the key element for light sources, for material cutting and welding, for plasma spraying, for waste disposals, for thermal plasma chemical and vapour deposition and for plasma synthesis of fine powders and plasma densification [6].

Before the Second World War, little was known about the fundamental processes occurring in arc discharges although there was a sufficient amount of knowledge on low pressure positive column [7]. The discovery of nuclear fusion and the subsequent realisation of the potential of controlled thermal nuclear fusion attracted intense research activities in basic plasma physics during and immediately after the war [8]. Researchers derived the basic equations describing the behaviour of plasmas ranging from collisionless to collision dominated. In parallel with the development of basic plasma theory, diagnostic techniques, especially after the invention of the lasers, have been developed to such an extent that the measurement of basic plasma parameters has become common.

Switching arcs as typical plasmas are widely investigated for a better understanding of their behaviour in fault current interruption in power system. This thesis is exclusively concerned with the studies on dynamic characteristics and decaying behaviour of SF_6 arcs in switching applications.

1.3 Review of Research on Dynamic Characteristics and Decaying Behaviour of SF_6 Arc in Current Interruption

The current interruption phenomenon has not yet been elucidated completely as a result of its extreme complexity. Therefore, many scientists and engineers have published a large number of academic papers to introduce their works on theoretical and experimental investigation with related to current interruption process. In this section, a brief review of recent investigation on SF_6 arcs is presented as follows:

Theoretical work for an arc can be distinguished as two types: one is to theoretically calculate fundamental data on SF_6 properties including radiation transfer, species composition,

dielectric properties, thermodynamic properties and transport coefficients. The other is to simulate dynamic behaviour of the arc and hot gas adopting the fundamental data by means of computer magnetohydrodynamic (MHD) modelling which is closely linked with the development of arc mathematical and physical models. Numerous experimental investigations have been carried out to measure only macroscopic parameters such as the voltage across the electrode gap and the current passing through the arc discharge channel. However, recent investigation has been gradually focused on the physical information related to the arc itself such as the pressure, electrons density, temperature, and species composition. Relevant research work is reviewed in detail as follows:

Due to the importance of the application field through circuit breakers, there has been a noticeable amount of work on the calculation of the composition, thermodynamic and transport properties in pure SF_6 plasma or in SF_6-containing mixtures under LTE state. Chervy et al. have obtained the equilibrium composition, thermodynamic properties and transport coefficients of SF_6/Cu mixture in a wide temperature range of 300K to 30000K and a wide pressure range of 1atm to 10atm for molar fraction of copper between 0 and 10%[9]. It is found that the material property that is most affected by the presence of copper is the electrical conductivity for temperatures up to 10000 K which increases remarkably in proportion to copper vapour concentration. Paul et al. performed a calculation of thermodynamic properties and transport coefficients of SF_6 under multimixed condition by PTFE ($-C_2F_4-$) reinforced with alumina ($-Al_2O_3-$) or BN particles [10]. The results show that the change of electron density and hence electrical conductivity is significant for alumina-reinforced PTFE, but insignificant for BN-reinforced PTFE contamination. Henceforth, the electrical conductivity varies only for alumina-reinforced PTFE contamination. The thermal conductivity, however, changes distinctly by mixing alumina-reinforced PTFE as well as by mixing BN-reinforced PTFE. Chervy also computed the properties of SF_6 mixed with tungsten vapor [11]. The results show that for tungsten proportions under 10%, the properties of pure SF_6 can be used except for the electrical conductivity. Speckhofer et al. [12] and Zhang et al. [13] computed the thermodynamic properties and transport coefficients of SF_6/PTFE mixtures. It was presented that the properties of gas mixture are quite different from that of pure SF_6. It is noted that Speckhofer et al. also took into account the influence of solid graphite formation in the arcing phase showing that sold graphite can greatly change the

properties of gas mixture as well. The test results of arc plasma properties are difficult to carry out. Hertz et al. determine the gas properties of SF_6 such as thermal conductivity and electrical conductivity by electrical and spectroscopic measurements an interrupted DC arc without flow [14]. They also show that the good quenching capability of SF_6 was due to energy transport mechanisms taking place below 10 000 K. Dayal and Stokes performed a test made on wall stabilized cascade arcs of 3 and 5 mm diameter using spectroscopy [15]. They have firstly found the pressure dependence of thermal conductivity and the effect of thick radiation absorption within the arc on thermal conductivity experimentally showing that the radiation was strongly absorbed within the SF_6 arc. It is likely that this radiative transfer mechanism, along with some degree of turbulence rather than turbulence alone, may be responsible for the enormously high heat-loss rates observed in this gas.

Arc radiation is one of the significant factors to formulate the energy balance in arc. Gleizes et al. have calculated the net emission coefficients radiated from isothermal cylindrical SF_6-Cu arc column [16]. The emission radiated at the centre of an arc is absorbed at its cool edge. Therefore, the net emission coefficients decrease with increasing arc radius. They found that the influence of copper on radiation is preponderant on the temperature field at higher currents whereas the effect on electrical conductivity is important at lower currents. They also calculated the net emission coefficients of SF_6/N_2 mixture [17]. The results show that the resonance lines, although they are strongly absorbed, make up a large part of the net radiation-about as much as the continuum. Also, the nitrogen lines are more strongly absorbed than the lines of sulphur or fluorine. At low temperatures the radiation of SF_6 is stronger than that of nitrogen. When T>12000 K the net radiation of the mixture is not proportional to the net radiations of the gases owing to variations in emissivity and line broadening with temperature and composition of the mixture. Aubrecht et al. calculated the net emission coefficients of SF_6/PTFE mixtures showing that the net emission coefficients vary very little with various admixtures of PTFE [18].

In order to predict the interruption capability under transient recovery voltage after arc extinction, it is more particularly necessary to know the breakdown electric fields during the recovery phase or SF_6 thermal relaxation which corresponds to a temperature range from about 3000 K down to room temperature. In fact, there are only a few works devoted to

measurements or calculations of hot SF_6 breakdown. On the one hand, the main research works undertaken in the experimental case are those of Eliasson and Schade [19], Nagata et al [20], and Rothhardt et al. [21]-[22]. Eliasson and Schade have measured SF_6 breakdown voltage for a temperature varying from 1300 to 2300 K and a pressure of 0.2 MPa in the wake of cross-arc flow. The gas is heated by an arc shock wave propagating along a channel with a velocity which is measured in order to estimate the gas temperature. Nagata et al. have also measured the SF_6 breakdown voltage for a temperature not exceeding 1000 K and for several quite low gas pressures 6.7, 13.3, and 20 kPa. A long graphite tube is used as a resistance to heat the gas inside the discharge chamber. Rothhardt et al. using a shock tube technique in which the gas temperature was estimated from the gas flow velocity measurement, have studied the breakdown voltage up to 2900 K for a gas pressure of 0.1 MPa. On the other hand, the main research works devoted to critical breakdown field calculations of SF_6 are those of Yan et al. [23], Cliteur et al. [24] and Yousfi et al. [25]-[26]. In the case of SF_6 at 3000 K under 0.2 MPa gas pressure, Yan et al. take into account six reaction processes of generation and loss of charged particles, positive and negative ions under a diatomic equilibrium assumption in their calculation. Then from a Druyvesteyn approximation of the electron distribution function, they calculate the critical electric field at a fixed temperature 3500K corresponding to the balance between the processes of electrons creation and disappearance. Cliteur et al. and Yousfi et al. present the calculation of critical breakdown field in a wide temperature and pressure range using the LTE species compositions. Due to a lack of the electron-neutral collision cross section data, some electron impact cross sections are approximated and the dielectric strength is evaluated as a balance between the electron generation and loss using a two-term or multi-term Boltzmann equation solution for the determination of the electron energy distribution function.

For the arc dynamic characteristics and decaying behaviour, Lewis et al. have measured diameters of arcs across the Cu-W electrodes for 78 Hz in a model SF_6 gas-blast circuit breaker [27]. They find that an arc diameter increases in proportion to the absolute current decay rates. Lewis et al. also have measured arc temperature around current zero for current frequency of 78Hz by two-line method of Cu spectral lines at wavelengths of 515.3nm and 510.5nm [28]. Tanaka et al. present an estimation of transient axial temperature distribution in a post-arc channel in a flat-type SF_6 gas-blast quenching chamber using two Fe

spectral lines at wavelength of 426.0 nm and 442.7 nm which make it possible to predict the post-arc channel temperature below 3500K at 100μs after current zero [29]. Moreover, Tanaka et al. have estimated the axial distribution of iron vapor concentration in a SF_6 gas blast quenching chamber with iron electrode based on the spectroscopy which adopts the relative radiation intensity of background spectra at 455.0nm to Fe spectral line at 426.0 nm [30]. With a spectroscopic observation, Jones et al. obtained the spectra of Copper emission lines and irregularly occurring tungsten emission lines from entrained contact material and identified the ratio of the number density of tungsten to copper atoms estimated from the line intensities along with an approximate radial distribution of both copper and tungsten line intensities [31]. Kozakov et al. perform spectroscopic measurements of arc temperature profiles of a wall-stabilized arc in a PTFE nozzle and observed spectral lines of fluorine and ionized carbon observed. The pressure build up is of great significance for the gas blast cooling during the arcing phase and current zero period [32]. Seeger et al. have experimentally investigated the dielectric recovery in high-voltage circuit breakers after interruption of high-current amplitudes in a test device [33]. A leader inception model using test parameters explains under which condition leader inception occurs, causing breakdown of the gap. Based on this model, they give the scaling laws for leader inception. Mori et al. have measured pressure in puffer chamber in a model gas-blast circuit breaker showing that the installation of the inner-nozzle for the pressure rise successfully contributed to the enhancement of short circuit fault interruption performance [34]. Meanwhile, the pressure measurement is also a popular technique to be used to verify the effectiveness of turbulent enhancing pressure build up [34]-[36].

With the continuous development of the arc model and computational fluid dynamics (CFD) commercial code, it is possible for using the numerical method to obtain arc information, and the simulation is becoming an effective approach to complement the experimental research on the arc behaviour. Recent progress in the computer modelling of arc dynamic behaviour enables the transient characteristics to be investigated theoretically. The mathematical description of the arc plasma includes mass, momentum and energy transport equations coupled with electric field and magnetic field based on the assumption of LTE.

For the purpose of predicting the thermal interruption capability, Fang et al. have theoretically analyzed the transient behaviour of arcs before and after current zero using

Prandtl mixing length turbulence model [37]. It is identified that taking into account the turbulence effects lead to excellent agreement between calculation results and experimental tests. However, it is not possible to determine the most appropriate turbulence model according to current research because several turbulence models are adopted in arc behaviour modelling and recommended by various authors[35]-[36],[38]. In modern circuit-breakers the puffer effect is often associated with an overpressure caused by controlled material ablation due to vaporization and it is associated with a mechanical piston movement. Zhang et al. performed a computer modelling taking account of the effects of nozzle ablation and the mixing process of PTFE vapour with SF_6 for a full-scale auto-expansion circuit breaker with a moving contact [39]. They found that the energy brought into the expansion volume by the hot PTFE vapor is mainly responsible for the pressure buildup. The propagation of the pressure wave in the expansion volume is responsible for the pressure peaks in the second loop of arcing. Results show that the use of the properties of SF_6-PTFE vapor mixture substantially improves the agreement between the predicted and measured pressure rise in the expansion volume. In SF_6 plasma, the light radiation by the arc core is partly or completely absorbed by the cold gas around the arc edge. The traditional net emission coefficient radiation (NEC) model [40], which gives a good approximation of the radiation losses from the hottest regions, is unable to treat radiation absorption. To take this phenomenon into account, Fang and his team use a modified NEC, considering that part of the radiation escaping from the hottest regions is absorbed in the outer regions [41]-[42]. Another two methods which have been widely used are P1 model [43] and partial characteristics method [44]. The former one was assumed that the absorption coefficient is constant, or an effective value, which is a function of composition and temperature by some averaging technique such as the weighted-sum-of-grey-gases, was found. The basic assumption of partial characteristics method is that in the integration of the equation of radiation transfer the temperature varies linearly between the point of interest and the current point on the integration path. This allows the integration over frequency to be done in advance and the results tabulated. Additionally, metal vapor resulting from electrode erosion is inevitably injected into the arc plasma. Its influence on arc behaviour has been investigated widely [45]-[46] and shows that vaporization of the electrode material has a cooling effect at the arc center and broadens the arc column. It has been predicted that the contact erosion has a negligible effect on the interruption capability of the breaker.

However, regardless of a large number of publications made contributing to the model and test as mentioned above, the systematic investigation on arc-shock interaction is rare. It is recognized that shock wave can generate in the diverging section of the nozzle under the condition that the ratio of exit pressure to inlet stagnation pressure exceeds certain critical value and can greatly influence the arc dynamic characteristics and decaying behaviour during the current interruption process. Meanwhile, the presence of an SF_6 arc, which is usually turbulent and unstable, can have significant effect on the shock wave. Experimental observation was limited to the arc section outside the nozzle or to that downstream of an orifice plate [47]-[49]. The theoretical investigations of the arc-shock interaction with computer simulation model have been reported are restricted to the steady state case and only the discharge area without taking into account the influence of the downstream contact on flow filed [50]-[52].

In the computation of arc behaviour with a MHD model, it is often assumed that the plasmas are under LTE state. However, it is not always the case and departure from equilibrium often takes place during the transient and decaying process of arcs or under high electric field. Sometimes, in regions where electric field is high and electrons density is low, the collisions between electrons and heavy species are not sufficiently frequent to ensure that the energy gained by an electron from the electric field in one mean free path is transferred to heavy species, thus causing electron temperature being substantially higher than that of heavy species and a thermally non-equilibrium takes place [53]. Moreover, when the arc temperature decays too rapidly under gas blast with a very strong quenching rates of heavy species temperature, the species in the chemical system do not have enough time to reach equilibrium because the reaction rate is finite, chemical non-equilibrium may occur in the arc system. In total, despite the usefulness of the LTE assumption, and its applicability to many thermal plasma processes, there are many important application areas for which deviations from LTE prevail, and it is therefore of utmost importance to understand the non-equilibrium processes

For chemically non-equilibrium effect, much work has been performed to obtain the species composition. Brand and Kopainsky have used reaction kinetics to analyze time variation in particle densities under free recovery [54]. They conclude that during the about

100μs after current zero there is a strong deviation from the equilibrium and the overpopulation of electron density. Gleizes et al [55] and Adamec et al. [56] also carried out similar work for species composition of SF_6 plasma under non-chemical equilibrium condition. They usually ignore the molecular ions in order to reduce the computation effort. When thermally non-equilibrium takes place, a two temperature property model has been developed to meet the requirement of complete data sets of thermophysical plasma properties. As for pure SF_6 gas, several papers have so far dealt with the particle compositions in two-temperature state from which the effect of an increase in electron temperature is described [57]-[67]. Gleizes et al. compare two sets of two-temperature Saha laws and recommend the expressions proposed by Van de Sanden et al.'s method [68]. For the reaction excitation temperature, Gleizes et al. [68] and Tanaka et al. [69] also give their corresponding derivations. However, although some computation of thermodynamic properties and transport coefficients for SF_6 plasmas under LTE state are available in the literature, there are relatively few papers concerned with the calculation of two-temperature properties.

For the dielectric strength of SF_6, the physical and chemical processes responsible for the breakdown of a hot gas immediately after the thermal extinction of the arc are expected to be very different from those of SF_6 at room temperature. This is because the composition of such a hot gas is complex and is dependent on the temperature decay rate during thermal recovery. A careful examination of all relevant chemical reactions consistent with the time scale for dielectric breakdown is therefore required. Further, it is widely found that PTFE vapor caused by the arc radiation ablation can entrain into the arcing gaseous system and influence the dielectric strength of hot gas and residual plasma after arc extinction and an investigation of the influence of PTFE vapor on critical breakdown field is also expected.

Great progress has been achieved in the simulation of non-equilibrium DC arcs [72]-[75]. These simulations have helped to achieve a better understanding of the operation of DC arc torches and have sometimes led to improved torch designs and plasma processes. However, there are, to our knowledge, only two relevant studies in the literature for the investigation of non-equilibrium effects during the SF_6 arc decaying [76]-[77]. Girard et al. used a two-temperature model to examine the influence of departures from thermal equilibrium on the characteristics of laminar wall-stabilized arc at atmospheric pressure in

one-dimensional geometry. They find that taking departures from thermal equilibrium into account leads to a slower cooling rate of the plasma. However, as they noted, it was not possible to draw conclusions on the effect of departures from thermal equilibrium for real circuit-breaker geometry, in which convection is the dominant process. Furthermore, the validity of the governing equations used in their paper should be examined carefully. Gonzalez et al. investigated the influence of both thermal and chemical departures from LTE on the interruption capability of circuit-breaker arcs from a cut off current under free recovery, studying the extinction of a blown SF_6 arc in a simplified two-dimensional geometry concluding that the departures from equilibrium tend to decrease the interruption capability predicted by the model. Regardless of the declaration of a chemically non-equilibrium model, However, the properties used in the modelling are obtained under chemical equilibrium. Above all, a more real model taking into account the high-current phase and the evolution of the decaying current to study the influence of departures from thermal equilibrium on the decay behaviour of the arc is also required.

1.4 Outline of the Thesis

As previously discussed, the transient and decaying processes of gas blast arcs are often vital in fault current interruption. Achieving an effective utilization and exploitation of the interruption capability of SF_6 requires a thorough understanding of the plasma properties and its physical process. Therefore, the focus of the present investigation is the computer modelling and experimental investigation of such process in order to elucidate some basic phenomena during the process.

The contents of the thesis are arranged into 8 chapters. The first chapter gives a brief introduction of this thesis, the review of the progress and the remaining problem for elucidation of SF_6 gas-blasted arc interruption phenomena. The scope of investigation is also given.

Chapter 2 covers the updated computation of species composition, thermodynamic properties and transport coefficients of SF_6 plasmas under LTE state using a higher order approximation because much relevant experimental and theoretical work of individual species

database has been performed and more accurate representations of the intermolecular potentials using a phenomenological approach, which can reduce the uncertainties in the values of transport coefficients, are available recently. The influence of different pressures and ions shielding effects in the Debye length was analysed. A comparison between our improved properties data set and previous theoretical and experimental results is performed as well.

Chapter 3 gives the computation results of species composition, thermodynamic properties and transport coefficients of a two-temperature SF_6 plasma. This chapter focuses on study how the choice of two-temperature mass action laws (Saha equations and Guldberg-Waage equations) affects the thermodynamic properties and transport coefficients of SF_6 plasmas under both thermal equilibrium and non-equilibrium conditions. The electrons and heavy species are treated as two different gases with Maxwell-Boltzmann distribution but with different temperatures. The species composition is numerically determined using two typical forms of two-temperature mass action laws, i.e. Potapov's method and Van de Sanden et al.'s method. By applying the modified Chapman-Enskog approach, the two-temperature transport coefficients of electrons and heavy species are computed independently under different non-equilibrium degrees of electrons and heavy species temperature ratio. The great influence of the choice of two-temperature mass action laws expressions and the excitation temperature on properties is discussed as well.

Chapter 4 describes arc-shock interaction and its influence on dynamic characteristics and decaying behaviour of SF_6 arcs in a supersonic nozzle with hollow contact, which is representative of switching arcs in a gas blast high voltage circuit breaker, using the magneto-hydro-dynamic (MHD) theory with a fixed inlet stagnation pressures and at five different exit pressure to inlet stagnation pressure ratios (referred to as pressure ratios). The physical parameters, such as the arc radius, the flow field, the temperature, and the electric field strength before and after current-zero during the arc decaying process have been obtained. The significant quantity in determining the thermal interruption capability of a circuit breaker, i.e. the critical rate of rise of recovery voltage (RRRV), was predicted and compared with available experimental test results. The deterioration of thermal interruption capability of a

supersonic nozzle under shock conditions which has been observed in previous test is discussed by current arc model.

Chapter 5 performs the computation modelling of the dynamic characteristics and decaying behaviour for a supersonic nozzle SF_6 arc in a two-temperature hydrodynamic model. In the flow affected region of the arc, the continuum approach and charge neutrality are assumed with electrons and heavy species have the same velocity but different temperatures. A general multi-fluid model is used to derive the conservation equations. The arc decaying characteristics are simulated by simultaneous solving of the sets of conservation equations under well defined boundary and with the effect of turbulence considered using the Prandtl mixing length model. The computational results are compared with the experimental results and with prediction by LTE model. The influence of departure from equilibrium along with the arc radiation reabsorption on decaying behaviour is discussed as well.

Chapter 6 investigates the influence of chemically non-equilibrium effects on species evolution utilizing a kinetic global model concerning the period when the electrons disappear in post-arc phase during the decaying process of gas blast SF_6 arc. The main mechanisms of electrons elimination in a wide temperature range from 12000K to room temperature are investigated using most recent chemical reaction kinetics. The critical breakdown field of hot SF_6 and its mixture with PTFE vapour after arc extinction are computed based on a two-term Boltzmann equation solution of electrons energy distribution function (EEDF) using improved cross section sets and a comparison with available test results is given. Furthermore, combined with kinetic analysis of species decaying, the influence of departure from chemical equilibrium on dielectric strength of hot SF_6 is discussed.

Chapter 7 carries out an experimental investigation of dynamic characteristics and decaying behaviour of SF_6 arcs with a model gas blast interrupter using various diagnostic actions such as voltage & current waveforms, pressure sensor, optical access together with displacement sensor under different test sets. An emission spectroscopy diagnostic of arcing is used to identify the elements existing in the arc plasma and an optical fibre together with photon detector is adopted to obtain the evolution characteristics of arc radiation. Moreover, the arcing behaviour and interruption capability of carbon dioxide and nitrogen is compared

with sulphur hexafluoride considering their possible replacement of SF_6 and the deviation of interruption capability is explained by means of gas properties.

Finally, in chapter 8, appropriate conclusions are drawn and possible future work discussed.

1.4 References

[1] Faraday, Michael (1839, 1844). Experimental Researches in Electricity, vols. i. and ii.. Richard and John Edward Taylor.; vol. iii. Richard Taylor and William Francis (1855).

[2] William Crookes, On Radiant Matter. Lecture delivered before the British Association for the Advancement of Science, at Sheffield, Friday, August 22, 1879. The Popular Science Monthly, Volume 16. D. Appleton (1880).

[3] J. J. Thomson and G. P. Thomson, "Conduction of Electricity through Gases", London: CUP (1933).

[4] J. S. Townsend, "Electricity in Gases", Oxford University Express (1914).

[5] L. Tonks and I. Langmuir, "A General Theory of the Plasma of an Arc", Phy. Rev., 34, 876 (1929).

[6] M. I. Boulos, P. Fauchais and E. Pfender, "Thermal Plasmas", Vol. 1, Plenum Press, London and New York (1994).

[7] C. Guy Suits, Editor, "The Collective Works of Irving Langmuir", Vol. 5, Pergamon Press (1961).

[8] A. Simon, "Introduction to Thermonuclear Research", Pergamon Press (1959).

[9] B. Chervy, A. Gleizes and M. Razafinimanana, "Thermodynamic properties and transport coefficients in SF_6-Cu mixtures at temperatures of 300-30000 K and pressures of 0.1-1 MPa", J. Phys. D: Appl. Phys., 27, 1193 (1994).

[10] K. C. Paul, T. Sakuta and T. Takashima, "Transport and thermodynamic properties of SF_6 gas contaminated by PTFE reinforced with Al_2O_3 and BN particles", IEEE Trans. Plasma Sci., 25, 786 (1997).

[11] B. Chervy, "The influence of the presence of tungsten on SF_6 arc plasmas", J. Phys. D: Appl. Phys., 29, 2156 (1996).

[12] Speckhofer G et al, "A consistent set of thermodynamic properties and transport coefficients for high temperature plasmas", 14th Int. Symp. On Plasma Chemistry, Prague, Czech Republic, 1999.

[13] J. L. Zhang, J. D. Yan, A.B. Murphy, W. Hall and M. T. C. Fang, "Computational investigation of arc behaviour in an auto-expansion circuit breaker contaminated by ablated nozzle vapor", IEEE Trans. Plasma Sci., 2, 706 (2002).

[14] W. Hertz, H. Motschmann and H. Wittel, "Investigations of the properties of SF_6 as an arc quenching medium", 1971, Proc. IEEE, 59, 485.

[15] A. R. Dayal and A. D. Stokes, "Measurement of transport properties of SF_6 at high temperatures and pressures", J. Phys. D: Appl. Phys., 32, 2949 (1999).

[16] A. Gleizes, J. J. Gonzalez, B. Liani and G. Raynal, "Calculation of net emission coefficient of thermal plasmas in mixtures of gas with metallic vapour", J. Phys. D: Appl. Phys., 26, 1921 (1993).

[17] A. Gleizes, J. J. Gonzalez, B. Liani and G. Raynal, "Calculation of net emission coefficient in N_2, SF_6 and SF_6-N_2 arc plasmas", J. Phys. D: Appl. Phys. 24, 1300(1991).

[18] V. Aubrecht, and M. Bartlova, "Net Emission Coefficients of Radiation in Air and SF_6 Thermal Plasmas", Plasma Chem. Plasma Proc., 29, 131 (2009).

[19] B. Eliasson and E. Schade, "Electrical breakdown of SF_6 at high temperatures (<2300 K)", 1977, Proc. 13th Int. Conf. Phenomena in Ionized Gases (Berlin) pp. 409–10.

[20] M. Nagata, I. Miyachi, Y. Yokoi and K. Isaka, ''Breakdown Characteristics of High Temperature Air and SF_6 Gas'', 1980, Proc. 6th IEE Conf. Gas Discharges and Their Applications -London: IEE, pp. 78.

[21] L. Rothhardt, J. Mastovsky and J. Blaha, "Dielectric strength of SF_6 at elevated temperatures", J. Phys. D: Appl. Phys., 14, L215 (1981).

[22] L. Rothhardt, J. Mastovsky and J. Blaha, "Breakdown experiments in diluted SF_6 at elevated temperatures", J. Phys. D: Appl. Phys., 18, L155 (1985).

[23] J. D. Yan, M. T. C. Fang and Q. S. Liu, "Dielectric breakdown of a residual SF_6 plasma at 3000K under diatomic equilibrium", IEEE T DIELECT EL IN, 4, 114 (1997).

[24] G. J. Cliteur, Y. Hayashi, E. Haginomori and K. Suzuki, "Calculation of the uniform breakdown field strength of SF_6 gas", IEEE T DIELECT EL IN, 5, 843 (1998).

[25] M. Yousfi, Ph. Robin-Jouan, Z. Kanzari, "Breakdown Electric Field Calculations of Hot SF_6 for High Voltage Circuit Breaker Applications", IEEE T DIELECT EL IN, 12, 1192 (2004).

[26] Ph. Robin-Jouan, M. Yousfi, "New Breakdown Electric Field Calculation for SF_6 High Voltage Circuit Breaker Applications," Plasma Sci. Technol., 9, 690 (2007).

[27] E. Lewis, N. Y. Shammas and G. R. Jones, “The current zero SF_6 blast arc at high di/dt”, in Proc.8th Int. Conf. on Gas Discharges and Their Applications, 1985, pp.35-38.

[28] E. Lewis, A. N. Prasad and G. R. Jones, “Current zero spectroscopy of a high power SF_6 circuit breaker arc”, in Proc.8^{th} Int. Conf. on Gas Discharges and Their Applications, 1985, pp.31-34.

[29] Y. Tanaka, Y. Yokomizu, T. Matsumura and Y. Kito, “Transient behaviour of axial temperature distribution in post-arc channel after current zero around nozzle throat in flat-type SF_6 gas-blast quenching chamber”, J. Phys. D: Appl. Phys., 28, 2095 (1995).

[30] Y. Tanaka, Y. Yokomizu, T. Matsumura and Y. Kito, “Transient distribution of metallic vapour concentration in a post-arc channel after current zero along the nozzle axis in a flat-type SF_6 gas-blast quenching chamber”, J. Phys. D: Appl. Phys., 29, 1540 (1996).

[31] G. R. Jones, W. Hu and S. M. Ei-Kholy, “A spectroscopic investigation of electrode material entrained into the extinguished arc of an SF_6 circuit breaker”, J. Phys. D: Appl. Phys., 21, 1414 (1988).

[32] R. Kozakov, M. Kettlitz, K. Weltmann, A. Steffens and C. M. Franck, “Temperature profiles of an ablation controlled arc in PTFE: I. Spectroscopic measurement”, J. Phys. D: Appl. Phys., 40, 2499 (2007).

[33] M. Seeger, M. Schwinne, R. Bini, N. Mahdizadeh, T. Votteler, “Dielectric recovery in a high-voltage circuit breaker in SF_6”, J. Phys. D: Appl. Phys., 45, 395204 (2012).

[34] T. Mori, H. Ohashi, H. Mizoguchi, K. Suzuki, “Investigation of technology for developing large capacity and compact size GCB”, IEEE Transactions on Power Delivery, 12 ,747 (1997).

[35] R. Bini, N.T. Basse, and M. Seeger, “Arc induced turbulent mixing in an SF_6 circuit breaker model”, J. Phys. D: Appl. Phys., 44, 25203(2011).

[36] J. J. Gonzalez, P. Freton, F. Reichert and D. Randrianarivao, “Turbulence and magnetic field calculations in high voltage circuit breakers”, IEEE Trans. Plasma Sci., 40, 936 (2012).

[37] M.T. C. Fang, Q. Zhuang and X. J. Guo, “Current zero behaviour of an SF_6, gas blast arc. Part II: turbulent flow”, J. Phys. D: Appl. Phys., 27, 74 (1994).

[38] J. D. Yan, R. E. Blundel and Fang M T C, "A comparative study of turbulence models for SF_6 arcs in supersonic nozzle", J. Phys. D: Appl. Phys., 32, 1401 (1999).

[39] J. L. Zhang, J. D. Yan, A.B. Murphy, W. Hall and M. T. C. Fang , "Computational investigation of arc behaviour in an auto-expansion circuit breaker contaminated by ablated nozzle vapor", IEEE Trans. Plasma Sci., 2 ,706 (2002).

[40] R. W. Liebermann, and J. J. Lowke, "Radiation emission coefficients for sulphur hexafluoride arc plasmas", J. Quantum Spectrosc. Radiat. Transfer, 14, 11 (1974).

[41] J. F. Zhang, M. T. C. Fang and D. B. Newland, "Theoretical investigation of a 2 kA arc in a supersonic nozzle", J. Phys. D: Appl. Phys., 20, 368 (1987).

[42] C. M. Dixon, J. D. Yan and M. T. C. Fang, "A comparison of three radiation models for the calculation of nozzle arcs', J. Phys. D: Appl. Phys., 37, 3309 (2004).

[43] S. D. Eby, J. Y. Trepanier and X. D. Zhang, " Modeling radiative transfer in SF_6 circuit breaker arcs with the P-1 approximation", J. Phys. D: Appl. Phys., 31, 1578 (1998).

[44] V, Aubrecht and J, J, Lowke, "Calculations of radiation transfer in SF_6 plasmas using the method of partial characteristics", J. Phys. D: Appl. Phys., 27, 2066 (1994).

[45] V. K. Liau, B. Y. Lee, K. D. Song and K. Y. Park, "The influence of contacts erosion on the SF_6 arc ", J. Phys. D: Appl. Phys., 39, 2114 (2006).

[46] J. L. Zhang, J. D. Yan, and M. T. C. Fang, "Electrode evaporation and its effects on thermal arc behaviour," IEEE Trans. Plasma Sci., 3, 1352 (2004).

[47] R. R. Sturzenegger and H. J. Schoetzau, "Influence of a shock wave on the electric field strength distribution in a gas blast interrupter," IEEE Trans. Power App. Syst., PAS-99, 1957 (1980).

[48] D. M. Benenson, G. Frind, R. E. Kinsinger, H. T. Nagamatsu, H. O. Noeske, and R. E. Sheer Jr., "Fundamental investigation of arc interruption in gas flows," EPRI Rep., EL–1455, Res. Project 246–2, 26 (1980).

[49] L. C. Campbell, J. F. Perkins, and J. L. Dallachy, "Effect of nozzle pressure ratio on SF_6 arc interruption," in Proc. 4th Int. Conf. Gas Discharges, Swansea, 1976, pp. 44–47.

[50] M. T. C. Fang, S. Kwan, and W. Hall, "Arc-shock interaction inside a supersonic nozzle," IEEE Trans. Plasma Sci., 24, 85 (1996).

[51] J. D. Yan, M. T. C. Fang, and C. Jones, "Electrical and aerodynamic behaviour of arcs

under shock conditions," IEEE Trans. Plasma Sci., 25, 840 (1997).

[52] J. L. Zhang, J. D. Yan, M. T. C Fang, "Investigation of the effects of pressure ratios on arc behaviour in a supersonic nozzle," IEEE Trans. Plasma Sci., 28, 1725(2000).

[53] V. Rat, A. B. Murphy, J. Aubreton, M. F. Elchinger, and P. Fauchais, "Treatment of non-equilibrium phenomena in thermal plasma flows", J. Phys. D: Appl. Phys., 41, 183001 (2008).

[54] K. P. Brand and J. Kopainsky, "Particle Densities in a Decaying SF_6 Plasma", Appl. Phys., 16, 425 (1978).

[55] A. Gleizes, F. Mbolidi and A.A.M. Habibt, "Kinetic model of a decaying SF_6 plasma over the temperature range 12000 K to 3000 K", Plasma Sources Sci. Technoi. 2, 173 (1993).

[56] L. Adamec and O. Coufal, "On kinetics of reactions in HV circuit breakers after current zero", J. Phys. D: Appl. Phys., 32, 1702(1999).

[57] V. Rat, P. André, J. Aubreton, M.F. Elchinger, P. Fauchais, and A. Lefort, "Two-Temperature Transport Coefficients in Argon–Hydrogen Plasmas—II: Inelastic Processes and Influence of Composition", Plasma Chem. Plasma Process. 22, 475 (2002).

[58] S. Ghorui, J. V. R. Heberlein, and E. Pfender, "Thermodynamic and Transport Properties of Two-temperature Oxygen Plasmas", Plasma Chem. Plasma Process. 27, 267 (2007).

[59] J. Aubreton, M.F. Elchinger, and P. Fauchais, "New Method to Calculate Thermodynamic and Transport Properties of a Multi-Temperature Plasma: Application to N_2 Plasma", Plasma Chem. Plasma Process. 18, 1 (1998).

[60] J. Aubreton, M.F. Elchinger, P. Fauchais, V. Rat, and P. André, "Thermodynamic and transport properties of a ternary Ar–H_2–He mixture out of equilibrium up to 30000K at atmospheric pressure", J. Phys. D: Appl. Phys. 37, 2232 (2004).

[61] J. Aubreton, M. F. Elchinger, V. Rat, and P. Fauchais, "Two-temperature transport coefficients in argon–helium thermal plasmas", J. Phys. D: Appl. Phys., 37, 34 (2004).

[62] J. Aubreton and M. F. Elchinger, "Transport properties in non-equilibrium argon, copper and argon–copper thermal plasmas", J. Phys. D: Appl. Phys. 36, 1798 (2003).

[63] S. Ghorui, J.V.R. Heberlein, and E. Pfender, "Thermodynamic and Transport Properties of Two-Temperature Nitrogen-Oxygen Plasma", Plasma Chem. Plasma Process. 28, 553

(2008).

[64] V. Colombo, E. Ghedini, and P. Sanibondi, “Thermodynamic and transport properties in non-equilibrium argon, oxygen and nitrogen thermal plasmas”, Prog. Nuclear Energy 50, 921 (2008).

[65] V. Colombo, E. Ghedini and P. Sanibondi, “Two-temperature thermodynamic and transport properties of argon–hydrogen and nitrogen–hydrogen plasmas”, J. Phys. D: Appl. Phys. 42, 0552131 (2009).

[66] V. Colombo, E. Ghedini and P. Sanibondi, “Two-temperature thermodynamic and transport properties of carbon–oxygen plasmas”, Plasma Sources Sci. Technol. 20, 035003 (2011).

[67] W.Z. Wang, M. Z. Rong, J. D. Yan, A. B. Murphy, and J.W. Spencer, “Thermophysical properties of nitrogen plasmas under thermal equilibrium and non-equilibrium conditions”, Phys. Plasmas, 18, 113502 (2011).

[68] A. Gleizes, B. Chervy, and J. J. Gonzales, “Calculation of a two-temperature plasma composition: bases and application to SF_6”, J. Phys. D: Appl. Phys. 32, 2060 (1999).

[69] Y. Tanaka, Y. Yokomizu, M. Ishikawa, and T. Matsumura, “Particle composition of high-pressure SF_6 plasma with electron temperature greater than gas temperature”, IEEE Trans. Plasma Sci. 25, 991 (1997).

[70] G. J. Cliteur, K. Suzuki, Y. Tanaka, T. Sakuta, T. Matsubara, Y. Yokomizu, and T. Matsumura, “On the determination of the multi-temperature SF_6 plasma composition”, J. Phys. D: Appl. Phys. 32,1851 (1999).

[71] V. Rat, P. André, J .Aubreton, M. F .Elchinger, P. Fauchais, and A. Lefort, “A modified pseudo-equilibrium model competing with kinetic models to determine the composition of a two-temperature SF_6 atmosphere plasma”, J. Phys. D: Appl. Phys. 34, 2191 (2001).

[72] J. P. Trelles, C. Chazelas, A. Vardelle, and J. V. R. Heberlein, “Arc Plasma Torch Modeling “, Journal of Thermal Spray Technology, 18, 728 (2009).

[73] V. Colombo, E. Ghedini, M. Boselli, P. Sanibondi and A. Concetti, “3D static and time-dependent modelling of a dc transferred arc twin torch system’, J. Phys. D: Appl. Phys., 44, 194005 (2011).

[74] K. C. Hsu and E. Pfender, “Two-temperature modeling of the free-burning high intensity arc”, J. Appl. Phys., 54, 4359 (1983).

[75] J. Haidar, “Non-equilibrium modelling of transferred arcs”, J. Phys. D: Appl. Phys., 32 263(1999).

[76] R. Girard, J. J. Gonzalez and A. Gleizes, “Modelling of a two-temperature SF_6 arc plasma during extinction”, J. Phys. D: Appl. Phys., 32, 1229 (1999).

[77] J. J. Gonzalez, R. Girard and A. Gleizes, “Decay and post-arc phases of a SF_6 arc plasma: a thermal and chemical non-equilibrium model’, J. Phys. D: Appl. Phys., 33, 2759 (2000).

CHAPTER 2 THERMODYNAMIC PROPERTIES AND TRANSPORT COEFFICIENTS OF HIGH TEMPERATURE EQUILIBRIUM SF_6 PLASMAS

2.1 Introduction

The structural geometry of Sulfur Hexafluoride (SF_6) gas molecule has octahedral geometry, containing sulfur atom at the center connecting six fluorine atoms around sulfur atom. The majority of its applications lie in electrical industry used as dielectric and arc quenching medium in circuit breakers and in switch gears [1]-[2]. SF_6 circuit breakers and SF_6 switchgears become more popular in high voltage engineering at present days because of better arc quenching ability and compactness. SF_6 gas is used as insulating medium between live parts of the high voltage equipment. So the clearances required between live parts reduce thus making the power system compact. When current fault takes place, based on electrode separation, an arc in the SF_6 environment is created and it must be rapidly extinguished in order to protect the power system. Investigation into the behaviour of the arc plasma is of great relevance to the development of switching devices. In order to understand the characteristics of high voltage SF_6 arc, mainly experimental investigations have been carried out so far, although it is expensive and time consuming. Whereas it is still insufficient to obtain some internal parameters of the arc plasma, such as gas velocity, current density, and so on. With the continuous development of the arc model and computational fluid dynamics (CFD) commercial code, it is possible for using the numerical method to obtain arc information, and the simulation is becoming an effective approach to complement the experimental research on the arc behaviour.

Numerical modelling is an important means of obtaining the information required to improve our understanding of the processes by which current interruption occurs. Of particular note is that accurate data for the composition, thermodynamic properties and transport coefficients are a prerequisite for reliable numerical simulation of thermal plasmas in setting up the physical models. Unfortunately, transport coefficients are difficult to calculate, and large discrepancies still remain in the values presented by different authors.

These partly result from the uncertainties in the gas composition and approximations made in the calculations, but are mainly due to uncertainties in the values of the intermolecular potentials from which the transport coefficients are derived [3]. The literature reports a fair number of calculations of these properties for pure SF_6 plasmas and its mixtures with other gases [4]-[20]. The input data utilized, such as the intermolecular potentials, were adequate representations over limited temperature ranges. However, much relevant experimental and theoretical work has been performed since that time and more accurate representations of the intermolecular potentials, which can reduce the uncertainties in the values of transport coefficients, are available.

This chapter is organized as follows: in section 2, the determination of chemical equilibrium composition including the fundamental principles, the computational techniques along with the individual database for a large set of species produced from SF_6 plasmas are described. Calculation of the thermodynamic properties, including mass density, molar weight, sonic velocity, specific heat ratio, enthalpy, entropy, and specific heat is presented in section 3. In section 4, the method of calculation of the transport coefficients, namely diffusion coefficients, thermal conductivities, electrical conductivity and viscosity is outlined. The collision integrals, the choice of intermolecular potentials used in evaluating them and various approaches used in determining transport properties are presented in Section 5. Calculated species composition, thermodynamic properties and transport coefficients for pure SF_6 and a comparison with available literature data at high temperature, are given in section 6. Meanwhile, the influence of pressure and Debye length definition on computed properties is illustrated as well. Finally, conclusions are drawn in Section 7.

2.2 Theory of Chemical Equilibrium

2.2.1 Determination of Species Composition

The calculations are based on the assumption of local thermodynamic equilibrium (LTE). The assumption of LTE is generally accepted to be consistent with observations for thermal plasmas such switching arcs at atmospheric and higher pressures. By this it is meant that at any point in the plasma, the electrons, ions, and neutral particles have the same kinetic temperature and

chemical equilibrium has been achieved locally. Plasma properties are then calculated from the equilibrium compositions which are functions of plasma temperature and pressure only. Thus the first step is to calculate the equilibrium compositions. The chemical equilibrium composition is determined as a function of temperature and pressure by finding the species composition that minimizes the Gibbs free energy of reacting mixtures system [21], which is a standard technique in equilibrium chemistry [22]-[24] and will be briefly described later. This method is applicable to closed isothermal and isobaric systems.

The thermodynamic properties of the system are completely determined by the total Gibbs free energy in terms of the chemical potentials.

$$g = \sum_{i=1}^{w} n_i \mu_i \tag{2.1}$$

where g is the Gibbs free energy of system; w is the total number of species occurring in the system; n_i and μ_i are the number density and chemical potential of species i respectively. Once chemical equilibrium is attained, the total Gibbs free energy of the system is minimized subject to the constraints of mass balance.

$$\sum_{j=1}^{w} a_{ij} n_j = b_i^0 \quad i = 1,\ 2,\ \ldots\ldots,\ m \tag{2.2}$$

where a_{ij} are the stoichiometric coefficients of element i in chemical species j, b_i^0 is the assigned number of moles of element i in the total reactants, and m is the number of elements present.

Define a term $G = g + \sum_{i=1}^{w} \lambda_i (\sum_{j=1}^{w} a_{ij} n_j - b_i^0)$ where λ_i is the Lagrangian multiplier, the condition for equilibrium becomes

$$\delta G = \sum_{j=1}^{w} (\mu_j + \sum_{i=1}^{l} \lambda_i a_{ij}) \delta n_j + \sum_{i=1}^{l} (a_{ij} n_i - b_i^0) \delta \lambda_i = 0 \tag{2.3}$$

Treating the variation δn_j , $\delta\lambda_i$ as the independent gives

$$\mu_j + \sum_{i=1}^{l} \lambda_i a_{ij} = 0 \tag{2.4}$$

And also gives the mass-balance equation.

The chemical potential of species i can be evaluated as follows:

$$\mu_i = \mu_i^0 + RT\ln(P/P_0) + RT\ln(n_i / \sum_{i=1}^{w_{\max}^g} n_i) \qquad \text{for gaseous and plasmas species;}$$

$$\mu_i = \mu_i^0 \qquad \text{for condensed species}$$

$$\mu_i^0 = H_{T,i}^0 - T \cdot S_{T,i}^0 \tag{2.5}$$

where μ_i^0 and P_0 are the chemical potential and reference pressure in the standard state respectively; $S_{T,i}^0$, $H_{T,i}^0$ are respectively the standard-state specific entropy and standard-state specific enthalpy of specie i, $w_{\max}^g$ is the total number of gaseous and plasmas species. For gaseous species, the standard state is a hypothetical state in which the gas is behaving ideally at unit fugacity and obeying the ideal gas equation whereas the standard state of a pure condensed substance is its most stable state for under a total pressure of 0.1MPa.

Along with the law of mass balance, the equilibrium rule must be combined with the law of electrically quasi-neutrality and Dalton's Law [24]. The Debye–Hückel correction, which is an adjustment to the usual expression for the Gibbs free energy representing the additional effect of electrostatic interactions between the charged particles, is taken into account in determining the chemical potential of charged species and the total number density of the plasma, as described by Kovitya [25]. This requires correction terms to be added to the expression given in Eq. (2.5) for the gaseous species and to Dalton's Law, i.e. the equation of state, as presented in Eq. (2.6) and (2.7) respectively:

$$\mu_i = \mu_i^0 + RT\ln(P/P_0) + RT\ln(n_i / \sum_{i=1}^{w_{\max}^g} n_i) - RT(eZ_i)^2 / (8\pi\varepsilon_0 kT\lambda_D) \quad (2.6)$$

$$P + kT/(24\pi\lambda_D^3) = \sum_{i=1}^{w_{\max}^g} n_i kT \quad (2.7)$$

where Z_i is the charge number of species i, e and ε_0 are the electron charge and permittivity of free space respectively, and λ_D is the Debye length calculated including both the contribution from electrons and heavy ions.

The relations used to determine the composition are not all linear in the independent variables and therefore an iteration procedure is generally required for their solution. The method of Gordon and McBride using Lagrange multipliers along with steepest descent Newton–Raphson iteration is utilized to solve the non-linear equation system numerically [21].

2.2.2 Determination of Thermodynamic Properties

The thermodynamic properties of gaseous mixtures, such as mass density, molar weight, enthalpy and specific heat at constant pressure can be determined relatively simply once the chemical equilibrium composition is known, using the standard formulas.

- **Mass Density**

$$\rho = \sum_{i=1}^{w_{\max}^g} m_i n_i \quad (2.8)$$

where m_i is the mass of species i.

- **Molar Weight**

$$M = \sum_{i=1}^{w_{\max}^g} x_i M_i \quad \text{with} \quad x_i = n_i / \sum_{i=1}^{w_{\max}^g} n_i \quad (2.9)$$

where x_i and M_i are the molar fraction and molar mass of species i.

- **Specific Enthalpy**

$$h = \sum_{i=1}^{w_{\max}^g} x_i H_{T,i}^0 / M \tag{2.10}$$

where $H_{T,i}^0$ is the standard state molar enthalpy of species i.

- **Specific Heat at Constant Pressure**

$$C_p = (\frac{\partial h}{\partial T})_p = \sum_{i=1}^{w_{\max}^g} n_i c_{p,i}^0 + \sum_{i=1}^{w_{\max}^g} n_i H_{T,i}^0 (\frac{\partial \ln n_i}{\partial \ln T})_P / T \tag{2.11}$$

where $c_{p,i}^0$ is the standard-state specific heat of specie *i*, the first term in the right hand side of Eq. (2.11) is the specific heat of the mixture if no reaction between species are considered and it is usually called the frozen specific heat. The second term is the reactional contribution to the specific heat.

- **Specific Entropy**

$$s = \sum_{i=1}^{w_{\max}^g} x_i S_i / M \qquad \text{with} \quad S_i = S_{T,i}^0 - R\ln(x_i) - R\ln(P/P_0) \tag{2.12}$$

where $S_{T,i}^0$ is the standard-state specific entropy of species i.

- **Specific Heat Ratio**

$$\gamma = \frac{C_p}{C_v} \tag{2.13}$$

With $C_v = C_p - \frac{R}{M}\frac{(T\alpha)^2}{P\beta}$ being specific heat at constant volume. where α, β are isobaric thermal expansion coefficient and isothermal compressibility respectively.

- **Sonic Velocity**

$$v_s = \sqrt{\frac{\gamma RT}{P\beta M}} \tag{2.14}$$

Corrections to perfect gas behaviour have been determined using the Debye-Hückel theory as described in the literature [26]-[28].

2.2.3 Calculation of Thermochemical Function

The thermochemical functions $C_{p,i}^0$, $H_{T,i}^0$ and $S_{T,i}^0$ should be input for each species. The required thermodynamic data are calculated from reported values of rotational constants, fundamental vibrational frequencies, excited electronic state energies, and enthalpies of formation, and are determined by standard statistical mechanical methods. The coefficients are fitted using a least-squares method, constructing the three thermodynamic functions of specific heat, enthalpy and entropy as functions of temperature in a form compatible to most computational plasma aerodynamics codes by means of the NASA computer program CEA (Chemical Equilibrium with Applications)[29]. The standard form of Gordon and McBride is employed as follows [30].

- **Specific Heat**

$$C_P^0 / R = a_1 + a_2 T + a_3 T^2 + a_4 T^3 + a_5 T^4 \tag{2.15}$$

- **Enthalpy**

$$H_T^0 / RT = a_1 + a_2 T / 2 + a_3 T^2 / 3 + a_4 T^3 / 4 + a_5 T^4 / 5 + a_6 / T \tag{2.16}$$

- **Entropy**

$$S_T^0 / R = a_1 \ln T + a_2 T + a_3 T^2 / 2 + a_4 T^3 / 3 + a_5 T^4 / 4 + a_7 \tag{2.17}$$

where R is the ideal gas constant and T is temperature.

All these thermodynamic data involve the determination of partition function of each species which establish the link between the coordinates of microscopic systems and macroscopic thermodynamic properties. The properties are expressed as functions of the internal partition function [30].

$$\frac{C_P^0}{R} = T^2 \frac{d^2(\ln Q_{\text{int}})}{dT^2} + 2T \frac{d(\ln Q_{\text{int}})}{dT} + 2.5 \tag{2.18}$$

$$\frac{H_T^0 - H_0^0}{RT} = T \frac{d(\ln Q_{\text{int}})}{dT} + 2.5 \tag{2.19}$$

$$\frac{S_T^0}{R} = T \frac{d(\ln Q_{\text{int}})}{dT} + \ln Q_{\text{int}} + 1.5 \ln M + 2.5 \ln T + S_c$$

$$S_c = \ln[k(\frac{2\pi k}{N_0 h^2})^{1.5}] \tag{2.20}$$

where S_c ， N_0 are the Sackur-Tetrode constant and Avogadro constant respectively.

In general, the partition function can be expressed as:

$$Q_t = Q_{tr} \cdot Q_{rot} \cdot Q_{vib} \cdot Q_{el} \cdot Q_{nucl} = Q_{tr} \cdot Q_{\text{int}} \tag{2.21}$$

where the individual partition functions represent translational, rotational, vibrational, electronic, and nuclear contributions respectively. The nuclear partition function is usually assumed to the degeneracy of nuclear ground state because it usually need thousands of eV to reach nuclear excitation indicating that the chemical reactions contributes no change in the nuclear energy levels in thermal plasmas. The nuclear partition function does not affect the internal energy of a species, as well as other properties because its logarithmic derivative is zero in the temperature of 100000K.

2.2.4 Evaluation of Partition Function

- **Monatomic Species**

For monatomic molecules, internal energy consists of electronic energy only

$$Q_{int} = Q_{el} = \sum_{e}^{\varepsilon_j < E_{ieff}} g_{e,j} \exp^{-\varepsilon_j / kT} \tag{2.22}$$

where ε_j electronic excitation energy, and $g_{e,j}$ statistical weight, respectively, for the j^{th} electronic state.

An infinite number of bound states exist below the ionization limit for a hypothetical isolated atom [30]. In as much as the partition function diverges and approaches infinity, the summation must be cut off. The ionization potential is reduced by a quantity referred to as the ionization potential lowering which in this case is a function of temperature only. The partition function is then permitted to include only those levels below the lowered ionization potential. It was suggested that the ionization potential be lowered by an amount equal to the temperature function *kT*. In addition to the divergence problem, there is the problem of whether to include observed energy levels only or to also include levels for predicted terms which, so far, have not been observed. When the statistical weights g_i corresponding to predicted terms were examined, it was determined that for many chemical elements the sum of the statistical weights can be expressed by the following simple function of the principal quantum number *n* (except for the ground state n of most species):

$$\sum g_{e,j} = \sum (2J_j + 1) = bn^2 \tag{2.23}$$

where J_j is total angular momentum quantum number for the j^{th} electronic state. *b* is the derived constant which has been contained in previously published literature . Equation (2.23) applies only to terms arising from excitation of the emission electron and does not account for other possible terms.

- **Diatomic and Polyatomic Species**

For a diatomic molecule, the internal partition functions are determined by means of the Morse potential minimization method [31].

$$\begin{aligned} Q_{\text{int}} &= Q_{el} \cdot Q_{vib} \cdot Q_{rot} \\ &= \frac{1}{\sigma_c} \sum_j g_{e,j} \exp(-\varepsilon_j / kT) \sum_v^{v_{\max}} \exp(-\varepsilon_{vib}(v) / kT) \sum_J^{J_{\max}} (2J+1) \exp(-\varepsilon_{rot}(v) / kT) \end{aligned} \tag{2.24}$$

With the vibration energy of the *v*-th vibrational state and *n*-th electronic state computed as:

$$\frac{\varepsilon_{vib}(n,v)}{hc} = \omega_e(v+\frac{1}{2}) - \omega_e x_e(v+\frac{1}{2})^2 + \omega_e y_e(v+\frac{1}{2})^3 + \omega_e z_e(v+\frac{1}{2})^4 \tag{2.25}$$

$$\frac{\varepsilon_{rot}(n,v,J)}{hc} = B_v J(J+1) - D_v(J(J+1))^2$$

$$B_v = B_e - \alpha_e(v+1/2)$$

$$D_v = D_e - \beta_e(v+1/2) \tag{2.26}$$

where $\varepsilon_{vib}(n,v)$ is the vibrational energy of the vth vibrational state and nth electronic state. $\varepsilon_{rot}(n,v,J)$ the rotational energy of the Jth rotational state with the vth vibrational state and nth electronic state. σ_c is a symmetry factor that has values of 1 and 2 for heteronuclear and homonuclear molecules, respectively. v and J are the vibrational and rotational quantum number respectively, and other parameters are spectroscopically-determined constants.

Maximum quantum number J_{max} of rotational energy levels can be computed following Drellishak et al. [31]. When the equilibrium radii r_e(n), the depth of the potential well $D_e^{'}(n) = D_0(n) + \varepsilon_{vib}(n,0)$ and spectroscopic constants $B_e(n)$ and $\omega_e(n)$ of the nth electronic state are known, the potential energy for a diatomic irrotational ($J=0$) molecule can be written as a function of internuclear distance through the Morse potential.

$$U_0(r) = D_e^{'}(1 - e^{-2\beta\xi}) \tag{2.27}$$

where $\xi = (r - r_e)/r_e$

$$\beta = \frac{\omega_e}{4\sqrt{BeD_e^{'}}} \tag{2.28}$$

When $J \neq 0$ the potential energy is given by the Morse potential plus the centrifugal potential.

$$U_J(r) = D_e^{'}(1 - e^{-2\beta\xi}) + \frac{h}{8\pi^2 c\mu r^2} J(J+1) \tag{2.29}$$

where h is the Planck constant and μ is the reduced mass of the two atoms in the molecule. For a given n and v, varying J we have different curves for the potential energy. These curves present a local maximum for radii greater than r_e, if $0 < J < J_{max}$. With $J = 0$ the Morse potential alone does not present a local maximum; with $J > J_{max}$ the curve of potential energy does not have a minimum for stable states. $J_{\max}$ is a function of n and v and can be calculated with the comparison between the rovibrational energy (The rovibrational energy is given by the sum of vibrational energy and rotational energy.) and the energy corresponding to the local maximum of the potential energy: for a given n and v, $J_{\max}$ is the minimum J for which the rovibrational energy is greater than the local maximum of the potential energy. The radii r_m corresponding to the local maximum of the potential energy is computed equating to zero of the derivative of Eq. (2.29) with respect to r; the potential energy in this point is $v_{\max} = U_J(r_m)$.

Due to the lack of accurate spectroscopic data for polyatomic species, the harmonic oscillation-rigid rotation approximation was used to describe the partition function of both the linear and non-linear polyatomic species and therefore, the calculation of the internal partition function is simplified: the discrete summations on rotational quantum numbers are replaced by an integral form [32].

$$Q_i == Q_{el} \cdot Q_{vib} \cdot Q_{rot} = \sum_j g_{e,j} \exp(-\varepsilon_j / kT) \prod_i [\frac{\exp(-\omega_i / 2kT)}{1 - \exp(-\omega_i / kT)}]^{g_i} (T / \theta_{rot})^{3/2} \tag{2.30}$$

where g_i is the statistical weight of vibration and θ_{rot} is the rotational constant. In the case of the

polyatomic specie, the rotational energy is that of a classical asymmetric top and expressed as a function of the three principal moments of inertia I_A, I_B and I_C.

$$(\frac{T}{\theta_{rot}})^{3/2} = \frac{\pi^{1/2}}{\sigma_c h^3}(I_A I_B I_C)^{1/2}(8\pi kT)^{3/2} \tag{2.31}$$

where k is the Boltzmann's constant.

2.2.5 Data for the Individual Species

In the calculation, it is assumed that the mixture of high temperature SF_6 gas is composed of a total of 25 different species including relevant atoms, ions and molecules as well as electrons: SF_6, SF_5, SF_4, SF_3, SF_2, SF, SSFF, FSSF, F_2, S_2, F, S, SF^+, SF^-, S^+, F^+, S^-, F^-, S^{2+}, F^{2+}, S^{3+}, F^{3+}, S_2^+, F_2^+ and e. Other molecular ions are neglected because of their low amount appearing in the system. The large number of species allows a precise determination of the equilibrium concentrations, even if the small concentration of some species does not have a significant influence on the transport coefficients. For example, the maximum concentration of S^- is quite low and will not change the final value of transport coefficient. However, they are also considered in order to show all relevant species concentration variation as the temperature and pressure changes.

The required thermodynamic data calculated from the internal partition functions for neutral atoms and positively-charged atomic ions were derived from the electronic energy levels tabulated by Moore [33]-[34]. Data for other species such as the gaseous diatomic and polyatomic species were taken from the JANAF Thermochemical Tables [35].

2.3 Derivation of Transport Coefficient

Transport coefficients, namely diffusion coefficients, electrical conductivity, thermal conductivities and viscosity, are calculated approximately using the classical Chapman–Enskog method, which has been analyzed exhaustively in the literature [36]-[38]. The distribution function of the different species is assumed to be a Maxwellian with a first-order perturbation if

LTE is assumed which accounts for a slight departure from Maxwellian distribution. The first-order perturbation function is developed by means of a series of Sonine polynomials and then expressed in terms of expansion coefficients, yielding a linearization of the Boltzmann equation and leading to the introduction of systems of linear equations. The solution of these linear equations to a selected order allows the transport coefficients to be determined.

2.3.1 Diffusion Coefficients

The expression of ordinary diffusion coefficients and thermal diffusion coefficients is presented as follows:

$$D_{ij}(\xi) = \frac{\rho n_i}{2 n m_j} \sqrt{\frac{2kT}{m_i}} c_{i0}^{j,i}(\xi) \tag{2.32}$$

$$D_i^T(\xi) = \frac{n_i m_i}{2} \sqrt{\frac{2kT}{m_i}} a_{i0}(\xi) \tag{2.33}$$

where the argument ξ is the number of terms used in the Sonine polynomial expansions.

The coefficients $c_{i0}^{j,i}(\xi)$, $a_{i0}(\xi)$ can be calculated from the following sets of linear equations [36]-[38].

$$\sum_j \sum_{m'=0}^{\zeta-1} \tilde{Q}_{ij}^{mm'} c_{im'}^{(h,k)}(\zeta) = 3\sqrt{\frac{kT}{2m_i}} (\delta_{ik} - \delta_{ih}) \delta_{m0} \tag{2.34}$$

$$\sum_j \sum_{m'=0}^{\zeta-1} \tilde{Q}_{ij}^{mm'} a_{jm'}(\zeta) = -\frac{15 n_i}{2} \sqrt{\frac{kT}{2m_i}} \delta_{m1} \tag{2.35}$$

$$\tilde{Q}_{ij}^{mm'} = \begin{cases} Q_{ij}^{mm'} & \mathrm{t}_{jm'}^{(h,k)} = b_{jm'} \\ Q_{ij}^{mm'} - \dfrac{n_j \sqrt{m_j}}{n_i \sqrt{m_i}} Q_{ij}^{mm'} \delta_{m0} \delta_{m'0} & \mathrm{t}_{jm'}^{(h,k)} = a_{jm'}, c_{jm'}^{(h,k)} \end{cases} \tag{2.36}$$

where the bracket integrals $Q_{ij}^{mm'}$ can be expressed as a linear combination of a set of collision integrals.

2.3.2 Viscosity

The viscosity of the plasma mixture can be calculated by

$$\eta(\xi) = \frac{kT}{2} \sum_j b_{j0}(\xi) \tag{2.37}$$

The coefficients $b_{j0}(\xi)$ can be calculated from the following sets of linear equations.

$$\sum_j \sum_{m'=0}^{\zeta-1} \tilde{Q}_{ij}^{mm'} b_{jm'}(\zeta) = -5 n_i \delta_{m0} \tag{2.38}$$

2.3.3 Thermal Conductivity

The thermal conductivity of the plasma mixture can be defined as the sum of internal, reaction and translational thermal conductivities.

$$\lambda_{total} = \lambda_{int} + \lambda_{reac} + \lambda_{trt} \tag{2.39}$$

The presence of internal degrees of freedom as a result of vibrational, rotational and electronic excitation can affect the heat flux vector and is included using an internal thermal conductivity, which has been derived using the Hirschfelder–Eucken approximation [39]-[41].

$$\lambda_{int} = \sum_{i=2}^{w} \frac{n D_{ii} (m_i C_{p,i} - 2.5k)}{\sum_{j=1}^{w} (D_{ii} x_j / D_{ij} x_i)} \tag{2.40}$$

where D_{ii}, $C_{p,i}$ and x_i are the self diffusion coefficient, specific heat at constant pressure and the molar fraction of the *i*th species respectively.

Chemical reactions (dissociation, recombination, ionization and so on) in a plasma in

chemical equilibrium leads to additional heat transfer. This leads to an additional reactive thermal conductivity, which was studied by Butler and Brokaw for neutral gas mixtures [42]; their expressions were subsequently extended to ionized gases by Meador and Stanton [43]. The reaction thermal conductivity is:

$$\lambda_{reac} = R\sum_{i=1}^{\mu}\frac{\Delta H_i}{RT}\lambda_{r,i} \tag{2.41}$$

where ΔH_i is the heat of reaction for reaction i, and

$$\Delta H_i = \sum_{k=1}^{\upsilon} a_{ik} H_k \qquad i = 1, 2, \ldots, \mu \tag{2.42}$$

where H_k is the specific enthalpy of the k th specie, a_{ik} are the stoichiometric coefficients for the chemical reactions involving species A_k as follows:

$$\sum_{k=1}^{\upsilon} a_{ik} A_k = 0 \qquad i = 1, 2, \ldots, \mu \tag{2.43}$$

The term $\lambda_{r,i}$ can be obtained by solving the following linear algebraic equation as derived by Meador and Stanton [43]:

$$\sum_{j=1}^{\mu} g_{ij}\lambda_{r,i} = \Delta H_j / RT \tag{2.44}$$

$$g_{ij} = \sum_{k=1}^{\mu-1}\sum_{l=k+1}^{\mu}\left[\frac{x_k x_l kT}{PD_{kl}}\left(\frac{a_{ik}}{x_k} - \frac{a_{il}}{x_l}\right)\times\left(\frac{a_{jk}}{x_k} - \frac{a_{jl}}{x_l}\right)\right] \tag{2.45}$$

where D_{kl} is the binary diffusion coefficient between species k and l.

The translational thermal conductivity can be determined by

$$\lambda_{trt} = \lambda^{'} + \frac{\rho k}{n} \sum_{i,j=1}^{\nu} \frac{E_{i,j} D_i^T D_j^T}{n_i m_i m_j} \tag{2.46}$$

$$\lambda^{'}(\xi) = -\frac{5}{4} k \sum_j n_j \sqrt{\frac{2kT}{m_i}} a_{i1}(\xi) \tag{2.47}$$

where $E_{j,i}$ is defined as an element of the inverse of the matrix whose general element is $D_{ij} m_j$. The coefficients $a_{i1}(\xi)$ can be calculated from Eq.(2.32). Using the decoupled method between electrons and heavy species [44], the translational thermal conductivity for electrons λ_{tre} and heavy species λ_{trh} can be separately obtained for comparison with total translational thermal conductivity λ_{trt}.

2.3.4 Electrical Conductivity

The electrical conductivity is given as:

$$\sigma = \frac{e^2 n}{\rho k T} \sum_{j=1, j\neq e}^{\zeta} (n_j m_j Z_j D_{ej} - Z_j \sum_{i=1}^{\zeta} n_i m_i Z_i D_{ji}) \tag{2.48}$$

where m_i, n_i, Z_i are the mass, number density, the electric charge and the thermal diffusion coefficient of specie *i* respectively. Ignoring the influence of heavy species, we can take into account only the contribution of electrons and simplify the expression of electrical conductivity.

$$\sigma \approx \frac{e^2 n}{\rho k T} \sum_{j=1, j\neq e}^{\zeta} n_j m_j Z_j D_{ej} \tag{2.49}$$

When electron number densities are relatively low, the accuracy of the electrical conductivity is limited by the accuracy of the electron-neutral cross section and the relatively slow convergence rate of the Chapman-Enskog approximations when applied to electron-neutral interaction.

2.3.5 Choice of the Terms Used in the Sonine Polynomial Expansions

The terms chosen in the terms used in the Sonine polynomial expansions governs the dimensions of the system of linear equations with which the distribution function and the Boltzmann equation are solved with an expansion expression. The accuracy of the transport properties is improved by increasing the terms. However, this requires a greater number of effective collision integrals, which are terms appearing in the expressions of the transport coefficients, and the number of calculations rapidly becomes prohibitive. It has been found that at least a third-order approximation is needed at low temperatures around 5000 K for the ordinary diffusion for interactions involving electrons [45]. The first-order approximation for viscosity can differ by more than 10% at high temperature from the third-order approximation [46]. It was concluded that in this case the second-order approximation was adequate [46]. Therefore, this thesis utilizes the third-order approximation for transport properties except viscosity, for which the second-order approximation is considered.

2.4 Collision Integrals

The transport coefficients rely on collision integrals which take into account the interaction potential between two species i and j. They are statistical averages over a Maxwellian distribution of the collision cross-sections for pairs of species and defined as follows [36]-[38]:

$$\Omega_{ij}^{(l,s)} = \sqrt{\frac{kT}{2\pi\mu_{ij}}} \int_0^\infty \exp(-\gamma_{ij}^2)\gamma_{ij}^{2s+3} Q_{ij}^{l}(g) d\gamma_{ij} \tag{2.50}$$

where the indices (l, s) are directly related to the order of approximation used for the transport coefficients and k is Boltzmann's constant, T is the temperature, μ_{ij} is the reduced mass and γ_{ij} is the reduced initial speed of the species i and j, given by:

$$\frac{1}{\mu_{ij}} = \frac{1}{m_i} + \frac{1}{m_j}$$

$$\gamma_{ij} = \sqrt{\frac{\mu_{ij}}{2kT}} g_{ij} \tag{2.51}$$

where g_{ij} is the initial relative speed of the species, and the transport cross sections $Q_{ij}^{l}(g)$ are defined by:

$$Q_{ij}^{l}(g) = 2\pi \int_{0}^{\infty} (1 - \cos^{l} \chi) b db \tag{2.52}$$

The parameters χ and b are the angle by which the molecules are deflected in the centre of gravity coordinate system and the impact parameter of the colliding molecules i and j respectively.

$$\chi = \pi - 2b \int_{r_m}^{\infty} \frac{dr / r^2}{\sqrt{1 - \left[\varphi_{ij}(r) / 0.5 \mu_{ij} g_{ij}^2 \right] - \left(b^2 / r^2 \right)}} \tag{2.53}$$

The term r_{m} is the outermost root of the equation:

$$1 - \frac{\varphi_{ij}(r)}{\frac{1}{2}\mu_{ij} g_{ij}^2} - \frac{b^2}{r_m^2} = 0 \tag{2.54}$$

And $\varphi_{ij}(r)$ is the potential energy of interaction between the colliding particles.

Each encounter between particles can be classified into one of four types: (a) neutral-neutral encounters; (b) neutral-ion encounters; (c) electron-neutral encounters; (d) encounters between charged particles.

2.4.1 Neutral–neutral Interactions

Many types of intermolecular potential have been used to determine the collision integrals for

interactions between neutral species. For example, Aubreton and coauthors performed calculations of Hulbert–Hirschfelder and exponential repulsive potentials, whose parameters were evaluated by non-linear regression to known potential energy curves of electronic bounded and unbounded states, respectively, for a wide range of species [47]-[49]. Besides the accuracy of original potential energy curves, the uncertainty of such approach mainly arises from the accuracy of the fit. For a good fit, the energy values must be reproduced as accurately as possible by the potential function. However, under some conditions, it is debatable whether the fitted potential is accurate outside the fitting range. André et al. used the classical Lennard–Jones potential and simple combining rules for the potential parameters of neutral–neutral interactions to obtain the transport coefficients for nitrogen and hydrogen plasmas, and plasmas of composition corresponding to the Mars and Titan atmospheres, obtaining satisfactory agreement with the results of other authors who used more complex approaches [50].

Recently, a new phenomenological model potential developed by Capitelli and co-workers [51]-[52] has been widely studied. The phenomenological potential provides an improved representation of the short-range region with a less hard repulsive wall, and moreover reproduces very well the interaction obtained by accurate ab-initio calculation in the long-range region. When comparing with complete set of quantum mechanical interaction potentials arising from the electronic configurations of separate partners, excellent agreement is achieved [53]. Therefore, it can provide an accurate estimation of those interaction potentials for which reliable experimental data or accurate theoretical calculations are not available.

The phenomenological potential has the following form [51]-[52]:

$$\varphi = \varepsilon_0 \left[\frac{m}{n(x)-m} \left(\frac{1}{x} \right)^{n(x)} - \frac{n(x)}{n(x)-m} \left(\frac{1}{x} \right)^{m} \right] \tag{2.55}$$

where $x = r / r_e$, $n(x) = \beta + 4\chi^2$ and the parameter r_e is the equilibrium distance. For neutral species interactions, the parameter *m* has the value of 6. β is determined by a simple empirical formula with the polarizability α as the input parameter.

$$\beta = 6 + \frac{5}{s1 + s2} \tag{2.56}$$

where the subscripts 1 and 2 identify the colliding partners. The softness s, entering in Eq. (2.56), is defined as the cubic root of the polarizability. For open-shell atoms and ions a multiplicative factor, which is the ground state spin multiplicity, should be also considered. For neutral–neutral systems, the phenomenological method represents the binding energy, e_0, and the equilibrium distance, r_e, in terms of polarizabilities of the interacting partners, by the following correlation formulas:

$$r_e = 1.767 \frac{\alpha_1^{1/3} + \alpha_2^{1/3}}{(\alpha_1 \alpha_2)^{0.095}} \tag{2.57}$$

$$\varepsilon_0 = 0.72 \frac{C_d}{r_e^6} \tag{2.58}$$

where r_e is given in Å , α in Å^3 and ε_0 in eV. The C_d constant is an effective long-range London coefficient:

$$C_d = 15.7 \frac{\alpha_1 \alpha_2}{[\sqrt{\alpha_1 / N_1} + \sqrt{\alpha_2 / N_2}]} \tag{2.59}$$

where N is the effective number of electrons which contribute to the polarization of the neutral species.

Unfortunately, experimental data are extremely limited for polarizabilities of most species that are present in our work. Coverage of dipole polarizabilities is particularly sparse. However, for these species, quantum chemical predictions for polarizabilities can be quite accurate if determined with a good correlated method. The values used here for heavy species are listed in table 2.1 and all these data are taken from the NIST Computational Chemistry Comparison and Benchmark Database [54].

Table 2.1 Species polarizability values ($Å^3$)

Species	Polarizability	Species	Polarizability	Species	Polarizability
F	0.557	S_2	14.3	S^-	6.583
SF_6	6.540	F_2	1.380	S_2^+	4.340
SF_5	5.951	FFSS	6.790	S	2.900
SF_4	3.579	FSSF	6.737	S_2^-	9.069
SF_3	4.837	F_2^+	0.913	SF^+	2.165
SF_2	8.300	F^-	2.294	SF^-	5.424
SF	7.700	F^+	0.262	S^+	1.613

We developed a new computer program, based on the work of Barker, Fock and Smith, to compute the collision integrals for the phenomenological potential [55].

2.4.2 Neutral–ion Interactions

For neutral–ion Interactions, two kinds of processes should be taken into account, purely elastic collisions and the resonant charge-exchange inelastic process. For odd l (l = 1 and 3), the latter plays important role in determining the collision integrals $\Omega_{ij}^{(l,s)}$. We follow the work of Murphy [56] and estimate the total collision integrals from the elastic and inelastic contributions with the empirical mixing rule:

$$\Omega^{(l,s)} = \sqrt{\left(\Omega_{in}^{(l,s)}\right)^2 + \left(\Omega_{el}^{(l,s)}\right)^2} \tag{2.60}$$

where the subscripts in and el denote the collision integrals derived from the inelastic and the elastic interactions, respectively.

The phenomenological potential model has been extended to neutral–ion elastic interactions introducing the parameter ρ_{di}, representative of the relative role of dispersion and induction attraction components in proximity to the equilibrium distance [51]-[52]:.

$$r_e = 1.767 \frac{\alpha_i^{1/3} + \alpha_n^{1/3}}{(\alpha_i \alpha_n (1 + 1/\rho_{di}))^{0.095}} \tag{2.61}$$

$$\varepsilon_0 = 5.2 \frac{Z^2 \alpha_n}{r_e^4} (1 + \rho_{di}) \tag{2.62}$$

$$\rho_{di} = 15.7 \frac{\alpha_i}{Z_i^2 [1 + (2\alpha_i / \alpha_n)^{2/3}] \sqrt{\alpha_n}} \tag{2.63}$$

where Z_i is the ion charge, α_i, α_n are the polarizability of charged and neural species respectively. For neutral and charged species interactions, the parameter *m* has the value of 4.

The polarizability values needed for ion species and the sources of these data are tabulated in table 2.1; only the ground states of the ions were considered.

No accurate experimental data or theoretical calculations are available in the literature for the polarizability of higher order ions $S^{2+}, F^{2+}, S^{3+}, F^{3+}$. Hence, collision integrals for interactions involving these species have been derived using a polarization potential model [57]:

$$\varphi_{in}(r) = (\frac{1}{4\pi\varepsilon_0})^2 \frac{(Z_i e)^2 \alpha_n}{2r^4} \tag{2.64}$$

Note that the polarization potential, unlike the phenenomelogical potential, is independent of the polarizability of the charged species.

The collision integrals for the polarization potential were obtained by a closed form, which leads to simple relations as follows:

$$\Omega_{i,n}^{(1,1)} = 424.443 Z_i \frac{\sqrt{\alpha_n}}{T}$$

$$\Omega_{i,n}^{(1,2)} = 0.833 \Omega_{i,n}^{(1,1)} \quad \Omega_{i,n}^{(2,2)} = 0.870 \Omega_{i,n}^{(1,1)} \quad \Omega_{i,n}^{(1,3)} = 0.729 \Omega_{i,n}^{(1,1)} \quad \Omega_{i,n}^{(2,3)} = 0.761 \Omega_{i,n}^{(1,1)}$$

$$\Omega_{i,n}^{(1,4)} = 0.656 \Omega_{i,n}^{(1,1)} \quad \Omega_{i,n}^{(2,4)} = 0.685 \Omega_{i,n}^{(1,1)} \quad \Omega_{i,n}^{(1,5)} = 0.602 \Omega_{i,n}^{(1,1)} \quad \Omega_{i,n}^{(3,3)} = 0.842 \Omega_{i,n}^{(1,1)} \tag{2.65}$$

In order to numerically evaluate the charge transfer collision integrals, it is necessary to know the charge transfer cross section. For interactions between a parent atom or molecule X and its ion X^- or X^+, especially for high energies, the transport cross section can be evaluated from charge transfer cross-section written as:

$$Q^l(g) = 2Q_{ex} \tag{2.66}$$

The charge transfer cross section is approximated by the following representation:

$$Q_{ex} = (A - B\ln E)^2 \tag{2.67}$$

where E is the collision energy. The constants A and B can be obtained from experiment data or theoretical calculations. The charge exchange cross-sections for collisions between unlike species (e.g. $\mathrm{Y}^{\pm} + \mathrm{X} \rightarrow \mathrm{X}^{\pm} + \mathrm{Y}$) are small compared to the elastic collision integrals, and are neglected in this work. Collision integrals with even l are wholly determined by the elastic interactions.

For the charge exchange cross sections of both the interactions between S-S^+ and F-F^+, we used the theoretical data presented by Copeland et al. [58] to obtain the constants A and B required to determine the resonant charge-exchange cross-section by least squares fitting technique.

No accurate experimental data or theoretical calculations are available in the literature for the charge-exchange interactions between S and S^-, F and F^-. The constants A and B were determined using an empirical formula [58].

$$A = (22.9 + 1.4105\ln M) / I^{1/2} \tag{2.68}$$

$$B = 1.4105 / I^{1/2} \tag{2.69}$$

where I is the ionization potential for the reaction $X \rightarrow X^+ + e$ and M is the atomic weight of X.

The charge exchange cross-sections for collisions between unlike species (e.g. $Y^{\pm} + X \rightarrow X^{\pm} + Y$) are small compared to the elastic collision integrals, and are neglected in this work. Collision integrals with even *l* are wholly determined by the elastic interactions.

2.4.3 Charged-charged Interactions

The collision integrals for the charged–charged interactions were calculated using the screened Coulomb potential which is given by:

$$\varphi_{in}(r) = \frac{Z_1 Z_2 e^2}{4\pi\varepsilon_0 r} \exp(-r / \lambda_d) \tag{2.70}$$

The Debye length taking into account the shielding effects of both ions and electrons has the form:

$$\lambda_d^{-2} = \frac{e^2}{\varepsilon_0 k}\left[\frac{n_e}{T_e} + \sum_{t=1, t\neq e}^{w} \frac{z_t^2 n_t}{T_h}\right] \tag{2.71}$$

The second term in the brackets is neglected when only the shielding effect of electrons is considered**.** The effective collision integrals were calculated from the works of Mason et al.[59]-[60].

2.4.4 Electron–neutral interactions

The collision integrals for interactions between electrons and neutral species have been calculated by straightforward integration over energy assuming a Boltzmann distribution based on the transport cross sections $Q_1(E)$, $Q_2(E)$ and $Q_3(E)$ as functions of electron energy. When $Q_2(E)$ and $Q_3(E)$ are not available, different techniques are used to estimate them.

For the interactions *e-F* and *e-S*, we use the recommended techniques by Laricchiuta et al. [61] to determine transport cross sections. The ratio $Q^2(E)/Q^1(E)$ and $Q^3(E)/Q^1(E)$ are evaluated from the known $Q^1(E)/Q^0(E)$ assuming a model angular dependence of the

differential cross section:

$$\frac{1}{(1-h(E)\cos\theta)^2} \tag{2.72}$$

where h is here an adjustable parameter as a function of the electron energy, determined from the $Q^1(E)/Q^0(E)$ ratio. If $Q^0(E)$ cross section was not known, the value of h can be fixed according to Born scattering for a Coulomb screened potential

$$\frac{1}{(1+2\eta)^2} \quad \text{With} \quad \eta = 10.9Z^{2/3}/E \tag{2.73}$$

For atomic fluorine and sulphur, elastic cross section are from reference [62], Coulomb screening respectively with $Z = 9$ and $Z = 16$ for the calculation of $Q^2(E)$ and $Q^3(E)$.

For other electron–neutral interactions, unfortunately, to our knowledge, no available experimental or calculated data are available in the literature. The cross-sections were estimated by assuming that the cross-sections are independent of energy and dominated by polarization effects [63]

2.5 Calculation Results

2.5.1 Equilibrium Composition

The equilibrium composition of pure SF_6 plasmas, are depicted in Fig. 2.1. The calculations were carried out for the temperature range from 300 to 30 000 K and at atmospheric pressure. Dissociation of SF_6 takes place at around 1600 K, mainly into F and SF_4. SF_4 starts to dissociate mainly into F and SF_2 at around 2100 K. Further temperature increase brings the dissociation of SF_2 into SF and F at around 2500 K. Ionization of the plasma starts at around 2500 K. At these low temperatures there are very few free electrons. They become attached to the F atoms to form F^- ions, the positive species being mainly the S_2^+ ions. As the temperature increases, the ionization of sulfur atoms into its first ions takes place and its number density reach a peak

value at around 1100K. Fluoride atoms have a higher ionization potential of 17.4 eV and start to ionize at a relatively higher temperature range. Almost total ionization of the medium takes place from 17000 K.

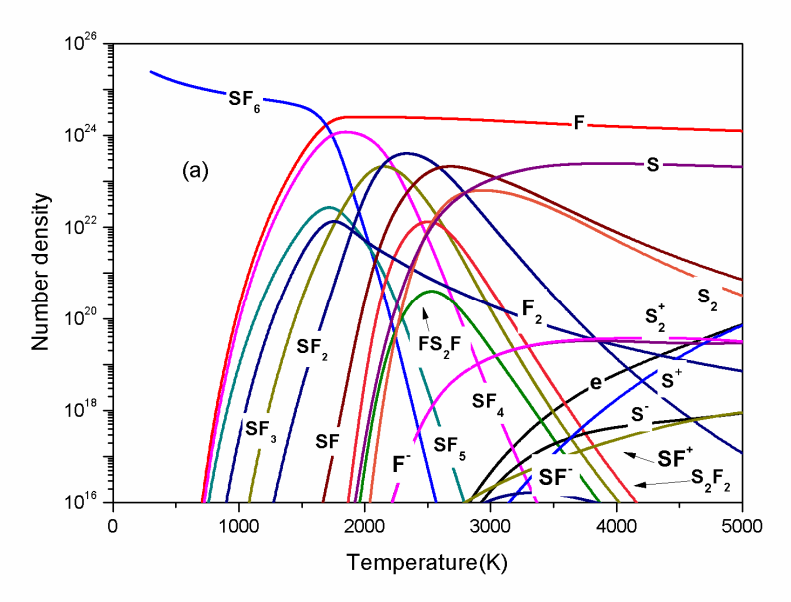

(a)

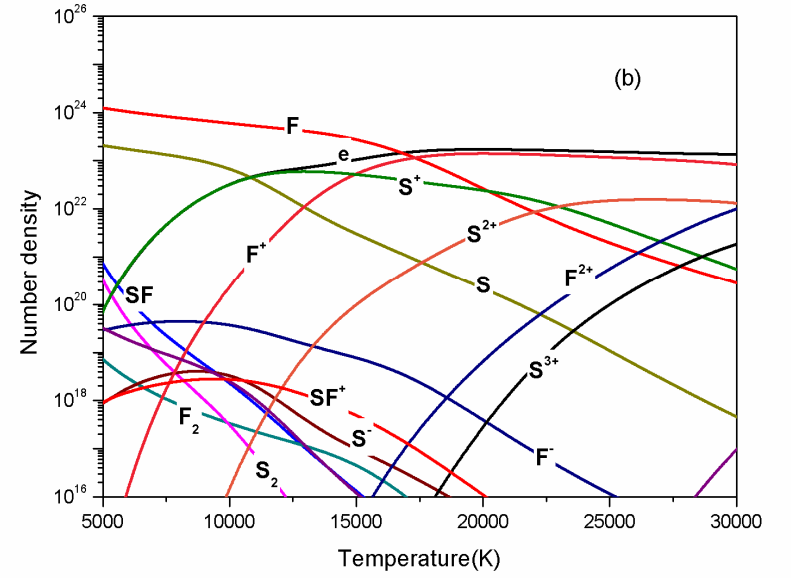

(b)

Figure 2.1 Temperature dependence of equilibrium composition of SF_6 plasmas at atmospheric pressure

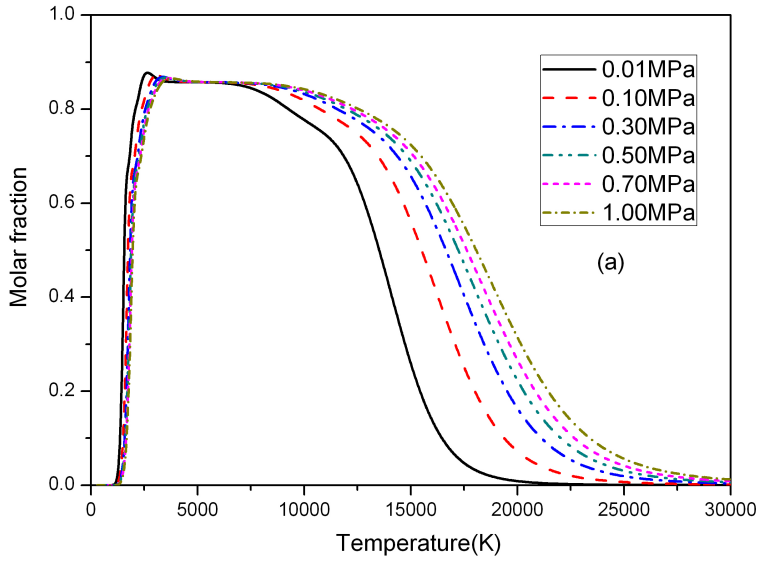

(a)

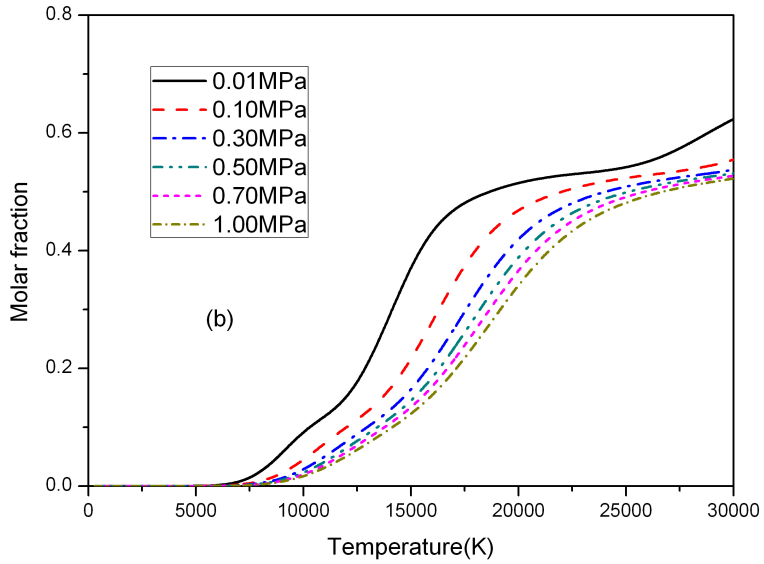

(b)

Figure 2.2 Temperature dependence of molar fraction of fluoride atoms (a) and electrons (b) in SF_6 plasmas in the pressure range from 0.01MPa to 1.0MPa.

Fig. 2.2 gives the temperature dependence of molar fraction of fluoride atoms and electrons in SF_6 plasmas in the pressure range from 0.01MPa to 1.0MPa. As the continuous dissociation of sulfur fluoride, the molar fraction of atomic fluoride increases fairly rapidly and then decreases at a high temperature due to its high ionization potential. Hence, the free fluorine atom dominates in a wide temperature range from 3000 K to 17000 K. The decrease

in the molar fraction of electrons at a given temperature as pressure increases can be explained by the suppression of successive ionization reactions. According to Le Chatelier's principle, an increase in pressure tends to suppress dissociation and ionization reactions. When pressure is increased to 1.0MPa, the molar fraction variation of atomic fluoride shows that they ionize at a higher temperature.

2.5.2 Thermodynamic Properties

Using the chemical equilibrium composition data presented in the previous section, we evaluated the thermodynamic properties of SF_6 arc plasmas, in particular the mass density, molar weight, enthalpy, specific heat at constant pressure, entropy, sonic velocity and specific heat, using Eqs. (2.8) to (2.14).

- **Mass Density and Molar Weight**

The variation of mass density and molar weight as a function of temperature at atmospheric pressure is shown in Figs. 2.3 and 2.4 respectively.

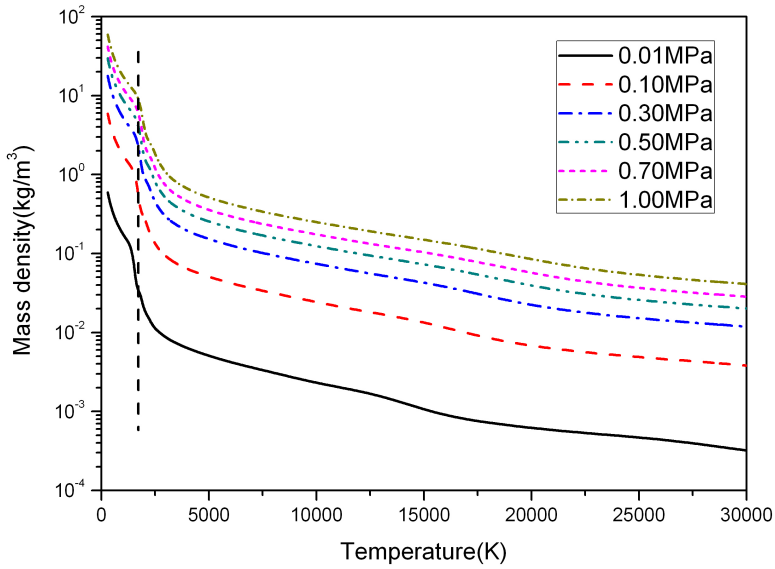

Figure 2.3 Temperature dependence of mass density of SF_6 plasmas in the pressure range from 0.01MPa to 1.0MPa.

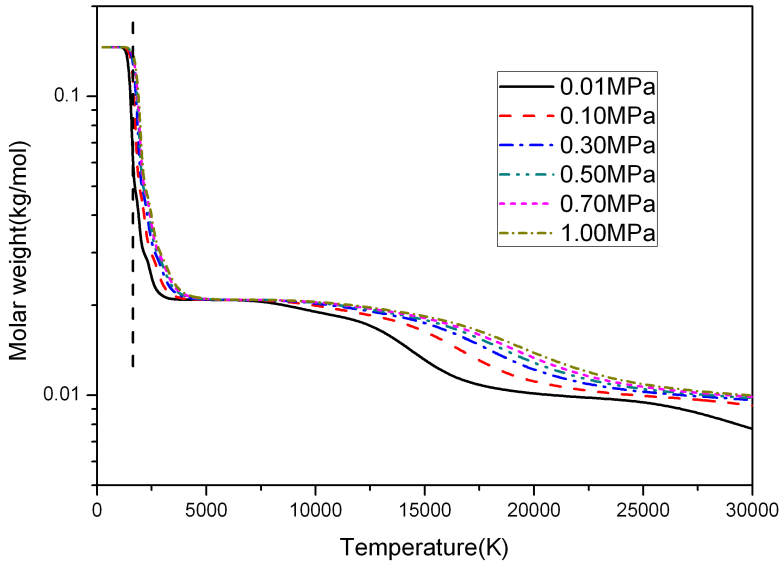

Figure 2.4 Temperature dependence of molar weight of SF_6 plasmas in the pressure range from 0.01MPa to 1.0MPa.

The two quantities are closely associated. If it was not for the chemical reactions such as dissociation and ionization, the mass density ρ would vary in inverse proportion to temperature and the molar weight would remain constant according to the state equation of an ideal gas. However, dissociation and ionization reactions cause both the mass density and molar weight of the gas mixtures to decrease monotonically as the temperature increases. The pressure increase inhibits the chemical reactions and brings the location of steep variation of mass density and molar fraction curves to a higher temperature.

- **Specific Enthalpy and Specific Entropy**

The specific enthalpy and specific entropy are shown in Figs. 2.5 and 2.6, respectively. As for the molar weight and mass density, chemical reactions also contribute strongly to these quantities. The steep variations in specific enthalpy are essentially due to the heats of reaction (dissociation and ionization). The influence of pressure on the specific enthalpy of an SF_6 plasma is also presented in Fig. 2.5. At a given temperature, the enthalpy of a gas increases as the pressure decreases due to the lower dissociation and ionization temperatures; a great deal of energy is needed to dissociate or ionize a gas, and thus the energy content is higher at temperatures exceeding the dissociation of ionization levels. Similar behaviour is also found

in Fig. 2.6 for specific entropy for which the steep variations are caused by the dissociation or ionization as well.

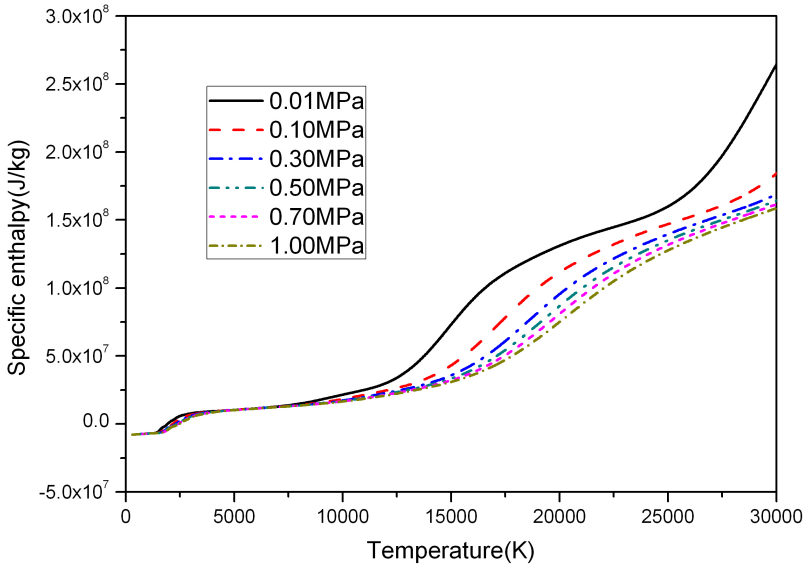

Figure 2.5 Temperature dependence of specific enthalpy of SF_6 plasmas in the pressure range from 0.01MPa to 1.0MPa.

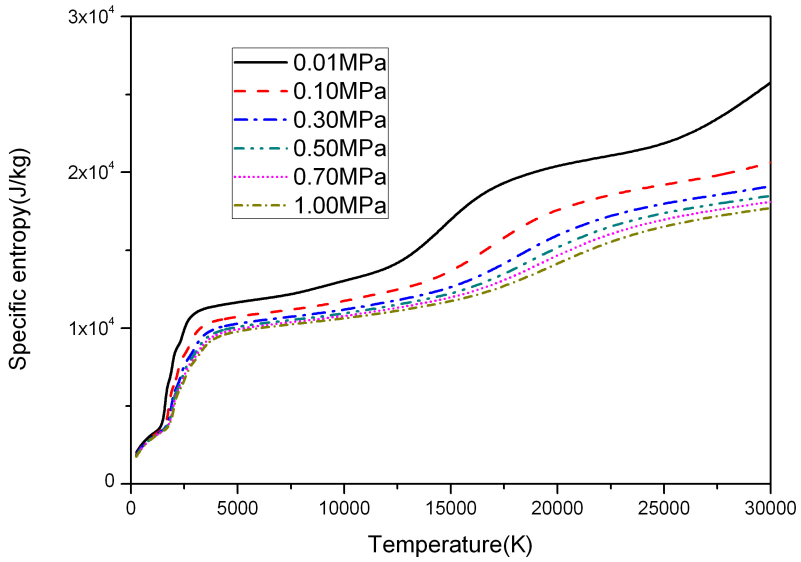

Figure 2.6 Temperature dependence of specific entropy of SF_6 plasmas in the pressure range from 0.01MPa to 1.0MPa.

- **Specific Heat at Constant Pressure**

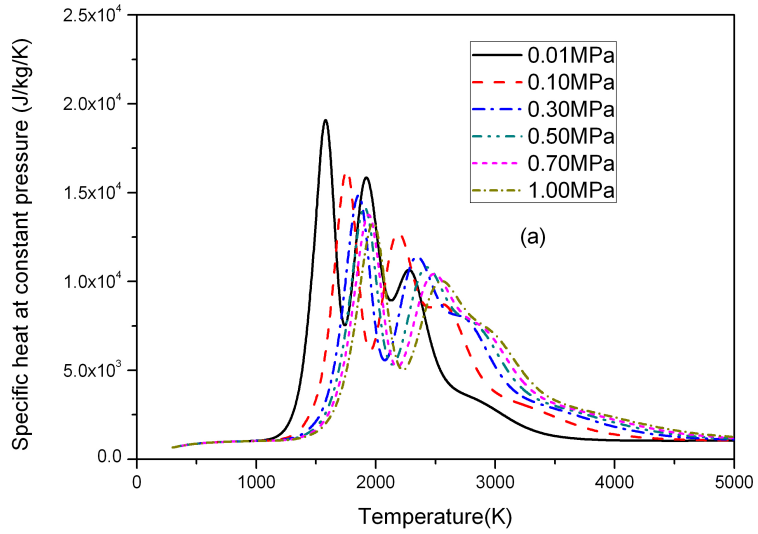

(a)

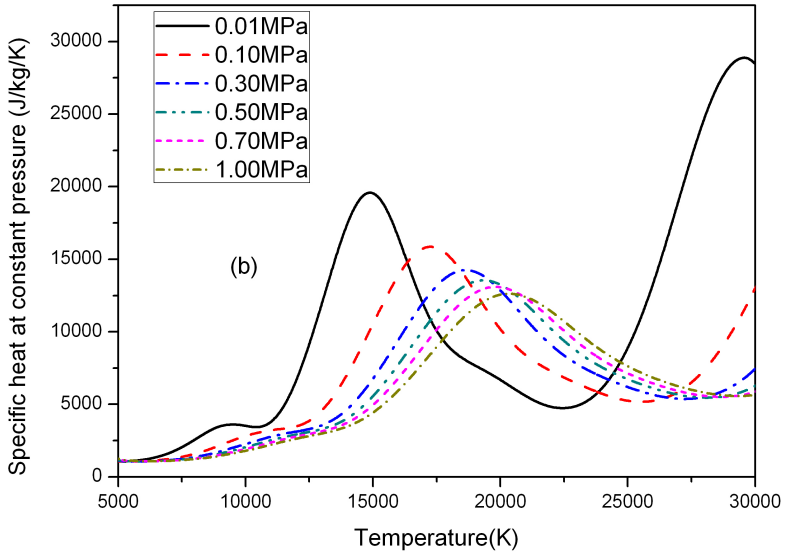

(b)

Figure 2.7 Temperature dependence of specific heat of SF_6 plasmas in the pressure range from 0.01MPa to 1.0MPa.

The steep changes in enthalpy corresponding to the respective peaks of the specific heat at constant pressure are essentially a consequence of the heats of reaction. As shown in Figs. 2.7a and b, the specific heat at constant pressure has multiple peaks. These are associated with, respectively, the continuous dissociation of sulfur fluoride from SF_6 into SF_4 at 1800 K, from

SF_4 into SF_2 at 2000 K, from SF_2 into SF at 2500 K at atmospheric pressure for the first three peaks. The three peaks presented in Fig. 2.7b are related to the ionization of atomic sulfur, atomic fluoride and the first sulfur ion.

- **Sonic Velocity and Specific Heat Ratio**

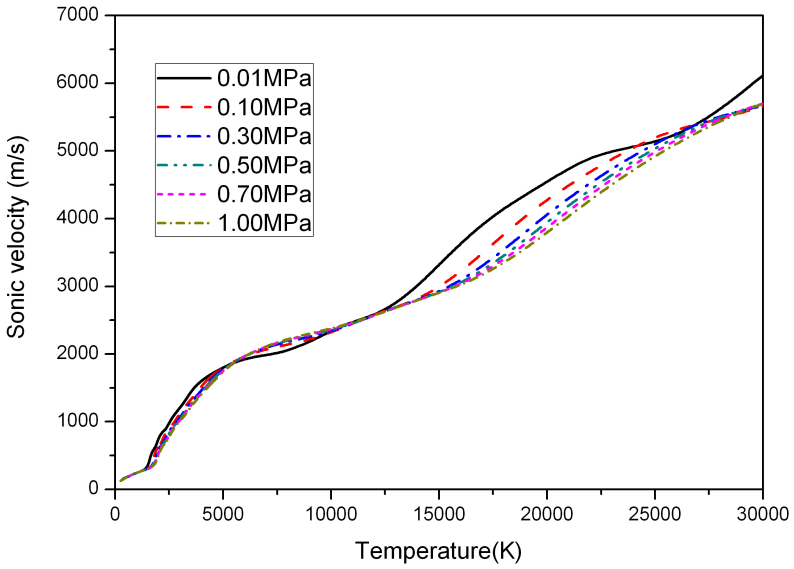

Figure 2.8 Temperature dependence of sonic velocity of SF_6 plasmas in the pressure range from 0.01MPa to 1.0MPa.

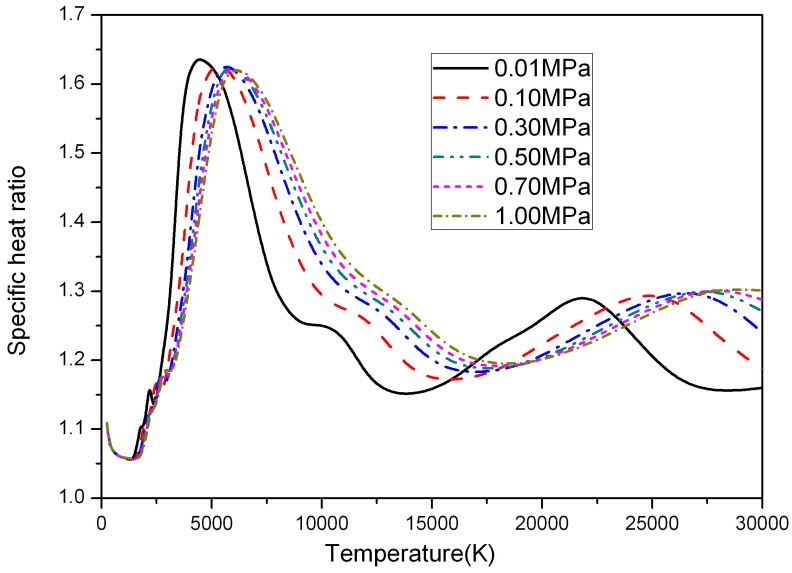

Figure 2.9 Temperature dependence of specific heat ratio of SF_6 plasmas in the pressure range from 0.01MPa to 1.0MPa.

The sonic velocity and the specific heat ratio are parameters that characterize a compressed fluid. The sonic velocity is the distance travelled per unit time by a sound wave propagating through an elastic medium and it expresses the pressure propagation speed, an extremely important property when studying the gas flow rate in the throat of circuit breakers and shock wave generation. The specific heat ratio, also known as the isentropic expansion factor, is the ratio of the specific heat at constant pressure to the specific heat at constant volume.

The calculated values of sonic velocity and specific heat ratio are shown in Figs. 2.8 and 2.9. In the low temperature range where chemical reaction does not occur, the sonic velocity and specific heat ratio does not change with the variation of pressures. The sonic velocity increases with temperature. Dissociation and ionization are reflected in changes in the slope. Similarly, the specific heat ratio shows several characteristic peaks, which are related to the chemical reactions that have been mentioned above.

2.5.3 Transport coefficients

- **Electrons Thermal Diffusion Coefficient**

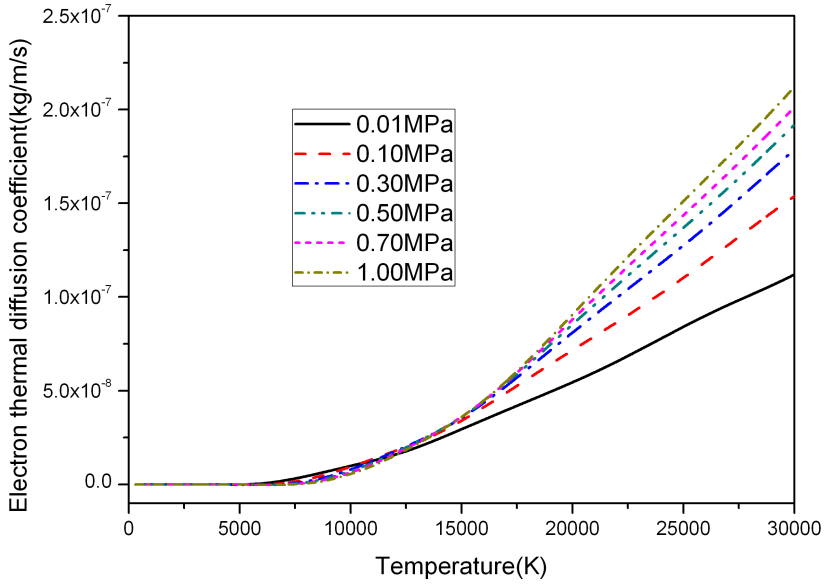

Figure 2.10 Temperature dependence of electrons thermal diffusion coefficient of SF_6 plasmas in the pressure range from 0.01MPa to 1.0MPa.

Because the number of the ordinary diffusion coefficients required to be describe in plasmas is large (one for each pair of species), only the values of the thermal diffusion coefficient of electrons are presented here. The behaviour of thermal diffusion coefficient of the electrons as a function of temperature and pressure is presented in Fig. 2.10. The electron thermal diffusion coefficient depends appreciably on the pressure. However, the dependence is significantly reduced at lower temperature owing to the very low concentration of electrons in the mixtures.

- **Viscosity**

The viscosity is a measure of momentum transport, which establishes the proportionality between the frictional force in the direction of the flow and the velocity gradient in the orthogonal direction. For pure gas, as a first approximation, viscosity is proportional to the square root of the product of mass and temperature and inversely proportional to the collision integrals, particularly for charged species molar fractions below 1%.

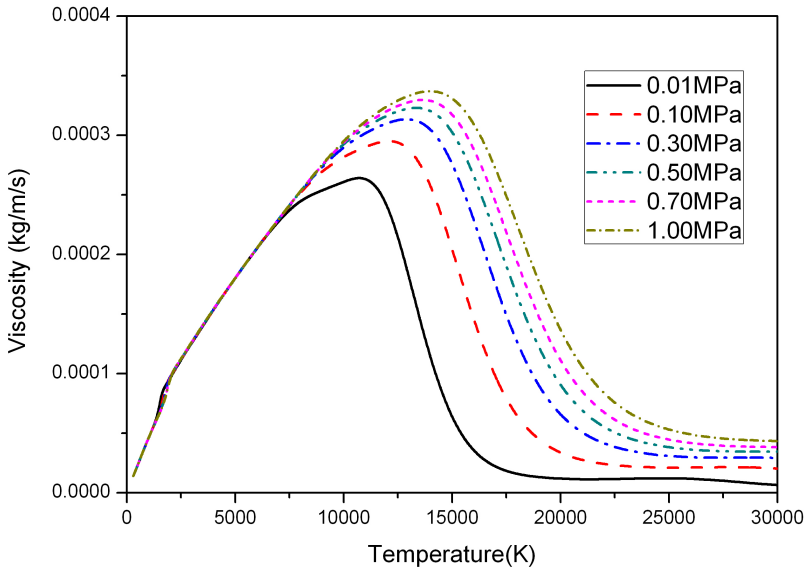

Figure 2.11 Temperature dependence of viscosity of SF_6 plasmas in the pressure range from 0.01MPa to 1.0MPa.

The dependence of the viscosity on pressure is much more pronounced, as shown in Fig. 2.11. The viscosity increases with temperature when neutral species dominate, and decreases when significant ionization occurs as a result of the large collision integrals for the

Coulomb interaction. Fig. 2.11 indicates that the viscosity at a given temperature increases with pressure, especially at those temperatures for which ionization is significant. This is because the degree of ionization decreases for increased pressure, so the Coulomb interactions become less important.

- **Thermal Conductivity**

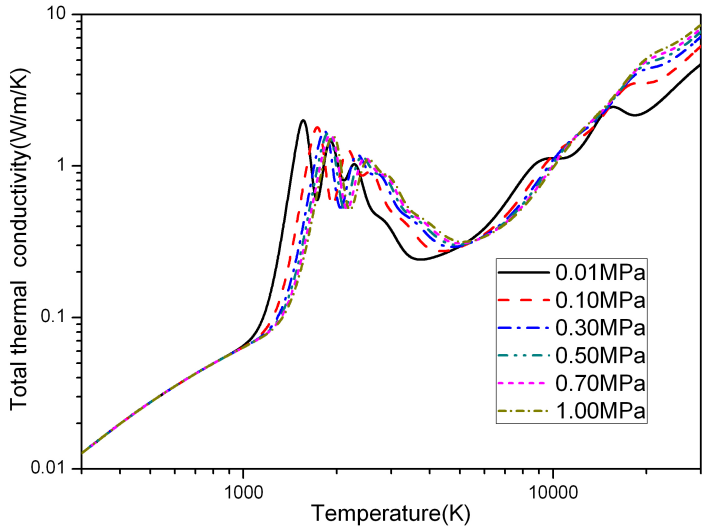

Figure 2.12 Temperature dependence of total thermal conductivity of SF_6 plasmas in the pressure range from 0.01MPa to 1.0MPa.

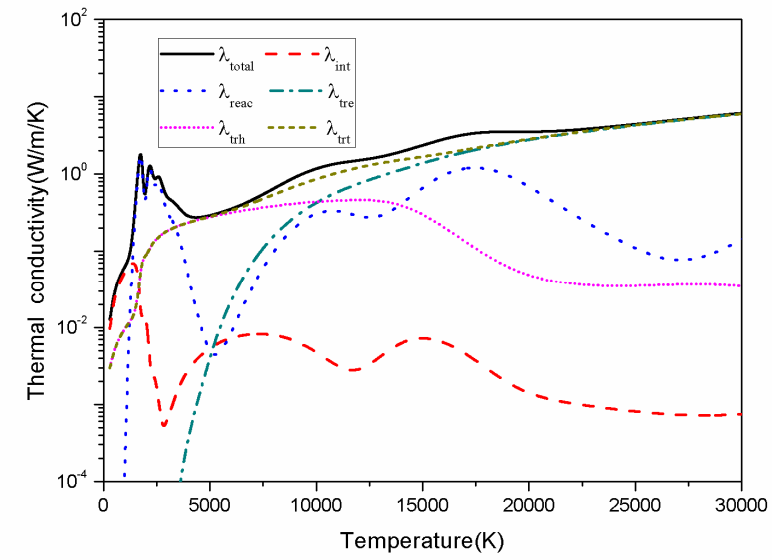

Figure 2.13 Temperature dependence of thermal conductivity components of SF_6 plasmas at atmospheric pressure.

We now consider thermal conductivity, which determines the heat transfer. Fig. 2.12 depicts the total thermal conductivity of pure SF_6 gas for the six aforementioned pressure values. As the pressure rises, the peaks that correspond to the dissociation and ionization are shifted to higher temperatures for the same reason as discussed in the case of specific heat.

Fig. 2.13 shows the different components of thermal conductivity of pure SF_6 gas at atmospheric pressure. The internal component makes a negligible contribution to the total thermal conductivity. For pure SF_6, the heavy species translational component increases slowly until around 10 000 K because the collision integrals for the interactions between neutral species decrease; after a plateau it then decreases slowly owing to the occurrence of ionization. The heavy species translational thermal conductivity plays a major role in the temperature range 6000 to 9000 K. The contribution of electron translation to the total thermal conductivity surpasses that of heavy species for temperatures exceeding 9000 K. Above around 17 000 K, the electron translational component dominates in the translational heat transfer and heavy species translation makes a negligible contribution.

Dissociation and ionization reactions lead to strong peaks in the thermal conductivity through the reaction thermal conductivity. The reaction thermal conductivity dominates in the temperature range from 1500K to 3000K in which continuous dissociation occurs. The multiple peaks are related to the continuous dissociation of sulfur fluoride molecules, and the first ionization of atomic sulfur and fluorine along with the second ionization of first sulfur ions, respectively. Due to the large difference of the first ionization energies, the ionization of atomic sulfur and fluorine produce separate peaks.

- **Electrical Conductivity**

The electrical conductivity is directly related to the electron density, i.e. the ionization degree of the plasma. The electrical conductivity decreases as the pressure increases at temperatures below about 10 000 K, as shown in Fig. 2.14. This is because the ionization temperature increases with pressure, so the ionization degree is lower at a given temperature. Above about 10 000 K, the electron density, and thus the electrical conductivity, increases with pressure. For the case of a pressure of 0.01MPa, the decrease of the electrical conductivity as temperature

increases in this temperature range from 25000 K to 30000K is a consequence of atomic sulfur's multiple ionization.

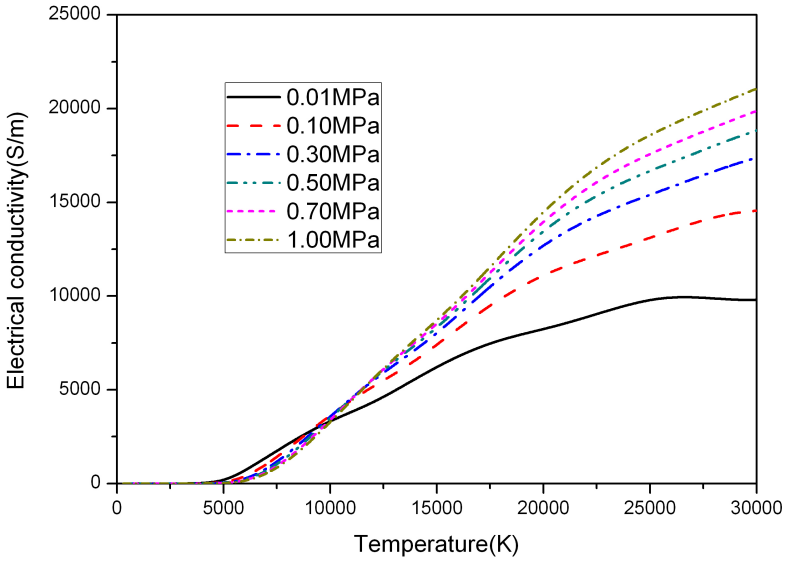

Figure 2.14 Temperature dependence of electrical conductivity of SF_6 plasmas in the pressure range from 0.01MPa to 1.0MPa.

2.5.4 Comparison with Available Literature Data

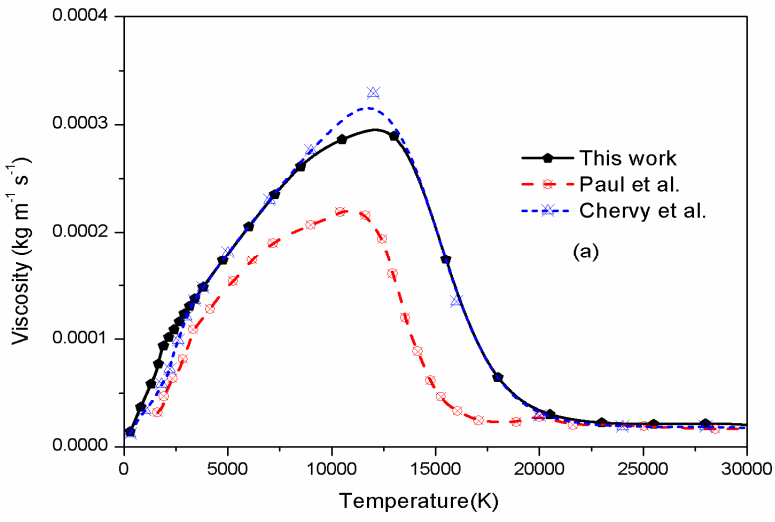

(a)

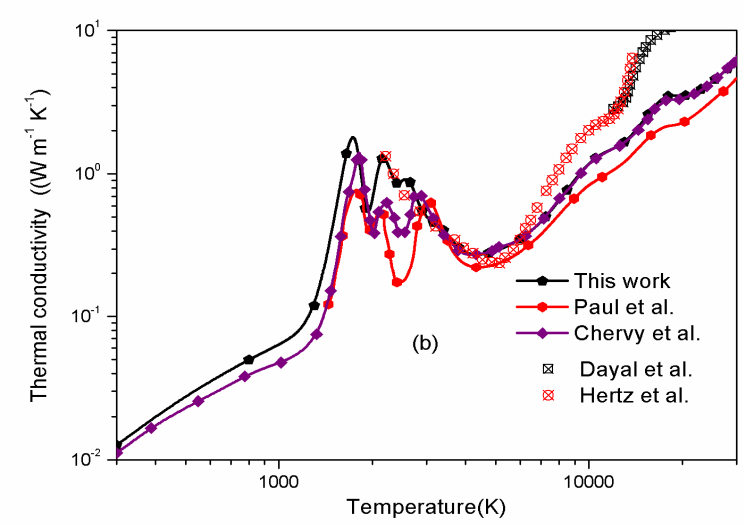

(b)

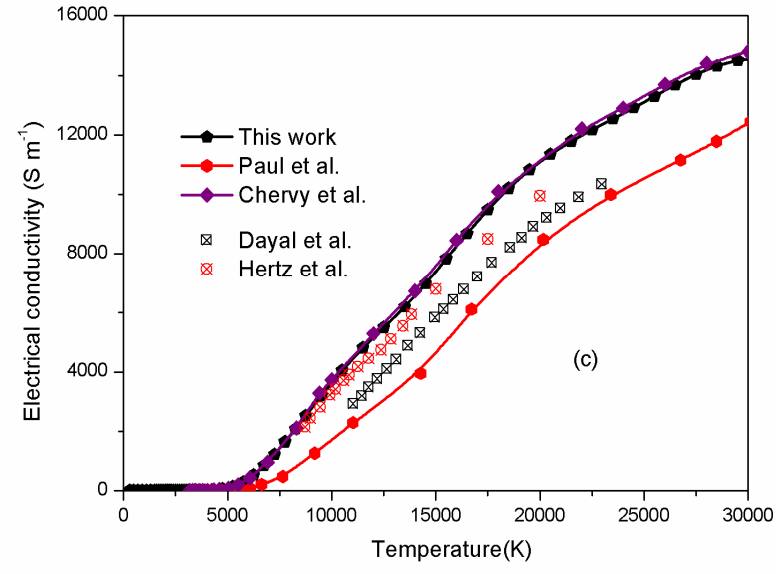

(c)

Figure 2.15 Comparison of computed transport coefficients with theoretical works of Chervy et al. [4] and Paul et al. [10] and experimental investigation of Dayal et al. [8] and Hertz et al. [16] at atmospheric pressure. (a) viscosity, (b) total thermal conductivity, (c) electrical conductivity.

Available results of transport coefficients of SF_6 under local thermodynamic equilibrium condition at atmospheric pressure can be found in the literature. Comparisons with recent tabulated property values provided by other researchers are presented and a general agreement can be observed. For transport coefficients, some discrepancies are observed in the values presented by different authors. These partly result from the uncertainties in the gas composition

and approximations made in the calculations, but mainly originate from uncertainties in the values of the intermolecular potentials from which the transport coefficients are derived. The viscosity at a given temperature is, to a good approximation, proportional to a weighted average of $[\Omega_{i,j}^{(2,2)}]^{-1}$ for the pairs of species *i, j* that are present. Our calculated viscosity shows almost exact agreement with those of Chervy et al. with a slight deviation in the temperature range where a peak value is obtained. The difference can be attributed to the differences in the interaction potential of atomic sulfur and its first ion. Agreement with the calculations of Paul et al. is not as good in the whole temperature range. Our calculated thermal conductivity agrees well with Chervy et al.'s results except in the temperature range where the dissociation of sulfur fluoride molecular takes place and the electrical conductivity shows excellent agreement with their calculation with the discrepancy in the low temperature range below 5000 K showing the difference of electron-neutral species interaction collision cross. However, a large deviation is found with those of Paul et al. especially in the temperature range where ionization takes place. This may be explained as the Debye length in Paul et al.' work was calculated including only electrons shielding. However, this cannot be verified since Paul et al. did not specify how they determined the Debye length. Inclusion of only electrons in the determination of shielding distance leads to a larger value of the Coulomb collision integrals, and therefore smaller transport coefficients.

The agreement of theoretical results of thermal conductivity with available experimental investigation is less satisfactory in the high temperature range regardless of good agreement with Hertz et al.'s results below 6000K. It is noted that Belov and Semenov's discussion concludes that the experimental results of Hertz et al. overestimate the thermal conductivity value [12]. For electrical conductivity, a better agreement with recent experimental work by Dayal et al. has been found comparing with the deviation from Hertz et al.'s results. It is noted that all the experimental investigations were performed based on approximate formulas in a limited temperature or pressure range and gave no uncertainty estimation as well. The theoretical estimation is of great need at present. In contrast, an internally consistent database of transport cross sections proposed by a phenomenological approach for interactions relevant to SF_6 has been applied in our current calculation of transport coefficients and should provide more accurate estimation.

2.5.5 Influence of the Ions Shielding in the Debye Length

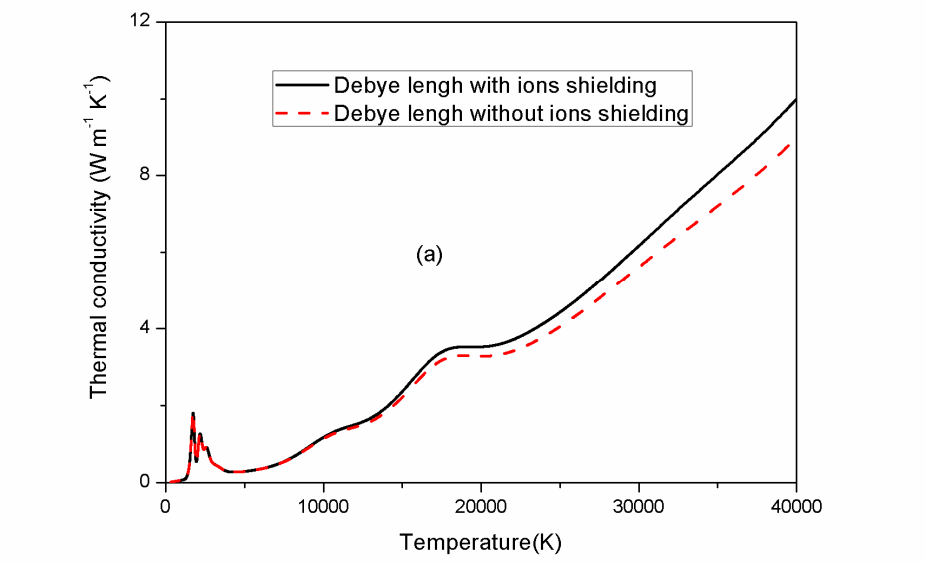

(a)

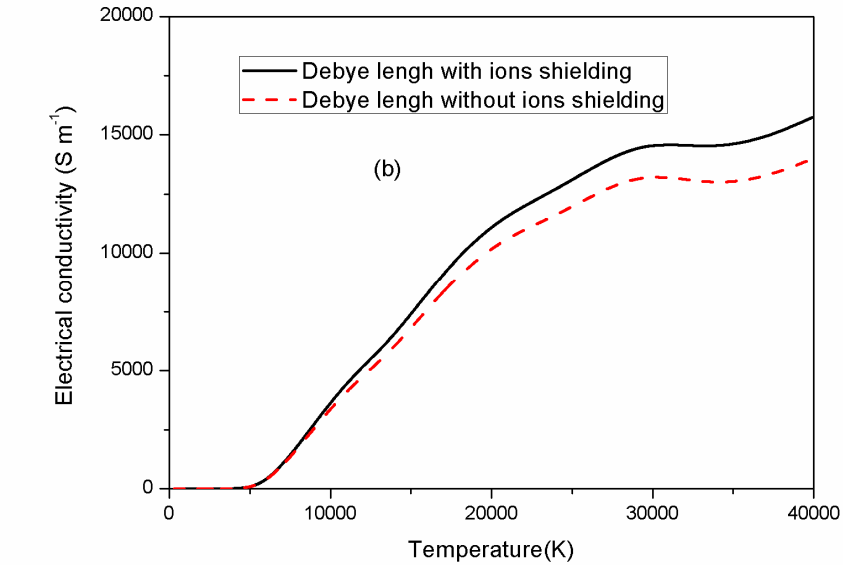

(b)

Figure 2.16 Influence of ions screening in the Debye length on properties in SF_6 plasmas under LTE state at atmospheric pressure. (a), total thermal conductivity; (b) electrical conductivity.

We also investigate the influence of the Debye length definition as presented in fig. 2.16. As well as affecting the plasma composition, transport coefficients became more sensitive to the choice of Debye length definition. This is partly due to the differences in plasma composition as

a consequence of the altered internal partition functions due to the cutoff in the computation caused by ionization lowering, but predominantly due to the different collision integrals for interactions between charged species, which are affected by the different screening distance used in evaluating the Coulomb potential. We note that the inclusion of both electrons and ions in calculating the Debye radius, which determines the screening distance, leads to a value of the Debye radius that is a factor of $\sqrt{2}/2$ smaller than if only electrons are considered under LTE conditions. This gives a smaller value of the Coulomb collision integrals, and therefore larger transport coefficients. The changes to the collision integrals have a much stronger effect on the transport coefficients than the changes to the plasma composition.

2.6 Conclusion

In this chapter, a considerable effort has been devoted to the calculation of transport coefficients of SF_6 under local thermodynamic equilibrium for temperatures from 300 to 30 000 K and pressures from 0.01MPa to 1.0MPa, which are conditions relevant to a wide range of applications. Comparing with previous studies, significant improvements of existing database were made due to the following performance:

(1) Full use of more reliable interaction potential studies was made to describe the interaction potentials involved in this work. The newly developed phenomenological description of interaction potentials for elastic collisions interactions was utilized to build an internally-consistent database characterized by a good accuracy. Meanwhile, updated experimental investigation and theoretical calculation on the more accurate electron-neutral as well as the resonant charge transfer cross section were used to improve the reliability of the relevant interaction potential.

(2) The transport properties namely diffusion coefficients, electrical conductivity, thermal conductivities and viscosity, are evaluated using the Chapman–Enskog method expanded up to the higher full third-order approximation (second-order for viscosity).

(3) Validation of the transport coefficients determined using these collision integrals was carried out by comparison with available theoretical and experimental data in the

literature.

It is noted that properties especially transport coefficients became sensitive to the choice of Debye length definition partly due to the differences in plasma composition as a consequence of the altered internal partition functions, but predominantly due to the different collision integrals for interactions between charged species, which are affected by the different screening distance used in evaluating the Coulomb potential. Additionally, the deviation of collision integrals used from different sources plays a major role in the determination of the discrepancy of computed transport coefficients. Pressures can also influence thermophysical properties. This can be explained by Le Chatelier's law as well as the modified species composition. The results presented here are expected to have high accuracy, and are reliable reference data for numerical modelling of SF_6 switch arc behaviour.

2.7 Reference

[1] R. D. Garzon 2002 High Voltage Circuit Breakers: Design and Applications 2nd Revised edn (Collection, Electrical Engineering and Electronics) (New York: Marcel Dekker) 456pp

[2] C. M. Franck and M. Seeger, "Application of High Current and Current Zero Simulations of High-Voltage Circuit Breakers", Contrib. Plasma Phys., 46, 787 (2006).

[3] A. B. Murphy, "Transport coefficients of helium and argon–helium plasmas", IEEE Trans. Plasma Sci., 25, 809 (1997).

[4] B. Chervy, A. Gleizes, and M. Razafinimanana, "Thermodynamic properties and transport coefficients in SF_6-Cu mixtures at temperatures of 300-30000 K and pressures of 0.1-1 MPa", J. Phys. D: Appl. Phys., 27, 1193 (1994).

[5] A. Gleizes, M. Razafinimanana, and S. Vacquie, "Calculation of thermodynamic properties and transport coefficients for SF_6-N_2 mixtures in the temperature range 1,000–30,000 K", Plasma Chem. Plasma Proc. 6, 65 (1986) .

[6] L. S. Frost and R. W. Libermann, "Composition and transport properties of SF_6 and their use in a simplified enthalpy now arc model", Proc. IEEE, 59, 474 (1971).

[7] B. Chervy and A. Gleizes, "Electrical conductivity in thermal plasma at low temperature (1000-5000 K)", J. Phys. D: Appl. Phys., 31, 2557 (1998).

[8] A. R. Dayal and A. D. Stokes, "Measurement of transport properties of SF_6 at high temperatures and pressures", J. Phys. D: Appl. Phys., 32, 2949 (1999).

[9] Coufal O, "Composition and thermodynamic properties of reacting mixtures", J. Phys. D: Appl. Phys., 31, 2025 (1998).

[10] K. C. Paul, T. Sakuta, and T. Takashima, "Transport and thermodynamic properties of SF_6 gas contaminated by PTFE reinforced with Al_2O_3 and BN particles", IEEE Trans. Plasma Sci., 25, 786 (1997).

[11] V. A. Belov and A. M. Semenov, "Calculation of the composition of the products from dissociation and ionization of sulphur hexafluoride at 1000 to 20,000 K and 1–10 atm", High Temp., 9 ,186 (1971).

[12] V. A. Belov and A. M. Semenov, "Calculation of the thermal conductivity of a sulphur hexafluoride plasma in the range 10000 to 20000 at pressures of 1, 2, 5, and 10 atm", High Temp., 9, 282 (1971).

[13] V. A. Belov and A. M. Semenov, “Electrical conductivity and viscosity of the products of the high-temperature decomposition of sulphur hexafluoride”, High Temp., 9, 717 (1971).

[14] P. Krenek, “Thermophysical properties of the reacting mixture SF_6 and Cu in the range 3000 to 50,000 K and 0.1 to 2 MPa. Part 3: Transport properties”, Acta Tech. CSAV, 37, 399 (1992).

[15] H. Dienemann, “Material functions of sulphur hexafluoride”, J. Phys. D: Appl. Phys., 16, 1651 (1983).

[16] W. Hertz, H. Motschmann and H. Wittel, “Investigations of the properties of SF_6 as an arc quenching medium”, Proc. IEEE, 59, 485 (1971).

[17] W .Frie, “Berechnung der Gaszusammensetzung und der Materialfunktionen von SF_6”, Z. Phys., 201, 269 (1967).

[18] B. Chervy, O. Dupont, A. Gleizes and P. Krenek, “The influence of the cross section of the electron-copper atom collision on the electrical conductivity of Ar-Cu and SF_6-Cu plasmas”, J. Phys. D: Appl. Phys, 28, 2060 (1995).

[19] B. Chervy, “The influence of the presence of tungsten on arc plasmas”, J. Phys. D: Appl. Phys., 29, 2156 (1996).

[20] A.Gleizes, M. Razafinimanana and S. Vacquie, “Transport coefficients in arc plasma of SF_6–N_2 mixtures”, J. Appl. Phys., 54, 3777 (1983).

[21] S. Gordon and B. J. McBride, “Computer program for calculation of complex chemical equilibrium composition, rocket performance, incident and reflected shocks, and chapman jouguet detonations”, NASA publication SP-273, 1971.

[22] A. B. Murphy, “Thermal plasmas in gas mixtures”, J. Phys. D: Appl. Phys., 34, 151 (2001).

[23] O. Coufal, “Composition and thermodynamic properties of thermal plasma up to 50 kK”, J. Phys. D: Appl. Phys., 40, 3371 (2007).

[24] P. Fauchais, M. I. Boulos and E. Pfender, “Thermal Plasmas-Fundamentals and Applications, Vol 1”, New York: Plenum, 1994.

[25] P. Kovitya, “Thermodynamic and transport properties of ablated vapors of PTFE, alumina, Perspex and PVC in the temperature range 5000-30000 K”, IEEE Trans. Plasma Sci., 12, 38 (1984).

[26] P. Kovitya, “Physical properties of high-pressure plasmas of hydrogen and copper in the

temperature range 5000 K to 30000 K", IEEE Trans. Plasma Sci., 13, 587 (1985).

[27] A. D'Angola, G. Colonna, C. Gorse and M. Capitelli, "Thermodynamic and transport properties in equilibrium air plasmas in a wide pressure and temperature range", Eur. Phys. J. D., 46, 129 (2008).

[28] O. ˇZivn′, "Composition and thermodynamic functions of non-ideal plasma", Eur. Phys. J. D., 54, 349 (2009).

[29] B. J. McBride and S. Gordon, "Computer program for calculating and fitting thermodynamic functions", NASA RP-1271, 1992.

[30] S. Gordon and B. J. McBride, "Thermodynamic data to 20,000 k for monatomic gases", NASA TP 1999-208523, 1999.

[31] K. S. Drellishak, D. P. Aeschliman, and Ali. B. Cambel, "Partition functions and thermodynamic properties of nitrogen and oxygen plasmas", Phys. Fluids, 8, 1590 (1965).

[32] J. Bacri and S. Raffanel, "Calculation of some thermodynamic properties of air plasmas: Internal partition functions, plasma composition, and thermodynamic functions", Plasma Chem. Plasma Proc., 7, 53 (1987).

[33] C. E. Moore, "Atomic energy level Circular 467 Vol. 1", US National Bureau of Standards, Washington, DC. ,1949

[34] C. E. Moore, "Atomic energy level Circular 467 Vol. 2", US National Bureau of Standards, Washington, DC. ,1952

[35] M. W. Chase and Jr. C. A. Davies, "NIST-JANAF Thermochemical Tables", 4th edn, American Institute of Physics for the National Institute of Standards and Technology, New York, 1998.

[36] J. O. Hirschfelder, C. F. Curtis and R. B. Bird, "Molecular Theory of Gases and Liquids", 2nd edn, Wiley, New York, 1964.

[37] S. Chapman, T. G. Cowling, "The Mathematical Theory of Non-uniform Gases", 3rd edn, Cambridge University Press, Cambridge, 1970.

[38] J. H. Ferziger and H. G. Kaper, "Mathematical Theory of Transport Processes in Gases", North-Holland, Amsterdam, 1972.

[39] L. Monchick, K. S. Yun, and E. A. Mason, "Formal kinetic theory of transport phenomena in. polyatomic gas mixtures", J. Chem. Phys., 39, 65 (1963).

[40] J. O. Hirschfelder, "Heat conductivity in polyatomic or electronically excited gases", J.

Chem. Phys., 26, 282 (1957).

[41] J. O. Hirschfelder, Proc. 6th Int. Symp. On Combustion (Reinhold, New York) p351 (1957).

[42] J. N. Butler and R. S. Brokaw, “Thermal conductivity of gas mixtures in chemical equilibrium”, J. Chem. Phys., 26, 1636 (1957).

[43] W. E. Meador and L. D. Stanton, “Electrical and thermal properties of plasmas”, Phys. Fluids, 8, 1694 (1965).

[44] R. S. Devoto, “Simplified expressions for the transport properties of ionized monatomic gases”, Phys. Fluids, 10. 2105 (1967).

[45] V. Rat, P. Andre´, J. Aubreton, M. F. Elchinger, P. Fauchais and A. Lefort, “Transport coefficients including diffusion in a two-temperature argon plasma”, J. Phys. D: Appl. Phys., 35, 981 (2002).

[46] R. S. Devoto, “Third approximation to the viscosity of multicomponent mixtures”, Phys. Fluids, 10, 2704 (1967).

[47] J. Aubreton, M. F. Elchinger, A. Hacala and U. Michon, “Transport coefficients of typical biomass equimolar CO–H_2 plasma”, J. Phys. D: Appl. Phys., 42, 095206 (2009).

[48] B. Sourd, J. Aubreton, M. F. Elchinger, M. Labrot and U. Michon, “High temperatures transport coefficients in e/C/H/N/O mixture”, J. Phys. D: Appl. Phys., 39, 1105 (2006).

[49] J. Aubreton, M. F. Elchinger and J. M. Vinson, “Transport coefficients in water plasma: Part I: Equilibrium plasma”, Plasma Chem. Plasma Process., 29, 149 (2009).

[50] P. André, J. Aubreton and S. Clain, “Transport coefficients in thermal plasma. Applications to Mars and Titan atmospheres”, Eur.Phys. J. D, 57, 227 (2010).

[51] M. Capitelli, D. Cappelletti, G. Colonna, C. Gorse, A. Laricchiuta, G. Liuti, S. Longo and F. Pirani, “On the possibility of using model potentials for collision integral calculations of interest for planetary atmospheres”, Chem. Phys., 338, 62 (2007).

[52] A. Laricchiuta, G. Colonna, D. Bruno, R. Celiberto, C. Gorse, F. Pirani, and M. Capitelli, “Classical transport collision integrals for a Lennard-Jones like phenomenological model potential”, Chem. Phys. Lett., 445, 133 (2007).

[53] L. Andrea and P. Federico, “A comparison of interatomic potentials for rare gas nanoaggregates”, J. Mol. Struct. (Theochem), 857, 22 (2008).

[54] NIST Computational Chemistry Comparison and Benchmark Database. In: R.D. Johnson III (Ed.), NIST Standard Reference Database Number 101, Release 10th ed., 2004.

[55] J. A. Barker, W. Fock and F. Smith, “Calculation of gas transport properties and the Interaction of argon atoms”, Phys.Fluids, 7, 897 (1964).

[56] A. B. Murphy and C. J. Arundell, “Transport coefficients of argon, nitrogen, oxygen, argon–nitrogen, and argon–oxygen plasmas”, Plasma Chem. Plasma Proc., 14, 451 (1994).

[57] D. Bruno, C. Catalfamo, M. Capitelli, G. Colonna, O. D. E. Pascale, P. Diomede, C. Gorse, A. Laricchiuta, S. Longo, D. Giordano and F. Pirani, “Transport properties of high-temperature Jupiter atmosphere components”, Phys. Plasmas, 17, 112315 (2010).

[58] F. B. M. Copeland and D.S .F. Crothers, “Cross Sections for Resonant Charge Transfer between Atoms and Their Positive Ions”, Nucl. Data Tables, 65, 273 (1997).

[59] E. A. Mason and R. J. Munn, “Transport coefficients of ionized gases”, Phys. Fluids, 10, 1827 (1967).

[60] R. S. Devoto, “Transport Properties of Ionized gas”, Phys. Fluids, 16, 616 (1973).

[61] A. Laricchiuta, D. Bruno, M. Capitelli, C. Catalfamo, R. Celiberto, G. Colonna, P. Diomede, D. Giordano, C. Gorse, S. Longo, D. Pagano and F. Pirani, “High temperature Mars atmosphere. Part I: transport cross section”, Eur. Phys. J. D, 54, 607 (2009).

[62] E. J. Robinson and S. Geltman, Single- and Double-Quantum Photo detachment of Negative Ions, Phys. Rev. 153,4 (1967).

[63] F. E. Spencer and A. V. Phelps, “Momentum transfer cross sections and conductivity integrals for gases of MHD interest”, Proc.15th Symp. Engineering Aspects of MHD (Univ. of Pennsylvania, Philadelphia, PA) p IX.9.1 (1976).

CHAPTER 3 THERMODYNAMIC AND TRANSPORT PROPERTIES OF TWO-TEMPERATURE SF_6 PLASMAS

3.1 Introduction

Circuit breaker, as a typical example of switchgear, is expected to successfully interrupt a load or fault current at the specified current and voltage ratings. The arc (the gaseous medium) between the arcing contacts is a key element responsible for current interruption. For high-voltage circuit-breakers, SF_6 is exclusively used because of its high insulation strength and high interruption capability of fault current. The interruption of alternate current relies on the instantaneous current passing through its zero points. At current-zero, the gaseous medium becomes a poor conductor as a result of decreasing temperature and size due to strong convection and turbulence cooling and rapidly increases its resistance. The assumption of local thermodynamic equilibrium (LTE), which the CFD-MHD simulation of SF_6 circuit-breaker arcs (Computation Fluid Dynamics-Magneto Hydrodynamics) was strongly based on in the high current phase, is no longer valid especially when large temperature gradient exists (near the cold walls or when the cold blown gas is injected with high cooling rates for heavy species) or when the electron number density is not high enough to allow sufficient transfer of energy between the electrons and heavy species [1]-[4]. In that case, the electron energy distribution function (EEDF) of each kind of particles remains Maxwellian, but the mean kinetic energy may be different for the electrons and heavy species.

For a better understanding of the arc quenching process, the physical state of discharge channel is very important. A two-temperature model which includes the assumption of local chemical equilibrium (LCE) has been developed in order to take into account the thermal departure, the two-temperatures being the electron temperature (T_e) and the heavy-particle temperature (T_h). Since the mass difference between the heavy species is tiny compared to that between electrons and heavy species, all the heavy species have the same temperature $T_{\underline{h}}$, which is sometimes called the plasma temperature or gas temperature. To model and optimize the performance of two-temperature plasma systems, thermodynamic and transport properties of the plasma gas are required. The accuracy of the property database is a key aspect in

producing correct modelling results.

Due to the importance of the application field through circuit breakers, there has been a noticeable amount of work on the calculation of the composition, thermodynamic and transport properties in pure SF_6 plasma or in SF_6-containing mixtures in the local thermodynamic equilibrium state [5]-[13]. For two-temperature plasmas, different authors have recently displayed calculations of the composition, thermodynamic and transport properties for some pure gases and some gas mixtures [14]-[25]. As for pure SF_6 gas, several papers have so far dealt with the particle compositions in two-temperature state [26]-[29] The determination of two-temperature plasma composition as a function of pressure, electron temperature and heavy species temperature is closely related to the mass action law of different reactions (Saha and Guldberg–Waage laws), the Dalton's law, species conservation law together with the electrical quasi-neutrality condition. Many attempts have been presented to generalize the Saha equations and Guldberg-Waage equations to two-temperature plasmas bringing in different expressions. The main methods are derived by Van de Sanden (case A) and Potapov et al. (case B) respectively [30]-[31]. The other issue which should be paid attention to in the determination of specie composition is related to the choice of the excitation temperature T_{ex} in the dissociation (Guldberg–Waage) and ionization (Saha) 2-T laws. Gleizes et al. presented a comparison between results obtained for a non-equilibrium atmospheric SF_6 plasma with Potapov's method and van de Sanden et al.'s method, where $T_{ex} = T_e$ for atoms and $T_{ex} = T_h$ for molecules in the pressure range between 1atm–16atm, for an electron temperature in the range 300–20 000 K with the thermal non-equilibrium degree $\theta = T_h/T_e$ ranging from 1 to 5 [27] Tanaka et al. presented their computation of two-temperature SF_6 plasma composition at the atmospheric pressure using the derivation of Saha and Guldberg–Waage laws by Van de Sanden et al. and an excitation temperature T_{ex} depending on elastic collisions which is close to T_h at low temperatures and to T_e at high temperatures [26] To our knowledge, no data with regard to the thermodynamic properties and transport coefficients of two-temperature SF_6 plasma has been published. The influence of the choice of expression forms of two-temperature Saha equations and Guldberg-Waage equations as well as the excitation temperature on the thermodynamic properties and transport coefficients of two-temperature SF_6 plasma should also be discussed.

For a two-temperature plasma, up to now, there exist different approaches to derive the transport coefficients of partially ionized plasma [32]-[37]. Among these, two methods are frequently adopted in the description of the two-temperature plasmas in which local chemical equilibrium is satisfied. Devoto [35]and Bonnefoi [36] developed a simplified theory neglecting the collisional coupling between heavy species and electron. Rat et al. [37] proposed a theory to take into account the coupling between heavy species and electrons, resulting in a set of new expressions for transport coefficients and coupling terms in the mass, momentum and energy flux definitions. It should, however, be noted that a recent study of two-temperature transport properties that compared the approaches of Devoto and of Rat et al. has shown that the coupling between electrons and heavy species does not lead to significant changes in the predicted non-equilibrium plasma transport coefficients, except for certain ordinary diffusion coefficients [23]. No significant discrepancies occur in the total thermal conductivity (including the reactive contribution), viscosity or electrical conductivity, even when they depend on ordinary diffusion coefficients.

The aim of this work is to develop a code for the computation of thermodynamic and transport properties of equilibrium and non-equilibrium SF_6 plasmas by means of a two-temperature model where heavy species and electrons still follow a Boltzmann energy distribution but with different temperatures. The calculation is performed for a wide pressure range between 0.01MPa to 1.00MPa and an electron temperature range of 300 K to 40,000 K. The great influence of the choice of Guldberg-Waage and Saha equations forms and the excitation temperature as well as various pressures on the plasma composition and hence the thermodynamic properties and transport coefficients are discussed as well. The phenomenological description of interaction potentials for elastic collisions allowing the construction of an internally-consistent database characterized by a good accuracy is applied in our current work as used in chapter two. The typical features of thermodynamic properties and transport coefficients using the electron and heavy species decoupling approach are carefully studied, enabling modelling of SF_6 arcs behaviour departure from thermal equilibrium.

3.2 Partition Functions and Plasma Composition

3.2.1 Determination of Plasma Composition

In the calculation, similarly, it is assumed that the mixture of SF_6 is composed of a total of 25 different species including relevant atoms, ions and molecules as well as electrons: SF_6, SF_5, SF_4, SF_3, SF_2, SF, SSFF, FSSF, F_2, S_2, F, S, SF^+, SF^-, S^+, F^+, S^-, F^-, S^{2+}, F^{2+}, S^{3+}, F^{3+}, S_2^+, F_2^+ and *e*. Other molecular ions are neglected because of their low amount appearing in the system as presented in chapter one for equilibrium plasmas.

A subject of debate has long existed for the determination of species composition in a two-temperature plasma system. Different relations in the literature were derived to describe the ionization and dissociation reactions and the main models include Potapov et al.'s method [30], Van de Sanden method [31], Gibbs free energy minimization method [43]-[44] as well as the kinetic model [45]. In chapter two, the minimization of Gibbs free energy was employed to determine the specie composition of equilibrium plasmas. This method no longer makes it necessary to define the free and bound species and no assumption about the reaction routes are required. Unfortunately, it has the disadvantage of requiring the calculation of all the unknowns, including the Lagrange multipliers. The Gibbs free energy minimization method has also been applied to multi-temperature plasmas [38]-[39]. However, Chen and Han [40] applied entropy maximization to a two-temperature plasma to define new equilibrium criteria. On the basis of these new criteria, Chen and Han argued that the Helmholtz or Gibbs free energy minimization approach usually used at equilibrium cannot be used in a two-temperature plasma. Chen and Han's view is argued by André et al. from statistical mechanics [41] and controversy is still continuing.

At present, associating the law of mass action (Saha's law and Gulberg–Waage's law) with those of electrical quasi-neutrality and conservation of stoichiometric equilibrium enables the species composition for two-temperature plasmas to be calculated as a function of temperature, pressure [42]. A Newton–Raphson algorithm is used to solve the system of equations until convergence of the plasma composition is obtained. The relevant nonlinear equations are described as follows [42]:

- **Conservation of Stoichiometric Equilibrium**

$$\sum_{i}^{v} c_{si} n_{si}^{'} = C \tag{3.1}$$

Eq. (3.1) expresses the mass conservation of the elements; $n_{si}^{'}$ is the amount of species *i* containing the element *s* in the plasma, c_{si} is the stoichiometric coefficient of the element *s* appearing in the species *i*, and *C* is a constant.

- **Dalton's Law**

$$P + \Delta P = \sum_{i \neq e}^{w} n_i k T_h + n_e k T_e$$

$$\Delta P = \frac{1}{24 \varepsilon_0 \pi \lambda_d^3} \sum_{i=1}^{w} Z_i^2 n_i$$

$$\lambda_d^{-2} = \frac{e^2}{\varepsilon_0 k} \left[\frac{n_e}{T_e} + \sum_{t=1, t \neq e}^{w} \frac{z_t^2 n_t}{T_h} \right] \tag{3.2}$$

Eq. (3.2) represents Dalton' Law taking into account the Coulomb field modification [27]; P and ΔP are the gas pressure and pressure correction caused by the charged particles interactions. The latter, which should be taken account of for non-equilibrium plasmas, was neglected in previous studies. λ_d is the Debye length defined including the ions shielding and w is the number of species in the system. k is Boltzmann's constant, ε_0 is the vacuum permittivity, Z_i and n_i are the charge number and number density of species *i* respectively, and T_e and T_h are the electron and heavy-particle temperatures respectively.

- **Electrically Quasi-neutrality**

$$\sum_{t} Z_t n_t^{'} - n_e^{'} = 0 \tag{3.3}$$

Eq.(3.3) describes electrical quasi-neutrality in the plasma; Z_t and $n_t^{'}$ are the charge number and number density of the charged species *t* respectively.

- **Law of Mass Action**

The law of mass action describes any chemical reaction at equilibrium and a total of 22 in independent ionization and dissociation reactions taken into account as reported in table 3.1.

Table 3.1 Chemical reactions in the computation

Number	Chemical reaction	Number	Chemical reaction
1	$SF_6 \leftrightarrow SF_5 + F$	12	$S^- \leftrightarrow S + e$
2	$SF_5 \leftrightarrow SF_4 + F$	13	$F \leftrightarrow F^+ + e$
3	$SF_4 \leftrightarrow SF_3 + F$	14	$S \leftrightarrow S^+ + e$
4	$SF_3 \leftrightarrow SF_2 + F$	15	$F^+ \leftrightarrow F^{2+} + e$
5	$SF_2 \leftrightarrow SF + F$	16	$S^+ \leftrightarrow S^{2+} + e$
6	$SF \leftrightarrow S + F$	17	$F^{2+} \leftrightarrow F^{3+} + e$
7	$SSFF \leftrightarrow SF_2 + F$	18	$S^{2+} \leftrightarrow S^{3+} + e$
8	$FSSF \leftrightarrow SF + SF$	19	$F_2 \leftrightarrow F_2^+ + e$
9	$F_2 \leftrightarrow F + F$	20	$S_2 \leftrightarrow S_2^+ + e$
10	$S_2 \leftrightarrow S + S$	21	$SF \leftrightarrow SF^+ + e$
11	$F^- \leftrightarrow F + e$	22	$SF^- \leftrightarrow SF + e$

For the law of mass action, two main derivations by Potapov's method and Van de Sanden et al.'s method are developed in previous literature. Using the argument that in the extreme cases of very high and very low electron number density, the dissociation and ionization laws must not depend on $\theta = T_h / T_e$, the same expressions as those of Van de Sanden et al.'s are recommended by Gleizes et al. through a comparative study of the composition of a two-temperature SF_6 plasmas in terms of both Van de Sanden et al.'s method and Potapov's method [27]. Following entropy maximization, Chen and Han also obtained a similar mass action law to that of van de Sanden et al. and they further argued that Potapov's method derived by Helmholtz free energy minimization is not valid in a multi-temperature plasma [41]. In these derivations, dissociation and ionization reactions are governed by the excitation temperature T_{ex}, which controls the population of the internal energy states of heavy species. Tanaka et al.[26], Gleizes et al. [27] and André et al. [46] respectively presented their own derivations of the excitation temperature. The choice of this temperature was discussed widely in previous studies

and still being debated. Generally, researchers chose one form as their preference to carry out the computation because no practical application of these works showing which Saha law and Guldberg-Waage law should be used under which particular experimental conditions has been reported. Up to now, only little work is involved in the comparison study for this issue [47]-[48]. These two deviations are both taken into account in current work in order to underline their influence on plasma composition and thermophysical properties. Following the generalized forms proposed by Gleizes et al. [27], both expressions are presented as follows:

- **Potapov's Method**

In the method of Potapov, the dissociation reaction $ab \leftrightarrow a + b$ is described at equilibrium with the heavy species kinetic temperature T_h and the ionization reaction $a^{r+} \leftrightarrow a^{(r+1)+} + e$ is described at equilibrium with the excitation temperature T_{ex}.

$$\frac{n_a n_b}{n_{ab}} = \frac{Q_a^* Q_b^*}{Q_{ab}^*} [\frac{2\pi k T_h}{h^2}]^{3/2} [\frac{m_a m_b}{m_{ab}}]^{3/2} \exp[-\frac{E_d}{kT_h}] \tag{3.4}$$

$$n_e [\frac{n_{r+1}}{n_r}]^{1/\theta} = 2 \left[\frac{Q_{r+1}^*}{Q_r^*} \right]^{1/\theta} [\frac{2m_e \pi k T_e}{h^2}]^{3/2} \exp[-\frac{E_{I,r+1} - \delta E_{I,r+1}}{kT_{ex}}] \tag{3.5}$$

where Q^*, $E_{I,r+1}$ and E_d are, the generalized internal partition function, the ionisation energy and dissociation energy respectively; h, $\partial E_{I,r+1}$ are the Planck constant and the lowering of the ionization energy. The subscript r indicates r-times ionized species. *ab, a* and *b* respectively denote the reactant and the two products of the dissociation chemical reactions, and T_{ex} is the excitation temperature of the species a^{r+}. The lowering of the ionization energy is taken into account using the following expression:

$$\Delta E_{I,r+1} = (r+1) \frac{e^2}{4\pi\varepsilon_0} \frac{1}{\lambda_d} \tag{3.6}$$

where λ_d is the Debye length representing the shielding effect of charged particles. It can be seen that the ionization potential lowering is inversely proportional to the Debye length. Different methods with or without considering the contributions of heavy ions are used to calculate λ_d in

the literature [49]. It implies that ions play an equally or even more important role in lowering the ionization potential in a two-temperature plasma.

- **Van de Sanden et al.'s Method**

In this case, the Guldberg–Waage equation and generalized Saha law are written as follows:

$$\frac{n_a n_b}{n_{ab}} = \frac{Q_a Q_b}{Q_{ab}} [\frac{2\pi k T_h}{h^2}]^{3/2} [\frac{m_a m_b}{m_{ab}}]^{3/2} \exp[-\frac{E_d}{kT_{ex}}] \tag{3.7}$$

$$n_e[\frac{n_{r+1}}{n_r}] = 2\left[\frac{Q_{r+1}}{Q_r}\right][\frac{2m_e \pi k T_e}{h^2}]^{3/2} \exp[-\frac{E_{I,r+1} - \delta E_{I,r+1}}{kT_{ex}}] \tag{3.8}$$

The heavy specie temperature T_h in the exponential term of Potapov's method is replaced by an effective excitation temperature T_{ex} in the work of Van de Sanden et al.

Concerning the choice of the reaction excitation temperature in the plasma, here we have taken into account the following different common hypothesis and their influence on composition and thermophysical properties are analyzed and discussed in current work.

[1] The heavy specie temperature T_h as an excitation temperature for dissociation reaction and molecular ionization reaction and the electron temperature T_e as an excitation temperature for atomic ionization reaction;

[2] The heavy specie temperature T_h as an excitation temperature for dissociation reaction and the electron temperature T_e as an excitation temperature for both atomic ionization and molecular ionization reaction;

3.2.2 Evaluation of Partition Function

Following the notation of Gleizes et al.[27], we assume that translational, rotational and vibrational motions of the heavy species are governed by T_h, but electronic excitation and

translational motion of the electrons are controlled by T_e. Hence, the partition functions are computed as follows:

- **Monatomic Species**

$$Q_i = Q_i^{el}(T_e) \tag{3.9}$$

where $Q_i^{el}(T_e)$ is the electron internal partition function of species i.

The excited levels of atomic particles are mostly populated by electron collisions so that the atomic internal partition function depends only on the electron temperature.

- **Diatomic and Polyatomic Species**

$$Q_i = Q_i^{el}(T_e) * Q_i^{vib}(T_h) * Q_i^{rot}(T_h) \tag{3.10}$$

where $Q_i^{vib}(T_h)$, $Q_i^{rot}(T_h)$ are the vibrational and rotational partition functions of species *i* respectively. The internal partition function for molecules is the product of electronic, vibration and rotation partition functions.

For generalized internal partition function Q^* appearing in the law of mass action (Saha law and Guldberg–Waage law) derived by Potapov's method, the calculation formula is reported as follows:

- **Monatomic Species**

$$Q_i^* = [Q_i^{el}(T_e)]^{\theta} \tag{3.11}$$

- **Diatomic and Polyatomic Species**

$$Q_i^* = [Q_i^{el}(T_e)]^{\theta} * Q_i^{vib}(T_h) * Q_i^{rot}(T_h) \tag{3.12}$$

Detailed computation method for partition function $Q_i^{el}(T_e)$， $Q_i^{vib}(T_h)$ and $Q_i^{rot}(T_h)$ is described in chapter 2 and not listed here.

3.3 Determination of Thermodynamic Properties

After obtaining the partition functions of each species, the calculation of the thermodynamic properties proceeds in a straightforward manner, employing standard thermodynamic relationships [25]. Among these, the computed specific enthalpy takes into account the translational, reactional and internal contributions due to the electrons excitation. There is some controversy about the correct expression of enthalpy for a multi-temperature plasma system especially in the last item for molecular species with regards to the internal contribution. Colombo et al. [22]-[24] used macroscopic temperature of species (identical with translational temperature) in the derivation of internal partition function. It is noted that the electronic excitation, molecular rotation and vibration of species are governed by electrons temperature and heavy species temperature respectively. Their contribution should be treated separately following relevant temperature as mentioned in Eqs. (3.5)-(3.8).

$$h = \sum_{i}^{w} h_i \tag{3.13}$$

Similarly, for electrons,

$$h_e = \frac{5}{2}\frac{k}{\rho} n_e T_e \tag{3.14}$$

For monatomic species,

$$h_i = \frac{5}{2}\frac{k}{\rho} n_i T_i + \frac{1}{\rho} n_i E_i + \frac{k}{\rho} n_i (T_e^2 \frac{\partial \ln Q_i^{el}}{\partial T_e}) \tag{3.15}$$

For molecular species,

$$h_i = \frac{5}{2}\frac{k}{\rho}n_i T_i + \frac{1}{\rho}n_i E_i + \frac{k}{\rho}n_i (T_e^2 \frac{\partial \ln Q_i^{el}}{\partial T_e} + T_h^2 \frac{\partial \ln(Q_i^{rot} Q_i^{vib})}{\partial T_h}) \tag{3.16}$$

As for specific heat, there exist different derivations as well. Colombo et al. [22]-[24] defined a total specific heat at constant pressure and constant non-equilibrium parameter by the differentiation of total specific enthalpy with respect to the electron temperature T_e.

$$C_{p,\theta} = \left.\frac{\partial h}{\partial T_e}\right|_{p,\theta} \tag{3.17}$$

In the numerical simulation of two-temperature plasma behaviour, we ususally treat electrons and heavy species separately and hence two definitions of specific heat are needed. Specific heat at constant pressure for electrons and heavy species are obtained respectively by the numerical differentiations of respective specific enthalpy components with respect to electron temperature and heavy species temperature [52].

$$\partial h_h = \frac{\partial h_h}{\partial p}\partial p + \frac{\partial h_h}{\partial T_e}\partial T_e + \frac{\partial h_h}{\partial T_h}\partial T_h \tag{3.18}$$

$$\partial h_e = \frac{\partial h_e}{\partial p}\partial p + \frac{\partial h_e}{\partial T_e}\partial T_e + \frac{\partial h_e}{\partial T_h}\partial T_h \tag{3.19}$$

$CP_P \frac{\partial h_h}{\partial p} = 1 + \left.\frac{\partial \ln \rho}{\partial \ln T}\right|_P$ is the specific heat caused by pressure change. This term is = 0 for ideal gases and < 0 for reacting gases in chemical equilibrium. The coefficients accompanying the terms ∂T_e and ∂T_h in Eqs. (3.18) and (3.19) can be interpreted as specific heats at constant pressure. Total specific heat at constant pressure and constant non-equilibrium degree for electrons and heavy species are obtained

$$CP_e = \frac{\partial h_e}{\partial T_e} + \frac{\partial h_e}{\partial T_h}\frac{1}{\theta} \tag{3.20}$$

$$CP_h = \frac{\partial h_h}{\partial T_e}\theta + \frac{\partial h_h}{\partial T_h} \tag{3.21}$$

$$CP_t = \frac{\partial h}{\partial T_e}\theta + \frac{\partial h}{\partial T_h} \tag{3.22}$$

where h_e and h_h are the specific enthalpy of electrons and heavy species respectively. For h_h , contributions from translational and internal partition functions as well as all relevant dissociation and ionization energies are included as defined in Eqs. (3.15)-(3.16).

3.4 Transport Coefficients and Collision Integrals

3.4.1 Determination of Transport Coefficients

Transport properties for two-temperature plasmas are also calculated approximately using the classical Chapman–Enskog method, which assumes that the particle distribution function is a first-order perturbation to the Maxwellian distribution [53]. Up to know there are two approaches to deal with the transport properties in non-equilibrium plasmas. Devoto [35] and Bonnefoi [36] developed a simplified theory neglecting the coupling between heavy species and electron and Rat et al.[37] developed a theory taking into account the coupling between heavy species and electrons, leading to a new set of transport coefficients and coupling terms in the flux definitions which are quite different from those derivation described in chapter two where a complete set of species interactions are employed in the computation of transport coefficient of equilibrium plasmas. It should, however, be noted that a recent study of transport coefficients in two-temperature plasmas that compared the approaches derived by Devoto et al. and Rat et al. has shown that decoupling between electrons and heavy species does not lead to significant changes in the predicted non-equilibrium plasma transport properties, except for certain ordinary diffusion coefficients [23]. No significant discrepancies occur in the total thermal conductivity (including the reactive contribution), viscosity or electrical conductivity, even when they depend on ordinary diffusion coefficients. Moreover, since calculation of transport properties using the coupled approach can be very time-consuming and therefore not suitable for its implementation in MHD equations solvers when the calculation on demand of properties is needed. Consequently, we have used the simplified approach of Devoto assuming that the change in the perturbation function in electrons is greater than that of heavy species during

interactions involving both types of particles with a third-order approximation for transport properties, except for viscosity for which the second-order approximation has been adopted.

3.4.2 Diffusion Coefficients

The binary diffusion coefficient used in determining the thermal conductivity is evaluated based on the derivation of two-temperature transport properties, as reported by Ramshaw [56]-[57]:

$$D_{ij}^{b} = \frac{3k^{2}T_{i}T_{j}}{16P\mu_{ij}T_{ij}^{*}\Omega_{ij}^{(1,1)}} \tag{3.23}$$

where Ω_{ij} is the collision integrals, μ_{ij} and T_{ij}^{*} are the reduced mass and the reduced temperature of the colliding molecules designated by i and j, which are effective temperature for collision interaction and respectively given by

$$\frac{1}{\mu_{ij}} = \frac{1}{m_i} + \frac{1}{m_j} \tag{3.24}$$

$$T_{ij}^{*} = \frac{(m_i T_j + m_j T_i)}{m_i + m_j} \tag{3.25}$$

Following the framework of Hirschfelder et al. [53], the ordinary diffusion coefficients can be obtained:

$$D_{ij}^{m} = \frac{F^{ji} - F^{ii}}{m_j |F|} \tag{3.26}$$

where F_{ij} are the cofactors of the matrix F whose elements are defined as

$$F_{ij} = \frac{1}{\rho}\left[\frac{n_i}{D_{ij}^{b}} + \sum_{l \neq l} \frac{n_l m_j}{m_i D_{il}^{b}}\right](1 - \delta_{ij}) \tag{3.27}$$

Ambipolar diffusion coefficients are computed by means of ordiniary diffusion

coefficients.

$$D_{ij}^{a} = D_{ij} + \frac{\alpha_i}{\beta}\sum_s Z_s D_{sj}$$

$$\alpha_i = \sum_j \frac{m_j n_j Z_j D_{ij}}{T_j}$$

$$\beta = \sum_i Z_i \sum_j \frac{m_j n_j Z_j D_{ij}}{T_j} \tag{3.28}$$

Z_j refer to the number of charges of species j.

The thermal diffusion coefficients of electrons and heavy species can be computed respecively in the 3rd approximation as

$$D_e^T = \frac{15 n_e^2 \sqrt{2\pi k T_e}}{4} \begin{vmatrix} q^{01} & q^{02} \\ q^{21} & q^{22} \end{vmatrix} \left(\begin{vmatrix} q^{00} & q^{01} & q^{02} \\ q^{10} & q^{11} & q^{12} \\ q^{20} & q^{21} & q^{22} \end{vmatrix} \right)^{-1} \tag{3.29}$$

$$D_i^T = \frac{15 n_i \sqrt{2\pi m_i k T_h}}{4} \left(\begin{vmatrix} q_{ij}^{00} & q_{ij}^{01} \\ q_{ij}^{10} & q_{ij}^{11} \end{vmatrix} \right)^{-1} \begin{vmatrix} q_{ij}^{00} & q_{ij}^{01} & q_{ij}^{02} \\ q_{ij}^{10} & q_{ij}^{11} & q_{ij}^{12} \\ q_{ij}^{20} & q_{ij}^{21} & q_{ij}^{22} \end{vmatrix} \tag{3.30}$$

q^{mp} , q_{ij}^{mp} elements are computed from associated collision integrals.

3.4.3 Viscosity

Owing to the mass ratio, this viscosity does not depend on the electrons:

$$\eta(\xi) = \eta_h + \eta_e \cong \eta_h \tag{3.31}$$

Only considering the heavy species, the viscosity of the plasma mixture in two-temperature plasmas can be calculated by

$$\eta_h(\xi) = \frac{kT_h}{2} \sum_{j, j \neq e} b'_{j0}(\xi) \tag{3.32}$$

The coefficients $b_{j0}(\xi)$ can be calculated from the following sets of linear equations.

$$\sum_{j, j \neq e} \sum_{m'=0}^{\zeta-1} \tilde{Q}_{ij}^{mm'} b'_{jm'}(\zeta) = -5 n_i \delta_{m0} \tag{3.33}$$

3.4.4 Thermal Conductivity

Under two-temperature consideration, we define separate total thermal conductivities for electrons and heavy species λ_e and λ_h following the definition of S. Ghorui et al. as follows [21]:

$$\lambda_e = \lambda_{tre} + \lambda_{re} \tag{3.34}$$

$$\lambda_h = \lambda_{trh} + \lambda_{rh} + \lambda_{\text{int}} \tag{3.35}$$

where λ_{tre} and λ_{trh} are the translational components and λ_{re} and λ_{rh} are the reactive components. λ_{int} corresponds to internal thermal conductivity of the heavy species.

Using the elements computed for diffusion coefficients of electrons, the translational thermal conductivity of electrons in the third approximation of Sonine polynomial terms can be expressed as

$$\lambda_{tre} = \frac{75 n_e^2 k}{8} \sqrt{\frac{2\pi k T_e}{m_e}} \left(q^{11} - (q^{12})^2 / q^{22} \right)^{-1} \tag{3.36}$$

Using elements of heavy specie diffusion coefficients, the translational thermal conductivity of heavy species is computed.

$$\lambda_{trh} = -\frac{75k}{8}\frac{\sqrt{2\pi kT_h}}{|q|}\begin{vmatrix} q_{ij}^{00} & q_{ij}^{01} & 0 \\ q_{ij}^{10} & q_{ij}^{11} & n_i \\ 0 & n_j/\sqrt{m_j} & 0 \end{vmatrix} \tag{3.37}$$

The presence of internal degrees of freedom can affect the heat flux vector, and gives rise to an internal thermal conductivity λ_{int}, which is derived using the Hirschfelder–Eucken approximation [37].

$$\lambda_{\text{int}} = \sum_{i\neq e}^{w} x_i D_{ii}^b k(C_{pi}/R - 2.5)(\sum_{j\neq e}^{w}\frac{x_j}{x_i}\frac{D_{ii}^b}{D_{ij}^b})^{-1} \tag{3.38}$$

where C_{pi} is the specific heat at constant pressure of the species i, D_{ii}^b and D_{ij}^b respectively the self-diffusion coefficient and the binary diffusion coefficient between species i and species j. R, P，x_i, and w respectively denote the molar gas constant, pressure, mole fraction of species i, and the total number of species.

An expression derived through reactive heat flux treating the electrons and heavy species separately is utilized to obtain the reactive thermal conductivity components of electrons and heavy species separately [21],[54].

$$\lambda_{re} = \left[\sum_{r=1}^{v}\Delta h_r \frac{n}{\rho k T_h}\sum_{j=1}^{w}\frac{T_h}{T_j}m_j D_{rj}^a \frac{\partial p_j}{\partial T_e}\right]$$

$$\lambda_{rh} = \left[\sum_{r=1}^{v}\Delta h_r \frac{n}{\rho k T_h}\sum_{j=1}^{w}\frac{T_h}{T_j}m_j D_{rj}^a \frac{\partial p_j}{\partial T_h}\right] \tag{3.39}$$

where n, v and Δh_r are species total number density, number of chemical reactions and reaction enthalpy change of reaction r respectively and D_{rj}^a is the ambipolar diffusion coefficient defined in terms of ordinary diffusion coefficients [55]. The partial derivative of partial pressure with respect to T_h and T_e can be determined by differential to the partial pressure equation with respect to taking T_h and T_e as independent variables. When thermal conductivity is evaluated

with respect to a heavy specie temperature gradient, a total reactive thermal conductivity can be defined as

$$\lambda_{reac} = \lambda_{re}\theta + \lambda_{rh} \tag{3.40}$$

3.4.5 Electrical Conductivity

The electrical conductivity is computed considering the contributions of electrons with the third approximation as

$$\sigma = \frac{3e^2 n_e^2}{2kT_e}\sqrt{\frac{2\pi kT_e}{m_e}}\begin{vmatrix} q^{11} & q^{12} \\ q^{21} & q^{22} \end{vmatrix}\left(\begin{vmatrix} q^{00} & q^{01} & q^{02} \\ q^{10} & q^{11} & q^{12} \\ q^{20} & q^{21} & q^{22} \end{vmatrix}\right)^{-1} \tag{3.41}$$

3.4.6 Volumetric Collision Frequency

The volumetric collision frequency between the electrons and the heavy species is computed as:

$$\xi_{eh} = \left(\frac{8kT_e}{m_e\pi}\right)^{1/2} n_e \sum_{j\neq e}^{v} n_j \overline{Q}_{ej}^{(1,1)} \tag{3.42}$$

3.4.7 Evaluation of Collision Integrals

Expressions for transport properties contain determinants that depend on collision integrals, which are averages over a Maxwellian distribution of the transport collision cross-sections for the binary interaction between species. For non-equilibrium plasmas, collision integrals have to be computed using reduced temperature T_{ij}^{*} as proposed by Eq. (3.43). The same set of interaction potentials as those used in determination of transport coefficients of equilibrium plasmas was adopted.

$$T_{ij}^{*} = \frac{(m_i T_j + m_j T_i)}{m_i + m_j} \tag{3.43}$$

3.5 Calculation Results

We present calculated compositions, thermodynamic properties and transport coefficients of SF_6 plasmas under equilibrium and non-equilibrium conditions ($\theta = T_e/T_h$ = 1, 2, 3, 5, 10, 15, 20) in a wide pressure range from 0.01MPa-1.00MPa for the electron temperature range of 300–40000 K. If not specified, we follow recommendation by Gleizes et al. and present the results at atmosphere obtained from Van de Sanden et al.'s expressions with the Debye length including the ions shielding contribution. Meanwhile, we use the heavy specie temperature T_h as an excitation temperature for dissociation reaction and molecular ionization reaction and the electron temperature T_e as an excitation temperature for atomic ionization reaction. The influence of the choice of mass action law forms and excitation temperature on species composition and thermophysical properties will be discussed.

3.5.1 Species Composition

Chemical equilibrium compositions for SF_6 plasmas as a function of electron temperature under different non-equilibrium degrees are shown in Figs. 3.1-3.2. For the thermal equilibrium case, SF_6 dissociates mainly at around 1800K into SF_4 and F. Further temperature increase brings the dissociation of SF_4 into SF_3, SF_2 and F at around 2300K and into SF and F at around 2650K. The ionization of plasma starts at very lower temperature around 2500K mainly by the attachment of electrons with atomic fluorine and produces the electric negative ion F^-. Meanwhile, S_2^+ has an important molar fraction comparing with the electrons in order to keep the charge neutrality. The first ionization of S and F respectively occurs at a relative higher temperature 14000K and 23000K due to their higher ionization energy. In the conditions out of thermal equilibrium, the dissociation reactions which are governed by heavy specie temperature are shifted towards higher electron temperature as presented in Fig. 3.1b for the non-equilibrium degree of 3. In the lower temperature range, the molar fraction of electrons exceeds that of F^-. Variations of the number density of electrons and fluorine atoms as a function of electron temperature under different non-equilibrium degrees are presented in Fig. 3.2. With the increase of non-equilibrium degree, the biggest molar fraction of atomic fluorine decreases due to the dramatic ionization once it is produced by the dissociation which is shifted towards a higher electron temperature. Similarly, the ionization takes place in a much narrower temperature

range and brings a much steeper variation of electrons molar fraction. When full ionization is reached at a high temperature, electrons molar fractions for different non-equilibrium degrees are almost identical.

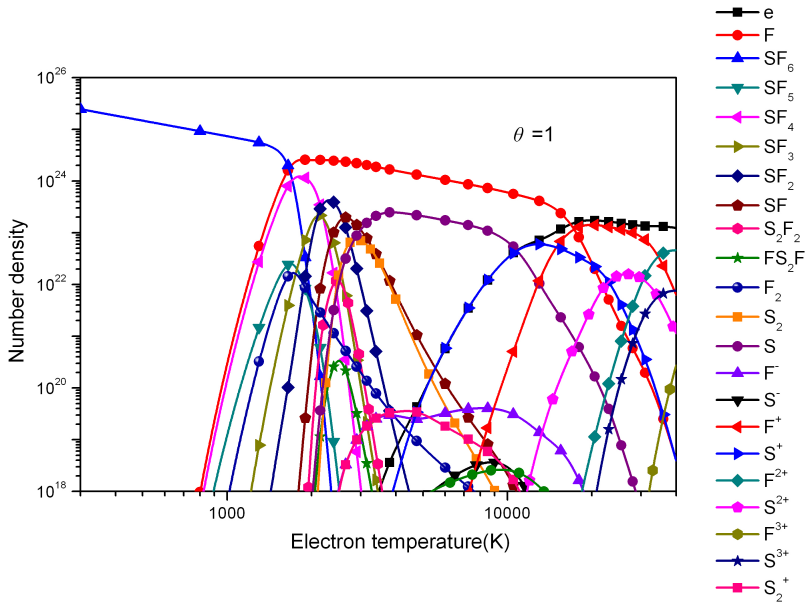

(a)

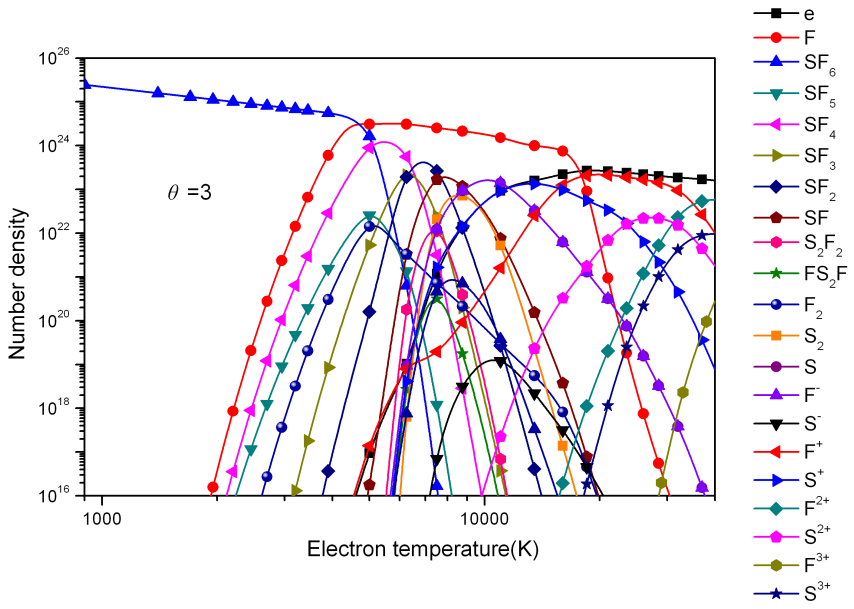

(b)

Figure 3.1 Temperature dependence of the number density of different species in SF_6 plasmas under non-equilibrium degree of 1 and 3 at atmospheric pressure

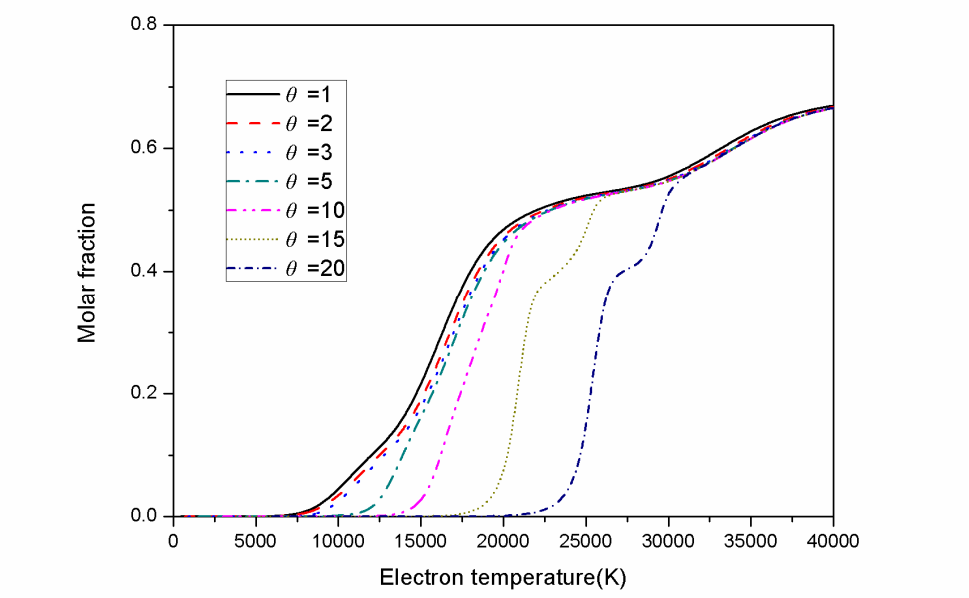

(a)

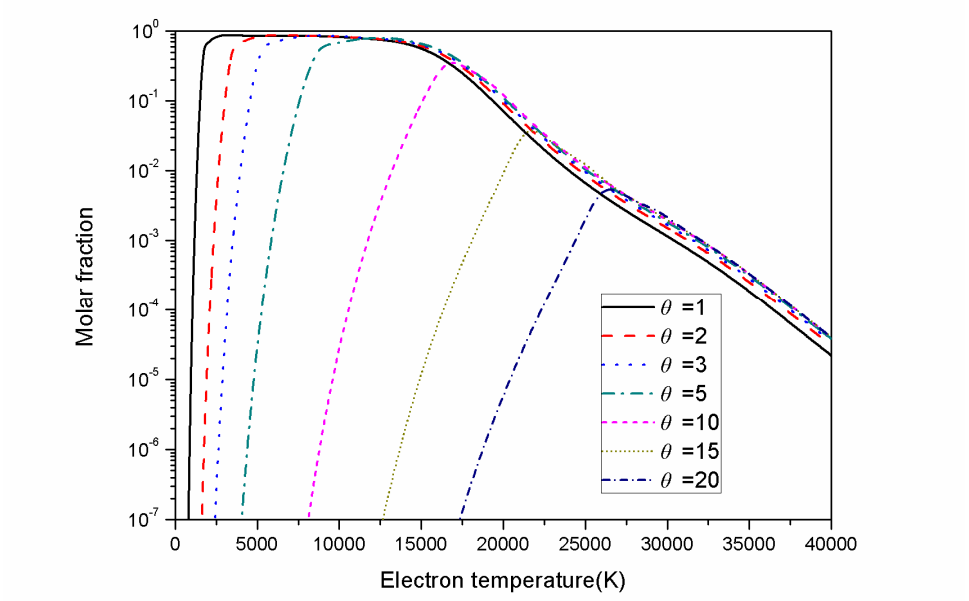

(b)

Figure 3.2 Temperature dependence of molar fraction of SF_6 plasmas under different non-equilibrium degrees at atmospheric pressure, (a) electron; (b) fluoride atom.

In a two-temperature plasma, the species composition at constant pressure is determined by two independent parameters, i.e. electron temperature and heavy specie temperature. Their influence on specie partial pressure can be evaluated by the differential derivatives $\partial p_i / \partial T_e$, $\partial p_i / \partial T_h$. In order to obtain these, the equations derived by two-temperature Saha's law and Gulberg–Waage's law involved in the generation of the plasma species together

with the equations for charge conservations, total pressure and mass ratio of parent gases are taken into account. Taking the logarithm of both sides of these equations and then taking the derivative with respect to T_e or T_h , differential derivative $\partial p_i / \partial T_e$ or $\partial p_i / \partial T_h$ can be obtained in terms of the solution of 25 simultaneous algebraic equations.

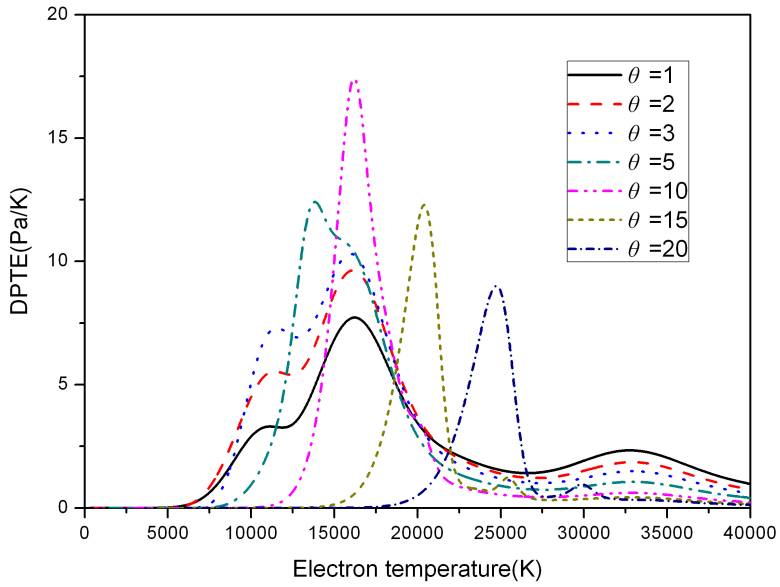

(a)

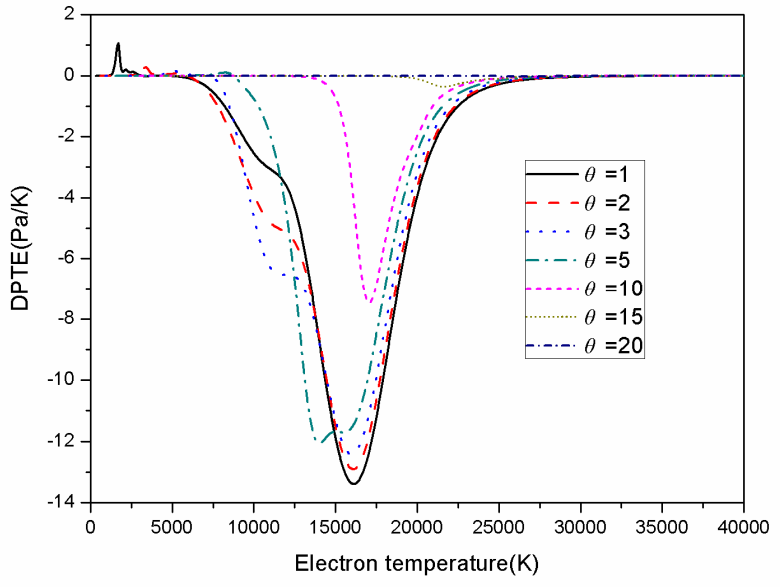

(b)

Figure 3.3 Temperature dependence of partial pressure derivative with respect to electron temperature in SF_6 plasmas under non-equilibrium degrees at atmospheric pressure,(a) electron; (b) fluoride atom.

The variations of the derivative $\partial p_i / \partial T_e$ for electrons and atomic fluorine as a function of electron temperature are presented in Fig. 3.3. Each curve peak corresponds to certain chemical reactions. Taking the $\partial p_i / \partial T_e$ for atomic fluorine in the equilibrium condition as an example, the dissociation and ionization reactions respectively bring the increasing and decreasing partial pressure of atomic fluorine if the electron temperature increases.

3.5.2 Thermodynamic Properties

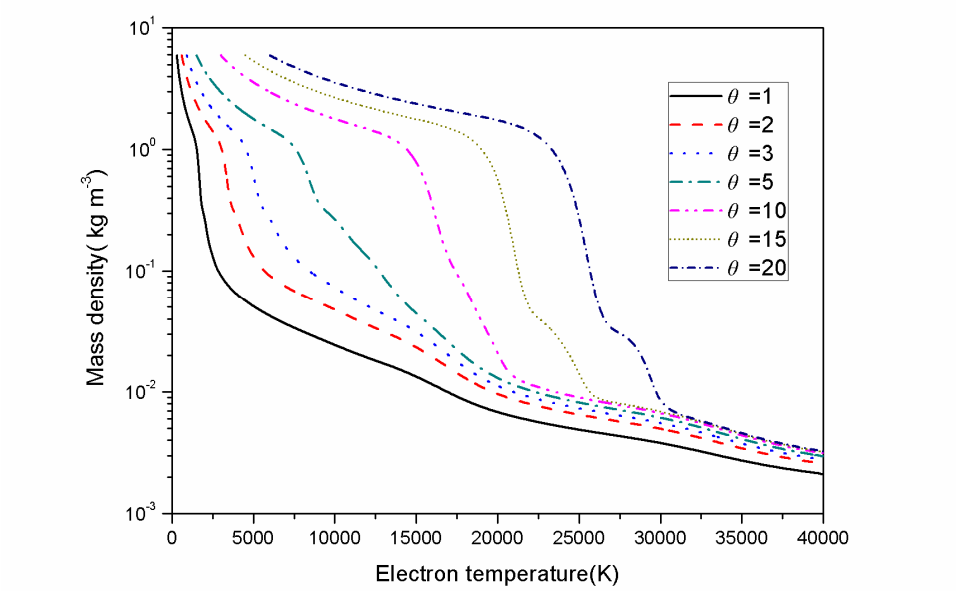

Figure 3.4 Temperature dependence of mass density of SF_6 plasmas under different degrees of non-equilibrium at atmospheric pressure

Mass densities for SF_6 plasmas as a function of electron temperature for different values of the non-equilibrium parameter are described in Fig. 3.4. The mass density increases at a fixed electron temperature as the θ value rises due to the delayed dissociation and ionization.

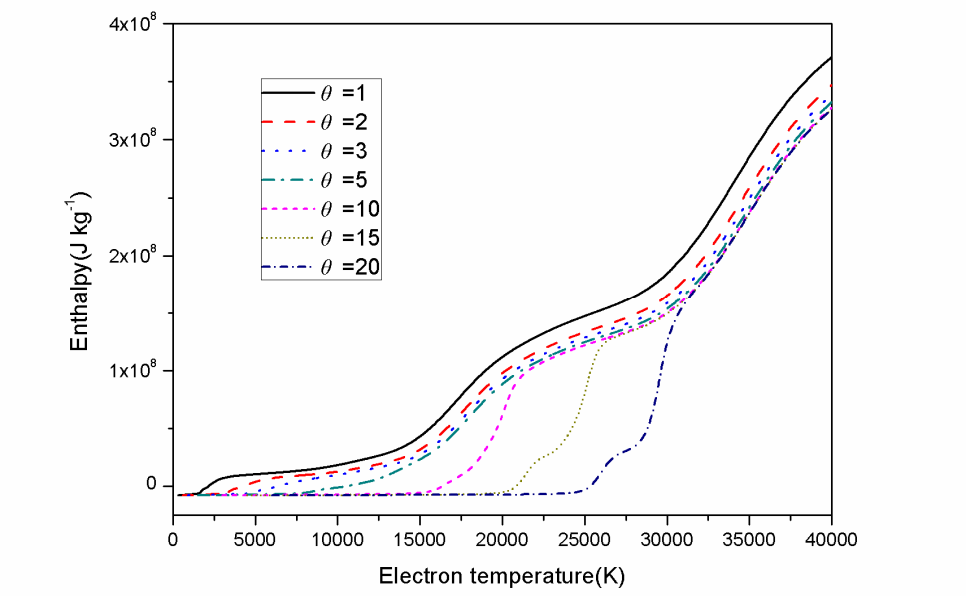

Figure 3.5 Temperature dependence of specific enthalpy of SF_6 plasmas under different degrees of non-equilibrium at atmospheric pressure

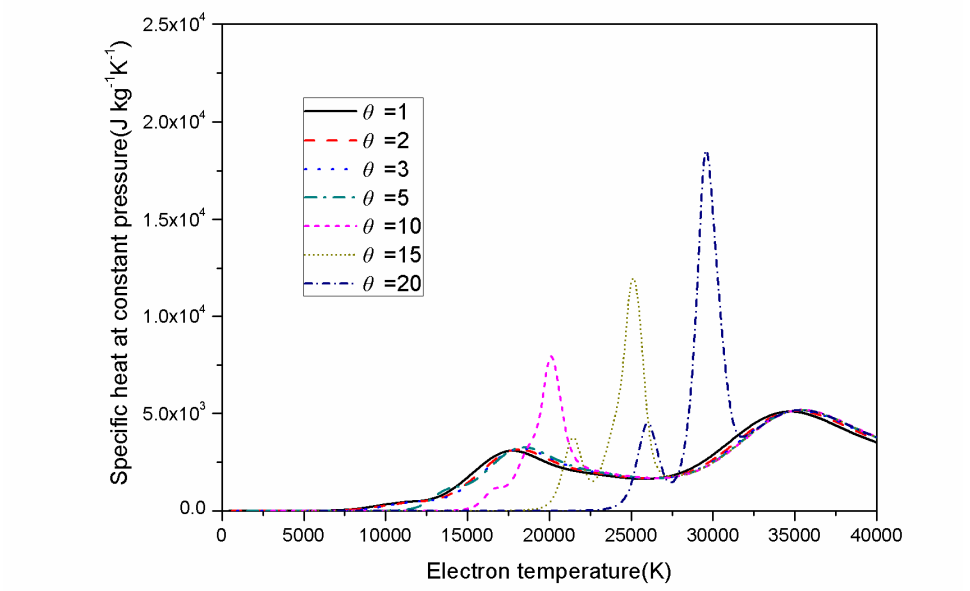

(a)

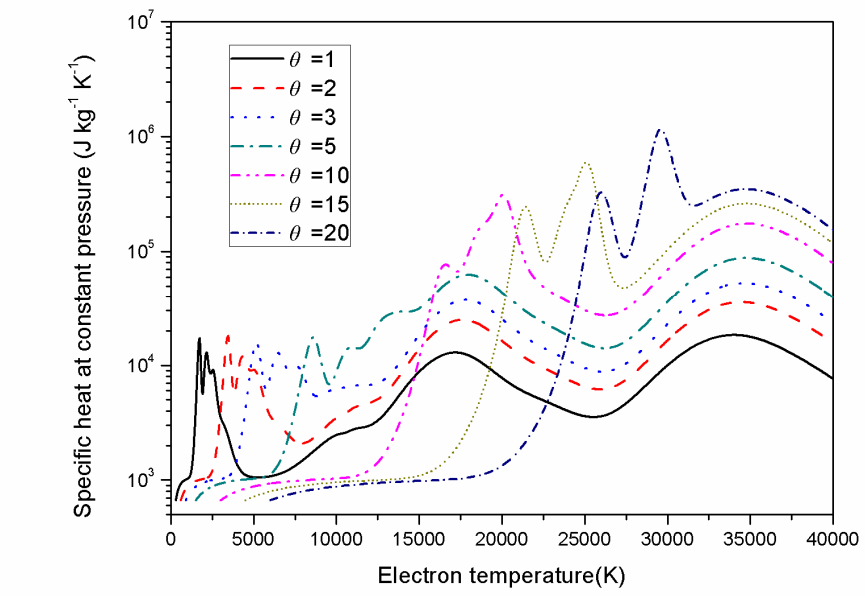

(b)

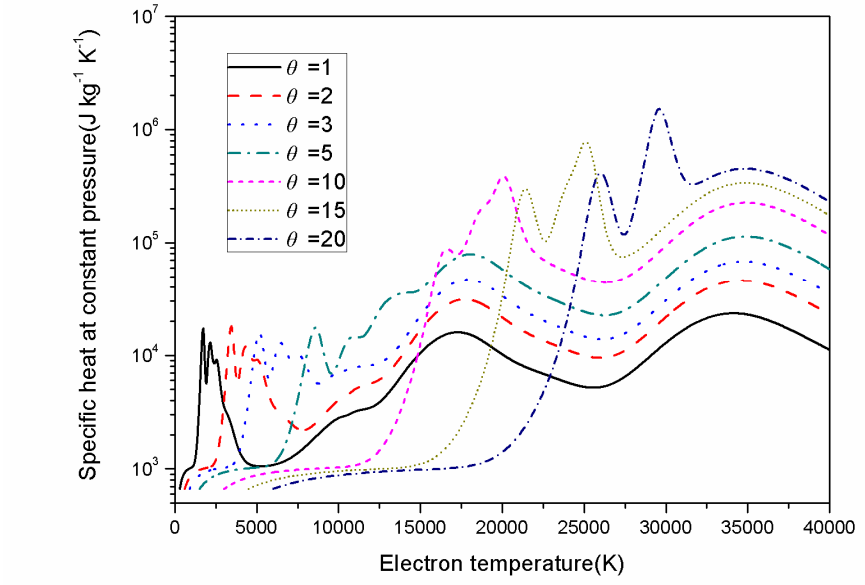

(c)

Figure 3.6 Temperature dependence of specific heat of SF_6 plasmas under different non-equilibrium degrees at atmospheric pressure, (a) CP_e; (b) CP_h; (c) CP_t.

The specific enthalpy and specific heat are shown as a function of electron temperature for different values of θ in Figs. 3.5–3.6. The specific enthalpy decreases with increasing θ values at a given electron temperature. With increasing electron temperature, the specific enthalpy becomes less sensitive to the change value of θ. The behaviour of electrons specific heat at constant pressure is closely connected with the variation of electron number density and

generates a peak each time ionization takes place. The more dramatic change of electron number density causes a much higher peak value of electrons specific heat at constant pressure. For heavy species, when the non-equilibrium degree is lower than 5, the peaks are respectively contributed by the multiple dissociations of SF_6 and the multiple ionizations of monatomic specie. For the value of θ>=5, it is difficult to separate the different contributions; the dissociation and ionization contributions are superimposed together. The can be explained that although enough high electron temperature has been reached, the dissociation reaction which is controlled by the heavy specie temperature does not take place to generate enough monatomic atoms. Once the dissociation temperature is arrived, the monatomic atoms undergo continuous ionization simultaneously bringing a high peak of specific heat curve. Comparing both results in the Fig. 3.6b-3.6c, it can be found that the heavy species play a most important role in determining the total specific heat at constant pressure.

3.5.3 Transport Coefficients

- **Comparison with Property Data of LTE Model**

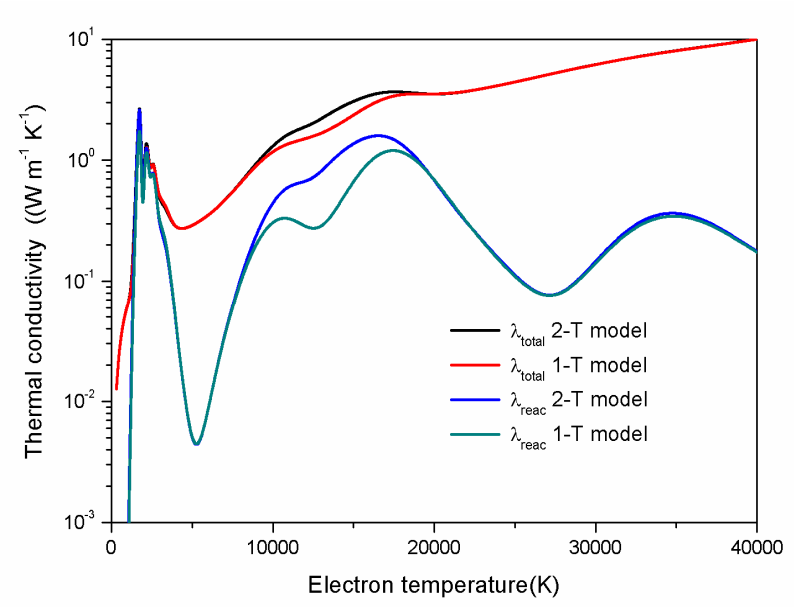

Figure 3.7 Temperature dependence of total and reactive thermal conductivity of SF_6 plasmas under equilibrium condition at atmospheric pressure.

When electrons and heavy species have the same temperature, the two-temperature model

reduces to the equilibrium case. Two-temperature model gives almost the same values except for thermal conductivity as obtained in chapter one. For species composition determination, the iterative solution of non-linear governing equations brings no difference from those obtained by Gibbs free energy minimization method because both methods are derived by the same fundamental principles. For thermodynamic properties determination, the standard thermodynamic relationships are employed, bringing the same values once the species composition is obtained. The slight discrepancy of transport coefficients obtained by two models is caused by the different coupled and decoupled approach. However, this discrepancy is negligible. The discrepancy of our calculated thermal conductivity with others in two-temperature model seems to be attributed to the different formulations in determining the reactive thermal conductivity (that of Kannappan and Bose [71] here, and that of Butler and Brokaw [72] by LTE model) as we can see in Fig. 3.7.

- **Diffusion Coefficients**

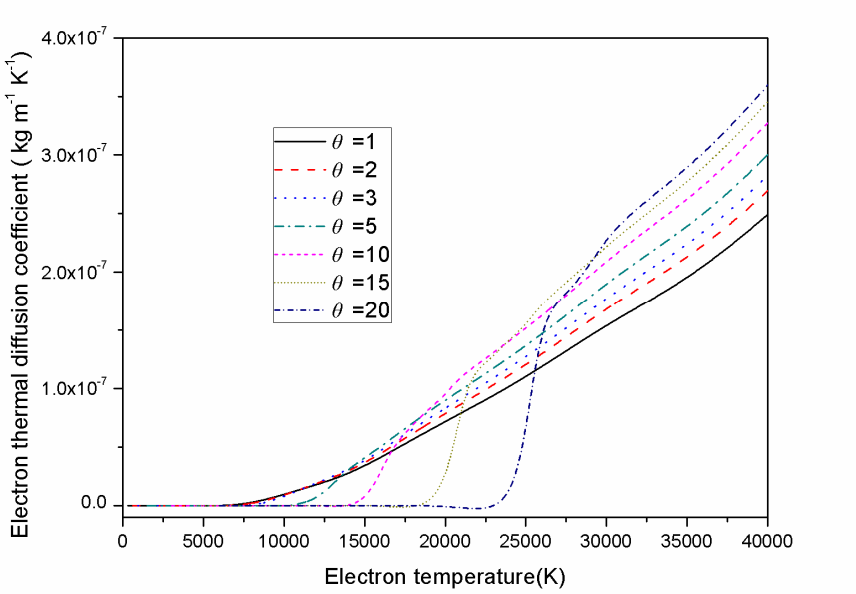

Figure 3.8 Temperature dependence of electron thermal diffusion coefficient of SF_6 plasmas under different non-equilibrium degrees at atmospheric pressure

Because the number of ordinary diffusion coefficients describing a plasmas is large (one for each pair of species), only the values of the thermal diffusion coefficient of electrons are presented here, although all diffusion coefficients are calculated. The values of electron

thermal diffusion coefficients strongly depend on the electron number density and the electron temperature. Ionisation reaction takes place at a higher electron temperature with increasing value of θ due to the delayed dissociation and results in a lower value of electron thermal diffusion coefficient. When temperature is further increased, the higher value of non-equilibrium degree brings a higher electron number density and hence a higher electron thermal diffusion coefficient.

- **Viscosity**

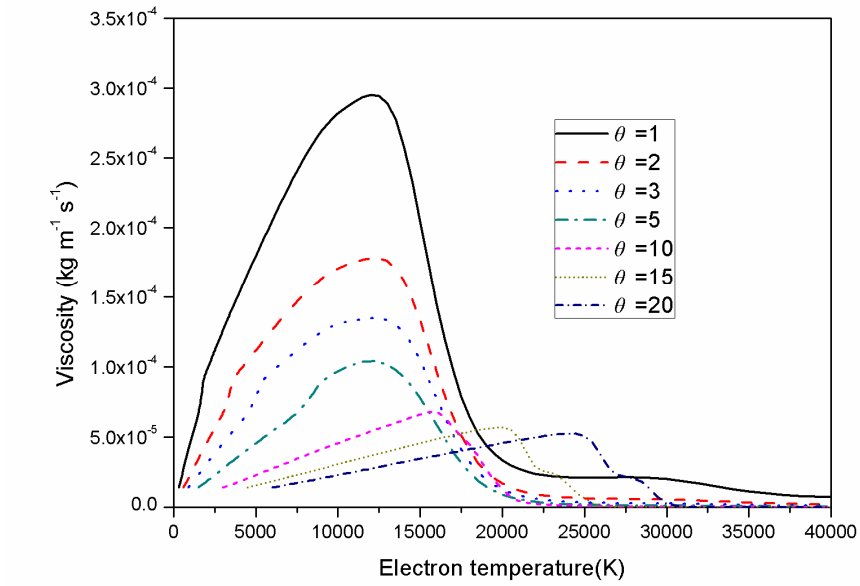

Figure 3.9 Temperature dependence of viscosity of SF_6 plasmas under different non-equilibrium degrees at atmospheric pressure.

Only the heavy species are included in the determination of viscosity. The viscosity first increases with temperature, and then decreases as the strong Coulomb interaction starts to dominate. The non-equilibrium degrees have a significant influence on the viscosity. With increasing values of θ, a decreasing viscosity peak height and a shift of ionization onset toward to higher electron temperature but to a lower heavy specie temperature is observed.

- **Thermal Conductivity**

Translational thermal conductivities of SF_6 for different values of θ are reported in Fig. 3.10.

The heavy specie component shows the behaviour of multiple peaks due to the continuous reactions occurring with the increasing electron temperature. The electron component closely depends on the electron number density and its interactions with other species similar with the electron thermal diffusion coefficients.

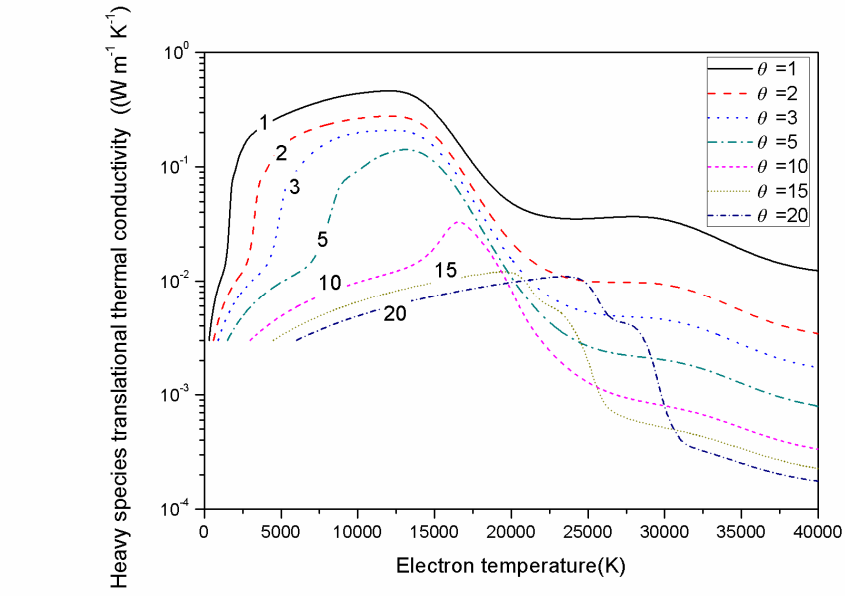

(a)

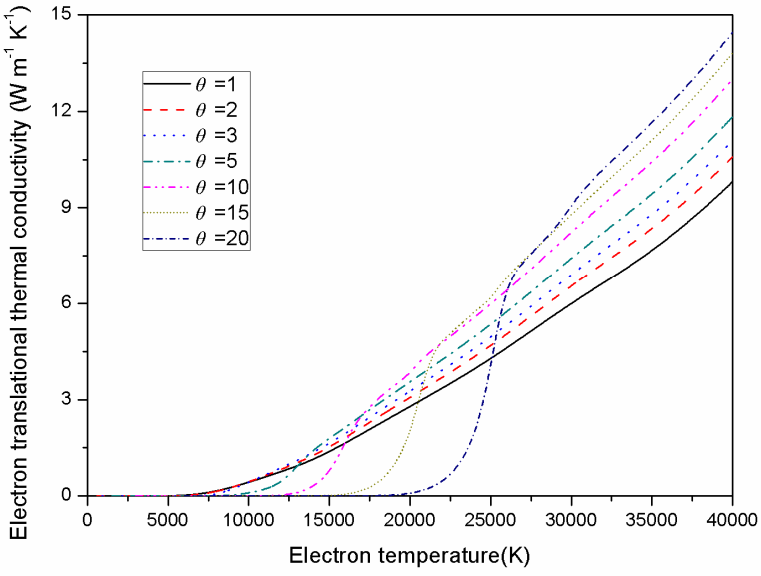

(b)

Figure 3.10 Temperature dependence of translational thermal conductivity (λ_{tr}) of SF_6 plasmas under different non-equilibrium degrees at atmospheric pressure, (a) heavy species; (b) electrons.

The internal thermal conductivity gives a slight contribution to total thermal conductivity as described in Fig. 3.11. The peak value of the internal component of the thermal conductivity (λ_{int}), arising from the transport of internal energy, also increases and moves towards higher electron temperature as θ increases.

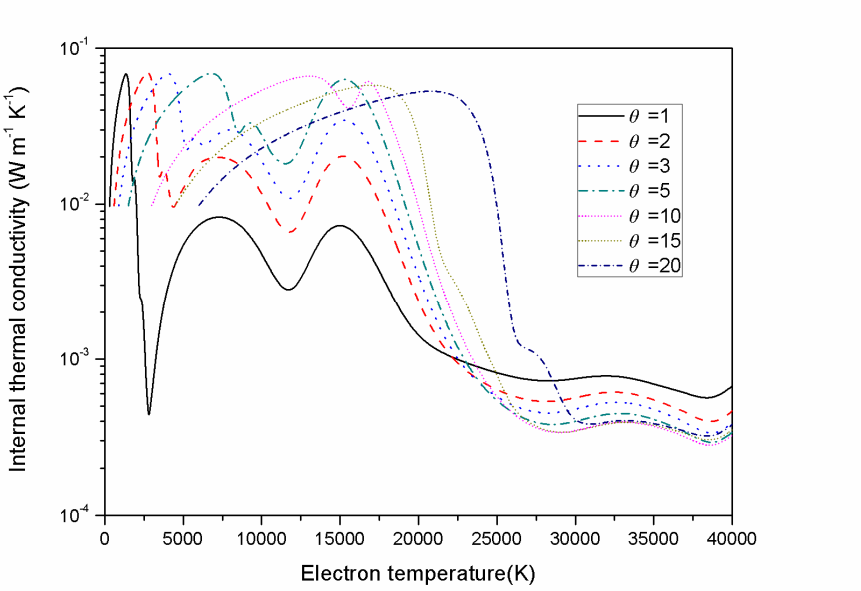

Figure 3.11 Temperature dependence of internal thermal conductivity (λ_{in}) of SF_6 plasmas under different non-equilibrium degrees at atmospheric pressure.

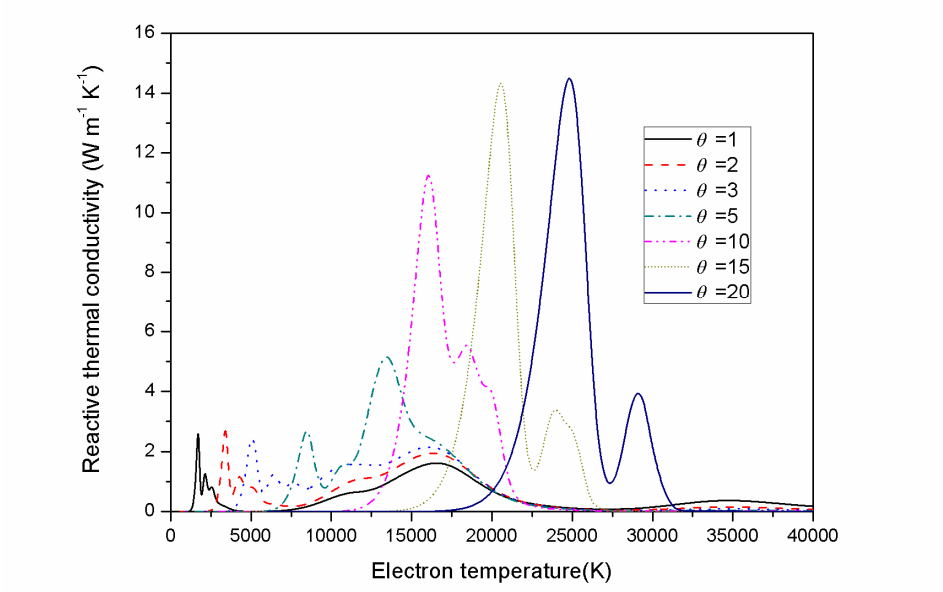

Figure 3.12 Temperature dependence of reactive thermal conductivity (λ_{reac}) of SF_6 plasmas under different non-equilibrium degrees at atmospheric pressure.

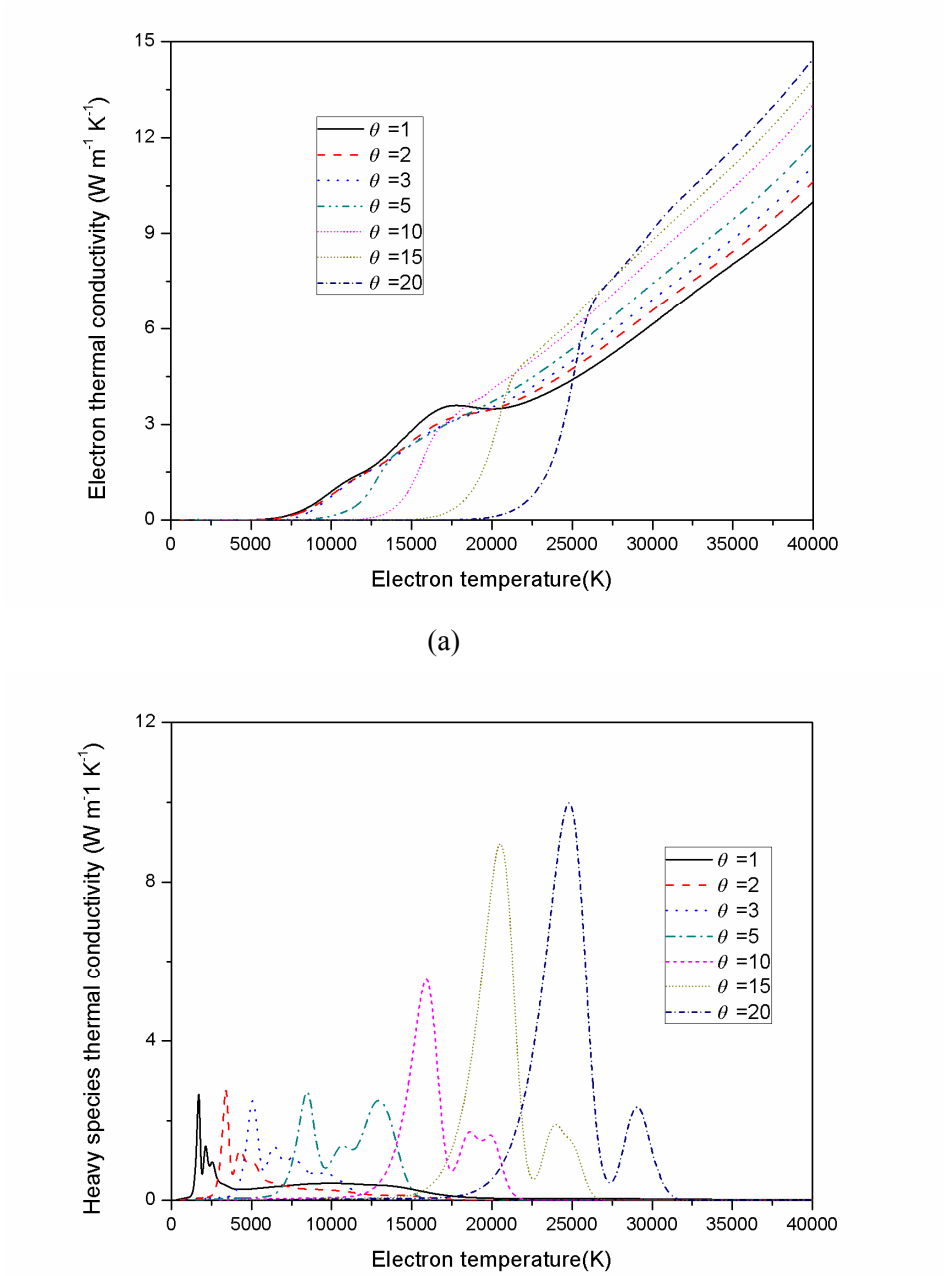

Figure 3.13 Temperature dependence of thermal conductivity (λ_e and λ_h) of SF_6 plasmas under different non-equilibrium degrees at atmospheric pressure, (a) electrons; (b) heavy species.

The total reactive thermal conductivity of electrons and heavy species as a function of electron temperature for different values of θ is presented in Fig. 3.12. The dissociation peak of SF_6 is shifted toward higher electron temperatures as the non-equilibrium degree increases because the dissociation reaction strongly relies on heavy specie temperature. Three continuous

peaks which correspond to multiple dissociations of SF_6 can be observed under the equilibrium condition, however when ionization electron temperature reaches the dissociation heavy specie temperature at the value of $\theta >= 5$, peaks are not clearly distinguishable.

Variation of the total thermal conductivity ($\lambda_e + \lambda_h$) is presented in Fig. 3.13. In the temperature range where dissociation and ionization take place, the reactive term makes a major contribution, while for electrons, the translational contribution becomes important in higher temperature range and for heavy species, the influence of translational contribution is small.

- **Electrical Conductivity**

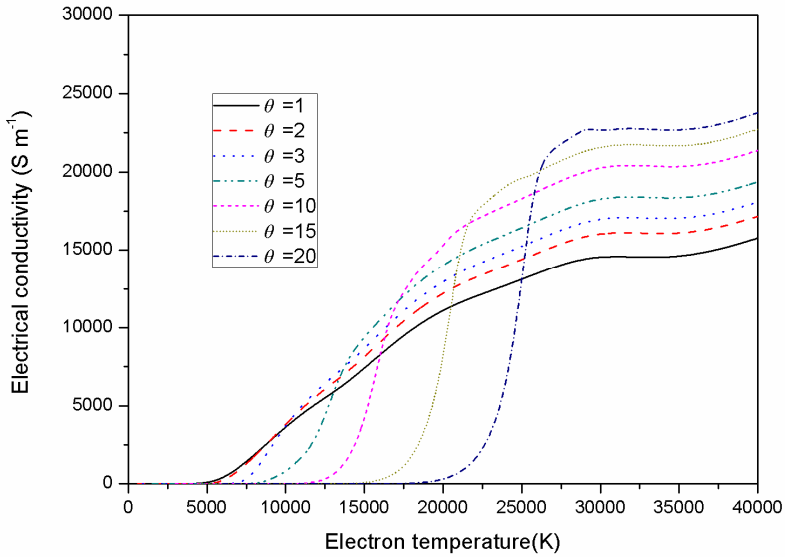

Figure 3.14 Temperature dependence of electrical conductivity of SF_6 plasmas under different non-equilibrium degrees at atmospheric pressure.

Dissociation of molecules, which is related to the heavy specie temperature, does not occur until the corresponding electron temperature is reached. This shifts the ionization towards higher electron temperature as θ increases. Once the dissociations starts, the electrical conductivity value rises fast because the ionization is favored. For each value of θ, the electrical conductivity first increases and then slightly decreases mainly caused by the variation of the electron number density.

- **Volumetric Collision Frequency**

The increasing electron temperature promotes the production of electrons by the ionization and hence a rising volumetric collision frequency between the electrons and the heavy specie. Further temperature increase causes the species number density decrease and therefore the volumetric collision frequency between the electrons and the heavy species decreases. The shift of the peaks as found in Fig. 3.15 can be attributed again to the behaviour of the dissociation controlled by heavy specie temperature for a fixed value of θ.

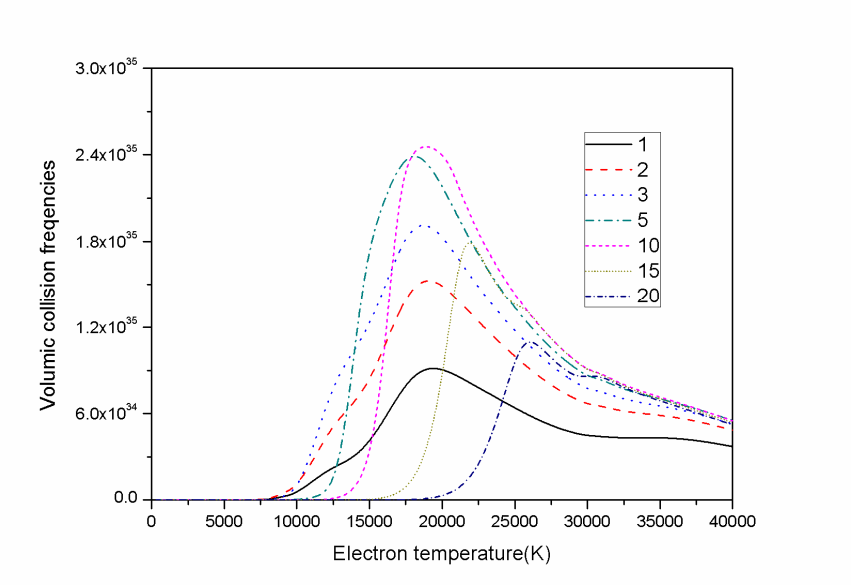

Figure 3.15 Temperature dependence of volumic collision frequency of SF_6 plasmas under different non-equilibrium degrees at atmospheric pressure.

3.5.4 Influence of Pressure on Properties

Fig. 3.16 presents the influence of pressure on the chemical equilibrium composition, specific heat and transport coefficients for pressures 0.01MPa, 0.10MPa, 0.40MPa, 1.0MPa for θ=3. According to Le Chatelier's law, the increase of the pressure opposes changes to the original state of equilibrium, so that dissociation and ionization at a given temperature are suppressed; therefore, the relevant properties curves are shifted to a higher electron temperature as the pressure increases.

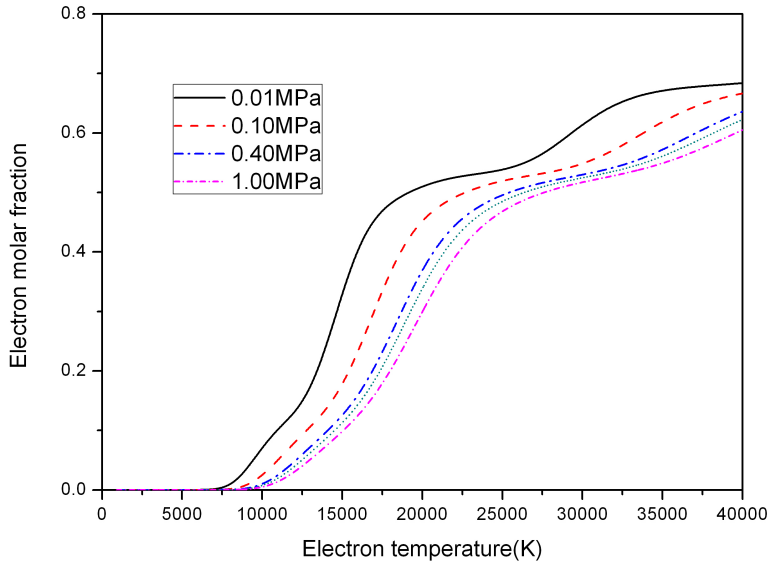
0.01MPa
0.10MPa
0.40MPa
1.00MPa
Electron molar fraction
Electron temperature(K)
0.0
0.2
0.4
0.6
0.8
0
5000
10000
15000
20000
25000
30000
35000
40000

(a)

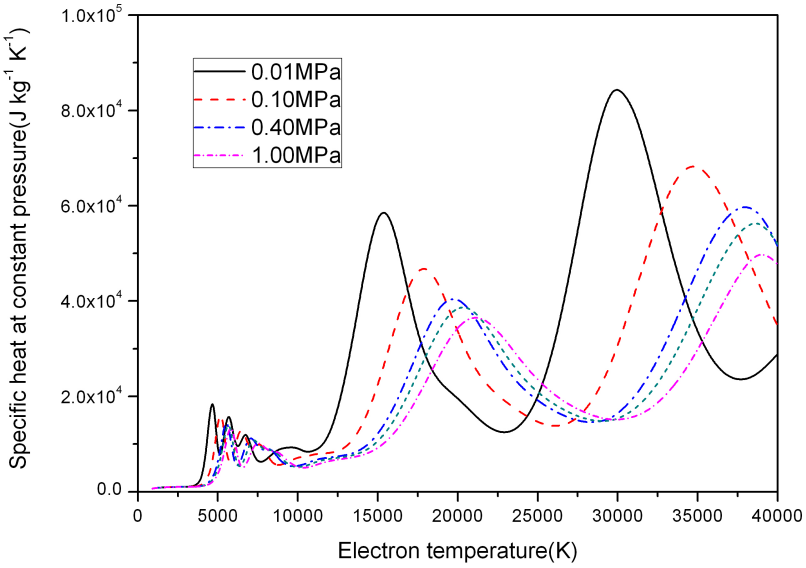
0.01MPa
0.10MPa
0.40MPa
1.00MPa
Specific heat at constant pressure(J kg-1 K-1)
Electron temperature(K)
1.0x10^5
8.0x10^4
6.0x10^4
4.0x10^4
2.0x10^4
0.0
0
5000
10000
15000
20000
25000
30000
35000
40000

(b)

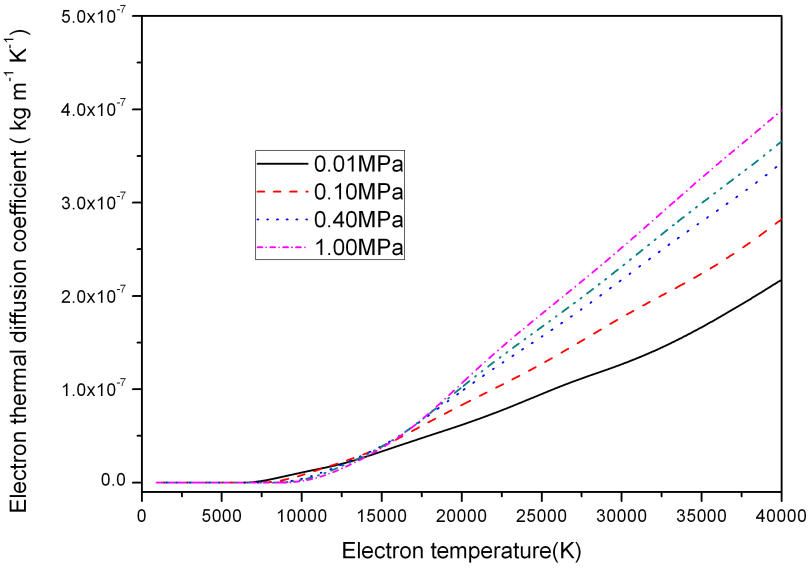
Electron thermal diffusion coefficient (kg m-1 K-1)
5.0x10-7
4.0x10-7
3.0x10-7
2.0x10-7
1.0x10-7
0.0
0.01MPa
0.10MPa
0.40MPa
1.00MPa
0
5000
10000
15000
20000
25000
30000
35000
40000
Electron temperature(K)

(c)

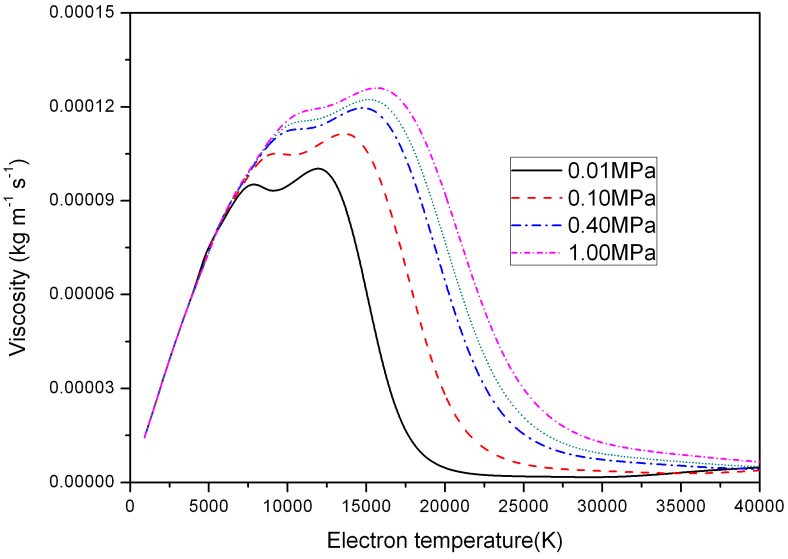
Viscosity (kg m-1 s-1)
0.00015
0.00012
0.00009
0.00006
0.00003
0.00000
0.01MPa
0.10MPa
0.40MPa
1.00MPa
0
5000
10000
15000
20000
25000
30000
35000
40000
Electron temperature(K)

(d)

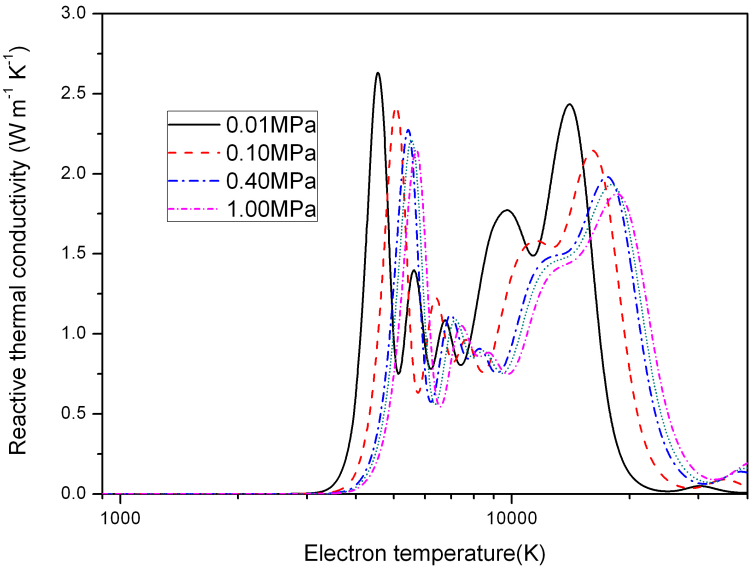
Reactive thermal conductivity (W m^{-1} K^{-1})
3.0
2.5
2.0
1.5
1.0
0.5
0.0
0.01MPa
0.10MPa
0.40MPa
1.00MPa
1000
10000
Electron temperature(K)

(e)

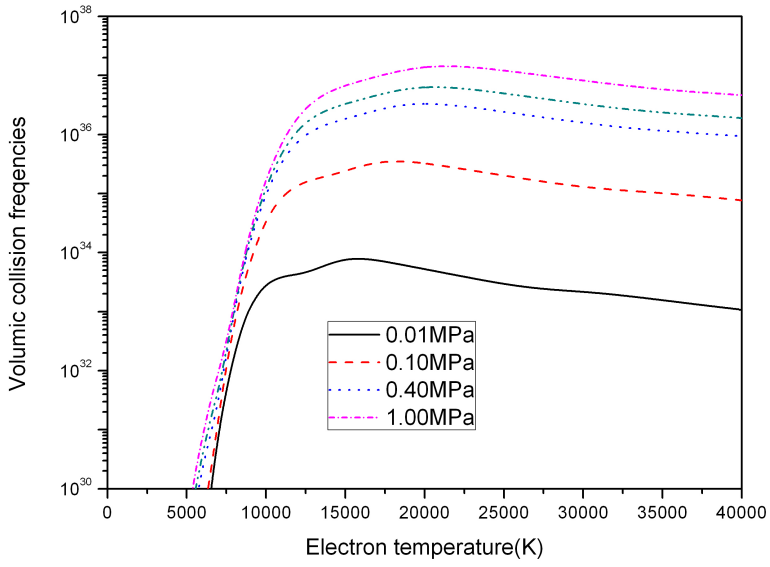
Volumic collision freqencies
10^{38}
10^{36}
10^{34}
10^{32}
10^{30}
0.01MPa
0.10MPa
0.40MPa
1.00MPa
0
5000
10000
15000
20000
25000
30000
35000
40000
Electron temperature(K)

(f)

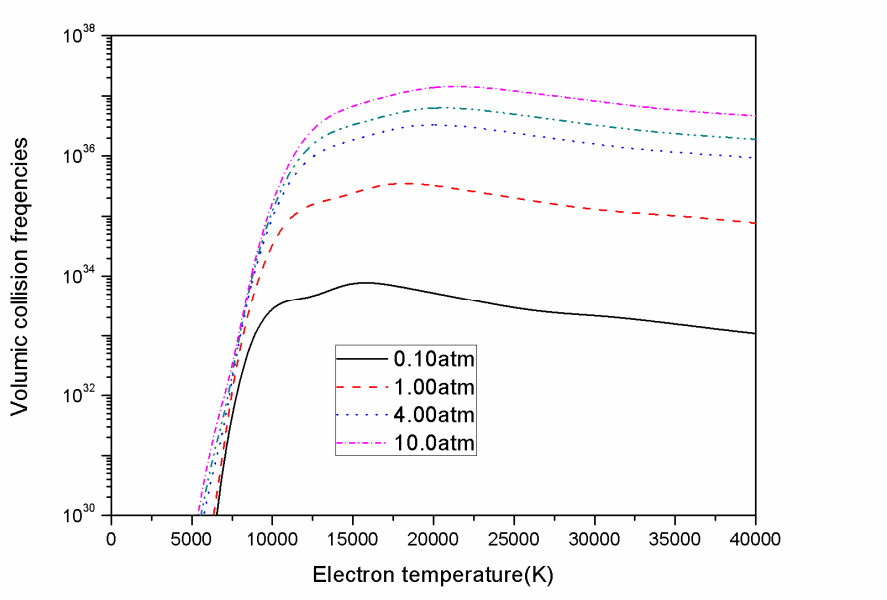

(g)

Figure 3.16 Influence of pressure on electron mole fraction (a), specific heat at constant pressure (b), electron thermal diffusion coefficients (c), viscosity (d), reactive thermal conductivity (e) and electrical conductivity (f), volumetric collision frequency (g) of SF_6 plasmas under different pressures 0.01MPa, 0.10MPa, 0.40MPa, 1.0MPa for $\theta=3$

3.5.5 Influence of Different Expressions of Mass action Law

In contrast, the difference between the two expressions of mass action law derived by Van de Sanden et al.'s method and by Potapov's method can be summarized as follows: For the dissociation reaction, existence of the power θ on the right side in the Potapov's derivation and the reaction excitation temperature T_{ex} replacing T_h in the exponential term of Van de Sanden et al.'s derivation; For the ionization reaction, existence of the power $1/\theta$ on the both left-hand and right-hand sides in the Potapov's derivation.

In order to study the influence of two different forms of mass action law, the excitation temperature in the exponent term on the right-hand side takes the same value, i.e. $T_{ex}=T_h$ for molecular ionization together with the dissociation and $T_{ex}=T_e$ for atomic ionization.

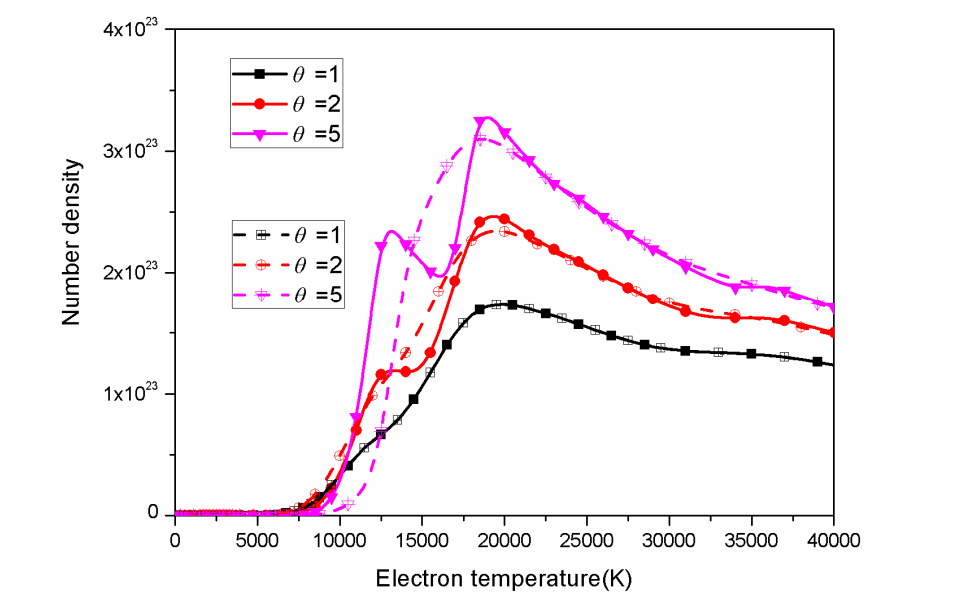
4x10^23
3x10^23
2x10^23
1x10^23
0
Number density
θ =1
θ =2
θ =5
θ =1
θ =2
θ =5
0
5000
10000
15000
20000
25000
30000
35000
40000
Electron temperature(K)

(a)

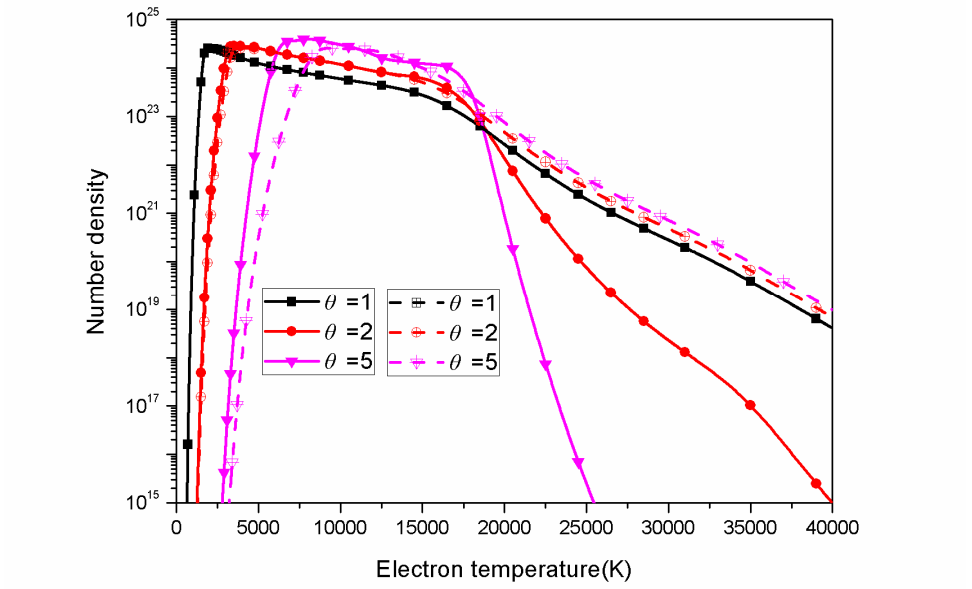
10^25
10^23
10^21
10^19
10^17
10^15
Number density
θ =1
θ =2
θ =5
θ =1
θ =2
θ =5
0
5000
10000
15000
20000
25000
30000
35000
40000
Electron temperature(K)

(b)

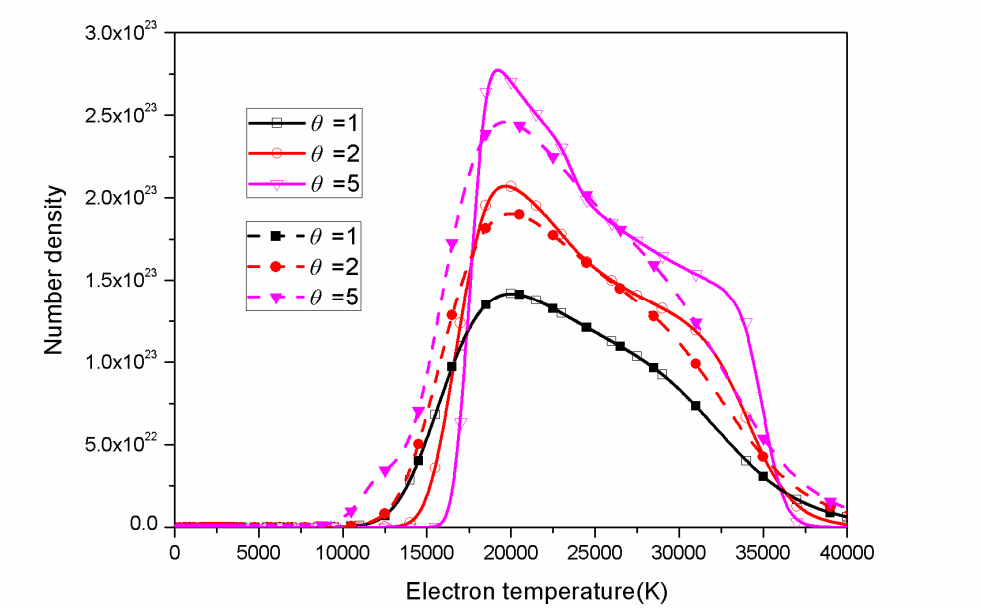

(c)

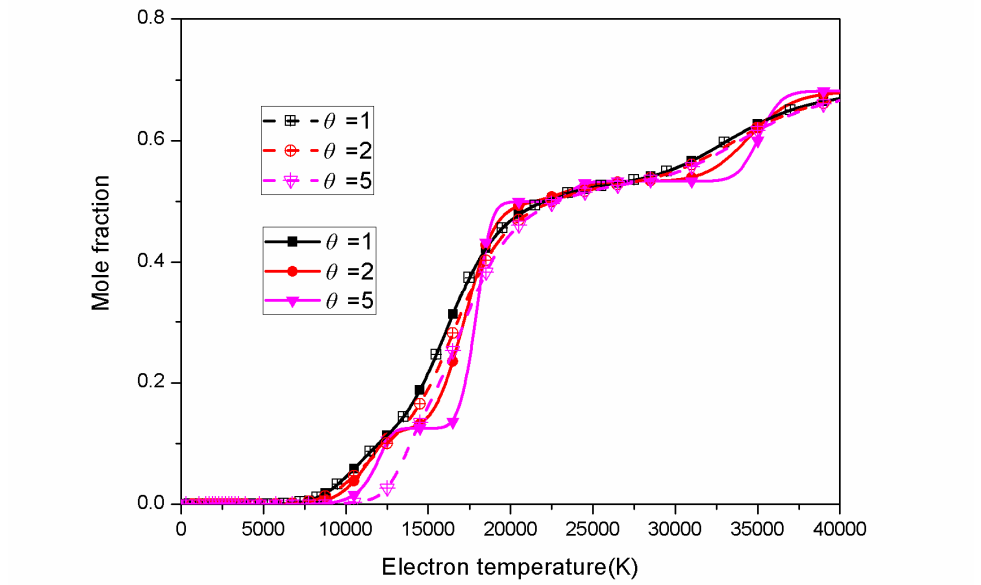

(d)

Figure 3.17 Comparison of equilibrium number densities and molar fraction in SF_6 plasmas from different Saha and Guldberg-Waage equations under non-equilibrium degrees of θ=1, θ=2, θ=5 at atmospheric pressure, dash line & symbols: results obtained by Van de Sanden et al.'s method; Solid line & symbols: results obtained by Potapov's method. (a), electrons number density; (b), fluorine atom number density; (c), fluorine ion number density; (d), electrons molar fraction.

For the equilibrium case of θ=1, both two forms reduce to the same expression and

hence brings completely the same properties. Before the ionization occurs, the only difference of the power θ on the right-hand side for Guldberg-Waage equations derived by Van de Sanden et al.'s method and by Potapov's method influences the species composition slightly when comparing the number density of atomic fluorine obtained by both methods in Fig. 3.17 where the molecular ionization excitation temperature equals T_h. The existence of the power θ on the right side in the Potapov's derivation brings a relatively higher atomic fluorine number density even under the same non-equilibrium degree, temperature and pressure. When ionization begins, both two derivations of two-temperature mass action law give dominant deviation of number densities and molar fractions for different species.

The electron number density obtained by Potapov's method shows the behaviour of multiple peaks when departure from thermal equilibrium takes place and marked differences in the molar fraction are observed as well in Fig. 3.17. Each drastic change of electron molar fraction corresponds to certain ionization reaction. For example, the change of electron molar fraction of non-equilibrium degree $\theta=5$ in the electron temperature 12000K, 17000K, 24000K and 35000K are closely connected with the continuous ionizations of sulfur and fluorine. We can see that the variation of electron molar fraction with the temperature obtained by the Potapov's derivation is more drastic than that by Van de Sanden et al.'s derivation and this behaviour can also be found from the number density evolution of first fluorine ion as a function of electron temperature. This behaviour can greatly influence the values of thermodynamic properties and transport coefficients.

From what have been discussed above, we can see that Potapov's derivation can cause much more intense change of species concentration when reaction takes place and hence a much more drastic change of partial specific heat at constant pressure which are defined as the partial differential of total specific enthalpy with regard to T_e (CPTE) and T_h (CPTH) as demonstrated in Fig. 3.18.

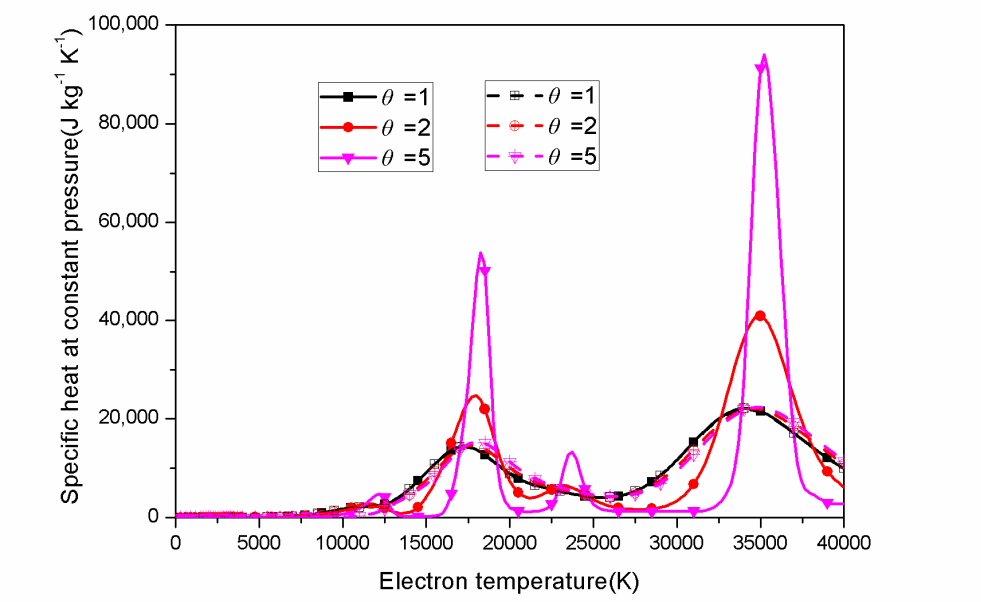

(a)

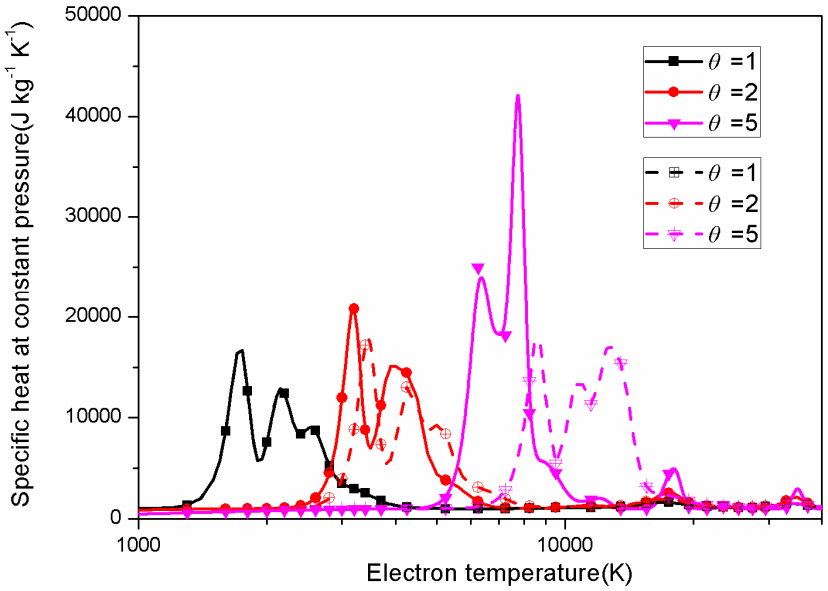

(b)

Figure 3.18 Comparison of partial specific heat at constant pressure in SF_6 plasmas from different Saha and Guldberg-Waage equations under non-equilibrium degrees of θ=1, θ=2, θ=5 at atmospheric pressure, dash line & symbols: results obtained by Van de Sanden et al.'s method; Solid line & symbols: results obtained by Potapov's method, (a), CPTE; (b), CPTH.

Due to the relevance of dissociation reaction and ionization reaction respectively with heavy species temperature and electron temperature, the peaks of CPTE and CPTH curves are

correspondingly related to the continuous ionization and dissociation. When ionization takes place, CPTH curves also presents peaks as well and this behaviour shows the significant influence of heavy specie temperature on ionization because T_h and T_e are not independent and closely coupled together for a fixed value of θ. We can also observe that the dissociation which is controlled by T_h is shifted to higher electron temperature with increasing values of θ. However, certain ionization reaction occurs at a fixed electron temperature regardless of the values of θ. This is because in the range of non equilibrium degree θ considered in our current work, the electron temperature at which the first ionization in the system occurs is lower than that of the last dissociation. When further increasing the value of θ, it is possible that some ionization will be inhibited until complete dissociation is finished. For this case, we have presented a study in previous section and detailed description will not be shown here.

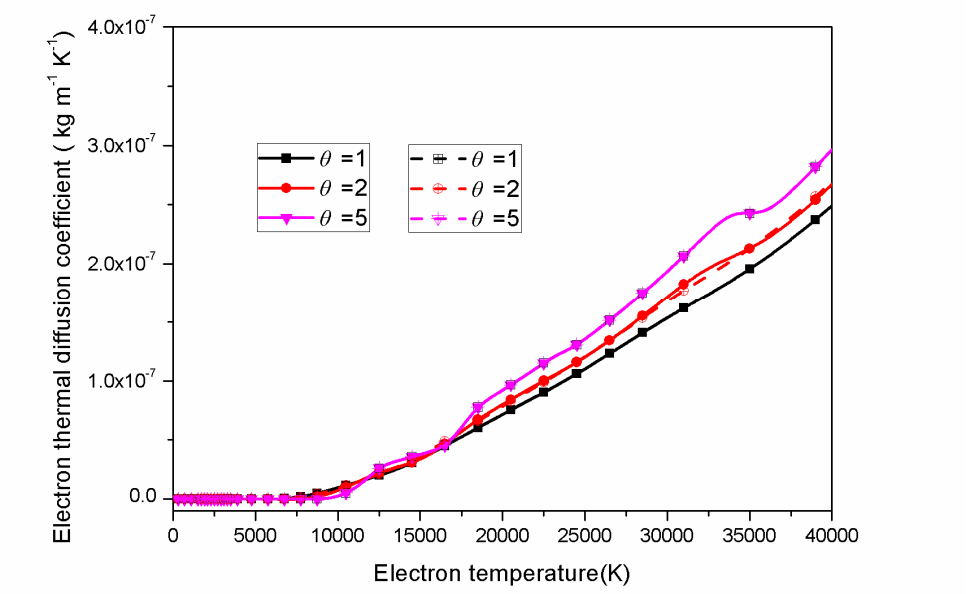

(a)

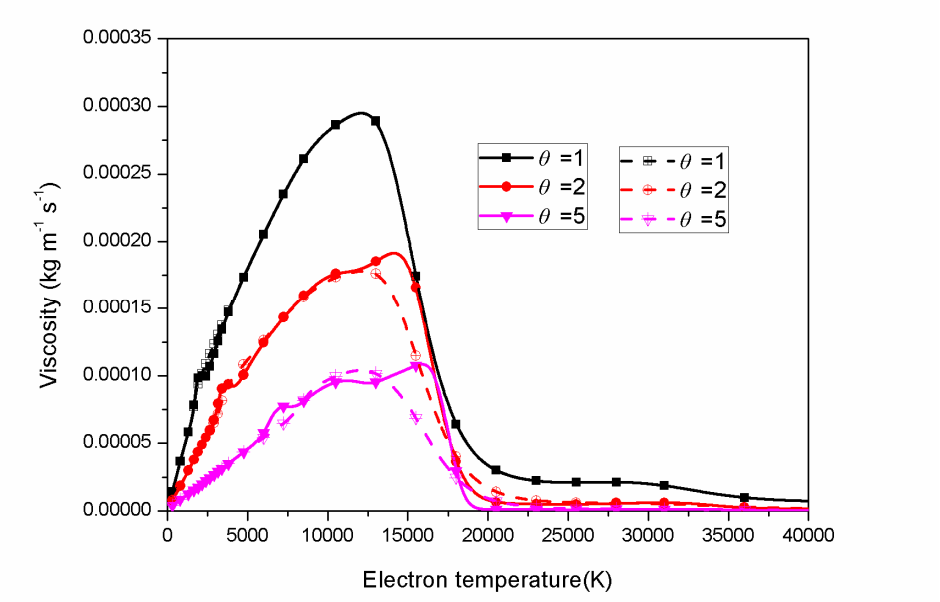
Viscosity (kg m^{-1} s^{-1})
0.00035
0.00030
0.00025
0.00020
0.00015
0.00010
0.00005
0.00000
0
5000
10000
15000
20000
25000
30000
35000
40000
Electron temperature(K)
θ =1
θ =2
θ =5
θ =1
θ =2
θ =5

(b)

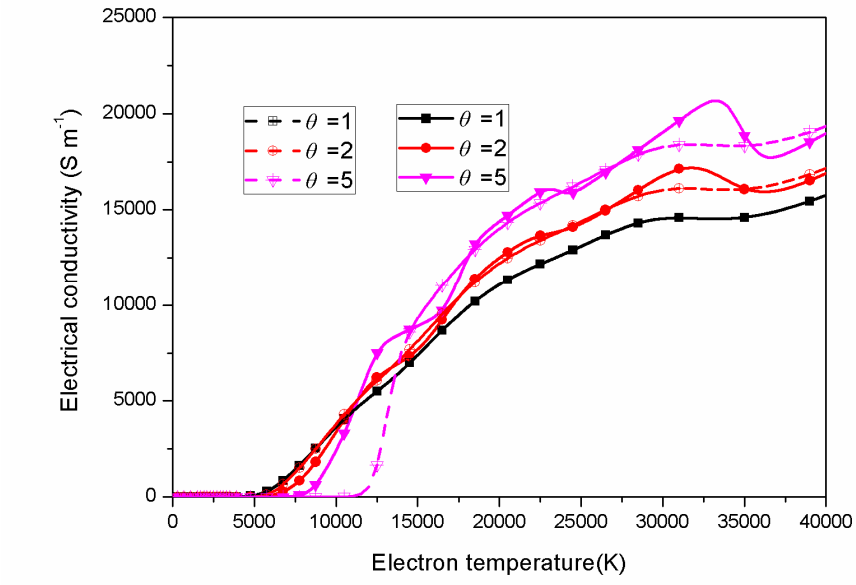
Electrical conductivity (S m^{-1})
25000
20000
15000
10000
5000
0
0
5000
10000
15000
20000
25000
30000
35000
40000
Electron temperature(K)
θ =1
θ =2
θ =5
θ =1
θ =2
θ =5

(c)

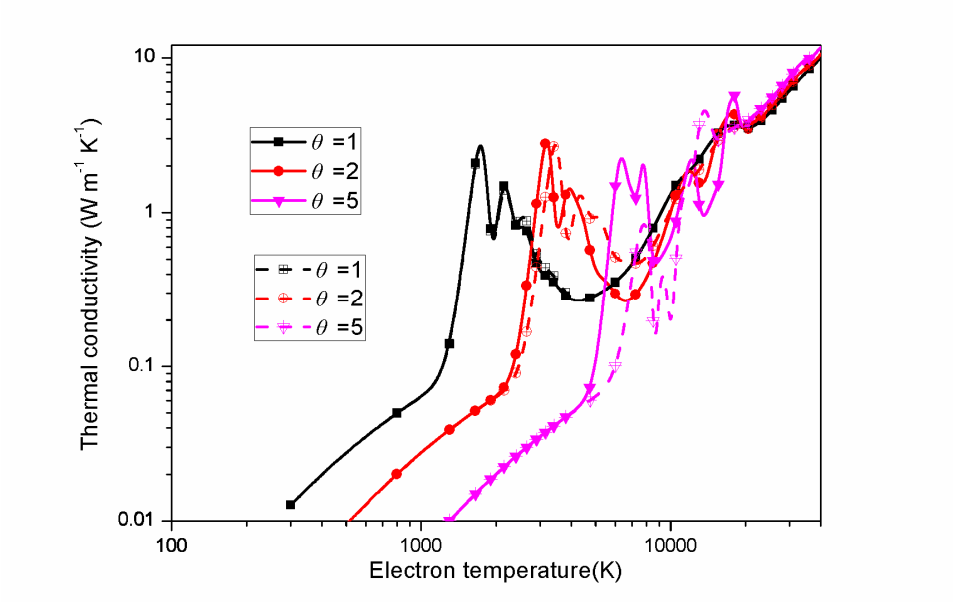

(d)

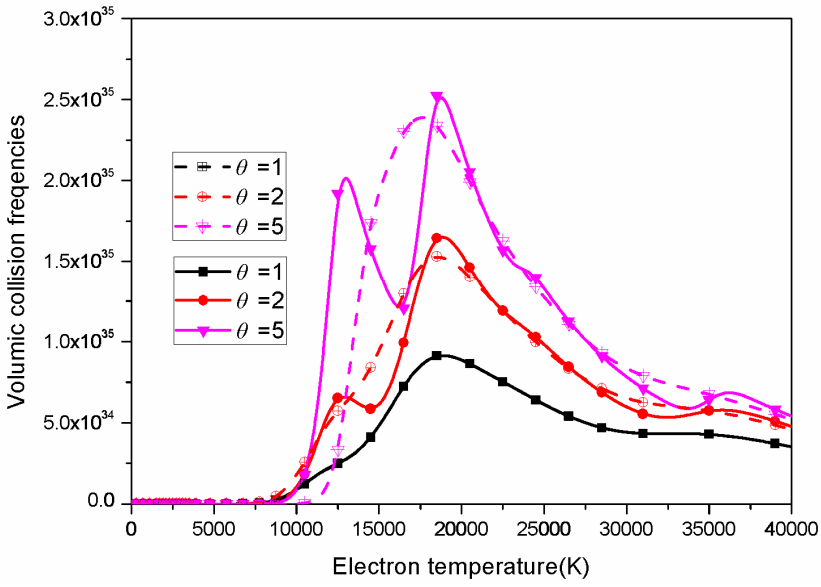

(e)

Figure 3.19 Comparison of transport coefficients in SF_6 plasmas from different Saha and Guldberg-Waage equations under non-equilibrium degrees of θ=1, θ=2, θ=5 at atmospheric pressure, dash line & symbols: results obtained by Van de Sanden et al.'s method; Solid line & symbols: results obtained by Potapov's method. (a), Electron diffusion coefficients; (b), Viscosity; (c), Electrical conductivity; (d), Thermal conductivity; (e), volumetric collision frequency.

Influence of different expressions of mass action law on transport coefficients are

described in Fig. 3.19. Of these, the electron diffusion coefficient and electrical conductivity are closely connected with electron number density, i.e. the ionization degree of the plasma. For example, from the electron number density results, for the value of θ=2, we can observe that the ionization is depressed from the Potapov's derivation when ionization just begins below the electron temperature 11000K and therefore, a slightly smaller values of electrical conductivity are obtained. However, for the value of θ=5, the ionization is favored in this range and hence a higher value of electrical conductivity. For viscosity, the position of the peak value is slightly shifted to a higher electron temperature with a higher height when the Potapov's derivation is adopted. As with the case of specific heat at constant pressure, the thermal conductivity peaks are shifted to higher electron temperature under the condition of Van de Sanden et al.'s method.

Volumetric collision frequency between electrons and heavy species is closely connected with electron number density and the collision cross section between electron and heavy species. As we can see in Fig. 3.19, for a fixed value of θ, below around the electron temperature 20000K, the increasing electron temperature promotes the production of electrons by the ionization and hence a rising value of volumetric collision frequency between electrons and heavy species. Above 20000K, a decreasing volumic collision frequency takes place. This is attributed to both the contributions of decreasing electron number density and the increasingly dominant interactions between electrons and charged particles. Both two forms of two-temperature mass action law apparently modify the behaviour of volumic collision frequency when departure from equilibrium occurs and these are mainly attributed to the influence of the electron number density.

3.5.6 Influence of different reaction excitation temperature

In previous papers, Gleizes et al. [27] showed the influence of the excitation temperature on the two temperature plasma composition. In Fig. 3.20, based on the general assumption that the excitation temperature for dissociation and atomic ionization are respectively T_h and T_e, we can investigate the influences of molecular ionization excitation temperature T_{ex} together with the choice of the different forms of mass action law on the electron number density, specific heat and transport coefficients at atmospheric pressure.

Using electron temperature as the molecular excitation temperature, it promotes the molecular ionization and leads to a higher value of electrons number density and positive molecular ions. It is observed that the choice of T_{ex} has a rather strong influence mainly at moderate temperatures in the temperature range from 7000K to 15000K regardless of the choice of mass action law forms, where diatomic molecules are present and ionization just begins.

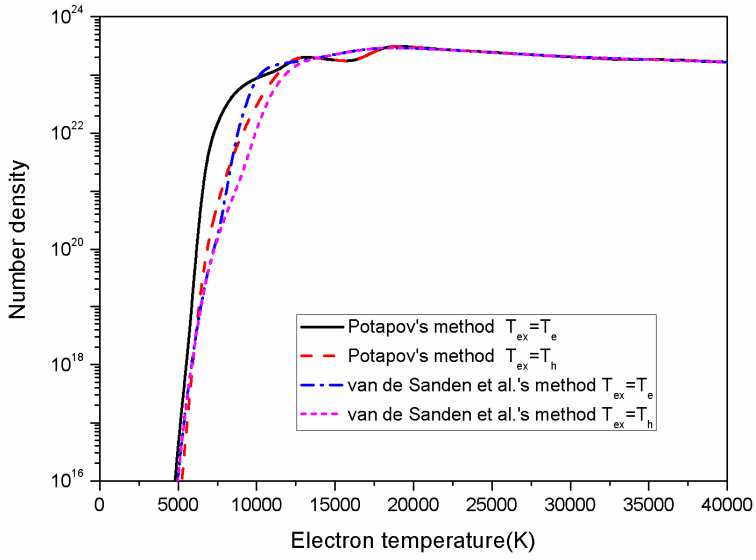

(a)

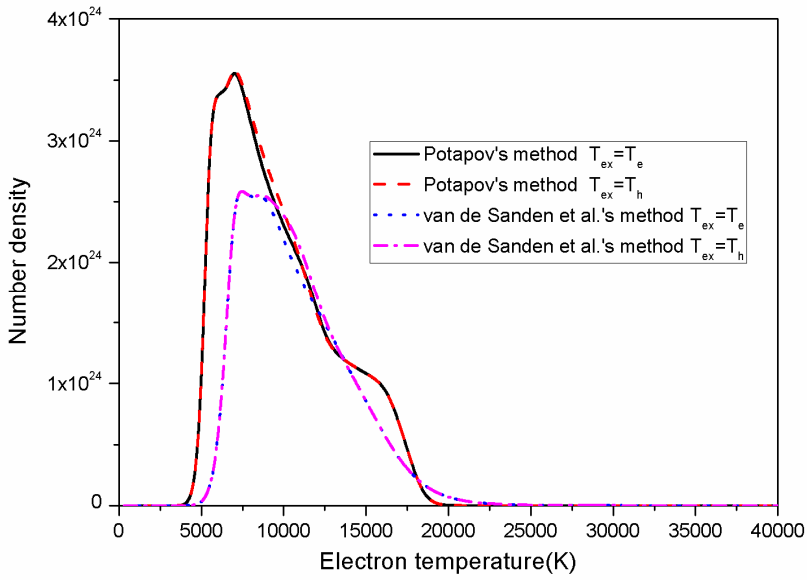

(b)

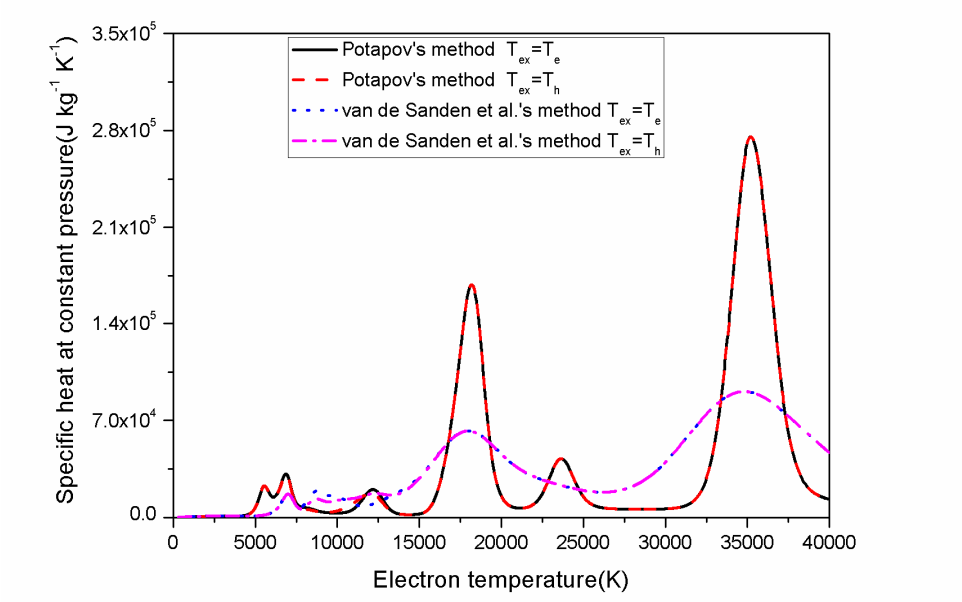
Potapov's method $T_{ex}=T_e$
Potapov's method $T_{ex}=T_h$
van de Sanden et al.'s method $T_{ex}=T_e$
van de Sanden et al.'s method $T_{ex}=T_h$
Specific heat at constant pressure(J kg^{-1} K^{-1})
3.5x10^5
2.8x10^5
2.1x10^5
1.4x10^5
7.0x10^4
0.0
0
5000
10000
15000
20000
25000
30000
35000
40000
Electron temperature(K)

(c)

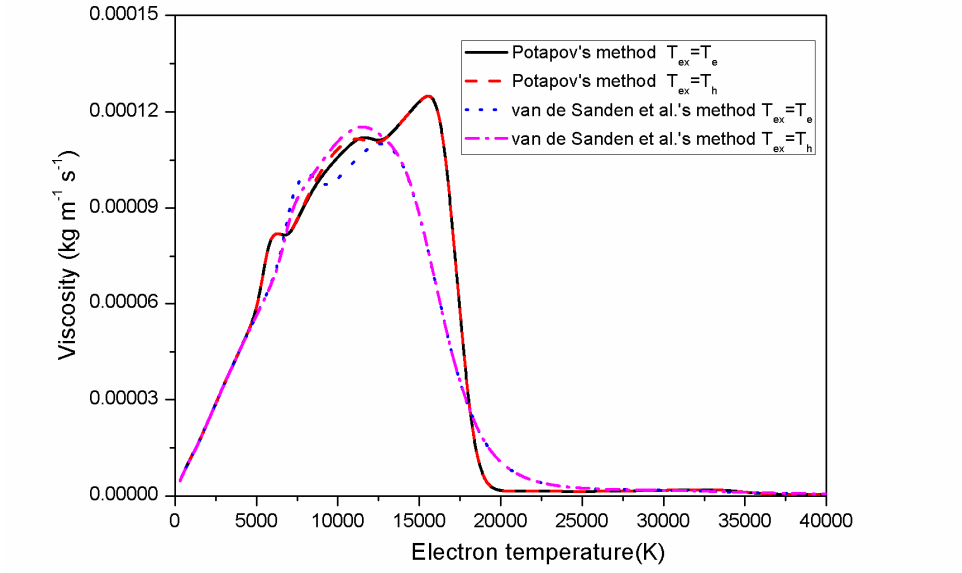
Potapov's method $T_{ex}=T_e$
Potapov's method $T_{ex}=T_h$
van de Sanden et al.'s method $T_{ex}=T_e$
van de Sanden et al.'s method $T_{ex}=T_h$
Viscosity (kg m^{-1} s^{-1})
0.00015
0.00012
0.00009
0.00006
0.00003
0.00000
0
5000
10000
15000
20000
25000
30000
35000
40000
Electron temperature(K)

(d)

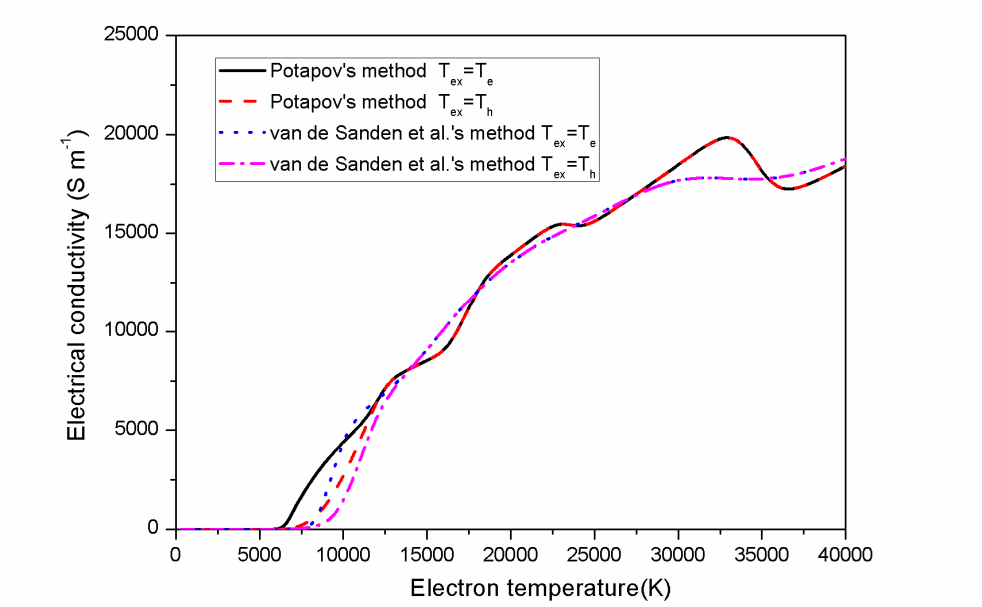
Potapov's method $T_{ex}=T_e$
Potapov's method $T_{ex}=T_h$
van de Sanden et al.'s method $T_{ex}=T_e$
van de Sanden et al.'s method $T_{ex}=T_h$
Electrical conductivity (S m^{-1})
Electron temperature(K)
0
5000
10000
15000
20000
25000
30000
35000
40000

(e)

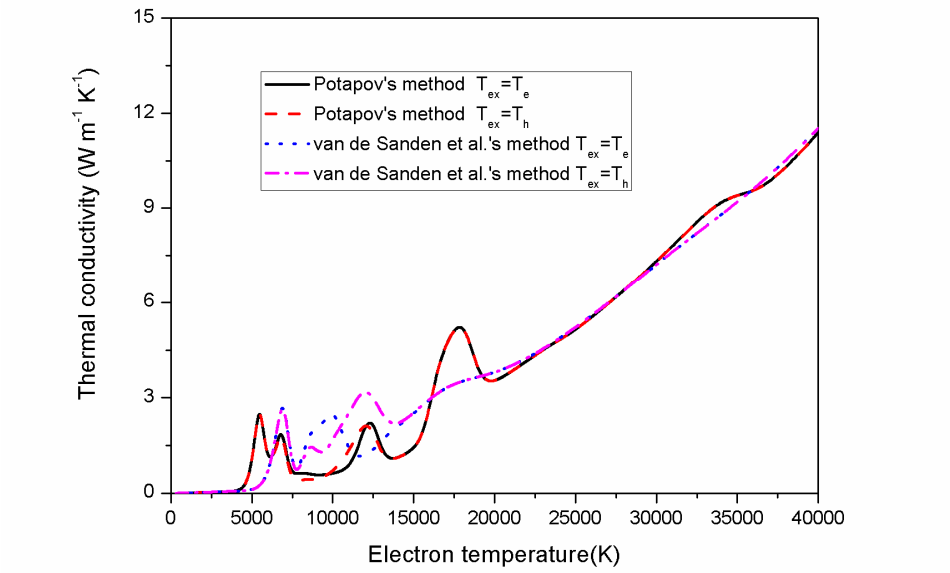
Potapov's method $T_{ex}=T_e$
Potapov's method $T_{ex}=T_h$
van de Sanden et al.'s method $T_{ex}=T_e$
van de Sanden et al.'s method $T_{ex}=T_h$
Thermal conductivity (W m^{-1} K^{-1})
Electron temperature(K)
0
3
6
9
12
15
0
5000
10000
15000
20000
25000
30000
35000
40000

(f)

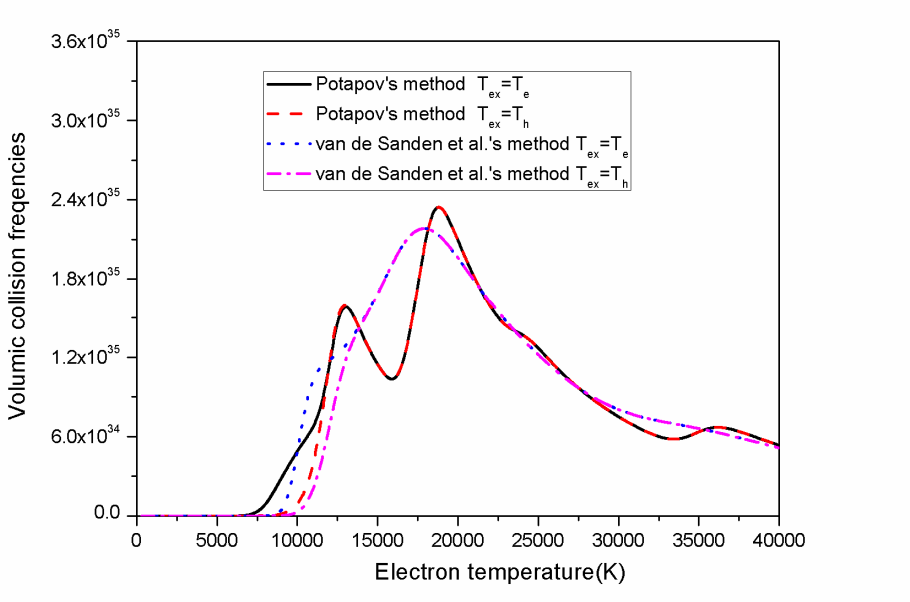

(g)

Figure 3.20 Comparison of properties in SF_6 plasmas from different reaction excitation temperature for molecular ionization under the non-equilibrium degree of 4 at atmospheric pressure. (a), Electron number density; (b), Atomic fluoride number density; (c), Total specific heat at constant pressure; (d), Viscosity; (e) Electrical conductivity; (f) ,Thermal conductivity; (g) ,Volumic collision frequency.

For example, as observed in Fig. 3.20, the peaks of total specific heat curves with Potapov's derivation as mass action law expression respectively corresponds to mainly the dissociation of SF_6 into SF_4 , SF_4 into SF_2 and SF, SF_2 and SF into S and F, and the continuous ionization of F and S. It is found that the peaks connected with the dissociation of SF_2 and SF into S and F and the ionization of atomic sulphur are coupled together due to delayed dissociation controlled by the heavy species temperature. The use of T_e as the molecular ionization excitation temperature shifts the peak connected with the first ionization of atomic sulfur slightly to higher temperature with a higher height and this can be explained by the promotion of the production of S_2^+.

For the expression derived by Van de Sanden et al.'s method, the peaks connected with the choice of T_h as the molecular excitation temperate are also related to respectively the dissociation of SF_6 into SF_4 , SF_4 into SF_2 and SF, SF_2 and SF into S and F, and the continuous ionization of F and S as well. However, for this form, if the choice of $T_{ex}=T_e$ is taken into account, only two peaks are apparent in the electron temperature range from 8000K to

14000K which are significantly linked with the dissociation of SF_4 into SF_2 and SF at the electron temperature 8500K and the dissociation of SF_2 and SF into S and F as well as the ionization of molecular S_2 and SF at the electron temperature 10000K. The peak related to the ionization of atomic sulfur is not apparent because it is shifted to a higher electron temperature and coupled together with the increasing contribution by the ionization of atomic fluorine when temperature rises. The influence of reaction excitation temperature on other properties also occurs in the electron temperature range from 7000K to 15000K where the ionisation just diatomic molecules are present and ionization just begins.

3.6 Conclusions

In this chapter, considerable effort has been devoted to the calculation of species composition, thermodynamic properties and transport coefficients of SF_6 plasmas in and out of thermal equilibrium under different values for the ratio of electron temperature T_e and heavy specie temperature T_h over a wide temperature range (300 to 40 000 K) and pressure range (0.01-1MPa), assuming chemical equilibrium.

The main conclusion that can be drawn from the results is that the results obtained for $T_e = T_h$ in two-temperature property model show in general good agreement with computed LTE data in chapter two regardless of different techniques used. The adopted forms of mass action law, i.e. Guldberg-Waage and Saha equations can modify the species composition, thermodynamic properties and transport coefficients as well as the elastic volumic collision frequencies between electrons and heavy species but can reduce to the same expression under LTE state. Moreover, the choice of reaction excitation temperature for molecular ionization can influence the species composition and hence the properties mainly in the moderate temperature range when the molecular species are present and the ionization degree is low. Under non-equilibrium condition, pressure increases also prohibits chemical reactions and shifts the relevant properties curves are shifted to a higher electron temperature. The results presented here can serve as reliable reference data for computational simulation of the behaviour of a two –temperature SF_6 plasmas.

3.7 Reference

[1] J. B. Belhaouari, J. J. Gonzalez, and A. Gleizes, "Simulation of a decaying SF_6 arc plasma: hydrodynamic and kinetic coupling study", J. Phys. D: Appl. Phys. 31, 1219 (1998).

[2] K. P. Brand and J. Kopainsky, "Particle densities in a decaying SF_6 plasma", Appl. Phys. 16, 425 (1978).

[3] S.Vacquie, A. Gleizes, and H. Kafrouni, "Measurements of electron density in a SF_6 arc plasma", J. Phys. D: Appl. Phys. 18, 2193 (1985).

[4] A.Gleizes, A.A.M. Habib, M. Razafinimanana, M. Sabsabi1, and S. Vacquié, "Departures from Saha equilibrium in SF_6 arc plasmas", Spectrochim. Acta, Part B 450, 789 (1990).

[5] L. S. Frost and R. W. Libermann, "Composition and transport properties of SF_6 and their use in a simplified enthalpy now arc model", Proc. IEEE, 59, 474 (1971).

[6] W. Hertz, H. Motschmann and H. Wittel, "Investigations of the properties of SF_6 as an arc quenching medium", Proc. IEEE, 59, 485 (1971).

[7] V. A. Belov and A. M. Semenov, "Calculation of the composition of the products from dissociation and ionization of sulphur hexafluoride at 1000 to 20,000 K and 1–10 atm", High Temp., 9, 186 (1971).

[8] A. Gleizes, M. Razafinimanana, and S. Vacquie, "Calculation of thermodynamic properties and transport coefficients for SF_6-N_2 mixtures in the temperature range 1,000–30,000 K", Plasma Chem. Plasma process., K 6(1), 65 (1986).

[9] P. Krenek, "Thermophysical properties of the reacting mixture SF_6 and Cu in the range 3000 to 50,000 K and 0.1 to 2 MPa. Part 3: Transport properties", Acta Tech. CSAV, 37, 399 (1992).

[10] T. Sakuta, S. Terachi, T. Takashima, and M. Ishikawa, "Transport properties of high temperature SF_6 gas contaminated with Cu and PTFE vapor at high", Trans. Inst. Electr. Eng. Jpn. B, 113, 342 (1993).

[11] B. Chervy, A. Gleizes, and M. Razafinimanana," Thermodynamic properties and transport coefficients in SF_6-Cu mixtures at temperatures of 300-30000 K and pressures of 0.1-1 MPa", J. Phys. D, Appl. Phys. 27, 1193 (1994).

[12] J. L. Zhang, J. D. Yan, A.B. Murphy, W. Hall and M. T. C. Fang, "Computational investigation of arc behaviour in an auto-expansion circuit breaker contaminated by ablated nozzle vapor", IEEE Trans. Plasma Sci., 2, 706 (2002).

[13] K. C. Paul, T. Sakuta and T. Takashima, "Transport and thermodynamic properties of SF_6 gas contaminated by PTFE reinforced with Al_2O_3 and BN particles", IEEE Trans. Plasma Sci., 25, 786 (1997).

[14] J. Aubreton, C. Bonnefoi, and J.M. Mexmain, Plasma, "Calcul de propriétés thermodynamiques et des coefficients de transport dans un plasma Ar-O_2 en non-équilibre thermodynamique et à la pression atmosphérique", Rev. Phys. 21, 365 (1986) (in French).

[15] V. Rat, P. André, J. Aubreton, M.F. Elchinger, P. Fauchais, and A. Lefort, "Two-Temperature Transport Coefficients in Argon–Hydrogen Plasmas—II: Inelastic Processes and Influence of Composition", Plasma Chem. Plasma Process. 22, 475 (2002).

[16] S. Ghorui, J. V. R. Heberlein, and E. Pfender, "Thermodynamic and Transport Properties of Two-temperature Oxygen Plasmas", Plasma Chem. Plasma Process. 27, 267 (2007).

[17] J. Aubreton, M.F. Elchinger, and P. Fauchais, "New Method to Calculate Thermodynamic and Transport Properties of a Multi-Temperature Plasma: Application to N_2 Plasma", Plasma Chem. Plasma Process. 18, 1 (1998).

[18] J. Aubreton, M.F. Elchinger, P. Fauchais, V. Rat, and P. André, "Thermodynamic and transport properties of a ternary Ar–H_2–He mixture out of equilibrium up to 30000K at atmospheric pressure", J. Phys. D: Appl. Phys. 37, 2232 (2004).

[19] J. Aubreton, M. F. Elchinger, V. Rat, and P. Fauchais, "Two-temperature transport coefficients in argon–helium thermal plasmas", J. Phys. D: Appl. Phys., 37, 34 (2004).

[20] J. Aubreton and M. F. Elchinger, "Transport properties in non-equilibrium argon, copper and argon–copper thermal plasmas", J. Phys. D: Appl. Phys. 36, 1798 (2003).

[21] S. Ghorui, J.V.R. Heberlein, and E. Pfender, "Thermodynamic and Transport Properties of Two-Temperature Nitrogen-Oxygen Plasma", Plasma Chem. Plasma Process. 28, 553 (2008).

[22] V. Colombo, E. Ghedini, and P. Sanibondi, "Thermodynamic and transport properties in non-equilibrium argon, oxygen and nitrogen thermal plasmas", Prog. Nuclear Energy 50, 921 (2008).

[23] V. Colombo, E. Ghedini and P. Sanibondi, “Two-temperature thermodynamic and transport properties of argon–hydrogen and nitrogen–hydrogen plasmas”, J. Phys. D: Appl. Phys. 42, 0552131 (2009).

[24] V. Colombo, E. Ghedini and P. Sanibondi, “Two-temperature thermodynamic and transport properties of carbon–oxygen plasmas”, Plasma Sources Sci. Technol. 20, 035003 (2011).

[25] W.Z. Wang, M. Z. Rong, J. D. Yan, A. B. Murphy, and J.W. Spencer, “Thermophysical properties of nitrogen plasmas under thermal equilibrium and non-equilibrium conditions”, Phys. Plasmas, 18, 113502 (2011).

[26] Y. Tanaka, Y. Yokomizu, M. Ishikawa, and T. Matsumura, “Particle composition of high-pressure SF_6 plasma with electron temperature greater than gas temperature”, IEEE Trans. Plasma Sci. 25, 991 (1997).

[27] A. Gleizes, B. Chervy, and J. J. Gonzales, “Calculation of a two-temperature plasma composition: bases and application to SF_6”, J. Phys. D: Appl. Phys. 32, 2060 (1999).

[28] G. J. Cliteur, K. Suzuki, Y. Tanaka, T. Sakuta, T. Matsubara, Y. Yokomizu, and T. Matsumura, “On the determination of the multi-temperature SF_6 plasma composition”, J. Phys. D: Appl. Phys. 32,1851 (1999).

[29] V. Rat, P. André, J .Aubreton, M. F .Elchinger, P. Fauchais, and A. Lefort, “A modified pseudo-equilibrium model competing with kinetic models to determine the composition of a two-temperature SF_6 atmosphere plasma”, J. Phys. D: Appl. Phys. 34, 2191 (2001).

[30] A.V. Potapov, “Chemical equilibrium of multitemperature systems”, High Temp. 4 (1), 48 (1966).

[31] M. C. M. van de Sanden, P. P. J. M Schram, A. G. Peeters, J. A. M.van der Mullen, and G. M. W. Kroesen, “Thermodynamic generalization of the Saha equation for a two-temperature plasma”, Phys. Rev. A 40, 5273 (1989).

[32] T. E. Magin, G. Degrez, “Transport properties of partially ionized and unmagnetized plasmas”, Phys. Rev. E, 70, 046412 (2004).

[33] A. F. Kolesnikov, G. A. Tirskiy, The equations of hydrodynamics for partially ionized multicomponent gas mixtures with transport coefficients in higher approximations, In: Molecular Gas Dynamics, Nauka, Moscow, 20 (1982).

[34] A. F. Kolesnikov, “Self-consistent Stefan–Maxwell relations for multi-component ambipolar diffusion in two-temperature plasma mixtures”, Technical Note 196, von

Karman Institute for Fluid Dynamics, Rhode Saint Genese, Belgium (1999).

[35] R. S. Devoto, “Simplified expressions for the transport properties of ionized monatomic gases”, Phys. Fluids, 10. 2105 (1967).

[36] C. Bonnefoi, Ph.D.thesis, Limoges University, France, 1983.

[37] V. Rat, P. André, J. Aubreton, M.F. Elchinger, P. Fauchais, and A. Lefort, “Transport properties in a two-temperature plasma: Theory and application”, Phys. Rev. E, 64, 26409 (2001).

[38] P. André, “Partition functions and concentrations in plasmas out of thermal equilibrium”, IEEE Trans. Plasma Sci., 23, 453 (1995).

[39] P. André, M. Abbaoui, A. Lefort and M. J.M. Parizet, “Numerical method and composition in multi-temperature plasmas: Application to an Ar-H_2 mixture”, Plasma Chem. Plasma Process, 16, 379 (1996).

[40] X.Chen and P. Han, “On the thermodynamic derivation of the Saha equation modified to a two-temperature plasma”, J. Phys. D: Appl. Phys, 32, 1711 (1999)

[41] P. Andr´e, J. Aubreton, M.F. Elchinger, V. Rat, P. Fauchais, A. Lefort and A. B. Murphy, “A Statistical Mechanical View of the Determination of the Composition of Multi-Temperature Plasmas”, Plasma Chem. Plasma Proc., 24,435 (2004).

[42] M. I. Boulos, P. Fauchais, and E. Pfender, Thermal Plasmas: Fundamentals and Applications (Plenum, New York, 1994).

[43] P. André, “Partition functions and concentrations in plasmas out of thermal equilibrium”, IEEE Trans. Plasma Sci. 23, 453 (1995).

[44] P. André, M. Abbaoui, A. Lefort, and M. J. Parizet, “Numerical method and composition in multi-temperature plasmas: Application to an Ar-H_2 mixture”, Plasma Chem. Plasma Process. 16, 379 (1996).

[45] E. Richley and D. T. Tuma, “On the determination of particle concentrations in multitemperature plasmas”, J. Appl. Phys. 53, 8537 (1982).

[46] P. André, J. Aubreton, M. F. Elchinger, P. Fauchais, and A. Lefort, “A New Modified Pseudoequilibrium Calculation to Determine the Composition of Hydrogen and Nitrogen Plasmas at Atmospheric Pressure”, Plasma Chem. Plasma Process. 21, 8 (2001).

[47] M. Capitelli, G. Collona and D. Giordano, “Two-Temperature Saha Equations: Effects on Thermophysical Properties of H Plasmas”, J. Thermophys. Heat Transfer, 16, 469 (2002).

[48] Z. Koalagaa, Influence of the choice of internal temperatures on the composition of

CxHyOzNt plasmas out of thermodynamic equilibrium: Application to CH_2 plasma, Phys. Plasmas 9, 4776 (2002).

[49] A. B. Murphy, "Transport Coefficients of Hydrogen and Argon–Hydrogen Plasmas", Plasma Chem. Plasma Process. 20, 279 (2000).

[50] K.S. Drellishak, D. P. Aeschliman, and A. B. Cambel, "Partition Functions and Thermodynamic Properties of Nitrogen and Oxygen Plasmas", Phys. Fluids 8, 1590 (1965)

[51] J. Bacri, and S. Raffanel, "Calculation of some thermodynamic properties of air plasmas: Internal partition functions, plasma composition, and thermodynamic functions", Plasma Chem. Plasma Processing. 7, 53 (1987).

[52] J. P. Trelles, J. V. R Heberlein, and E. Pfender, "Non-equilibrium modelling of arc plasma torches", J. Phys. D: Appl. Phys. 40, 5937 (2007).

[53] J. O. Hirschfelder, C. F. Curtiss, and R. B. Bird, Molecular Theory of Gases and Liquids (Wiley, New York, 1964).

[54] W.Z. Wang, M. Z. Rong, J. D. Yan, and Yi. Wu, "The Reactive Thermal Conductivity of Thermal Equilibrium and Nonequilibrium Plasmas: Application to Nitrogen", IEEE Trans. Plasma Sci., 40, 980 (2012).

[55] H. P. Li and X. Chen, "Diffusion in Two-Temperature Partially Ionized Gases", Chin. Phys. Lett. 18, 547 (2001).

[56] J. D. Ramshaw, "Hydrodynamic Theory of Multicomponent Diffusion and Thermal Diffusion in Multitemperature Gas Mixtures", J. Non-Equilibrium Thermodyn. 18,121 (1993).

[57] J. D. Ramshaw, "Simple Approximation for Thermal Diffusion in lonized Gas Mixtures", J. Non-Equilibrium Thermodyn. 21, 233 (1996).

[58] F. Pirani, M. Alberti, A. Castro, M. Moix Teixidor, and D. Cappelletti, "Atom–bond pairwise additive representation for intermolecular potential energy surfaces", Chem. Phys. Lett. 394, 37 (2004).

[59] M. Capitelli, D. Cappelletti, G. Colonna, C. Gorse, A. Laricchiuta, G. Liuti, S. Longo, and F. Pirani , "On the possibility of using model potentials for collision integral calculations of interest for planetary atmospheres", Chem. Phys. 338, 62 (2007).

[60] A. Laricchiuta, G. Colonna, D. Bruno, R. Celiberto, C. Gorse, F. Pirani, and M. Capitelli, "Classical transport collision integrals for a Lennard-Jones like phenomenological model potential", Chem. Phys. Lett. 445, 133 (2007).

[61] W.Z. Wang, J.D. Yan, M.Z. Rong, A.B. Murphy, and J.W. Spencer, "Thermophysical Properties of High Temperature Reacting Mixtures of Carbon and Water in the Range 400–30,000 K and 0.1–10 atm. Part 2: Transport Coefficients", Plasma Chem. Plasma Process. , 32, 495–518 (2012).

[62] NIST Computational Chemistry Comparison and Benchmark Database. In: R.D. Johnson III (Ed.), NIST Standard Reference Database Number 101, Release 10th ed., 2004

[63] B. Chervy and A. Gleizes, "Electrical conductivity in SF_6 thermal plasma at low temperature (1000-5000 K)", J. Phys. D: Appl. Phys. 31, 2557–2565 (1998).

[64] T. Kihara, M. H. Taylor, and J. O. Hirschfelder, "Transport Properties for Gases Assuming Inverse Power Intermolecular Potentials", Phys Fluids 3, 715 (1960).

[65] A. B. Murphy, "Transport coefficients of air, argon-air, nitrogen-air, and oxygen-air plasmas", Plasma Chem. Plasma Process. 15, 279 (1995).

[66] F. B. M. Copeland and D.S .F. Crothers, "Cross Sections for Resonant Charge Transfer between Atoms and Their Positive Ions", Nucl. Data Tables 65, 273 (1997).

[67] D, Rapp and W.E. Francis, "Charge Exchange between Gaseous Ions and Atoms", J. Chem. Phys. 37, 2631 (1962).

[68] A. Laricchiuta, D. Bruno, M. Capitelli, C. Catalfamo, R. Celiberto, G. Colonna, P. Diomede, D. Giordano, C. Gorse, S.Longo, D. Pagano, and F. Pirani, "High temperature Mars atmosphere. Part I: transport cross sections', Eur. Phys. J. D, 54, 607 (2009).

[69] E. J. Robinson and S. Geltman, "Single- and Double-Quantum Photodetachment of Negative Ions", Phys. Rev., 153, 4 (1967).

[70] F. E. Spencer and A.V. Phelps, Momentum transfer cross sections and conductivity integrals for gases of MHD interest, Proc.15th Symp. Engineering Aspects of MHD (Univ. of Pennsylvania, Philadelphia, PA) p IX.9.1 (1976).

[71] D. Kannappan, T.K. Bose, "Transport properties of a two-temperature argon plasma", Phys Fluids, 20, 1668 (1977).

[72] J. N. Butler and R. S. Brokaw, "Thermal Conductivity of Gas Mixtures in Chemical Equilibrium", J. Chem. Phys., 26, 1636 (1957).

CHAPTER 4 CURRENT ZERO BEHAVIOUR OF AN SF_6 BLAST ARC UNDER SHOCK CONDITION IN A SUPERSONIC NOZZLE WITH HOLLOW CONTACT

4.1 Introduction

Supersonic nozzles (converging–diverging nozzles) are commonly used in SF_6 gas blast high-voltage circuit breakers. Therefore, investigation into the behaviour of SF_6 arc in a supersonic nozzle is of great relevance to the development of switching devices and therefore, a large number of publications are made contributing to the model and test which greatly improve our understanding to many fundamental phenomena such as the radiation, turbulence, metal vaporization and wall ablation, demixing effect along with departure from equilibrium in the fault current interruption using SF_6 as a insulation and arc quenching medium [1]-[24]. It is recognized that shock wave can generate in the diverging section of the nozzle under the condition that the ratio of exit pressure to inlet stagnation pressure exceeds certain critical value and can greatly influence the arc behaviour during the current interruption process. Meanwhile, the presence of an SF_6 arc, which is usually turbulent and unstable, can have significant effect on the shock wave.

The systematic investigation on arc-shock interaction is rare. Experimental observation was limited to the arc section outside the nozzle or to that downstream of an orifice plate [25]-[27]. Photographs of the arc show that the arc is broadened after shock [25]. Benenson et al. [26] have found that a flow separation exists at the beginning and end of the straight section of the 15^o nozzle under shock wave condition. Campbell et al. [27] observed that the presence of strong shock waves in the flow field appears deleterious to the thermal recovery behaviour of a supersonic nozzle. The theoretical investigations of the arc-shock interaction with computer simulation model have been reported mainly by Fang and his colleagues [28]-[29]. They have verified that flow separation in the thermal layer between the high-temperature arc core and cold flow generates large vortices which deform the shape of the arc core. For the current range investigated, the center of the shock is not sensitive to the

current, but is moved upstream relative to that without the arc. Their investigations are restricted to the steady state case and only the discharge area without taking into account the influence of the downstream contact on flow field. Zhang et al. focuses on the effects of inlet stagnation pressure and exit pressure to inlet stagnation pressure ratio (hereafter referred to as pressure ratio) with two solid electrodes on arc extinction. The existence of downstream electrode can generate a shock and influence the flow field distribution [30]. As we know, there exist gas blast high voltage circuit breakers with different structures and different sizes in industry which are important for the optimism of the gas blast interrupter design parameter and their influences have been widely discussed [31]-[33]. The aim of this work is not to describe all the complex physical and aerodynamic processes occurring in the switch arcs, but to obtain qualitative understanding of the arc-shock interaction behaviour in transient dynamic interruption process. It is noted that hollows electrode are widely used in practice and therefore, our presented work has extended to the investigation of arc-shock interaction and its influence on both dynamic characteristics of SF_6 arcs and thermal recovery behaviour of current interruption with a hollow downstream contact. The similarity analysis and scaling law of in a turbulent, axially accelerating gas flow have been widely discussed in previous literatures[34]-[37] and not given in current work.

This chapter is arranged as follows: in section 2, we give the basic assumptions and mathematical model governing the arc behaviour. Computational results as well as their comparison with test are presented in section 3. Finally, a conclusion is drawn in section 4.

4.2 Mathematical Model and Boundary Condition

4.2.1 Governing Equations

The arcing SF_6 flow is rotationally symmetric and described by the usual Navier–Stokes equation except for associated source terms, duly modified by electromagnetic equation. All the equations included in the arc model can be written in a general formulation as follows [13]:

$$\frac{\partial(\rho\Phi)}{\partial t} + div(\rho\Phi\vec{V}) = div(\Gamma_{\Phi} grad\Phi) + S_{\Phi} \tag{4.1}$$

where $\boldsymbol{\Phi}$is the field variable described as follows. For each equation, Γ_Φ is the corresponding property coefficient of the arc plasma and S_Φ is the source term. The variables and parameters for these partial differential equations in axisymmetric form are described as follows:

- **Mass Conservation Equation**

$$\frac{\partial \rho}{\partial t} + \nabla \cdot (\rho \vec{u}) = 0 \tag{4.2}$$

where $\vec{u}$ the mass-averaged velocity of the plasma particles, ρ is the total mass density containing that of electrons and heavy particles obtained as below.

$$\rho = \sum_{i}^{w} m_i n_i \tag{4.3}$$

where m_i is the mass of species i and w is the species number.

- **Momentum Conservation Equation**

The radial and axial momentum equations can be separately written as

$$\begin{aligned}\frac{\partial(\rho v)}{\partial t} + \nabla \cdot (\rho \vec{u} v) = &-\frac{\partial p}{\partial r} + \nabla \cdot (\mu_{eff} \nabla v) + \frac{1}{r}\frac{\partial}{\partial r}(r\mu_{eff}\frac{\partial v}{\partial r}) + \frac{\partial}{\partial z}(r\mu_{eff}\frac{\partial w}{\partial r}) \\ &-\frac{2}{3}\frac{\partial}{\partial r}[\mu_{eff}\frac{1}{r}\frac{\partial}{\partial r}(rv) + \mu_{eff}\frac{\partial w}{\partial z}] - \frac{2\mu_{eff} v}{r^2} - j_z B_\theta + \rho g\end{aligned} \tag{4.4}$$

$$\begin{aligned}\frac{\partial(\rho w)}{\partial t} + \nabla \cdot (\rho \vec{u} w) = &-\frac{\partial p}{\partial z} + \nabla \cdot (\mu_{eff} \nabla w) + \frac{1}{r}\frac{\partial}{\partial r}(r\mu_{eff}\frac{\partial v}{\partial z}) + \frac{\partial}{\partial z}(r\mu_{eff}\frac{\partial w}{\partial z}) \\ &-\frac{2}{3}\frac{\partial}{\partial z}(\mu_{eff}\frac{1}{r}\frac{\partial}{\partial r}(rv) + \mu_{eff}\frac{\partial w}{\partial z}) - \frac{2\mu_{eff} v}{r^2} + j_r B_\theta\end{aligned} \tag{4.5}$$

where p, v and w are the total pressure, the mass-averaged radial and axial component of the velocity $\vec{u}$ and g is the gravity coefficient respectively. $\mu_{eff} = \mu_l + \mu_t$ is the effective viscosity including the contributions of laminar and turbulence. J_r and J_z are the radial and axial

components of the current density respectively and B_θ is the azimuthal magnetic field. The arc column is rotationally symmetric and the magnetic field is dominated in the azimuthal direction of the axis of the arc column. For similarity, only an azimuthal component of the magnetic field caused by the arc itself is taken into account. Assuming the permeability of the arcing medium μ_0 to be homogenous, the magnetic field can be calculated by Ampère's circuital law.

$$B_\theta = \frac{\mu_0 \int_0^r J_z 2\pi\xi d\xi}{2\pi r} \tag{4.6}$$

- **Energy Conservation Equation**

$$\frac{\partial(\rho h)}{\partial t} + \nabla \cdot (\rho h \vec{u}) = \frac{\partial}{\partial z}(k_{eff} \frac{\partial T}{\partial z}) + \frac{1}{r}\frac{\partial}{\partial r}(k_{eff} r \frac{\partial T}{\partial r}) - Q_{rad} + \vec{j} \cdot \vec{E} + \frac{5k_B}{2e}(j_z \frac{\partial T}{\partial z} + j_r \frac{\partial T}{\partial r}) \tag{4.7}$$

where $k_{eff} = k_l + k_t$ is the effective thermal conductivity including both the contributions of laminar and turbulent component, k_B the Boltzmann's constant, h the specific enthalpy and e is the electron elementary charge. Other source terms are the Joule heating $\vec{j} \cdot \vec{E}$ and the radiation losses Q_{rad} which is calculated with the approximate model of Zhang et al. [38]. The last term on the right-hand side of equation (4.7) represent the electron heat conduction.

The electrical field strength E and the current density j are calculated by the simplified Ohm's law.

$$I = E_z \int_0^R \sigma 2\pi r dr$$
$$\vec{j} = \sigma \vec{E} \tag{4.8}$$

where I is the arc current, σ the electric conductivity and R the arc radius. The simplified Ohm's law assumes that the radial component of the electric field is negligible in comparison with the axial component.

The equation of state is

$$\rho = f(P,T) \tag{4.9}$$

The gas flow in supersonic nozzle has been classified in the literature as unstable and turbulent [39]. The closure of the system equations requires extra relationships to calculate the turbulent enhanced viscosity and thermal conductivity. The Prandtl mixing length model is used considering its relatively preferable compared with other more sophisticated turbulence models. The turbulent eddy viscosity and thermal conductivity are related to the length scale and to the characteristic velocity of the turbulence. The turbulence viscosity is determined by

$$\mu_t = \rho l_m^2 \left| \frac{\partial w}{\partial r} \right| \tag{4.10}$$

$$l_m = c\delta \tag{4.11}$$

where δ is the arc's thermal radius defined by $(\theta_\delta/\pi)^{0.5}$. $\theta_\delta = \int_0^\infty (1-\rho/\rho_\infty) 2\pi r dr$, w is the axial velocity component and c is the turbulence parameter of which is to be adjusted according to experimental results.

The pressure field in the present case is, however, two dimensional and a difficulty exists in defining the upper limit of the integration since the term inside the square root could become negative when the radial pressure gradient is substantial. We adopt the definition of the arc thermal radius as the radial distance from the axis to the position of the 2000 K isotherm. This radial position characterizes the radial width of the high-speed jet.

The turbulence enhanced thermal conductivity, k_t, is related to the turbulent viscosity through the turbulent Prandtl number.

$$\mathrm{Pr} = \frac{\mu_t}{k_t / c_P} \tag{4.12}$$

It has been found that for turbulent arcs the turbulent Prandtl number can be assumed unity [7]. Thus, only the parameter c needs to be adjusted.

4.2.2 Computation Condition

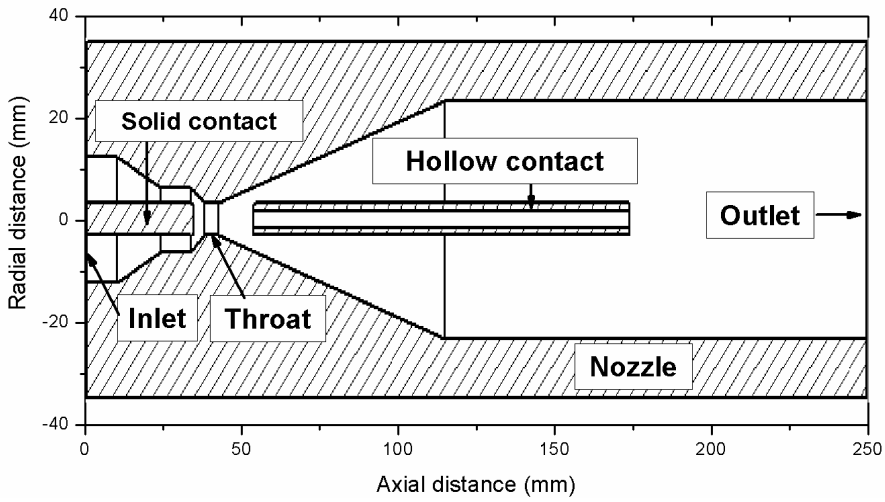

Figure 4.1 Nozzle geometry drawing

In this study, computer simulations of the physical phenomena occurring in the arc region before and after current zero were carried out in a Laval nozzle with a hollow contact tested by the research group of General Electric Company as presented in Fig. 4.1[26].

The total nozzle length is 257.41 mm, the inlet diameter 25.40 mm, the outlet diameter 46.36 mm, the diameter of the nozzle throat 6.33mm, and the throat position 24.22mm away from the inlet plane. The solid upstream and downstream contacts have the same diameter of the nozzle throat and their tip locates respectively at 35.36mm and 55.01 mm away from the inlet plane. The downstream contact has a length of 124.10 mm with a hollow internal diameter of 3.56mm. Electrical connections are made via the end plates and three pronged metal spiders into which the electrodes are mounted and which are designed for minimal flow disturbance. The downstream contact which was neglected and assumed to be the current collector in which arc can flow without blocking effect in previous study [28]-[29] is taken into account in our current work. Moreover, the computation domain is enlarged to an extended area located which is sufficiently far from the nozzle region in order not to affect the arcing range.

Results on arc-shock interaction, especially before current zero, are not substantially affected by the assumption on the plasma state. Therefore, local thermal equilibrium is

expected to exist during the arcing process. Hence, for the compressible flow and heat transfer simulations with SF_6 as the plasma working gas, based on the assumption of partial local thermodynamic equilibrium, tabulated pressure-temperature-dependent thermodynamic and transport properties including mass density, specific enthalpy, specific heat, sonic speed, the specific heat ratio, viscosity, thermal conductivity together with electrical conductivity in wide pressure and temperature ranges were calculated with our developed computer code in terms of more recent data and adopted in our current work in chapter 2. For the convenience of computation, in the region where electric conductivity is zero is set at a very small value of 10^{-6} (S/ m).Inside the solid electrode, the electric conductivity is set to 10^{6} (S/ m). The nozzle is made of insulating material PTFE; its electrical conductivity is also set as 10^{-6} (S/ m).

Axisymmetric boundary conditions are imposed: the radial velocity and the radial gradient of all dependent variables are zero on the axis. At the inlet, stagnation pressure and temperature are specified. The upstream stagnation pressure is 1.36MPa (200 Psi) and the stagnation temperature is set to 300 K. The inwards mass, momentum and energy fluxes are calculated by assuming isentropic expansion of gas from the stagnation pressure to the local pressure at the boundary cells. A fixed pressure exit is adopted and five different exit pressure to inlet stagnation pressure ratios (referred to as pressure ratios) 0.50, 0.33, 0.20, 0.10, and 0.01 which corresponds to the exit pressures of 0.680MPa, 0.453MPa, 0.272MPa, 0.136MPa and 0.0136MPa are carried out and compared.

For the arc and electrode interaction, an effective averaged thermal conductivity method has been used to treatment the large temperature gradient near the electrode surface [40]. In the internal part of the hollow contact, there is no Ohmic heating in the transparent contact which is used to collect the current due to the complexity of arc root and the radiation is taken into account. The thermal conduction into the nozzle wall which has a low thermal conductivity is negligible because, for the current range investigated (no greater than 1000A), there is a relatively low-temperature layer separating the arc from the wall.

The calculations have been carried out using PHOENICS [41], a commercially available Computational Fluid Dynamics (CFD) package code based on the solution of the

conservation equations for momentum and energy using Patankar's SIMPLE method [42].

4.3 Results and Discussion

4.3.1 Steady State Calculation

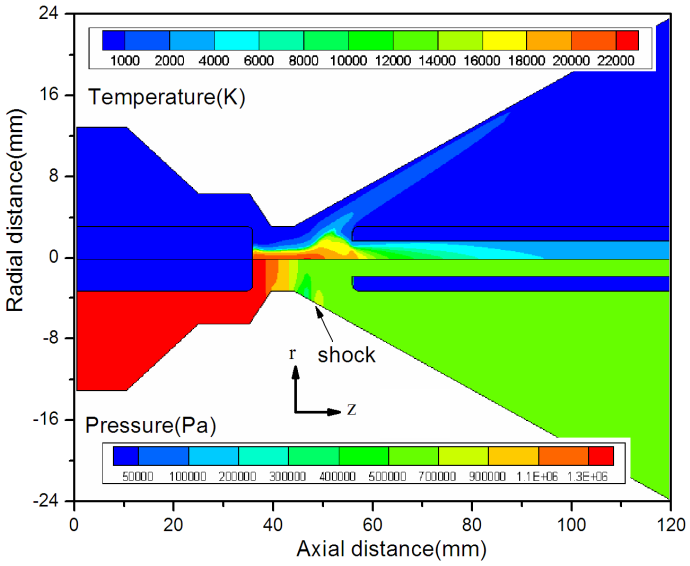

(a)

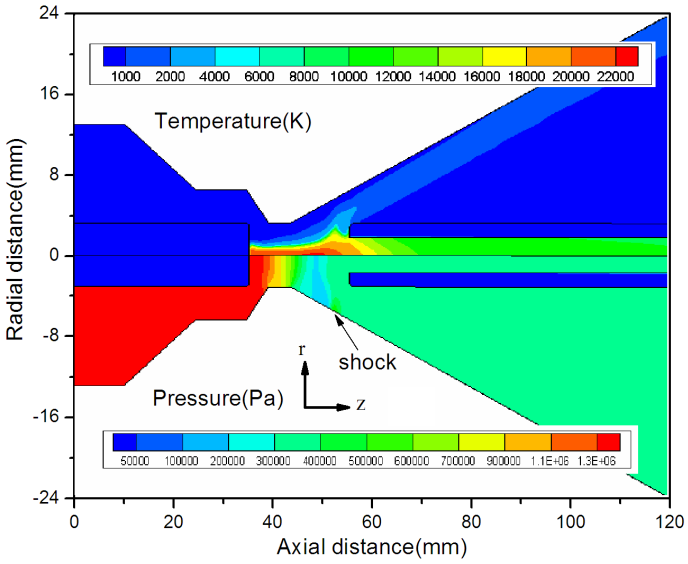

(b)

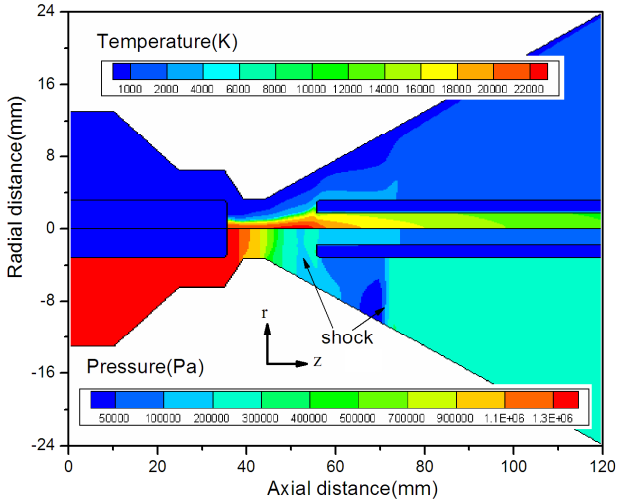

(c)

Figure 4.2 Temperature and pressure distribution of SF_6 arcs with a current of 600 A in a supersonic nozzle, the upper part: temperature; the bottom part: pressure. Exit pressure: (a), 0.680MPa; (b), 0.453MPa; (c), 0.272MPa.

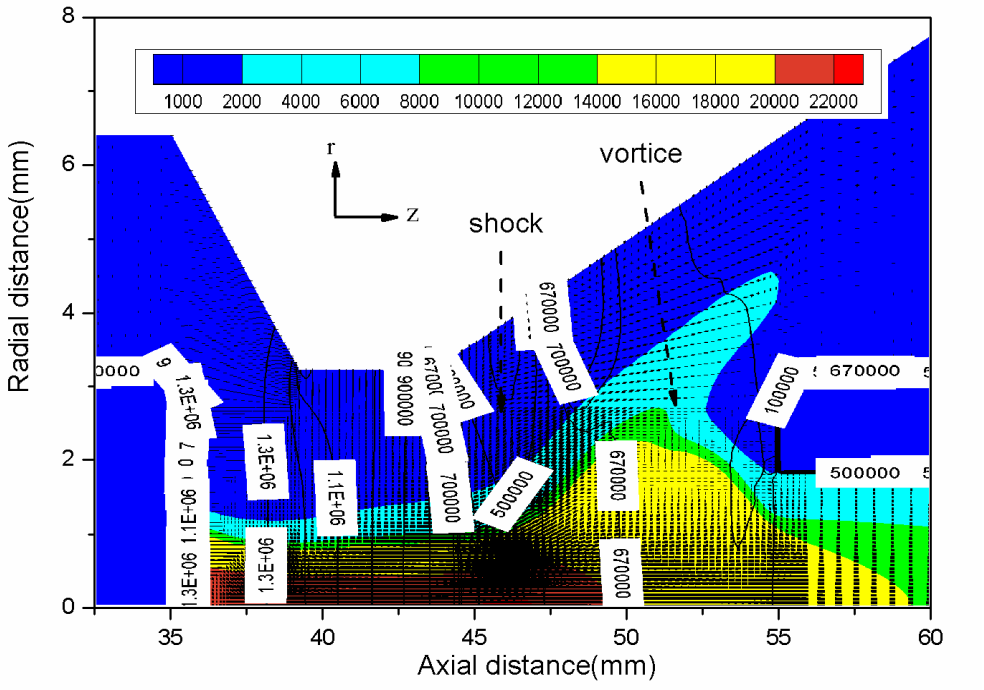

Figure 4.3 SF_6 arc column broadening in a supersonic nozzle with a current of 600 A and an exit pressure of 0.680MPa.

Previous study has shown that the presence of arc can significantly alter the flow and pressure field especially when a shock exists in the arcing area [28]. The pressure and temperature contours for a current of 600 A respectively with the exit pressures of 0.680MPa, 0.453MPa and 0.272MPa are given in Fig. 4.2.

We can find that the highest temperature occurs in front of the downstream tip and its position moves upstream as the exit pressure increases. The arc temperature in the hollow electrode passage decays gradually as the axial position increases because no Omic heating is taken into account. The largest pressure drop takes place mainly in the arcing area between the electrodes.

If the hollow downstream electrode under the condition of the exit pressure of 0.272MPa is not taken into account in the computation as it was usually treated before, it is found that the shock is generated not before but after the downstream tip as we can find the second shock existing in Fig. 4.2 and its influence on the arcing area is relatively low. Although there exists a hollow passage, flow on the axis is decelerated as a result of the downstream electrode's blocking effect through a shock whose center is slightly moved upstream with increasing exit pressure.

For the cases in which the exit pressure is lower than 0.272MPa, the field before the downstream tip is hardly affected by the decreasing pressure penetration bringing a similar arcing behaviour during fault current interruption and not presented here. With the exit pressures of 0.680MPa and 0.453MPa, a high pressure penetrates into the arcing area in front of the downstream tip and the space after the downstream electrode tip poses a similar pressure value with the exit. The adverse pressure gradient brings a subsonic external flow with relatively low velocity in the thermal layer which corresponds to an equivalent boundary layer between the arc core and the cold gas. Because the arc core has a quite high temperature and velocity, the high pressure penetration influences the thermal layer more intensely and leads to a vortex where a flow separation takes place. In the thermal layer, the hot arc core and the cold gas interacts strongly and this further modifies the pressure field distribution because the shock cannot penetrate into subsonic flow[29] as we can find in Fig. 4.3.

The high pressure penetration into the thermal layer along with the downstream electrode's blocking effect both contribute to a low flow entrainment into the arc core to form a shock and hence a broadening effect of the arc column.

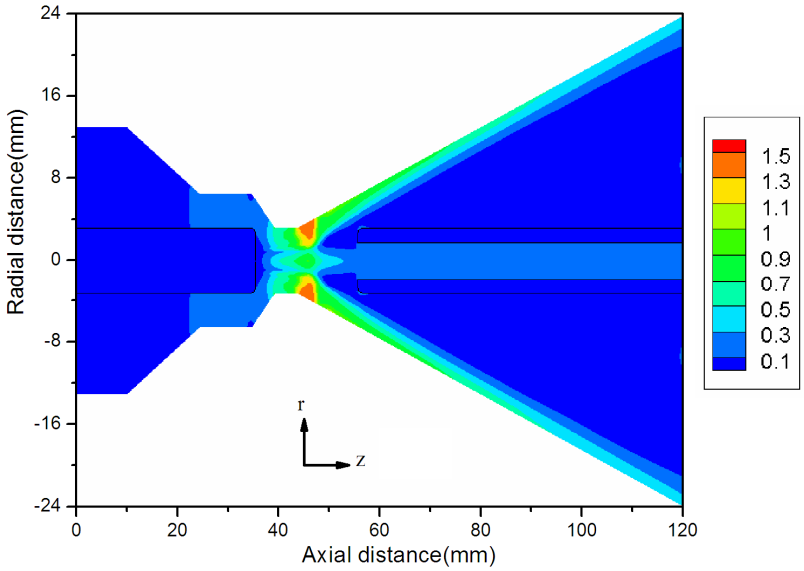

(a)

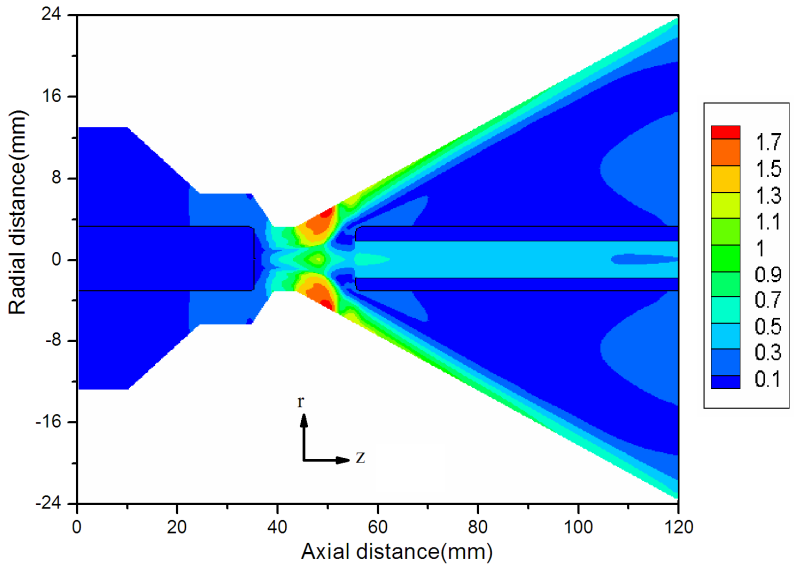

(b)

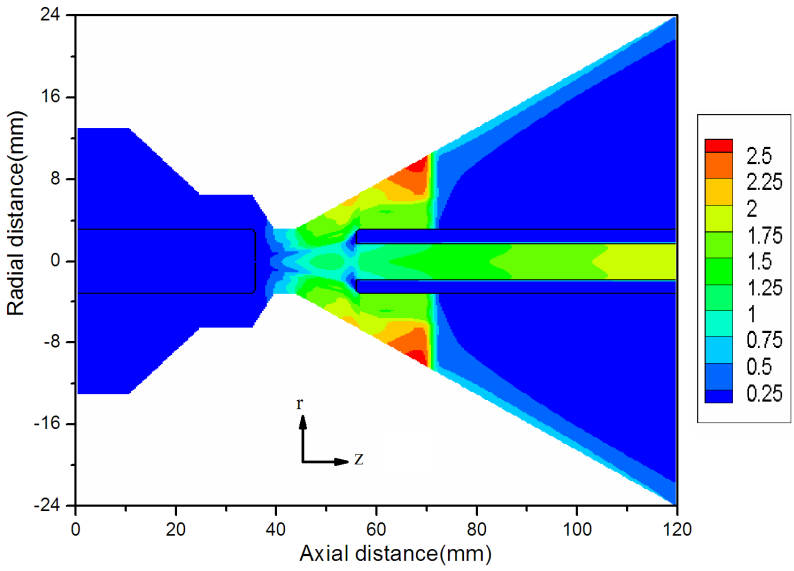

(c)

Figure 4.4 Mach number distribution of SF_6 arcs with a current of 600 A in a supersonic nozzle, Exit pressure: (a), 0.680MPa, (b), 0.453MPa; (c), 0.272MPa.

Fig. 4.4 gives the Mach number distribution of SF_6 arcs in the supersonic nozzle. The flow becomes subsonic in the diverging part after the pressure rise caused by the shock which brings the flow deceleration for all three cases. It also clearly shows the inhibition of a high exit pressure penetration to gas flow. For example, with the exit pressure of 0.680MPa, the gas flow along the central axis does not show supersonic characteristics before the shock. As presented, the highest Mach number in the nozzle mainly occurs along the wall surface in its diverging part. When the exit pressure is increased, its position gradually moves towards upstream with a decreasing value.

We can obtain the influence of high exit pressure penetration by comparing the axial variations of temperature, arc radius and pressure for a current of 800A under different exit pressures as presented in Figs. 4.5-4.6.

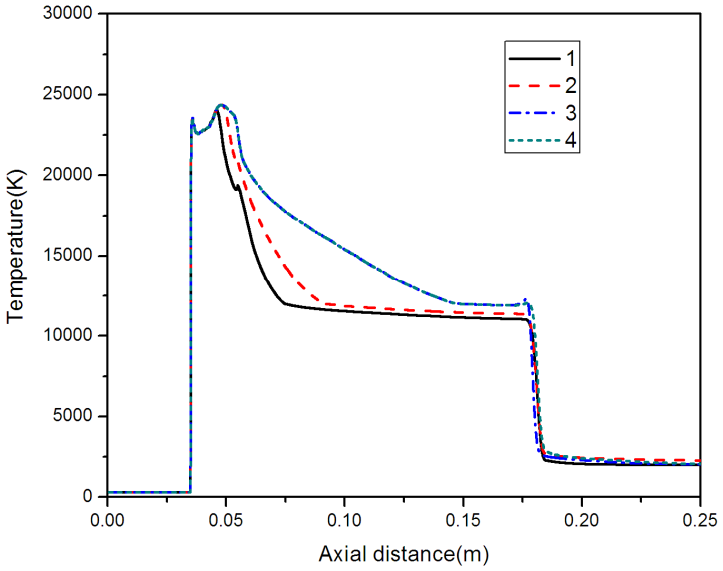

(a)

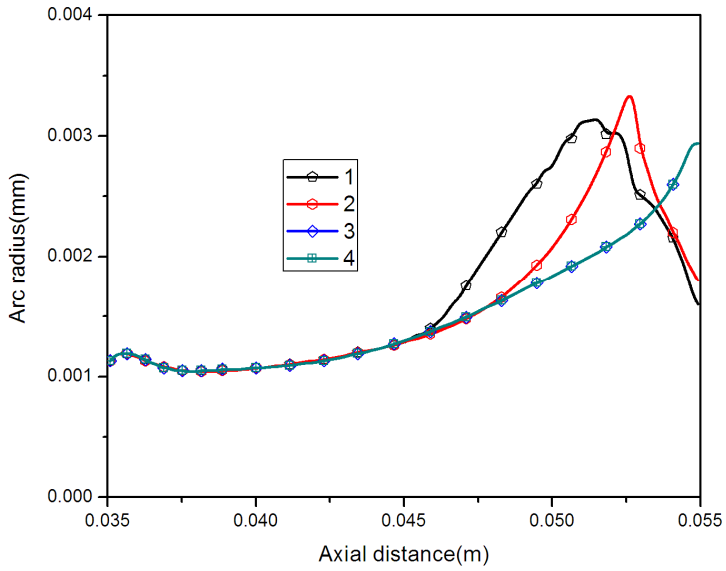

(b)

Figure 4.5 Axial variation of temperatures at r=0 (a) and arc radius (b) for a current of 800A. Exit pressure: 1, 0.680MPa; 2, 0.453MPa; 3, 0.272MPa; 4, 0.136MPa.

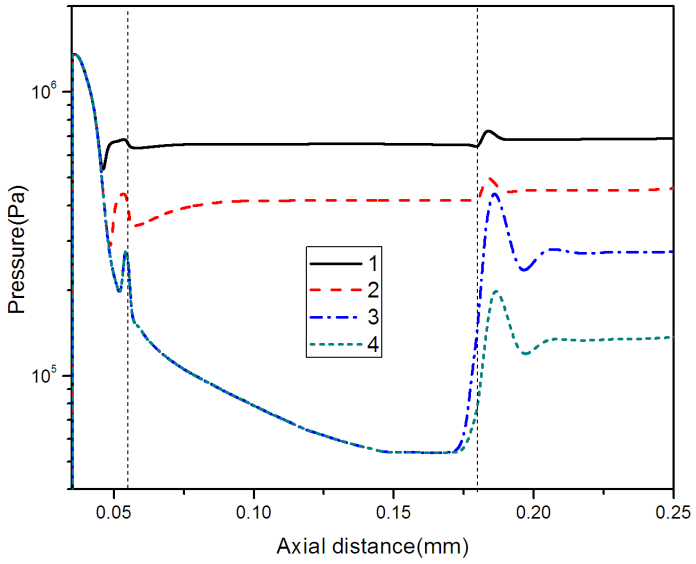

(a)

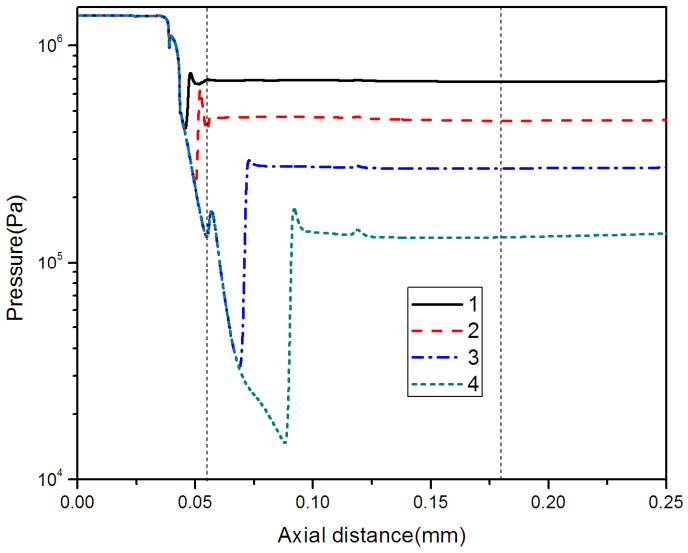

(b)

Figure 4.6 Axial variations of pressure along the central axis (a) and the wall surface (b) for a current of 800A. Exit pressure: 1, 0.680MPa; 2, 0.453MPa; 3, 0.272MPa; 4, 0.136MPa. Two lines correspond to the positions both left and right tip of the downstream electrode.

There exists a location before which the arc and its surrounding flow are hardly affected by the penetrated pressure and poses the same field distribution. Near and after the interaction zone, the arc shape is deformed by the arc-shock interaction with the arc radius

firstly enlarged and then decreased. Along the central axis, the pressure experiences a drop after the shock before the downstream electrode tip due to the influence of a shock. Because the pressure in the electrode hollow passage is lower than that outside at the same axial position in the nozzle diverging part, a rapid pressure rise along the central axis takes place near the right tip of the downstream electrode.

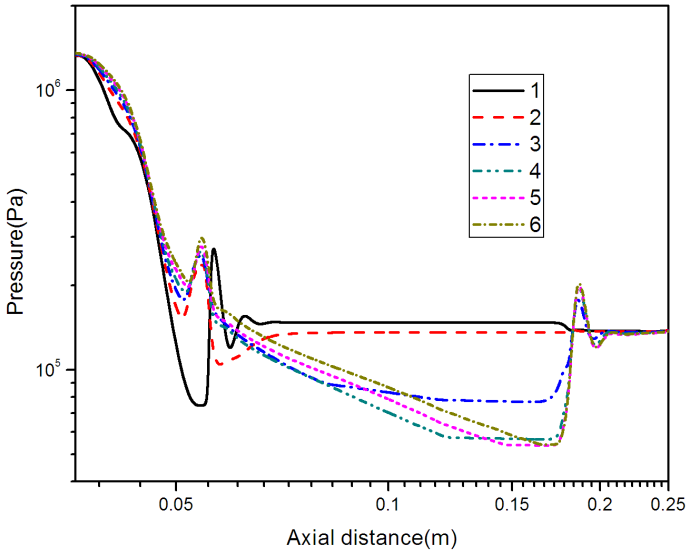

(a)

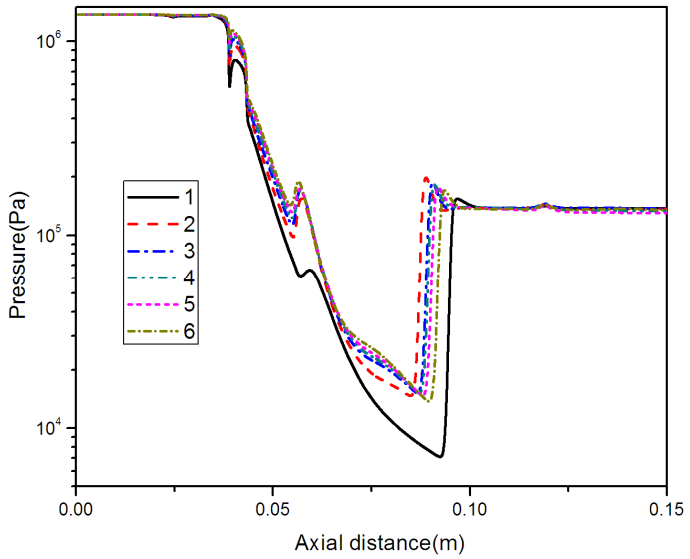

(b)

Figure 4.7 Axial variations of pressure along the central axis (a) and the wall surface (b) with exit pressure of 0.136MPa. 1, cold gas; 2, 200A; 3, 400A; 4, 600A; 5, 800A; 6, 1000A.

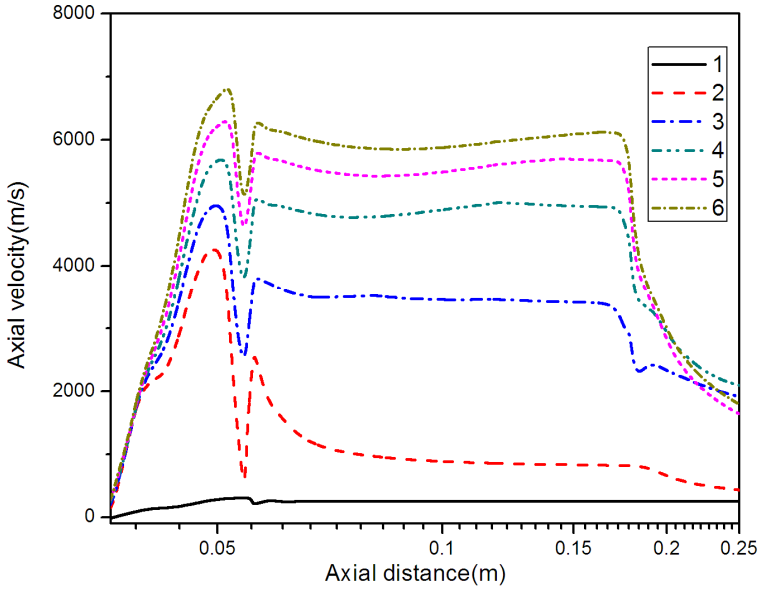

(a)

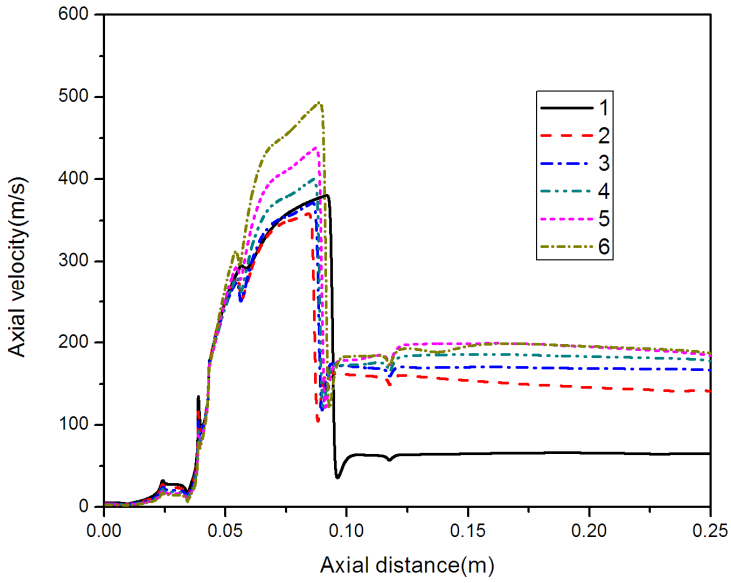

(b)

Figure 4.8 Axial variations of axial velocity along the central axis (a) and the wall surface (b) with exit pressure of 0.136MPa. 1, cold gas; 2, 200A; 3, 400A; 4, 600A; 5, 800A; 6, 1000A.

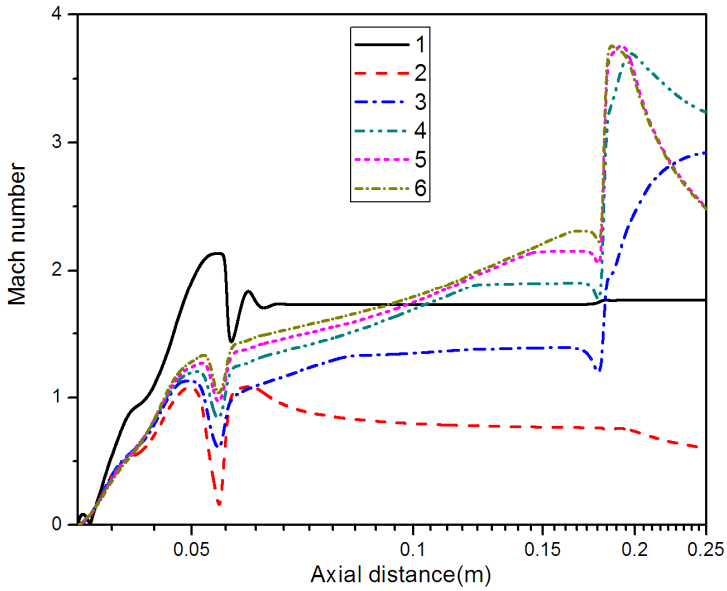

(a)

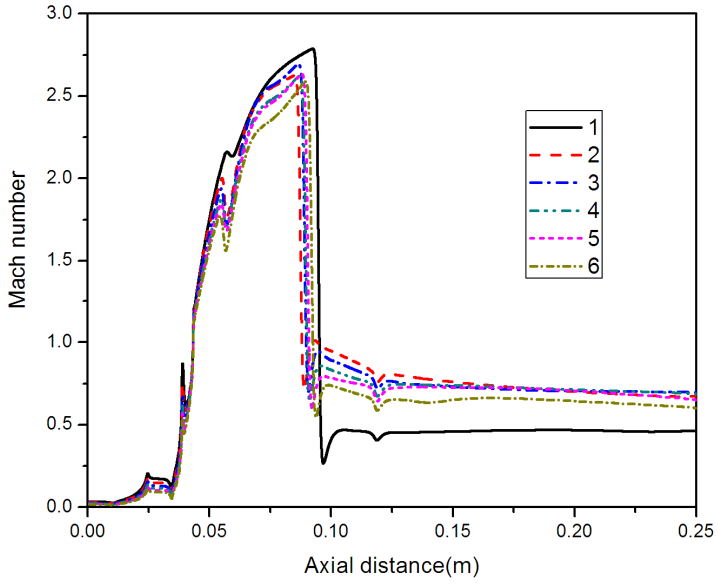

(b)

Figure 4.9 Axial variations of Mach number along the central axis (a) and the wall surface (b) with exit pressure of 0.136MPa. 1, cold gas; 2, 200A; 3, 400A; 4, 600A; 5, 800A; 6, 1000A.

The influences of different currents on axial variation of pressure, axial velocity and Mach number along the central axis and the wall surface with the exit pressure of 0.136MPa are presented in Figs. 4.7-4.9, respectively. Under this condition, the pressure penetration has negligible effect in the regions before the left tip of downstream electrode. Beside the shock

caused by the electrode blocking effect, a second shock is generated after the left tip of downstream electrode both in and outside the electrode hollow passage. Both shocks caused by the electrode blocking effect and the pressure penetration present a low dependence of its center location on the current value which slightly moves towards downstream as current increase showing increasingly significant influence of the arc. The axial velocity along the central axis increases as current increases in most regions with the exception near the exit. The flow velocity in the cold gas without the arc presents the lowest value along the axis. However, a different condition exists for the variation of axial velocity along the wall surface where the cold gas shows higher axial velocity because its shock center is significantly moved to downstream comparing the condition where an arc exists. The gas flow after the shock along the central axis for the cold gas and for the arc with a current of 1000A together with all cases along the wall surface is still supersonic. The flow Mach number along the central axis increases dramatically after the right tip of the hollow downstream electrode regardless of the increasing pressure and decreasing velocity. This is mainly attributed to the decreasing gas sonic velocity with a rapidly decaying temperature caused by the strong cooling effect that the cold gas outside the hollow electrode passage takes away the heat quite swiftly.

4.3.2 Transient State Calculation

4.3.2.1 Before Current Zero

In order to investigate the arc behaviour under transient condition, an initial arc conditions need to be chosen in such a way that the arc at current zero should not depend on the chosen initial conditions. A 1000A steady arc has been found to be satisfactory.

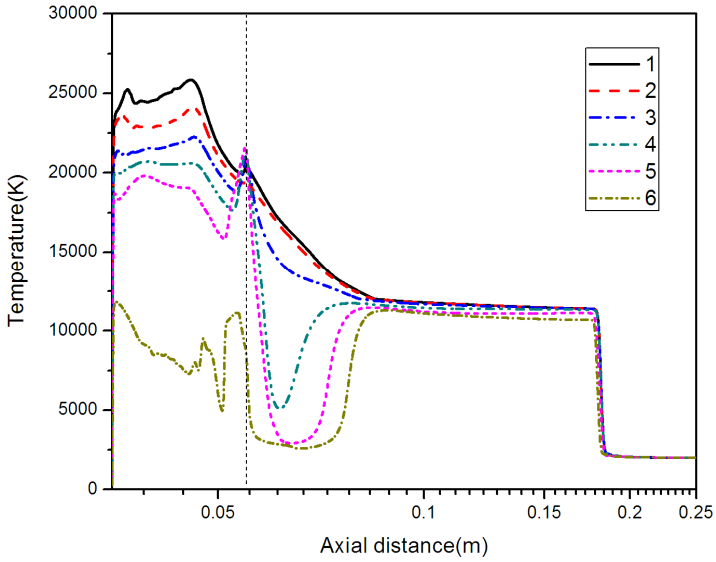

(a)

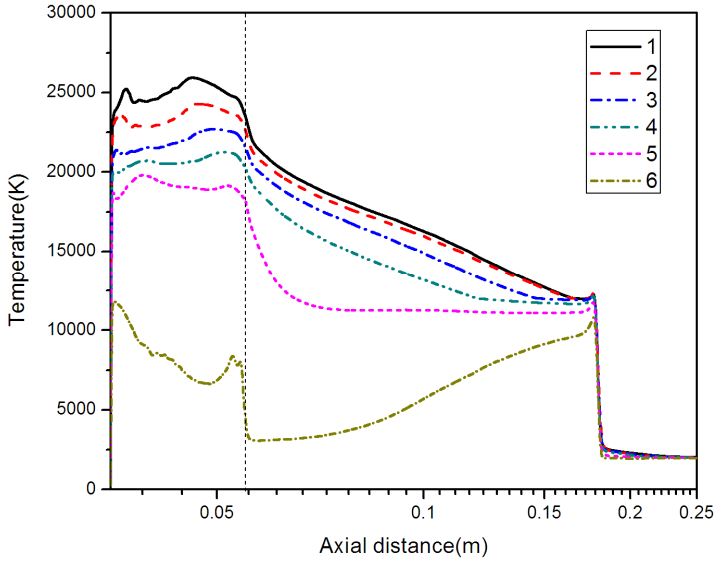

（b）

Figure 4.10 Axial variation of temperature along the central axis at various instants before current zero with a current decaying rate of 13 A/μs under the exit pressures of (a) 0.680MPa and (b) 0.272MPa. 1, 1000A; 2, 800A; 3, 600A; 4, 400A; 5, 200A; 6, current zero.

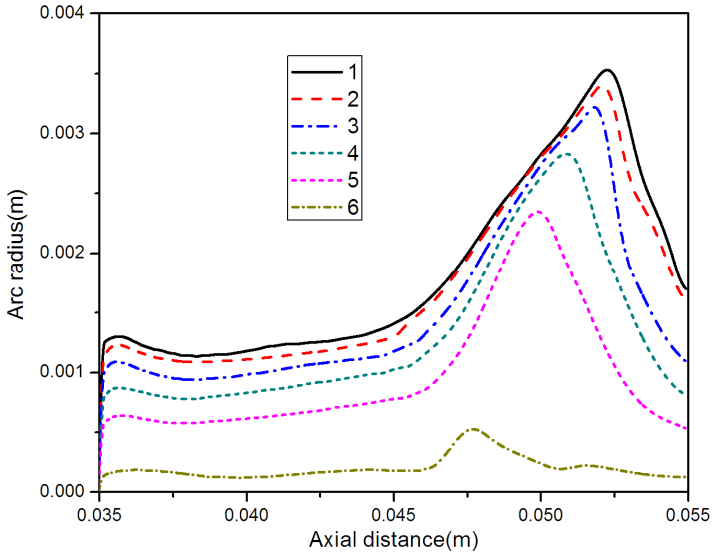

(a)

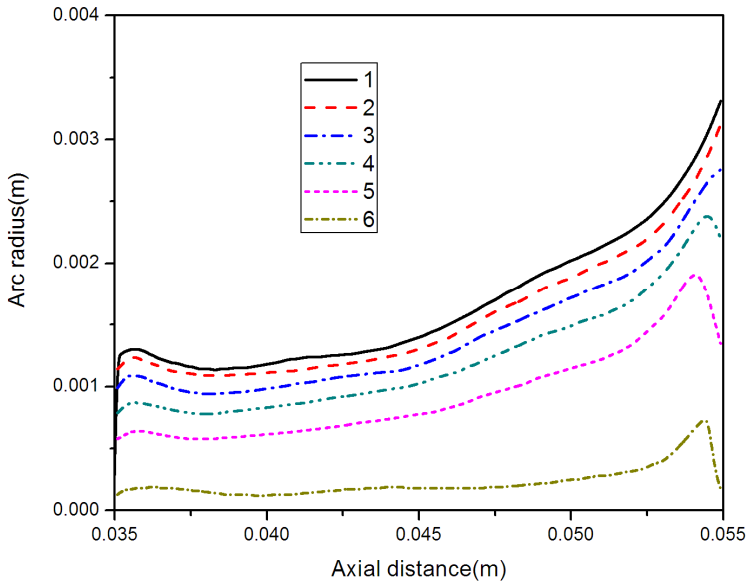

(b)

Figure 4.11 Axial variation of arc radius along the central axis at various instants before current zero with a current decaying rate of 13 A/μs under the exit pressures of (a) 0.680MPa and (b) 0.272MPa. 1, 1000A; 2, 800A; 3, 600A; 4, 400A; 5, 200A; 6, current zero.

Theoretical investigation has found that under the exit pressure ratio lower than 0.33 which corresponds to an exit pressure of 0.453MPa, the flow field distribution between two electrodes is hardly changed because the exit pressure cannot penetrate into this area. The typical axial

variation of temperature and arc radius along the central axis at various instants which respectively correspond to a current value of 1000A, 800A, 600A, 400A, 200A along with the current zero are presented in Figs. 4.10-4.11.

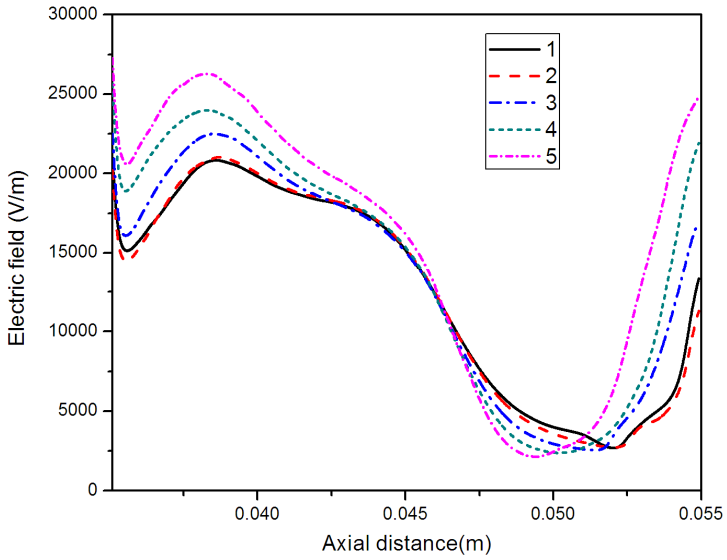

(a)

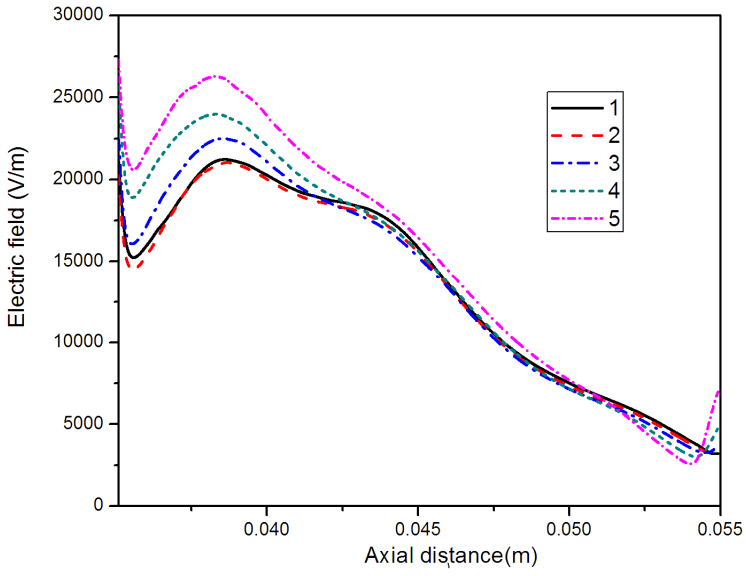

(b)

Figure 4.12 Axial variation of electric field along the central axis at various instants before current zero with a current decaying rate of 13 A/μs under the exit pressures of (a) 0.680MPa and (b) 0.272MPa. 1, 1000A; 2, 800A; 3, 600A; 4, 400A; 5, 200A; 6, current zero.

For both cases, with the decaying current, the arc radius gradually shrinks with different rates at various axial positions as a result of the accumulated turbulence cooling. With the exit pressure of 0.272MPa, the largest arc radius which appears aftershock moves firstly upstream then downstream near current zero. In contrast, under the exit pressure of 0.680MPa, the axial position where the largest arc radius appears still moves upstream near current zero due to the influence of sucked cold gas.

We can note that the axial temperature in front of the downstream electrode increases when the current decay to a value of 200A under the exit pressure of 0.680MPa. This can be explained that the penetrated pressure shrinks the arc radius near the hollow downstream electrode with sucked gas flow. Regardless of the decaying current, the electric field value near the hollow electrode increase as found in Fig. 4.12 and dominates to bring an increasing current density and hence a rising Ohmic heating density.

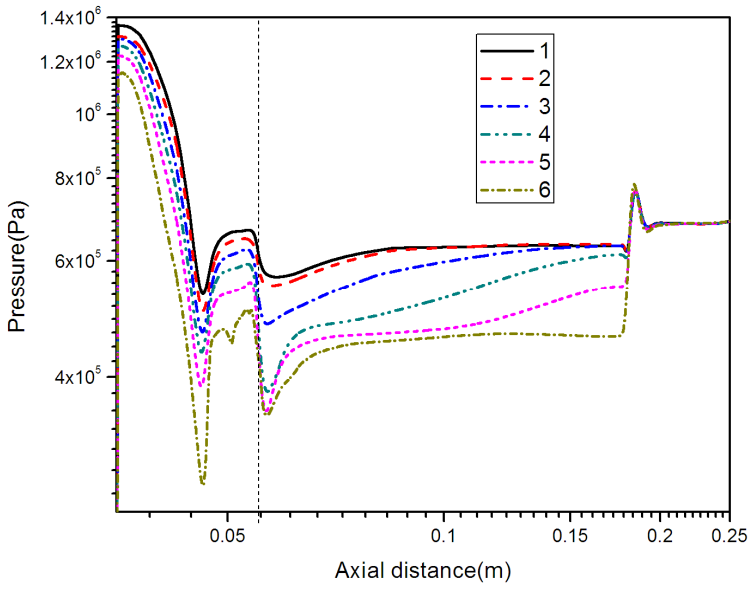

(a)

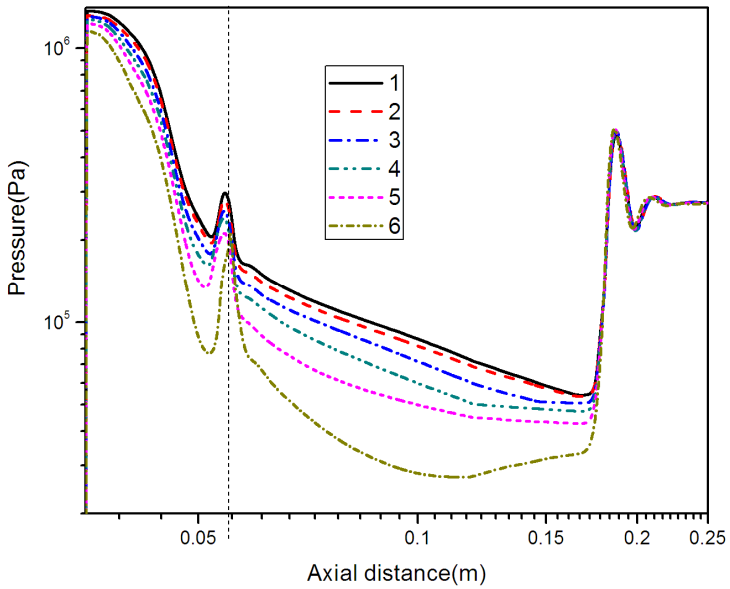

(b)

Figure 4.13 Axial variation of pressure along the central axis at various instants before current zero with a current decaying rate of 13 A/μs under the exit pressures of (a) 0.680MPa and (b) 0.272MPa. 1, 1000A; 2, 800A; 3, 600A; 4, 400A; 5, 200A; 6, current zero.

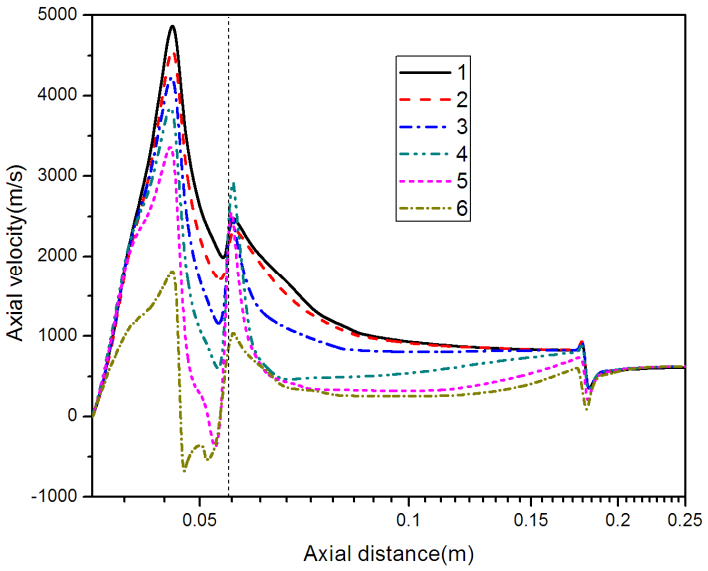

(a)

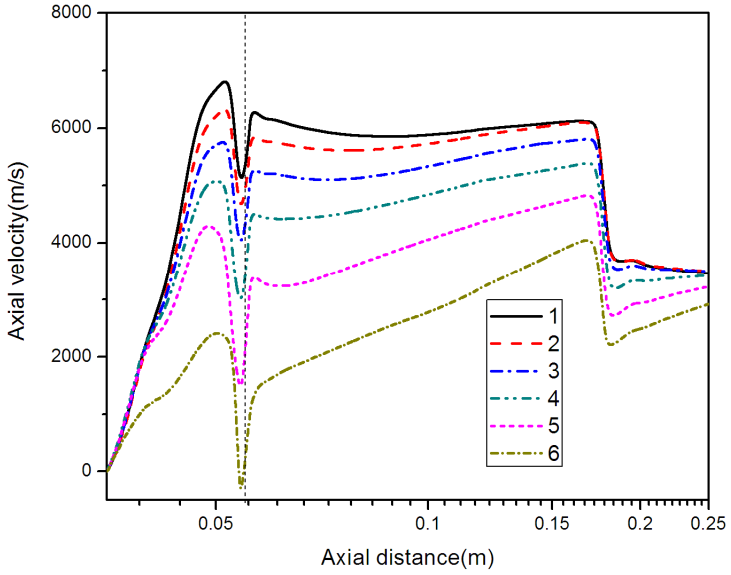

(b)

Figure 4.14 Axial variation of axial velocity along the central axis at various instants before current zero with a current decaying rate of 13 A/μs under the exit pressures of (a) 0.680MPa and (b) 0.272MPa. 1, 1000A; 2, 800A; 3, 600A; 4, 400A; 5, 200A; 6, current zero.

The temperature field distribution is closely connected with the flow field distribution for which the pressure and axial velocity variation as a function of the axial position along the central axis are presented in Figs. 4.13-4.14. Under the exit pressure of 0.680MPa, before the time instant which corresponds to a current of 200A, both the downstream electrode's blocking effect and the pressure penetration contribute to one shock along the central axis which brings only one velocity decelerations area after shock. Near current zero, these two factors contribute to two velocity decelerations areas as shown in Fig. 4.15. It is noted that the turbulence heat transfer pays an important role in the arc energy dissipation process when current decreases towards zero. The lowest temperature near current zero under the exit pressures of 0.680MPa occurs at the axial position of 51.0mm which locates near the center of the second shock caused by the downstream blocking effect. In this area, the turbulence viscosity and turbulence thermal conductivity is much higher than other parts due to the intense interaction between sucked cold flow and arc. The turbulence-enhanced momentum and energy transport dominates the cooling of SF_6 nozzle arcs in these region and leads to a lowest temperature value.

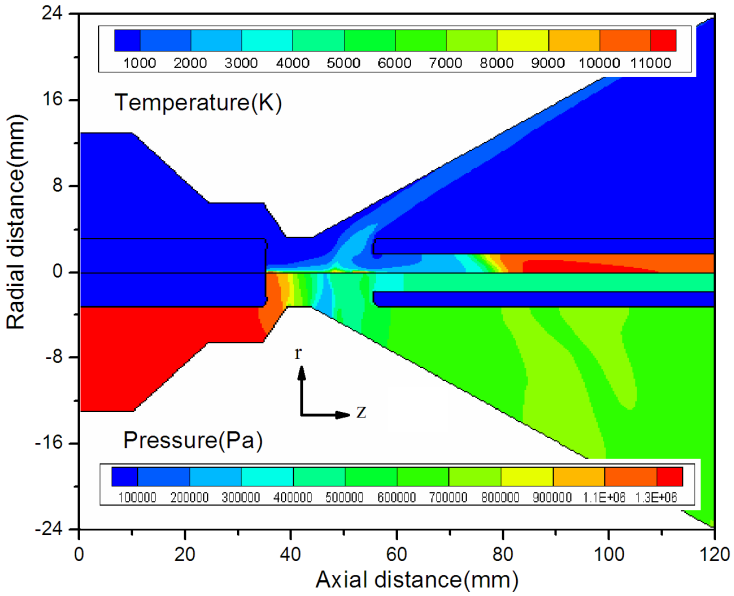

(a)

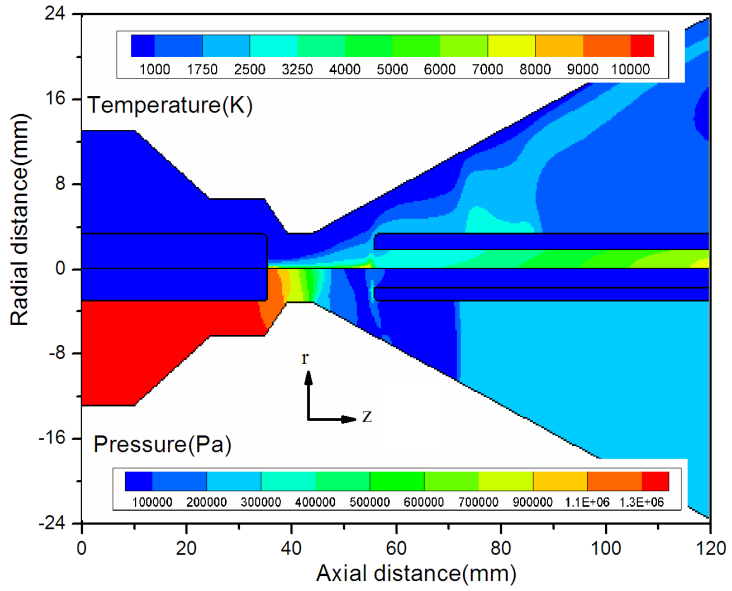

(b)

Figure 4.15 Temperature and pressure distribution of SF_6 arcs in a supersonic nozzle at current zero with a current decaying rate of 13 A/μs under the exit pressures of (a) 0.680MPa and (b) 0.272MPa. The upper part: temperature; the bottom part: pressure.

Comparing with a supersonic flow before the shock along the central axis with the exit pressure of 0.272MPa, the flow near current zero is subsonic along the whole central axis with the exit pressure of 0.680MPa as presented in Fig. 4.16. The supersonic flow mainly

occurs in the arc's surrounding regions. For both cases, there exists a stagnation-point in front of the downstream electrode where the gas flow velocity is zero. Due to the weak convective energy exchange in this area, the temperature remains relatively higher than other regions.

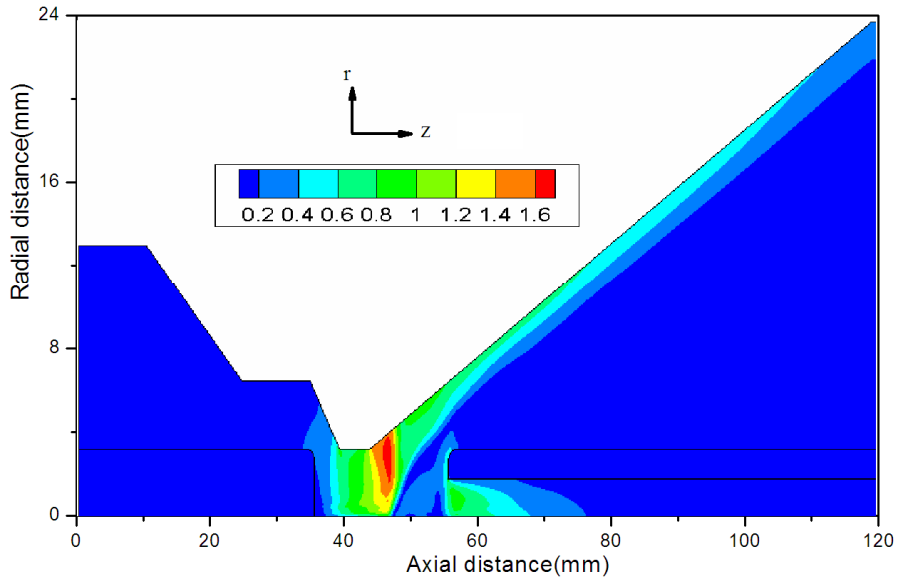

(a)

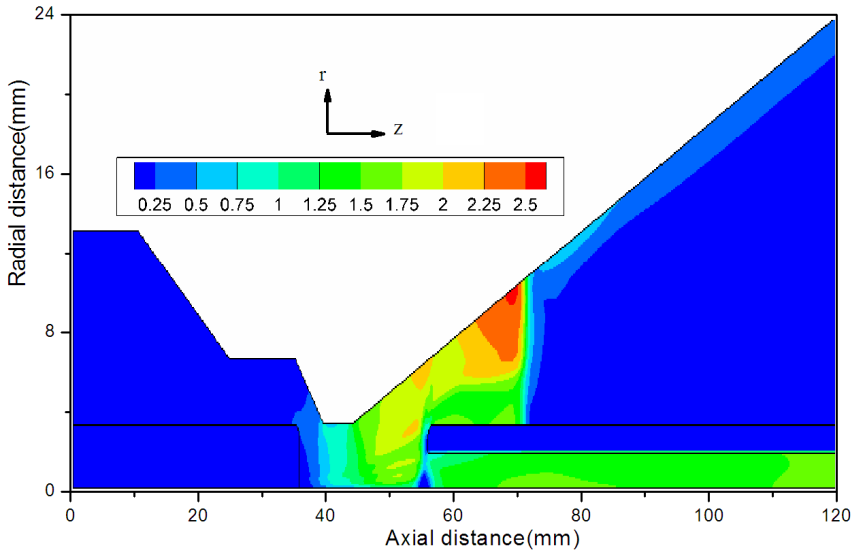

(b)

Figure 4.16 Mach number distribution of SF_6 arcs in a supersonic nozzle at current zero with a current decaying rate of 13 A/μs under the exit pressures of (a) 0.680MPa and (b) 0.272MPa.

4.3.2.2 After Current Zero

The thermal interruption capability of a circuit breaker is usually expressed as the critical rate of recovery voltage (RRRV). The RRRV of the nozzle arc is determined from the results of post arc current calculation by applying a linearly increasing recovery voltage after current zero [29]. The RRRV is defined as the value of dV/dT above which the arc will reignite with a discharge current increasing exponentially after current zero.

For a fixed inlet stagnation pressure, the flow field between the two electrodes remains unchanged as long as the exit pressure ratio is lower than 0.33 which corresponds to an exit pressure of 0.453MPa and leads to the same estimation of RRRV. Fig. 4.17 shows the post arc current variation as a function of time with three different recovery voltage rates. The calculated RRRV of 6.10kV/μs under the exit pressure of 0.0136MPa matches well with that measured result in which the downstream volume was evacuated by a mechanical pump [1]. Under an exit pressure of 0.680MPa, the flow field can be influenced by the penetrated pressure and a lower thermal interruption capability with a RRRV of 6.05kV/μs is obtained.

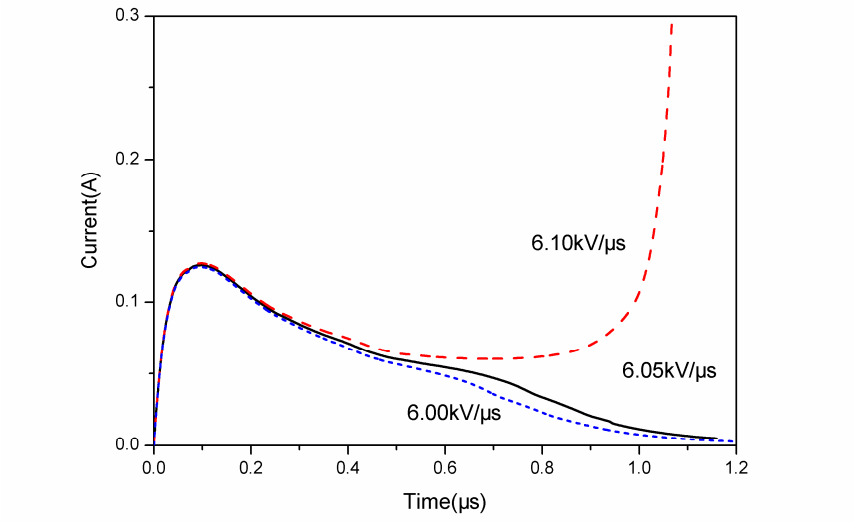

(a)

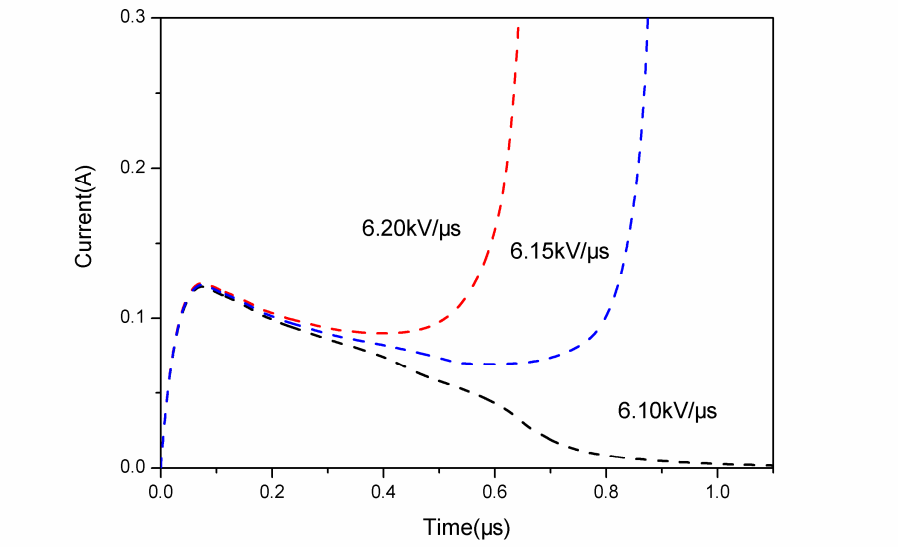

(b)

Figure 4.17 Post-arc current for different values of dV/dt under exit pressures of 0.680MPa (a) and 0.0136MPa (b) with a current decaying rate of 13 A/μs.

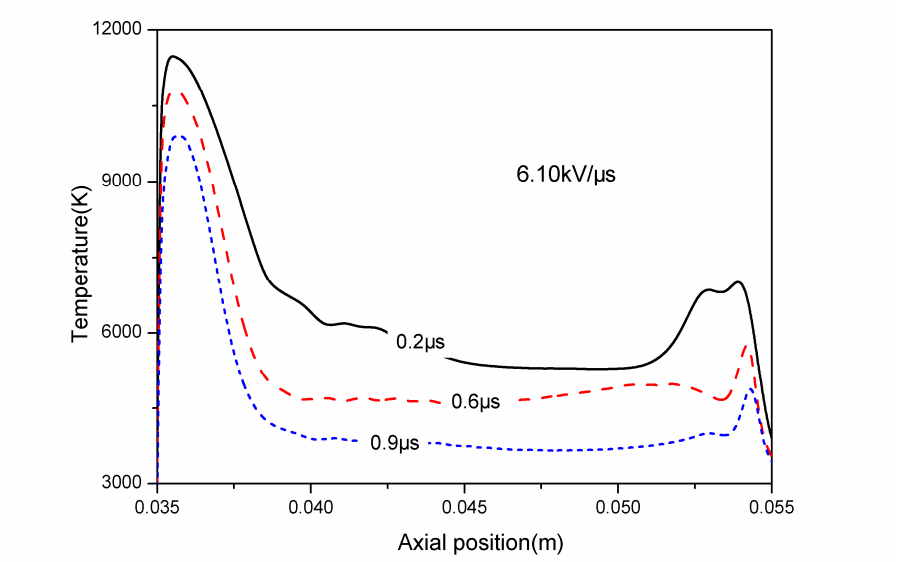

(a)

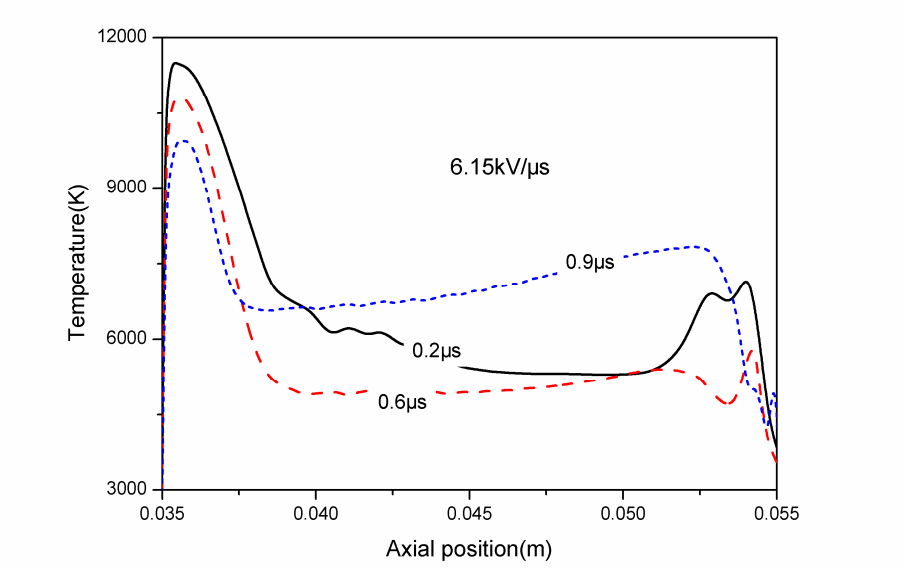

(b)

Figure 4.18 Axial temperatures at various instants after current zero under exit pressures of 0.0136MPa with a current decaying rate of 13 A/μs.

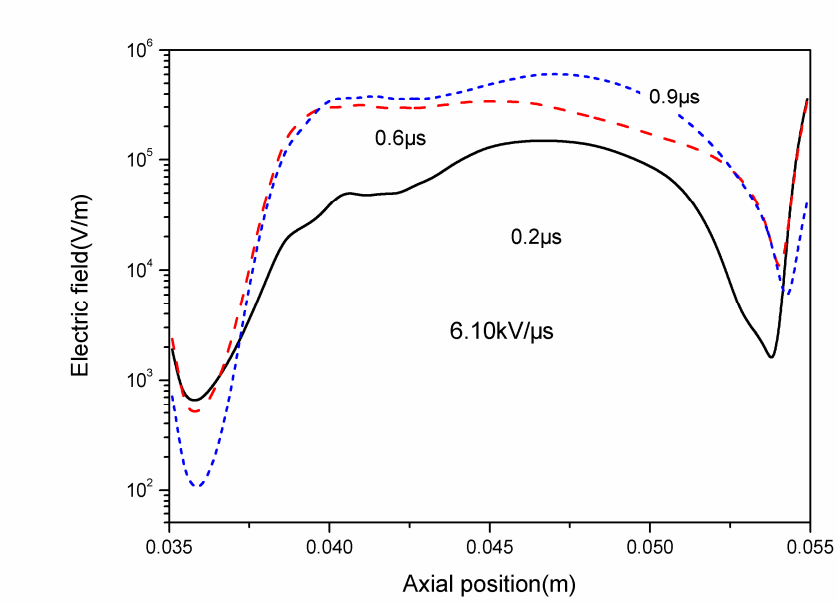

(a)

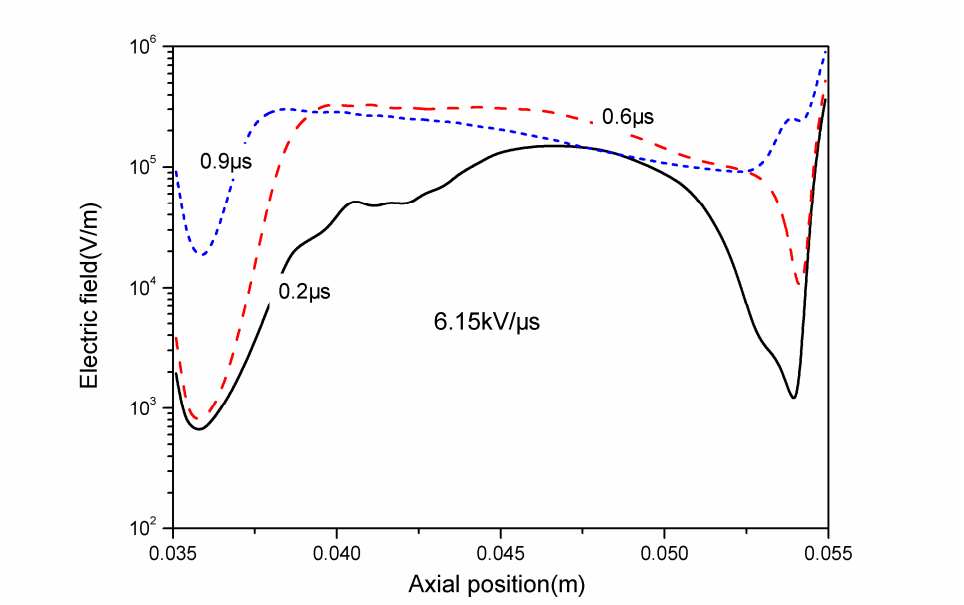

(b)

Figure 4.19 Axial electric field at various instants after current zero under exit pressures of 0.0136MPa with a current decaying rate of 13 A/μs

Figs. 4.18-4.19 give the axial temperature and axial electric field variations at various instants after current zero under an exit pressure of 0.0136MPa with a current decaying rate of 13A/μs with and without thermally interrupting the current. When the arc is thermally extinguished, the axis temperature decays rapidly. The axial temperature of the arc plasma has been cooled down to 4000 K in a region of 15-mm-long column at the instant of 0.8μs after current zero which takes up most of the recovery voltage. With a higher recovery voltage rate under which the arc plasma reignites, the axial temperature along the central axis firstly decreases and then increases in a section of column due to the electric energy input (Ohmic heating) which surpasses the energy dissipation by convection and turbulent cooling while that near the upstream electrode still decreases. Further increase in voltage with time leads finally to the re-ignition of the arc plasma. Correspondingly, the electric field in this region continuously increases in the first 0.9μs while the electric field in the middle column firstly increases and then decreases due to the rising temperature.

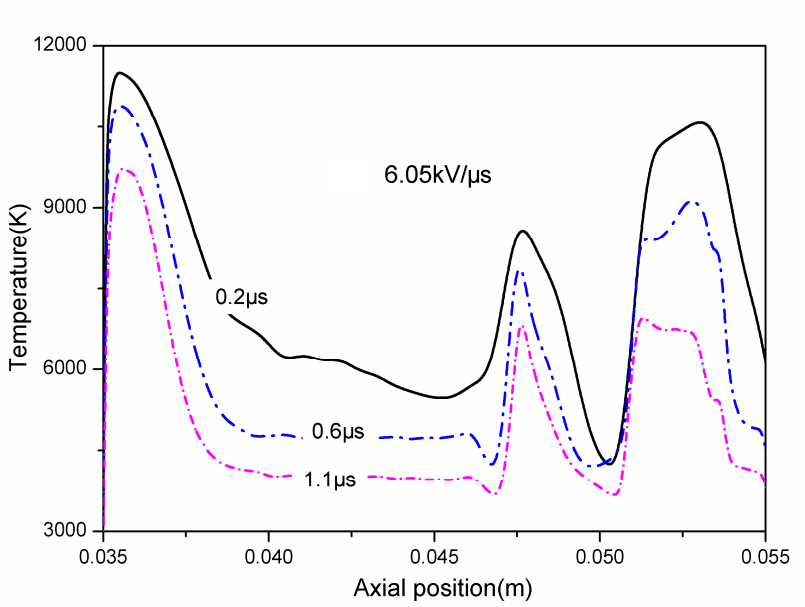

(a)

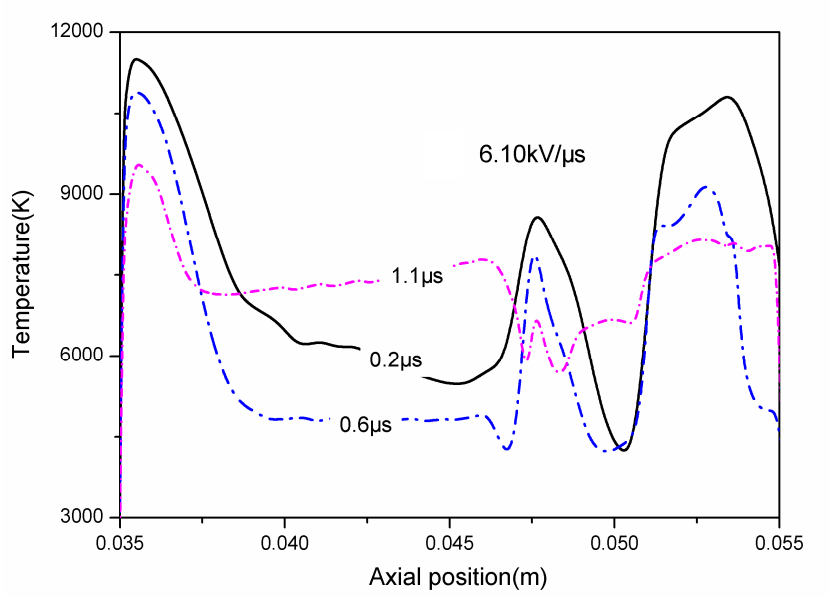

(b)

Figure 4.20 Axis temperatures at various instants after current zero under exit pressures of 0.680MPa with a current decaying rate of 13 A/μs.

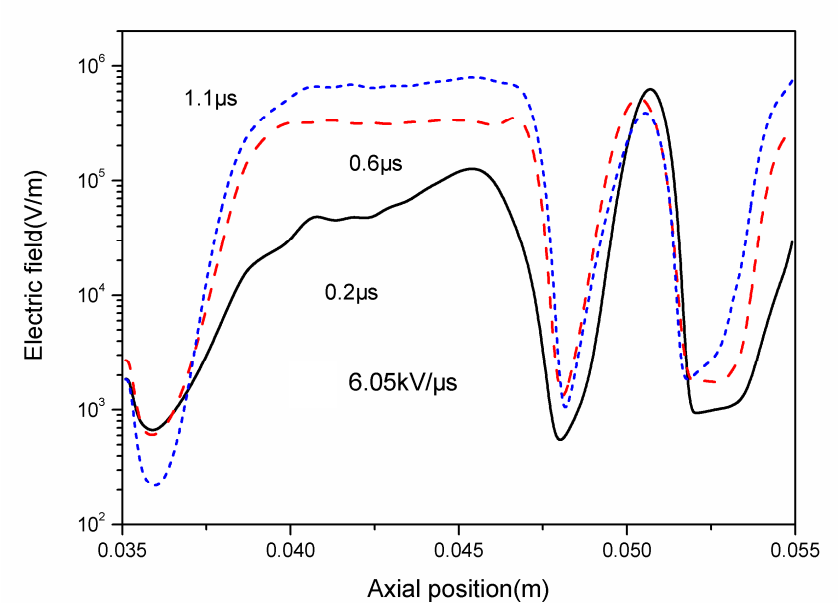

(a)

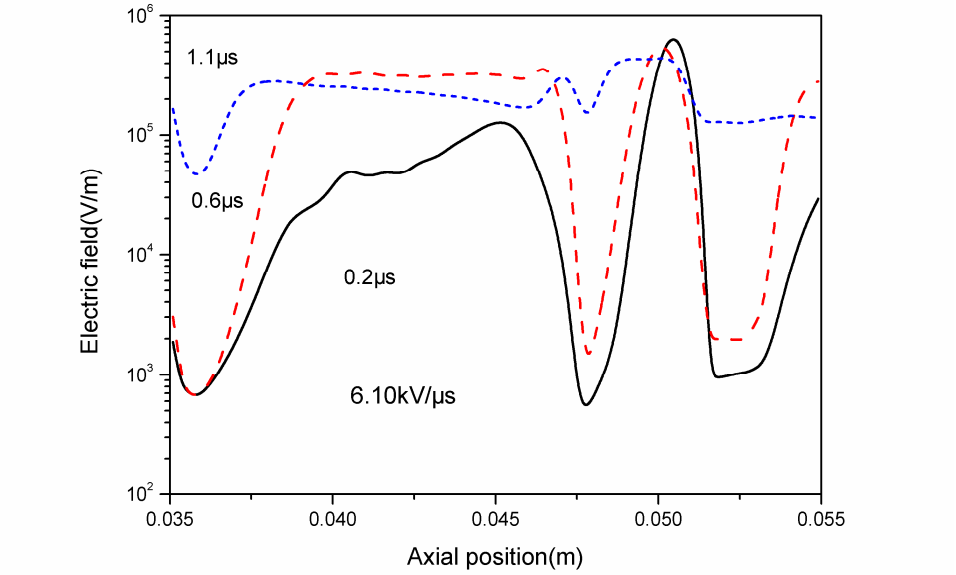

(b)

Figure 4.21 Axis electric field at various instants after current zero under exit pressures of 0.680MPa with a current decaying rate of 13 A/μs.

Under the exit pressure of 0.680MPa, the axial electric field also shows the inversely related characteristics with the axial temperature: the axial electric field presents a higher value where the axial temperature is lower. The temperature at the axial location of 51.0mm is

cooled down to 4000K firstly with most vigorous cooling act and therefore the beginning of current interruption occurs at this point. Comparing with the cases that the penetrated pressure can only influence outside the arcing area, two completive factors can influence the thermal interruption capability under the exit pressure of 0.680MPa. On the one hand, the shocks can decelerate the gas velocity and broaden the arc radius after shock which bring a slower temperature decaying rate and a relatively higher temperature. This appears deleterious to the thermal recovery behaviour of a supersonic nozzle. On the other side, the penetrated pressure with sucked gas flow can strongly cool down the residual arc plasma in the second shock center near current zero by effective turbulent enhanced convection and leads to a lowest temperature along the central axis between electrodes which firstly decreases to 4000K and causes an thermal interruption. When the influence of the first factor surpasses that of the second one, a lower thermal interruption capability can be expected as presented in current case. As a result of the important contribution of turbulence on arc cooling, fundamental work needs to be done in order to devise a suitable turbulence model for arcs in gas flow where compressibility, Ohmic heating, radiation transport, and electromagnetic fields are important [29].

4.4 Conclusions

In this chapter, a considerable effort has been devoted to arc-shock interaction and its influence on steady and dynamic characteristics of SF_6 arcs in a supersonic nozzle with hollow contact, which is representative of switching arcs in a gas blast high voltage circuit breaker. The physical parameters, such as the arc radius, the flow field, the temperature, and the electric field strength before and after current-zero have been obtained. The significant quantity in determining the thermal interruption capability of a circuit breaker, i.e. the critical rate of rise of recovery voltage (RRRV), was predicted and compared with available test results. The main conclusion of this work is summarized as follows:

The high pressure penetration into the thermal layer and the downstream electrode's blocking effect can both contribute to a low flow entrainment into the arc core to form shocks and hence a broadening effect of the arc column.

Both shocks caused by the electrode blocking effect and the pressure penetration present a low dependence of its center location on the current value which slightly moves towards downstream as current increase showing increasingly significant influence of the arc.

Different nozzle exit pressures can greatly influence arc behaviour between electrodes and hence the thermal interruption capability. For example, the penetrated pressure shrinks the arc radius near the hollow downstream electrode with sucked gas flow and lead to a temperature rise with decaying current. This is attributable to an increasing Ohmic heating density caused by a higher current density. There exists a location before which the arc and its surrounding flow are hardly affected by the penetrated pressure and poses the same field distribution for different exit pressures. There also exists a value of exit pressure below which the arc behaviour and flow field between electrodes remains unchanged and leads to the same estimation of thermal interruption capability from current model. Additionally, with increasing exit pressure, the gas flow along the central axis gradually does not show supersonic characteristics before the shock showing the inhibition of increased exit pressure. The highest Mach number in the nozzle mainly occurs along the wall surface in its diverging part and moves towards upstream with a decreasing value of exit pressure as well.

Regardless of the existence of a hollow flow passage, there exists a stagnation-point near current zero in front of the downstream electrode where the gas flow velocity is zero. Moreover, the arc plasma is locally broadened with decelerated velocity due to the blocking effect under the condition that the penetrated gas can hardly influence the flow field between electrodes. Due to the weak convective energy exchange in this area, the temperature remains relatively higher. Therefore, this region is expected to have adverse effects on dielectric recovery as well as on thermal recovery.

Results indicate that a critical region for thermal recovery exists which takes up a large proportion of the arc voltage after current zero. When the penetrated pressure can influence the arcing area, this region is divided to two parts by the separated shocks after current zero. Two completive factors, i.e. the velocity deceleration caused by the shocks and the enhanced turbulent cooling caused by the sucked gas and arc interaction, both pay a significant role in the determination of thermal interruption capability. Thus, the design of a

supersonic nozzle interrupter should ensure that the pressure ratio must be guaranteed at the last current zero of the circuit breaker operation to decrease the deterioration caused by shocks and enhance the turbulent heat cooling.

Turbulence heat transfer pays a significant role in the arc energy dissipation process when current decreases towards zero especially under the condition that the penetrated pressure can influence the arcing area between the electrodes. Fundamental work needs to be done in order to devise a suitable turbulence model for arcs in gas flow in future especially under shock condition.

We should note that it is not possible at present to compare with experiments in more cases. As mentioned previously, experimental observation so far has been limited to the case where the downstream volume was evacuated by a mechanical pump. The turbulence parameter used in this chapter is determined by matching with this case. However, our previous investigation shows that the turbulence parameter derived from one experimental investigation gives reasonable agreement with the test results when the pressure ratios change [29]. Meanwhile, some qualitative features are similar such as the broadening of the arc cross section. The slight discrepancy is mainly attributed to the uncertainty in the turbulence parameter.

4.5 Reference

[1] F. Reichert, J. J. Gonzalez and P. Freton, "Modelling and simulation of radiative energy transfer in high-voltage circuit breakers", J. Phys. D: Appl. Phys., 45, 375201 (2012).

[2] H. Z. Randrianandraina, Y. Cressault and A. Gleizes, "Improvements of radiative transfer calculation for SF_6 thermal plasmas", J. Phys. D: Appl. Phys., 44, 194012 (2011).

[3] C. M. Dixon, J. D. Yan and M.T. C Fang, "A comparison of three radiation models for the calculation of nozzle arcs", J. Phys. D: Appl. Phys., 37, 3309 (2004).

[4] V. Aubrecht and J. J. Lowke, "Calculation of radiation transfer in SF_6 plasmas using the method of partial characteristics", J. Phys. D: Appl. Phys., 27, 2066 (1994).

[5] S. D. Eby, J. Y. Trepanier and X. D. Zhang, "Modeling radiative transfer in SF_6 circuit breaker arcs with the P-1 approximation", J. Phys. D: Appl. Phys., 31, 1578 (1998).

[6] A. A. Iordanidis and C. M. Franck, "Self-consistent radiation-based simulation of electric arcs: II. Application to gas circuit breakers", J. Phys. D: Appl. Phys., 41, 135206 (2008).

[7] J. D. Yan, R. E. Blundel and M. T. C. Fang, "A comparative study of turbulent models for SF_6 arcs in supersonic nozzle", J. Phys. D: Appl. Phys., 32, 1401 (1999).

[8] R. Bini, N. T. Basse, and M. Seeger, "Arc induced turbulent mixing in an SF_6 circuit breaker model", J. Phys. D: Appl. Phys., 44, 25203 (2011).

[9] J. J. Gonzalez, P. Freton, F. Reichert and D. Randrianarivao, "Turbulence and magnetic field calculations in high voltage circuit breakers", IEEE Trans. Plasma Sci., 40, 936 (2012).

[10] M. Seeger, L. Niemeyer, T. Christen, M. Schwinne and R. Dommerque, "An integral arc model for ablation controlled arcs based on CFD simulations", J. Phys. D: Appl. Phys., 39, 2180 (2006).

[11] R. Kozakov, M. Kettlitz, K. Weltmann, A. Steffens and C. M. Franck, "Temperature profiles of an ablation controlled arc in PTFE: I. Spectroscopic measurement", J. Phys. D: Appl. Phys., 40, 2499 (2007).

[12] H. Schneidenbach, D. Uhrlandt, St. Franke and M. Seeger, "Temperature profiles of an ablation controlled arc in PTFE: II. Simulation of side-on radiances", J. Phys. D: Appl. Phys., 40, 7402 (2007).

[13] J. L. Zhang, J. D. Yan, A.B. Murphy, W. Hall and M. T. C. Fang , "Computational investigation of arc behaviour in an auto-expansion circuit breaker contaminated by

ablated nozzle vapor IEEE", Trans. Plasma Sci., 2 ,706 (2002).

[14] K. C. Paul, T. Sakuta, T. Takashima and M. Ishikawa, "The dynamic behaviour of wall-stabilized arcs contaminated by Cu and PTFE vapours", J. Phys. D: Appl. Phys., 30, 103 (1997).

[15] D. Eichhoff, A. Kurz, R. Kozakov, G. Gött, D. Uhrlandt and A. Schnettler, "Study of an ablation-dominated arc in a model circuit breaker", J. Phys. D: Appl. Phys, 45, 305204 (2012).

[16] V. K. Liau, B. Y. Lee, K. D. Song and K. Y. Park, "The influence of contacts erosion on the SF_6 arc ", J. Phys. D: Appl. Phys., 39, 2114 (2006).

[17] J. L. Zhang, J. D. Yan, and M. T. C. Fang, "Electrode Evaporation and Its Effects on Thermal Arc Behaviour", IEEE Trans. Plasma Sci., 3, 1352 (2004).

[18] K. D. Song, B. Y. Lee and K. Y. Park, "Analysis of thermal recovery for SF_6 gas-blast arc within Laval nozzle," Japan. J. Appl. Phys., 42, 7073 (2003).

[19] J. B. Belhaouari, J. J. Gonzalez and A. Gleizes, "Simulation of a decaying arc plasma: hydrodynamic and kinetic coupling study," J. Phys. D: Appl. Phys., 31, 1219 (1998).

[20] L. T. Isaac, J. W. Spencer, J. Humphries, G. R. Jones and W. Hall, "Optical-fibre-based investigations of contact travel, gas pressure and particle concentration in SF_6 puffer circuit breakers", IEEE Trans. Plasma Sci., 5, 453 (1999).

[21] Y. Tanaka, Y. Yokomizu, T. Matsumura and Y. Kito, "Transient behaviour of axial temperature distribution in post-arc channel after current zero around nozzle throat in flat-type SF_6 gas-blast quenching chamber", J. Phys. D: Appl. Phys., 28, 2095 (1995).

[22] Y. Tanaka, Y. Yokomizu, T. Matsumura and Y. Kito, "Transient distribution of metallic vapour concentration in a post-arc channel after current zero along the nozzle axis in a flat-type SF_6 gas-blast quenching chamber", J. Phys. D: Appl. Phys., 29, 1540 (1996).

[23] Y. Tanaka, Y. Yokomizu, T. Matsumura and Y. Kito, "The opening process of thermal plasma contacts in a post-arc channel after current zero in a flat-type gas-blast quenching chamber", J. Phys. D: Appl. Phys., 30, 407 (1998).

[24] S. Vacquié, A. Gleizes and H. Kafrouni, "Measurement of electron density in a SF_6 arc plasma," J. Phys. D: Appl. Phys., 1, 2193 (1985).

[25] R. R. Sturzenegger and H. J. Schoetzau, "Influence of a shock on the electrical field distribution," IEEE Trans. Power App. Syst., PAS-99, 1957 (1980).

[26] D. M. Benenson, G. Frind, R. E. Kinsinger, H. T. Nagamatsu, H. O. Noeske, and R. E.

Sheer Jr., “Fundamental investigation of arc interruption in gas flows,” EPRI Rep., EL–1455, Res. Project 246–2, 26 (1980).

[27] L. C. Campbell, J. F. Perkins, and J. L. Dallachy, “Effect of nozzle pressure ratio on SF_6 arc interruption,” in Proc. 4th Int. Conf. Gas Discharges, Swansea, 1976, pp. 44–47.

[28] M. T. C. Fang, S. Kwan, and W. Hall, “Arc-shock interaction inside a supersonic nozzle,” IEEE Trans. Plasma Sci., 24, 85 (1996).

[29] J. D. Yan, M. T. C. Fang, and C. Jones, “Electrical and aerodynamic behaviour of arcs under shock conditions,” IEEE Trans. Plasma Sci., 25, 840 (1997).

[30] J. L. Zhang, J. D. Yan, and M. T. C. Fang, “Investigation of the effects of pressure ratios on arc behaviour in a supersonic nozzle,” IEEE Trans. Plasma Sci., 28, 1725 (2000).

[31] J. C. Lee, and Y.J. Kim, “Effects of nozzle shape on the interruption performance of thermal puffer-type gas circuit breakers,” Vacuum, 80, 599 (2006).

[32] J. Sedlack, Z. Vostracky, H. Knobloch, H. Schramm, C. Wiesinger, “Optimization of high-voltage self-blast interrupters by gas flow and electric field computations,” IEEE Trans Power Deliv, 18, 1228 (2003).

[33] J. F. Perkins, and L. S. Frost, “Effect of nozzle parameters on SF_6 arc interruption,” IEEE Trans Pas, PAS-92, 961 (1973).

[34] M. T. C. Fang, S. Ramakrishnan and H. K. Messerle, “Scaling laws for gas-blast circuit-breaker arcs during the high current phase,” IEEE Trans. Plasma. Sci., 8, 357 (1980).

[35] K. Ragaller and D. T. Tuma, “Similarity relations for the electric arc in forced axial flows,” IEEE Trans. Plasma. Sci., 9, 75 (1981).

[36] R. E. Blundell, M. T. C. Fang and R. M. Terrill, “Similarity and scaling laws for transient low current arcs in a strongly accelerating gas flow,” J. Phys. D: Appl. Phys., 28, 2029 (1995).

[37] R. E. Blundell, and M. T. C. Fang, “The similarity and scaling of radiating arcs burning in a turbulent, axially accelerating gas flow,” J. Phys. D: Appl. Phys., 30, 628 (1997).

[38] J. F. Zhang, M. T. C. Fang, and D. B. Newland, “Theoretical investigation of a 2 kA arc in a supersonic nozzle,” J. Phys. D, Appl. Phys., 20, 368 (1987).

[39] M. T. C. Fang, Q. Zhuang, and X. J. Guo, “Current zero behaviour of an SF_6 gas-blast arc. Part II: Turbulent flow,” J. Phys. D, Appl. Phys., 27, 74 (1994).

[40] J. J. Lowke, R. Morrow and J. Haidar, “A simplified unified theory of arcs and their

electrodes", J. Phys. D: Appl. Phys., 30, 2033 (1997).
[41] PHOENICS is commercially available from CHAM Ltd, Bakery House, 40 High Street, Wimbledon Village, London, SW19 5AU, UK.
[42] S.V. Pantankar, Numerical Heat Transfer and Fluid Flow, Hemisphere, New York, 1984.

CHAPTER 5 INVESTIGATION OF THE DECAY OF AN SF_6 GAS-BLAST ARC USING A TWO-TEMPERATURE HYDRODYNAMIC MODEL

5.1 Introduction

Circuit breakers, as a typical example of switchgear, are expected to interrupt a load or fault current within the specified current and voltage ratings. For high-voltage circuit-breakers, SF_6 is widely used because of its high insulation strength and its high fault-current interruption capability, which is closely linked with the physical phenomena occurring in the electric arc that is formed in the circuit breaker. Before and at current zero the gaseous medium gradually becomes a poor conductor as a result of decreasing temperature and size of the arc, which are in turn due to the strong convective and turbulent cooling. After current zero, the residual plasma channel between the gaps is not a perfect dielectric medium; there still is a small current (up to 10 A) flowing under the recovery voltage in the circuit. The electrical energy input (Ohmic heating) competes with energy removal by convective and turbulent cooling. The rapidly increasing resistance in the contact gap forces the post-arc current to attenuate without the occurrence of thermal breakdown, and at the same time the gas recovers its dielectric strength as charged species combine into neutrals, allowing the gas to withstand the system recovery voltage.

In order to assess SF_6 circuit breaker capability during current interruption, a large number of publications are made contributing to the model and test [1]-[33]. However, these simulations are not satisfying because they do not succeed to predict the failure or the success of the circuit breaking correctly in most cases with the test. Most of the theoretical investigation of the arc behaviour around current zero and the thermal recovery process is based on local thermal equilibrium (LTE) assumption. However, during current-zero period, the assumption of local thermodynamic equilibrium (LTE), which the Computation Fluid Dynamics-Magneto Hydrodynamics simulation of SF_6 circuit-breaker arcs (CFD-MHD) strongly relies on in the high current phase, is no longer valid especially when large temperature gradient exists (near the cold walls and arc fringe or when the cold blown gas is

injected with high cooling rates for heavy species) or when the electron number density is not high enough to allow sufficient transfer of energy between the electrons and heavy species.

In order to better understand the arc behaviour during the current-zero periods, the hypothesis of LTE, including local chemical equilibrium and thermal equilibrium, must be reexamined, and special attention paid to the effects of departure from equilibrium state. It is noted that a two-temperature model in which electrons and heavy species are characterized by two different temperatures has been developed and adopted to investigate the arc behaviour mainly in steady state for different gases [34]. For SF_6 arcs used in high voltage circuit breaker, as a starting point, the mechanism of energy transfer between electrons and heavy species should be examined and quantified. However, there are, to our knowledge, only two relevant studies in the literature. Girard et al. [33] used a two-temperature model to examine the influence of departures from thermal equilibrium on the characteristics of laminar wall-stabilized arc at atmospheric pressure in one-dimensional geometry. As they noted, it was not possible to draw conclusions on the effect of departures from thermal equilibrium for real circuit-breaker geometry, in which convection is the dominant process. Gonzalez et al. [35] investigated the influence of both thermal and chemical departures from LTE on the interruption capability of circuit-breaker arcs, studying the extinction of a blown SF_6 arc in two-dimensional geometry. Some simplifications were required in their study due to the highly-complicated phenomena involved in the process of current interruption in the circuit breaker. For example, only the arc-free recovery from a current of 50 A at atmospheric pressure was examined, and the influence of the high current phase on thermal recovery was neglected. Additionally, species diffusion was not taken into account and the properties of SF_6 used in the simulation were determined by the two-temperature Guldberg–Waage and Saha equations, which require the assumption of local chemical equilibrium.

In the study presented here, we examine the influence of departures from thermal equilibrium in the case of a supersonic nozzle, which is widely used in high-voltage circuit breakers. Departures from chemical equilibrium, which may take place in the SF_6 arc decay phase, are neglected. The objective of the investigation is therefore not to examine the complete mechanism of transient SF_6 arc extinction, but rather to clarify the influence of departures from thermal equilibrium on the characteristics of the supersonic arc with strong

gas convection under turbulent conditions. Unlike previous work, we take into account the high-current phase and the evolution of the decaying current, allowing us to study for the first time the influence of departures from thermal equilibrium on the decay behaviour of the arc.

The chapter is arranged as follows. We first outline the basic assumptions and the mathematical model used. The method of calculation of the thermophysical property data, including composition, thermodynamic properties and transport coefficients, is described in Section 2. Section 3 presents the simulation results for both steady-state and transient cases. A comparison between the simulation and the experimental results for the steady-state case under well-defined conditions is presented and analyzed. The influence of departures from thermal equilibrium on the decay of the supersonic arc is discussed by comparing with the results obtained by LTE model. Finally, conclusions are given in Section 4.

5.2 Mathematical Model

5.2.1 Hypotheses

In the two-temperature model, the energy gained by electrons from the electric field cannot be transferred to heavy species sufficiently fast through elastic collisions to ensure the attainment of a single temperature. Thus, energy conservation for electrons and heavy species needs to be taken into account separately to give different electron and heavy-species temperatures. Electron species conservation must be considered for the calculation of plasma density. The plasma is assumed quasi-neutral. However, it is not necessary to set up a separate momentum equation for electrons because frequent collisions between electrons and heavy particles and ignored species diffusion ensure that all species of the plasma attain the same velocity. Influence of species diffusion will to taken into account in futural work.

The following assumptions and simplifications are adopted [34]-[39]:

(1) The plasma is in a state of local chemical equilibrium. Electrons are carried along with the heavy particles in their convection motion, and therefore species diffusion effects are neglected.

(2) Heavy particles and electrons separately follow a Maxwell–Boltzmann distribution but at different temperatures. The electron gas and the heavy species are considered as two different perfect gases.

(3) Anodic and cathodic sheaths have been neglected. The interaction between electrodes and arc is not taken into account in current study.

5.2.2 Governing Equations

The model considers the plasma as a continuum fluid that can be described by the usual Navier–Stokes equation except for associated source terms, duly modified by electromagnetic equation. For completeness and for ease of discussion, the governing equations of two-temperature model for an axisymmetric arc used in our current work are summarized as follows [34]. For the steady–state calculations, the transient term is not taken into account.

- **Mass Conservation Equation**

$$\frac{\partial \rho}{\partial t} + \nabla \cdot (\rho \vec{u}) = 0 \tag{5.1}$$

where $\vec{u}$ is the mass-averaged velocity of the plasma species, and ρ is the total mass density obtained from

$$\rho = \sum_{i}^{w} m_i n_i \tag{5.2}$$

where m_i is the mass of species *i* and *w* is number of species.

- **Momentum Conservation Equation**

$$\frac{\partial (\rho \vec{u})}{\partial t} + \nabla \cdot (\rho \vec{u}\vec{u}) = -\nabla p + \nabla \cdot \bar{\bar{\tau}} + \vec{J} \times \vec{B} + \rho \vec{g} \tag{5.3}$$

where *p* the total pressure, $\bar{\bar{\tau}}$ the viscous stress tensor, $\vec{J} \times \vec{B}$ the t Lorentz force, $\vec{J}$ being the

current density and $\vec{B}$ the magnetic field induced by the current, and g is the gravity coefficient. For the momentum conservation equations in axisymmetric form, the radial momentum equation is [13]:

$$\frac{\partial(\rho v)}{\partial t}+\nabla\cdot(\rho\vec{u}v)=-\frac{\partial p}{\partial r}+\nabla\cdot(\mu_{eff}\nabla v)+\frac{1}{r}\frac{\partial}{\partial r}(r\mu_{eff}\frac{\partial v}{\partial r})+\frac{\partial}{\partial z}(r\mu_{eff}\frac{\partial w}{\partial r})$$
$$-\frac{2}{3}\frac{\partial}{\partial r}[\mu_{eff}\frac{1}{r}\frac{\partial}{\partial r}(rv)+\mu_{eff}\frac{\partial w}{\partial z}]-\frac{2\mu_{eff}v}{r^2}-j_z B_\theta+\rho g \tag{5.4}$$

The axial momentum equations can be written as:

$$\frac{\partial(\rho w)}{\partial t}+\nabla\cdot(\rho\vec{u}w)=-\frac{\partial p}{\partial z}+\nabla\cdot(\mu_{eff}\nabla w)+\frac{1}{r}\frac{\partial}{\partial r}(r\mu_{eff}\frac{\partial v}{\partial z})+\frac{\partial}{\partial z}(r\mu_{eff}\frac{\partial w}{\partial z})$$
$$-\frac{2}{3}\frac{\partial}{\partial z}(\mu_{eff}\frac{1}{r}\frac{\partial}{\partial r}(rv)+\mu_{eff}\frac{\partial w}{\partial z})-\frac{2\mu_{eff}v}{r^2}+j_r B_\theta \tag{5.5}$$

where v and w are the mass-averaged radial and axial component of the velocity respectively and $\mu_{eff}=\mu_l+\mu_t$ is the effective viscosity including laminar and turbulent contributions. J_r and J_z are respectively the radial and axial components of the current density and B_θ is the azimuthal magnetic field. In our current model, the arc column is rotationally symmetric and the magnetic field is dominated by the azimuthal component, since the current density is predominantly directed parallel to the axis of the arc column. For simplicity, only this azimuthal component is taken into account. Assuming the permeability of the arcing medium μ_0 to be homogenous, the magnetic field can be calculated by Ampère's circuital law.

$$B_\theta(r)=\frac{\mu_0\int_0^r J_z 2\pi\xi d\xi}{2\pi r} \tag{5.6}$$

- **Energy Conservation Equation**

The energy conservation equations for electrons and heavy particles are respectively

$$\frac{\partial(\rho h_e)}{\partial t}+\nabla\cdot(\rho h_e\vec{u})=\nabla\cdot(k_{eeff}\nabla T_e)-\ Q_{eh}-Q_{rad}+Q_J+\frac{5k_B}{2e}\vec{J}\cdot\nabla T_e \tag{5.7}$$

$$\frac{\partial(\rho h_h)}{\partial t}+\nabla\cdot(\rho h_h\vec{u})=\nabla\cdot(k_{heff}\nabla T_h)+Q_{eh}+Q_{rab} \tag{5.8}$$

where $k_{eeff}=k_{el}+k_{et}$ and $k_{heff}=k_{hl}+k_{ht}$ are respectively the effective thermal conductivity for electrons and heavy particles, including both the laminar and turbulent contributions, k_B is the Boltzmann's constant, h_e and h_h are the specific enthalpy of electrons and heavy particles respectively and *e* is the electronic charge. Other source terms are the elastic collision energy exchange term between electrons and heavy species Q_{eh}, the Joule heating Q_J, the radiation losses Q_{rad} and the radiation reabsorption term Q_{rab} at the arc edge. The last term on the right-hand side of equation (5.7) represents the electron heat conduction.

For the energy conservation equations in axisymmetric form, their expressions for electrons and heavy particles are respectively

$$\begin{aligned}\frac{\partial(\rho h_e)}{\partial t}+\nabla\cdot(\rho h_e\vec{u})=&\frac{\partial}{\partial z}(k_{eeff}\frac{\partial T_e}{\partial z})+\frac{1}{r}\frac{\partial}{\partial r}(k_{eeff}r\frac{\partial T_e}{\partial r})-\ Q_{eh}-Q_{rad}\\&+jE+\frac{5k_B}{2e}(j_z\frac{\partial T_e}{\partial z}+j_r\frac{\partial T_e}{\partial r})\end{aligned} \tag{5.9}$$

$$\frac{\partial(\rho h_h)}{\partial t}+\nabla\cdot(\rho h_h\vec{u})=\frac{\partial}{\partial z}(k_{heff}\frac{\partial T_h}{\partial z})+\frac{1}{r}\frac{\partial}{\partial r}(k_{heff}r\frac{\partial T_h}{\partial r})+Q_{eh}+Q_{rab} \tag{5.10}$$

where *j* and *E* are the current density and electric field respectively.

The equations given above are closely coupled and all the thermophysical properties are determined by three independent variables: pressure, electron temperature and heavy-species temperature. Our equations 5.9 and 5.10 differ from the energy conservation equations for electrons and heavy species used by Girard et al. [35] in investigating a similar problem. Girard et al wrote their equations in terms of electron and heavy-species temperatures. Their equations can be derived from ours only by neglecting the dependence of enthalpy on pressure (i.e. by assuming $\partial h/\partial p=0$), and by assuming $\partial T_e/\partial T_h=\nabla T_e/\nabla T_h=T_e/T_h$. Both these approximations are incorrect, so our

equations will give more accurate results.

- **Electric Field Equation**

The electrical field strength and current density are calculated by the simplified Ohm's law.

$$I = E\int_0^R \sigma 2\pi r dr$$

$$j_z = \sigma E_z \tag{5.11}$$

where I is the arc current, σ the electric conductivity and R the arc radius. The simplified Ohm's law assumes that the radial component of the electric field is negligible in comparison with the axial component.

The elastic collision energy exchange between electrons and heavy particles Q_{eh} can be estimated as follows:

$$Q_{eh} = \sum_j \frac{3}{2} k_B (T_e - T_j) n_e \frac{2m_e}{m_j} \xi_{ej} \tag{5.12}$$

where n_e and n_j are the number density of electrons and heavy particles, and m_e and m_j are their respective masses. The volumetric collision frequency between the electrons and the heavy particle ξ_{ej} is given by [34]:

$$\xi_{ej} = (\frac{8k_B T_e}{m_e \pi})^{1/2} n_e n_j \overline{Q}_{ej}^{(1,1)} \tag{5.13}$$

where $\overline{Q}_{ej}^{(1,1)}$ is the collision cross section between electrons and heavy species j.

Radiative transfer is an important energy transport mechanism in SF_6 circuit breaker arcs. Theoretical calculations of the characteristics of an electric arc performed using an equilibrium model including a spectrally-resolved radiative transfer treatment, and an

experimental investigation of the relative absorption of the SF_6 arc radiation by cold SF_6 gas, showed that reabsorbed radiation is an additional source of gas heating [40]. The treatment of radiative transfer is rather more complicated when the arc is established in a molecular gas because of strong absorption mainly by photo excitation, photodissociation and photoionisation in the near UV region and it is virtually impossible to solve the fundamental radiative transport equation for SF_6 arcs. In most cases, radiative transfer in thermal plasma modelling is treated using the NEC (net emission coefficient) method, which gives a good approximation of the radiation losses from the hottest regions [41]. However, based on calculation of the net emission coefficient for isotherm plasma, it is not able to predict the absorption radiation in the cold surrounding regions. When modelling applications such as circuit breakers, in which the temperature of the edge region is important, it is necessary to also consider the absorption of radiation in cooler regions of the plasma and of the surrounding gases. In order to treat this issue, the NEC method can be modified to take into account the edge absorption of the radiation emitted by the arc core [42]-[43]. This model used here, that a modification of Zhang et al [42], is described schematically in Fig.5.1.

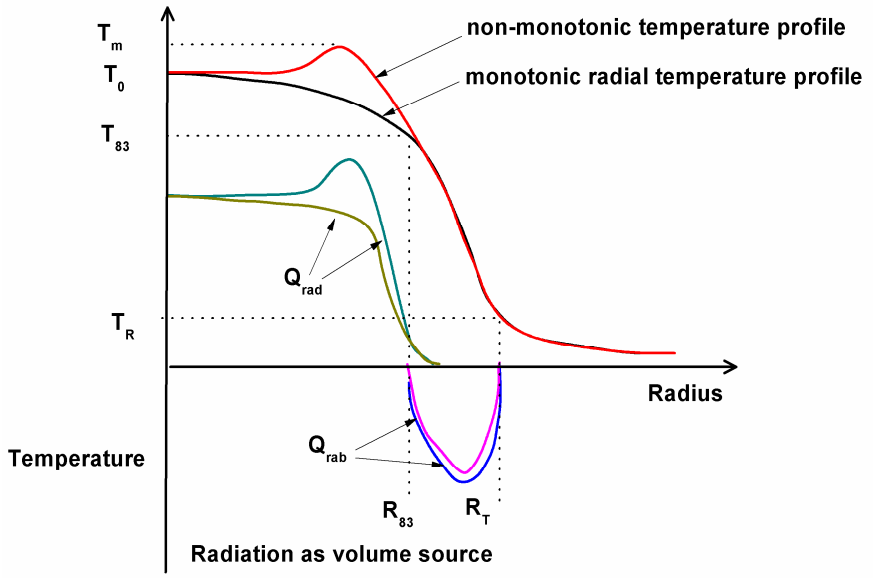

Figure 5.1 Diagram showing possible radial temperature profiles in nozzle arcs (either during iteration or after convergence) and the emission and reabsorption zones.

This model can be applied to both monotonic and non-monotonic radial temperature profiles. The arc core is defined as the region from the axis to the radial position of the

$0.83T_{max}$ isotherm. In the arc core, the net radiation emission energy is a function of temperature, pressure, and radiation radius, which are the three parameters of the NEC model. The accuracy of the NEC method is sensitive to the choice of the radiation radius of the arc column. This is because the NEC is based on a cylindrical column of uniform temperature, which is of course an approximation. Based on our experience, this radiation radius is between the radius R_{83}, corresponding to $0.83T_{max}$, and R_T, which corresponds to the arc radius where the electrical condutivity is low. Beside their own radiation, the radiation from the arc core is partly absorbed in the region between the core edge and the T_R isotherm. This region is called the reabsorption region. The profile of the re-absorption is assumed to be a parabola and the fraction of the radiation leaving the core boundary, which is re-absorbed, is fixed. For normal nozzle flows, where the arc is surrounded by fast flowing cold gas, 80% of the radiation from the arc core is reabsorbed at the arc edge.

To allow for heating of the cold gas (heavy species) due to reabsorption of radiation in a two-temperature model, we must separate the locally emitted radiation Q_{rad} in the arcing space from the reabsorbed radiation energy Q_{rab}. Since radiative emission depends mainly on the population of excited species and these, in turn depend primarily on the electron temperature, the net emission coefficient ε_r is evaluated as a function of the electron temperature based on the work of Liebermann R W and Lowke J J [41]:

$$Q_{rad} = 4\pi\varepsilon_r(P, T_h, T_e, R_{eff}) \approx 4\pi\varepsilon_r(P, T_e, R_{eff}) \tag{5.14}$$

Based on the assumption of Mitchner and Kruger [44], the radiation term in the arc core is included in the electron energy equation and not in the heavy particle energy equation as it is generally treated in the literatures [33], [45]. For the reabsorbed term, because the radiation reabsorption mainly takes place in the arc edge by the cold gas where the electron density is relatively low, the contribution of photo excitation, photodissociation and photoionisation of molecular is assumed to play a more significant role which bring the energy increases of the heavy particles and hence this energy term is distributed to heavy particles equation.

- **State Equation**

The equation of state is

$$\rho = f(P, T_e, T_h) \tag{5.15}$$

The gas flow in supersonic nozzle has been classified in the literature as unstable and turbulent [22]. Gonzalez et al also presented that turbulence must be taken into account during the extinction phase, and during the post-arc phase in the investigation of non-equilibrium arc decaying process [35]. Turbulence-enhanced momentum and energy transfer depends on the flow field. The closure of the system equations requires extra relationships to calculate the turbulence-enhanced viscosity and thermal conductivity. The modelling of turbulent flows has been intensively studied and a variety of methods has been applied. In commercial computational fluid dynamics codes, Reynolds-averaged Navier–Stokes and large eddy simulation approaches have been implemented. It is difficult to determine the most realistic turbulence model without reference to experimental data. Unfortunately, few experimental data are available on the development of turbulence in a supersonic nozzle. In our previous work, two turbulence models (the Prandtl mixing-length model and a standard K–ε model) have been applied to study their influence on the computational results [7]. The Prandtl mixing-length model was found to be preferable compared with other more sophisticated turbulence models. The Reynolds stresses in the momentum equation and their counterpart in the energy equation, which represent the turbulence-enhanced momentum and energy transport, are accounted for by the turbulent eddy viscosity and thermal conductivity. These two quantities are related to the length scale and to the characteristic velocity of the turbulence. The turbulence viscosity is given by

$$\mu_t = \rho l_m^2 \left| \frac{\partial w}{\partial r} \right| \tag{5.16}$$

$$l_m = c\delta \tag{5.17}$$

where $\delta = (\theta_\delta / \pi)^{0.5}$ is the arc's thermal radius, $\theta_\delta = \int_0^\infty (1 - \rho / \rho_\infty) 2\pi r dr$, w is the axial velocity component, ρ_∞ is the gas density in the cold flow and c is the turbulence parameter,

which is determine empirically. The turbulence-enhanced thermal conductivity, k_t, is related to the turbulent viscosity through the turbulent Prandtl number

$$\Pr = \frac{\mu_t}{k_t / c_P} \tag{5.18}$$

We follow the work of Gonzalez et al [35] which considers the two temperature plasma as the whole of two fluids, one fluid of electrons and one of heavy particles. They think that even if these fluids are linked through energy exchange, each of them has its own energy, which is distributed in space. Turbulence mixes each of them separately, carrying energy from hot regions to colder ones, increasing thermal conductivity. Hence, we apply turbulence to both electrons and heavy particles as presented in Eq. (5.19). With this treatment, the two-temperature energy conservation equation can reduce to the same form as that of the LTE equation if these two equations are added together. It has been found that for turbulent arcs, the turbulent Prandtl number can be assumed to be unity [7]. Thus, only the parameter c needs to be adjusted.

$$\Pr(h_e) = \frac{\mu_t}{k_{te} / c_{Pe}} \qquad \text{and} \qquad \Pr(h_h) = \frac{\mu_t}{k_{th} / c_{Ph}} \tag{5.19}$$

5.2.3 Property Data

Accurate data for the composition, thermodynamic properties and transport coefficients are a prerequisite for reliable numerical simulation of thermal plasmas. For compressible flow and heat transfer simulations with SF_6 as the plasma working gas, tabulated pressure-temperature-dependent thermodynamic and transport properties of equilibrium/non-equilibrium SF_6 plasmas in wide pressure and temperature ranges were calculated in chapter 3. Following the recommendation of Gleizes et al. [47], on the basis of a chemical kinetics approach, we adopted the forms of the Saha and Gulberg–Waage equations, which describe ionization and dissociation reactions respectively, proposed by van de Sanden et al.[50]. We chose the heavy-species temperature as the excitation temperature for dissociation and molecular ionization, and the electron temperature as the excitation temperature for atomic ionization.

5.2.4 Computational Domain and Boundary Condition

The geometry of the Aachen nozzle was used to compare the results obtained by the LTE and two-temperature models [51]-[52]. The length of the nozzle is 55 mm and the throat diameter is 36.7 mm. The distance between the inlet and the nozzle throat is 33 mm. The diameter and length of the upstream electrode are 10.86 mm 7.86 mm respectively.

At the inlet, stagnation pressure and temperature are specified. The upstream stagnation pressure is 0.90 MPa and the stagnation temperature is set to 300 K. The exit static pressure is 0.25 MPa. The inwards mass, momentum and energy fluxes are calculated by assuming isentropic expansion of gas from the stagnation pressure to the local pressure at the boundary cells. The experimental arrangement includes a downstream electrode, but this is not included here as the nozzle is such that the Mach number downstream of the throat exceeds unity.

Axisymmetric boundary conditions are imposed: the radial velocity and the radial gradient of all dependent variables are zero on the axis. The heat flux is set at zero on all solid surfaces which includes the nozzle and electrodes based on the following issues: Firstly, The boundary conditions for temperature at the electrodes are usually not known as the equations based on LTE are no longer valid for the region close to the electrode, which is a space charge dominated sheath region with a length scale determined by Debye length. The influence of the upstream boundary conditions on the arc solution is confined in a small region close to the upstream electrode. The overall arc voltage is hardly affected by using different upstream boundary conditions as pointed out by Zhang et al.[42]. Secondly, energy loss by thermal conduction into the nozzle wall which has a low thermal conductivity is negligible because, for the current region investigated, there is a low-temperature layer separating the arc from the wall. Lastly, it is reasonable to expect that the differences of electrical and aerodynamic behaviour for SF_6 arcs obtained by LTE model and two-temperature model are mainly caused by two effects: (1) the boundary conditions used for the electron energy equation and (2) the occurrence of a significant thermal non-equilibrium region within the domain [53]. In order to investigate the influence of the second effect, the same boundary condition for electron energy equation and heavy species energy equation is adopted for convenience.

The calculations have been carried out using PHOENICS [54], a commercially available commercial Computational Fluid Dynamics (CFD) package code based on the solution of the conservation equations for momentum and energy using Patankar's SIMPLE method [55]. The code uses the finite volume method on a structured grid. In order to solve arc problems PHOENICS requires the addition of extensive customized features. These are added using FORTRAN subroutines which are integrated into the package.

A 173 × 80 finite volume grid was used. The values used for the initial guesses did not affect the final converged results. The accuracy of the calculations was tested by repeating them with a finer grid system.

5.3 Results and Discussion

5.3.1 Steady State Calculations

Initial calculations were carried out for the steady-state case, and a comparison was performed between the predictions of LTE calculations and available experimental results for the Aachen nozzle under well-defined conditions. The turbulence parameter *c* used in the Prandtl mixing length model was set to 0.12, which gave the best agreement with the experimental data [51]-[52]. To simulate the experimental conditions for DC steady-state arc, a total number of 1000000 iterations are performed and it takes approximately 55 h on a personal computer system with a 3.4GHz processor for the two temperature simulation in current case.

The distributions of the electron and heavy-species temperatures obtained from the model for the SF_6 supersonic arc with current of 600 A are presented in Fig.5.2 to give the influence of departure from local thermodynamic equilibrium. In the arc core, the electron temperature and heavy-species temperature are approximately equal, despite of the intense gas flow driven by the pressure difference between the inlet and the exit. A large difference between the electron and heavy-species temperatures is, however, predicted in the arc fringe region, at temperatures less than 12000 K, where the arc and cold gas flow interact. This is clearly apparent in the distribution of non-equilibrium degree $\theta=T_e/T_h$, which is shown in Fig.5.3. The degree of thermal non-equilibrium increases as the flow progresses downstream,

away from the arc. This is attributed to the influence of incensing strength of the plasma–cold flow interaction and the decreasing pressure.

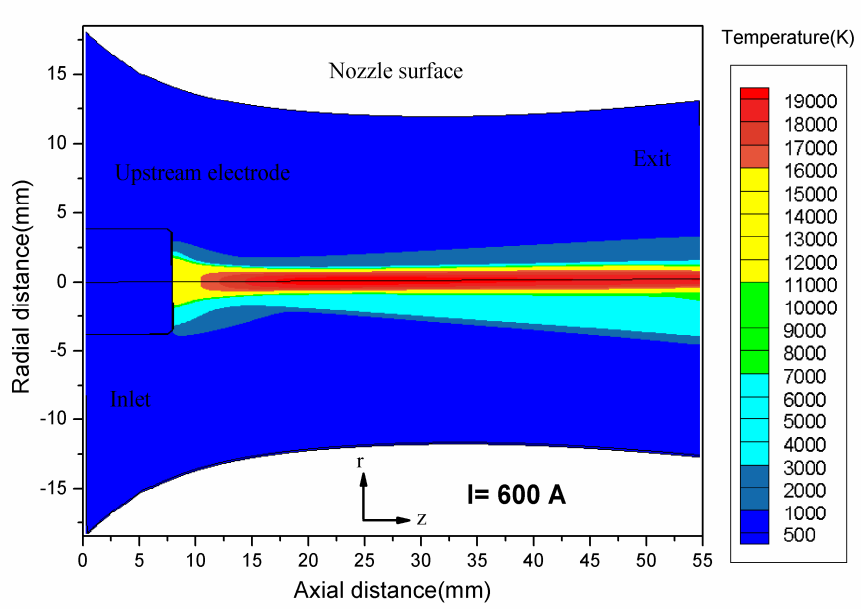

Figure 5.2 Temperature field within the nozzle for the supersonic SF_6 arc with arc current 600 A: upper half: heavy-species temperature; low half: electron temperature.

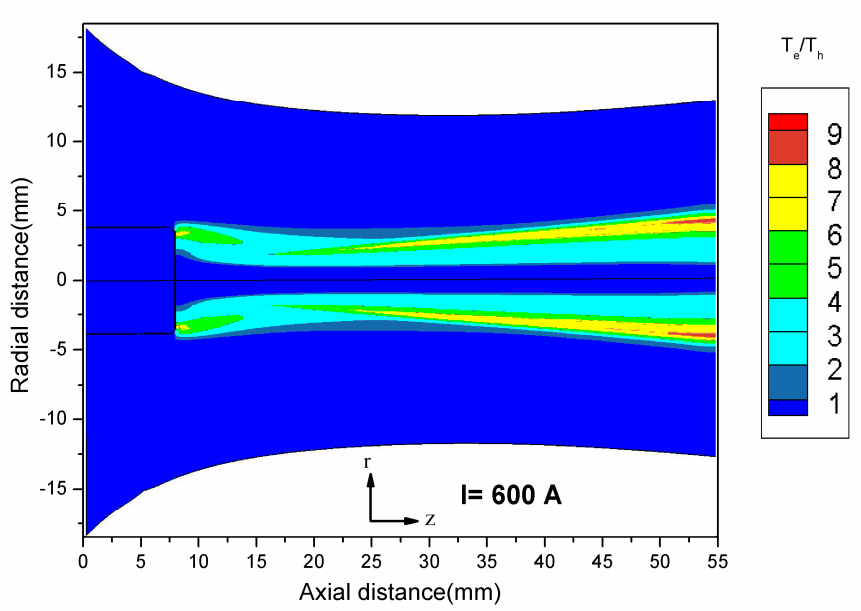

Figure 5.3 Distribution of the non-equilibrium degree within the nozzle for the supersonic SF_6 arc with arc current 600 A.

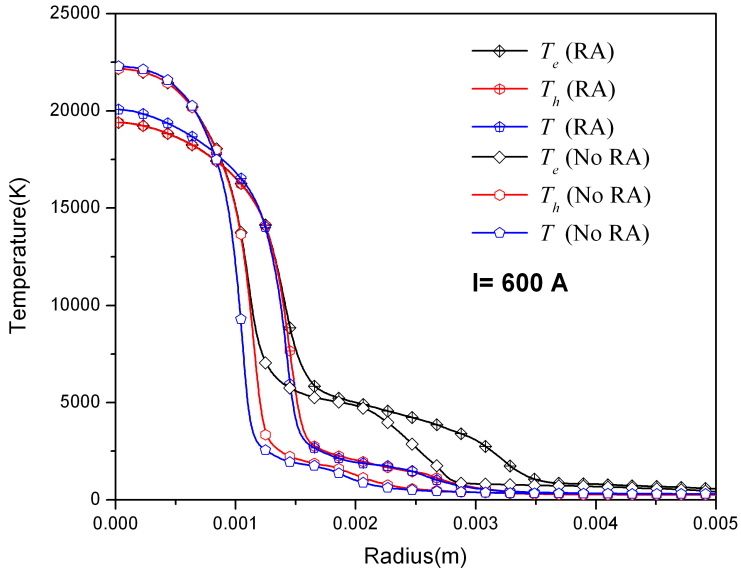

Figure 5.4 Radial temperature profiles of the supersonic SF_6 arc at the nozzle throat (z = 0.033 m) for a current of 600 A. Results are given for electron temperatures (T_e) and heavy-species temperatures (T_h)obtained from the two-temperature model, and temperatures obtained from the LTE model (T). Symbol: experimental values from Leseberg and Pietsch [51]-[52]. The terms "RA" and "NO RA" mean the results with and without radiation reabsorption respectively in this figure as well as the following figures.

Fig.5.4 presents a comparison of the computed electron and heavy-species temperature profiles along the radial direction at the nozzle throat with the measured values of Leseberg and Pietsch [51]-[52]. The temperatures predicted assuming LTE are also given. The measured values were obtained using emission spectroscopy, and therefore correspond to electron temperatures. In the central region, our predicted values of electron, heavy-species and LTE temperatures are approximately the same, and agree with the measured values within the experiment uncertainty.

Fig.5.4 also shows the influence of radiative reabsorption in the arc edge region. We find that neglecting the radiation reabsorption leads to higher temperatures in the arc core and a smaller arc radius showing that radiation transport, especially reabsorption, needs to be looked at more carefully since it is a dominant energy transport mechanism for high-pressure, high-temperature arcs. The absorption of radiation by the gas surrounding the plasma heats the gas and may lead to an increase of pressure and arc conducting section inside the circuit breaker and influence the apparatus behaviour.

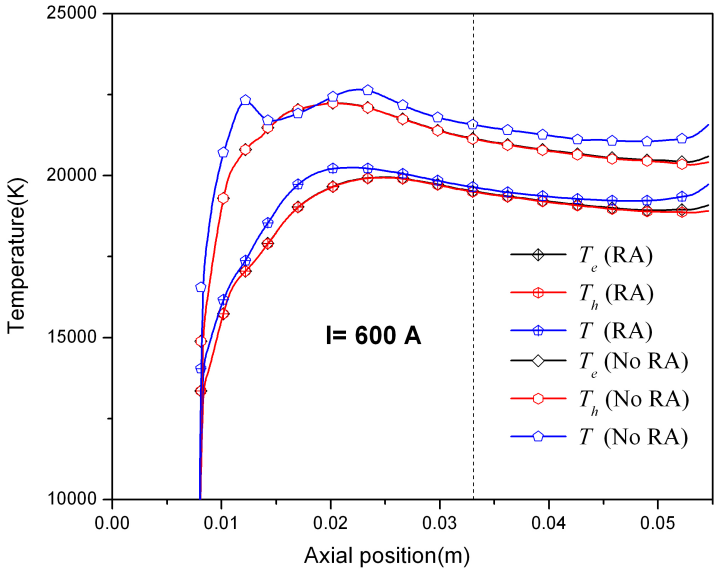

Figure 5.5 Axial temperature profiles for $r = 0$ for a current of 600 A. Results are given for electron and heavy-species temperatures obtained from the two-temperature model, and temperatures obtained from the LTE model. The same symbols are used as figure 5.4. The location of nozzle throat is shown for comparison with figure 5.4.

From the axial variation of electron and heavy-species temperatures along the axis presented in Fig.5.5, we observe that, in the arc core, the LTE temperature is mostly higher than the electron temperature. This is because electron–ion recombination is overestimated in the edge region when LTE is assumed, since reaction rates are effectively infinite in LTE. To compensate for the electron losses, the LTE temperature in the center must be higher than the electron temperature [56]. In contrast, high radiative reabsorption reduces radiation losses and result in improved thermal equilibrium in the arc core; this is reflected in the better agreement between the temperatures obtained assuming LTE and those obtained from the two-temperature model in Figs. 5.4 and 5.5.

It is notable that the electron and heavy-species temperatures are in agreement inside the nozzle along the central axis, with minor deviations occurring only in the low pressure zones adjacent to the exit. The reduced collision frequency at lower pressures plays a role in increasing the degree of temperature non-equilibrium at the nozzle exit. Much larger differences between the electron, heavy-species and LTE temperatures occur off axis, as shown in Fig.5.6.

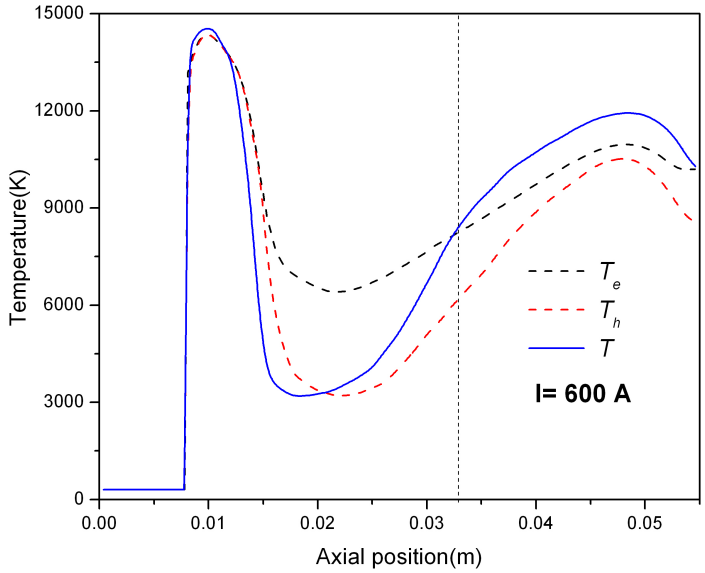

Figure 5.6 Axial variation of electron and heavy-species temperatures at r = 1.553 mm for a current of 600A. The LTE temperature is also shown.

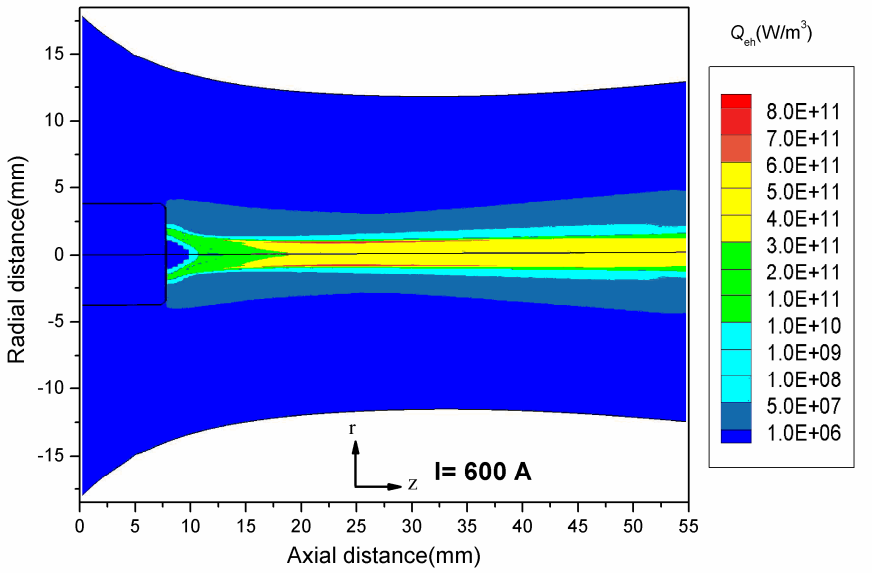

Figure 5.7 Elastic collision energy in the supersonic SF_6 arc with an arc current of 600 A

The electron and heavy-species temperature distributions are influenced by several processes. For the two-temperature model, the electrical energy introduced into the plasma initially heats the electrons. They transfer energy by means of elastic collisions with heavy species, increasing the heavy-species temperature and leading to the emission of line radiation. Meanwhile, gas flow removes the energy through convective heat transfer due to the

temperature gradient. Part of the radiation is reabsorbed in the arc edge by the cold gas. To demonstrate these mechanisms, the electron and heavy-species energy balance is evaluated in more detail. In Fig.5.7, we show the elastic collision energy distribution, which is expected to have a major influence on the heavy-species temperature distribution. It is observed that the elastic collision energy is largest in two regions, the upstream region near z = 20.0 mm and the nozzle exit region.

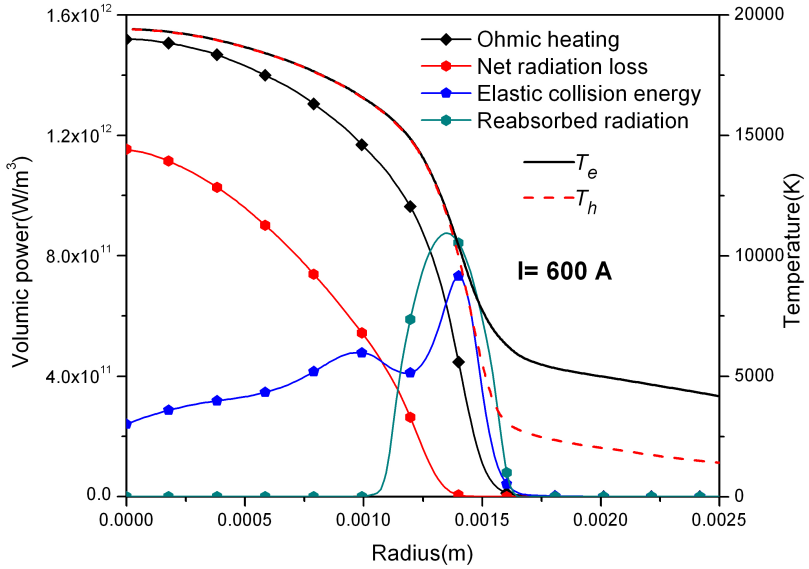

Figure 5.8 Radial profiles at the nozzle throat point (z = 0.033 m) of terms contributing to the electron and heavy-species energy balance in the supersonic SF_6 arc for a current of 600 A. The electron and heavy-species temperatures are also shown for comparison.

Some of the terms contributing to electron and heavy-species energy balance are shown as functions of radius at the nozzle throat point in Fig.5.8. Ohmic heating prevails in the arc core and decreases rapidly away from the arc region. The elastic collision energy exchange, which depends on the electron–heavy-species collision frequency, the electron number density and the difference between electron and heavy-species temperatures increases to a local maximum approximately 1.00 mm away from the axis, and then decreases slightly before reaching a second peak. The first peak can be explained by the fact that, for a given pressure, the collision frequency has a maximum value at a given temperature [57]. The second peak, near the arc edge, can be attributed to the contribution of the increasing temperature difference between electrons and heavy species, which outweighs the influence

of the decreasing electron number density and collision frequency. Outside the arc region, the collision frequency decreases by at least one order of magnitude. This means the exchange processes is ineffective, leading to the deviation from thermal equilibrium. The radiation loss decreases monotonically with radius due to the decreasing temperature. A strong absorption of the emitted energy from the arc central region occurs on the edge of the plasma. This effect is mainly due to the absorption of radiation which correspond to photodissociation and photoionisation of heavy species.

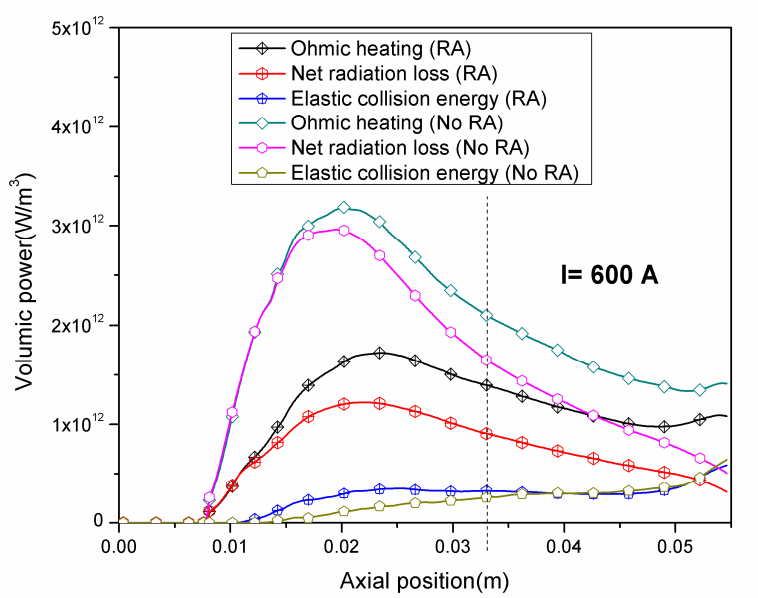

Figure 5.9 Axial variation at $r = 0$ of terms of the electron and heavy-species energy balance for a current of 600 A. Solid line and center symbol: simulation results obtained including radiation reabsorption in the edge region; solid line and open symbol: simulation results by two-temperature model without radiation reabsorption.

The axial variation of different terms of the electron and heavy-species energy balance is presented in Fig.5.9. Significantly different results are obtained with and without consideration of radiation reabsorption near the arc edge. Nevertheless, since radiation loss and Ohmic heating depend strongly on the temperature and pressure, both models present similar trends. The Ohmic heating makes the largest contribution, reaching a maximum of 1.725×10^{12} W m^{-3} and 3.185×10^{12} W m^{-3} respectively for the models with and without radiation reabsorption, at respective axial positions of 23 mm and 20 mm. It then decreases rapidly until a second increase near the exit. The next significant term is net radiation loss,

which reaches a maximum near the same location as the Ohmic heating term. The energy exchange due to elastic collisions between electrons and heavy species has a first peak at the same location as the maximum value of Joule heating when radiation reabsorption is considered, while when radiation reabsorption is neglected, the terms increases monotonically.

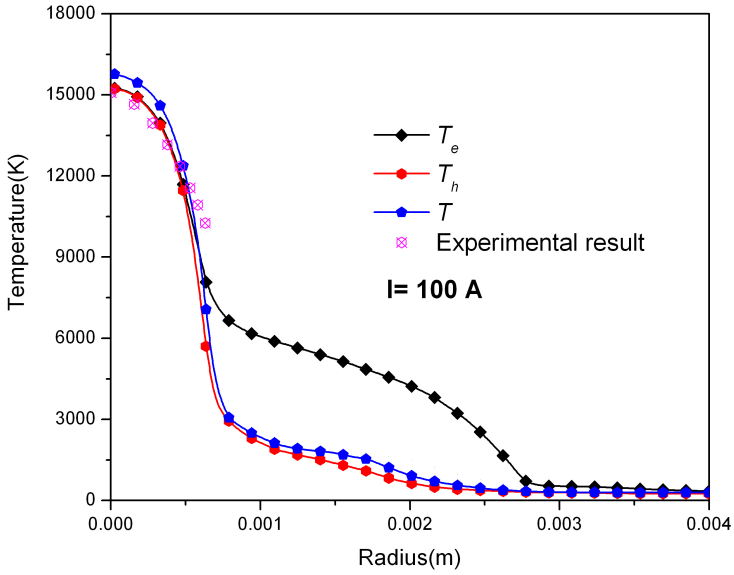

Figure 5.10 Radial temperature profiles at the nozzle throat point (z = 33 mm) for a current of 100 A. The experimental values of Leseberg and Pietsch [52] are presented for comparison.

In order to investigate the effect of the electric current on thermal equilibrium, we also obtained results for a current of 100 A. Fig.5.10 gives the radial temperature profiles as functions of the geometric radius at the nozzle throat point. Unless specially specified, only results with radiation reabsorption are presented and discussed. Our results again agree well with measurements [51]-[52]. There is a larger discrepancy than for 600 A between the heavy-species temperature and the electron temperature predicted by the two-temperature model in the central arc region, suggesting that the discharge tends toward thermal equilibrium as the arc current increases.

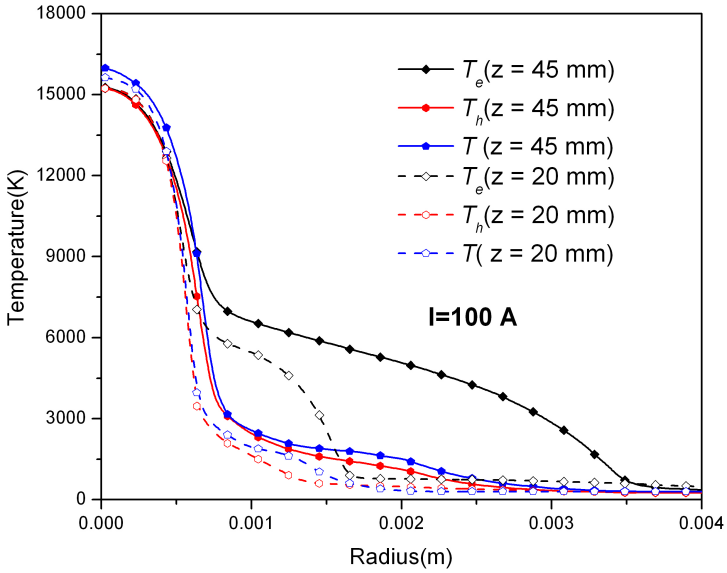

Figure 5.11 Radial temperature profiles at axial positions upstream and downstream of the nozzle throat for a current of 100 A. Solid line and solid symbol: values downstream of the nozzle throat (z = 45 mm); broken line and open symbol: values upstream of the nozzle (z = 20 mm).

Comparing the temperature profiles at downstream and upstream of the nozzle throat shown in Fig.5.11, we can observe that the difference between the heavy-species and electron temperatures in the downstream region is enlarged than in the upstream region. This is a consequence of the reduced collision frequency at lower pressures, which increases the temperature non-equilibrium.

5.3.2 Transient State Calculations

The discussion of transient SF_6 blast nozzle arcs may be conveniently divided into two phases: before and after current zero. In the first phase, current is ramped down linearly towards zero from an initial steady state at a current of I_0=600A. Unless otherwise specified, pre-current zero results are given for di/dt =-10 A μs^{-1}. The influence of the current damping rate is considered later. The current zero occurs at the time instant of 0 μs. The size of the time step in arc transient simulation is determined in consideration of the characteristic time of the physical process. For the first 40 μs, a step time size of 1 μs is employed and in the current zero period, a shorter time step size of 0.1 μs is taken into account in consideration of the characteristic time of the physical process.

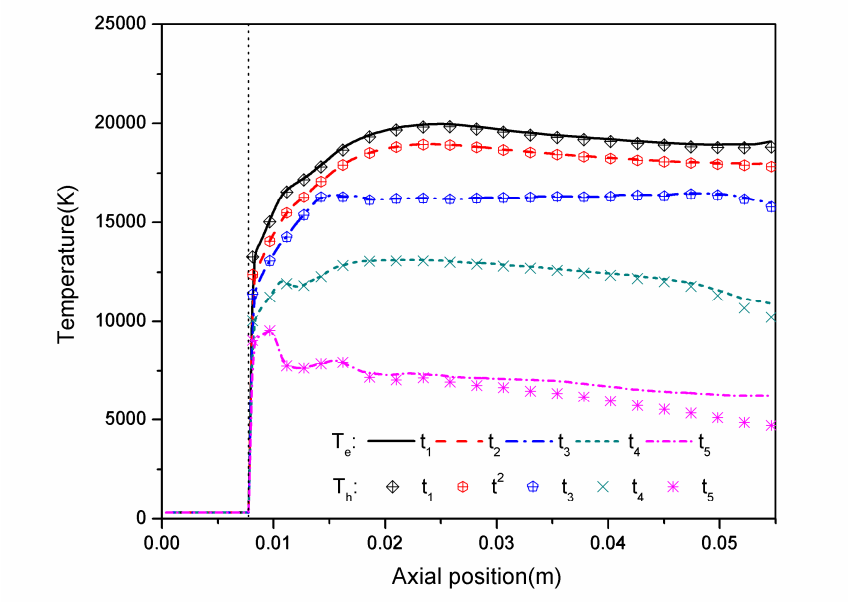
25000
20000
15000
10000
5000
0
Temperature(K)
0.00
0.01
0.02
0.03
0.04
0.05
Axial position(m)
T_e: t_1 t_2 t_3 t_4 t_5
T_h: t_1 t^2 t_3 t_4 t_5

(a)

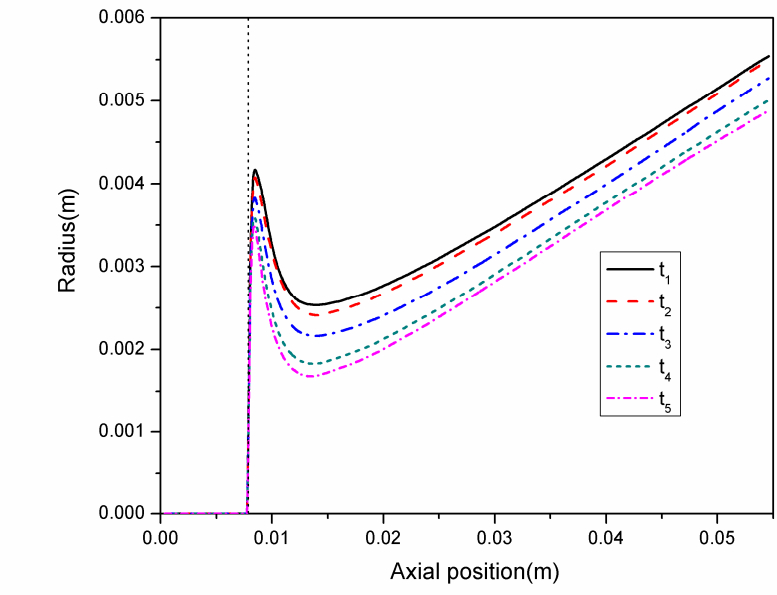
0.006
0.005
0.004
0.003
0.002
0.001
0.000
Radius(m)
0.00
0.01
0.02
0.03
0.04
0.05
Axial position(m)
t_1
t_2
t_3
t_4
t_5

(b)

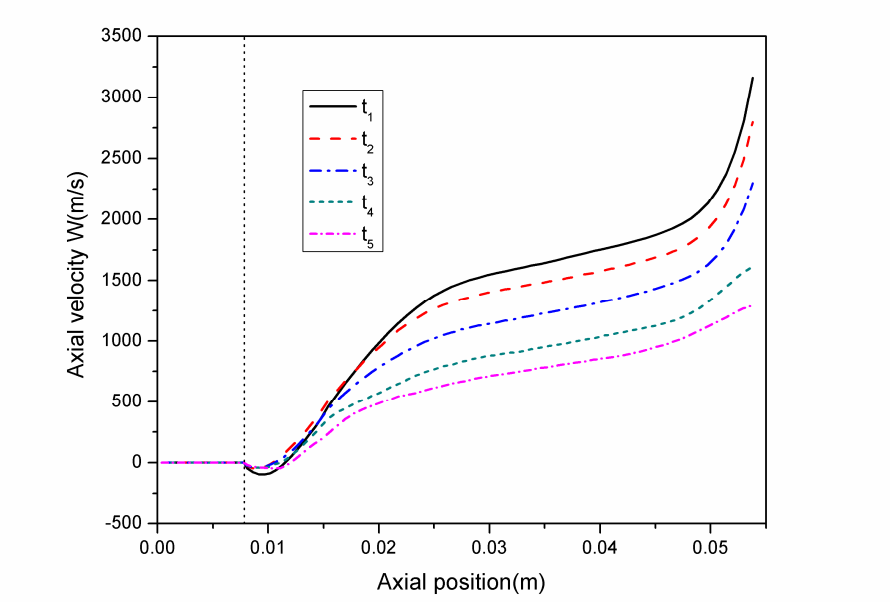
Axial velocity W(m/s)
Axial position(m)
t1
t2
t3
t4
t5

(c)

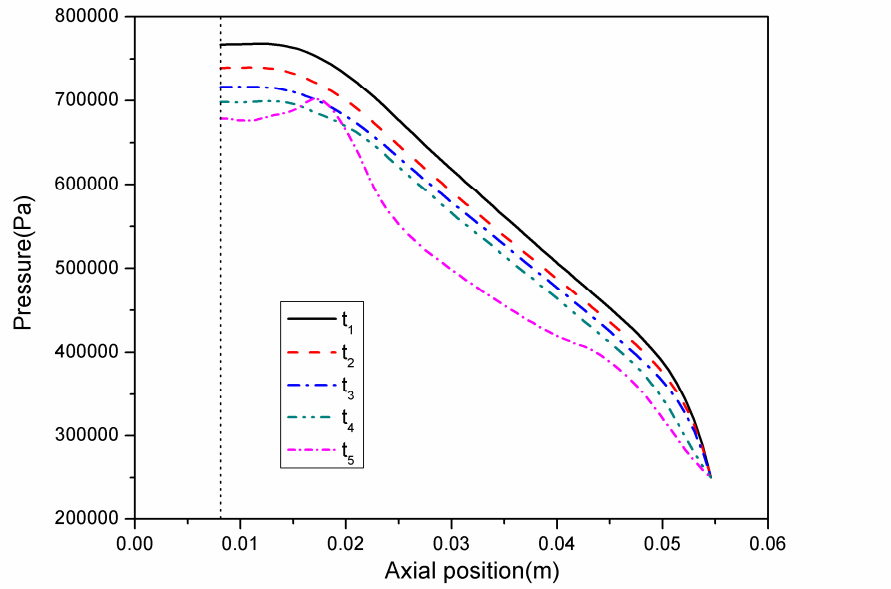
Pressure(Pa)
Axial position(m)
t1
t2
t3
t4
t5

(d)

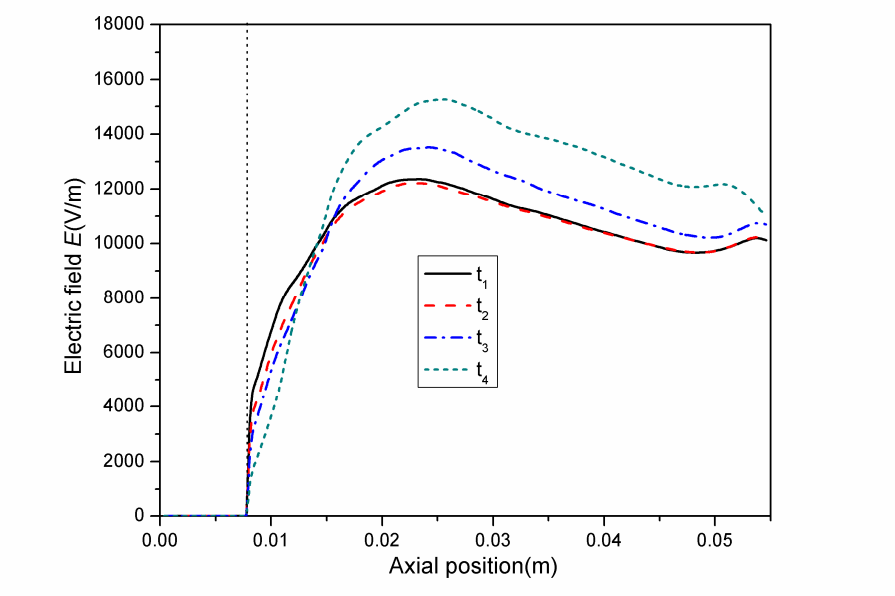

(e)

Figure 5.12 Axial position dependence of (a) temperature at $r = 0$, (b) radial position of $T_e = 4000$ K isotherm, (c) axial velocity at $r = 0$, (d) pressure at $r = 0$, and (e) electrical field at $r = 0$, at 5 time instants before and at current zero: $t_1 = -60\mu s$, $t_2 = -40\mu s$, $t_3 = -20\mu s$, $t_4 = -5\mu s$, $t_5 = 0\mu s$. These time instants respectively correspond to the current level s of 600A, 400A, 200A, 50A and current zero.

The axial distributions of temperature, axial velocity, pressure and electrical field on axis, as well as the radial position of the $T_e = 4000$ K isotherm, are given in Fig.5.12 for five different time instants before and at current zero. The temperature on axis decreases monotonically as the current is ramped down to zero. The rate of temperature decay along the central axis increases as current zero is approached, particularly from 5 μs before current zero, which corresponds to a current of 50 A. From this time, the electron and heavy-species temperature start to deviate from each other, due to the ineffective collisional energy exchange between electrons and heavy species.

It is found that the region near the upstream electrode has a lower temperature decay rate than in the downstream region, where heat transfer is stronger due to the turbulence. The presence of upstream electrode generates an adverse pressure gradient in the radial and axial direction in front of the electrode and leads to a flow circulation as presented in Fig.5.13. Near the edge of this area, there exists a flow separation where the arc and cold gas interaction is relatively weak and the arc column is thus locally broadened. The occurrence of a flow circulation in this upstream region will give a more pronounced influence on the energy

dissipation when current decays to zero, and may have adverse effects on dielectric recovery.

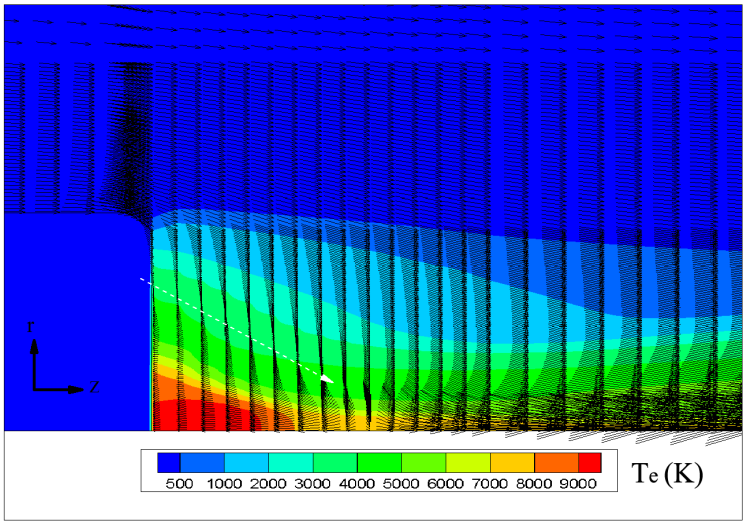

Figure 5.13 A schematic diagram of the flow circulation near the upstream electrode in a supersonic nozzle at current zero, the electron temperature is also presented. The arrow shows the velocity vector with arbitrary units.

As in the case of temperature on axis, the radial position of the $T_e = 4000$ K isotherm decreases rapidly in the final 5 μs before current zero. With the decaying current, the lowest radius of the $T_e = 4000$ K isotherm slightly moves towards upstream from the position $z = 14$ mm, which is well before the nozzle throat.

The flow stagnation point occurs at the tip of the upstream electrode, and its position changes only slightly with time. There is a strong axial acceleration due to the imposed pressure gradient. Even at current zero, the velocity on axis at $z = 55$ mm is about 1000 m s^{-1}. As can be seen from the temporal variation of axial pressure along the central axis, the pressure decreases rapidly near the upstream electrode during the current decay process. Moreover, the electric field near the upstream electrode decreases, which can be attributed to the slowly decaying temperature. However, outside the flow circulation area, the increasing electrical field with decaying current indicates that a voltage extinction peak occurs before current zero. As the temperature decreases, the location of the maximum electric field moves slightly downstream towards the nozzle throat.

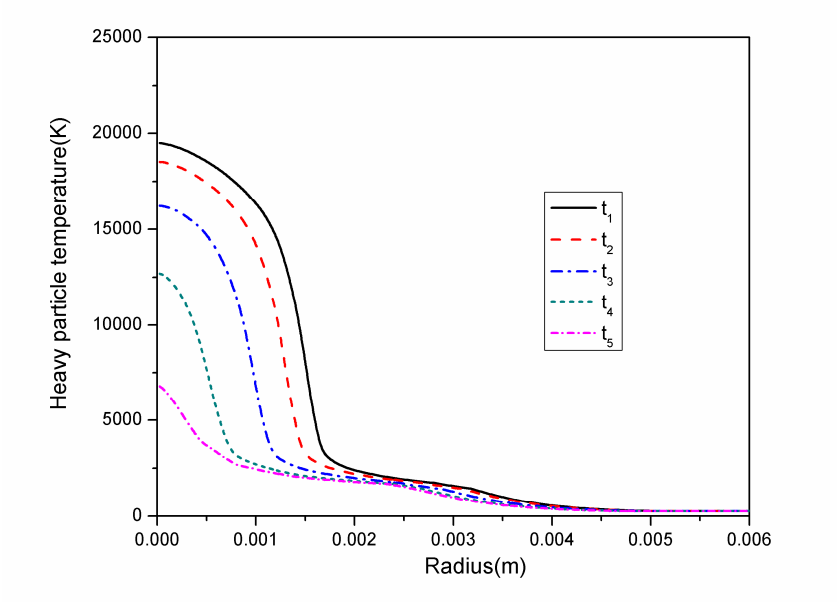

(a)

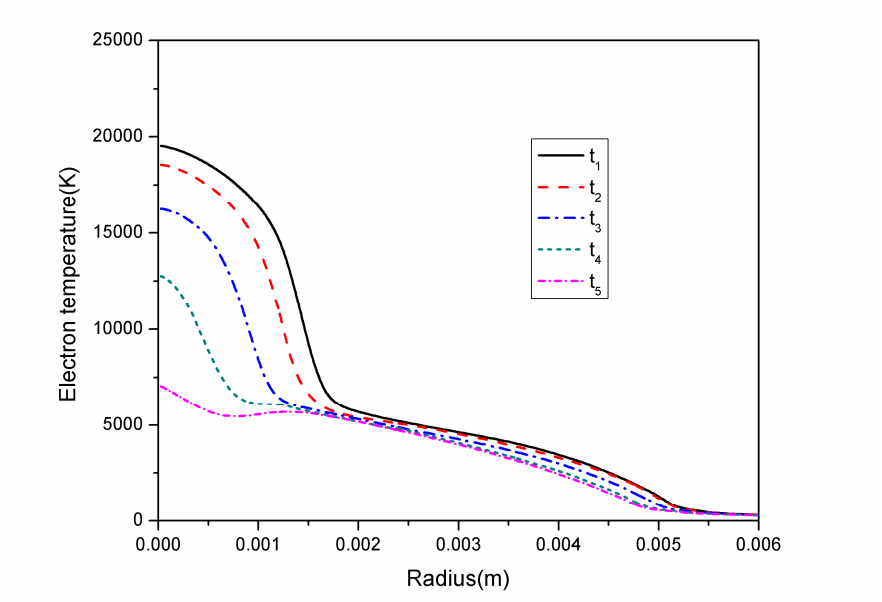

(b)

Figure 5.14 Radial dependence of heavy-species (a) and electron (b) temperature at the nozzle throat (z = 33 mm) at 5 times before and at current zero. t_1 = -60μs, t_2= -40μs, t_3= -20μs, t_4 = -5μs, t_5= 0μs (current zero).

The calculated radial temperature profiles at the nozzle throat given in Fig.5.14. The profiles exhibit characteristics of a turbulent arc. A second off-axis peak of the electron temperature occurs at and just before current zero; this is not found for the heavy-species temperature. The peak can be mainly attributed to the non-monotonic radial variation of the

net energy source term including the Ohmic heating input, the radiation loss along with elastic collision energy exchange between electrons and heavy species along the radial direction. Similar phenomenon was observed in [35] where the electron isotherms are also far less constricted than those of heavy particles with non-monotonic radial variation of the electron temperature appearing mainly beyond the arc core. We can also observe that for temperatures below 5000 K, the electron temperature decreases slowly due to the ineffective energy exchange.

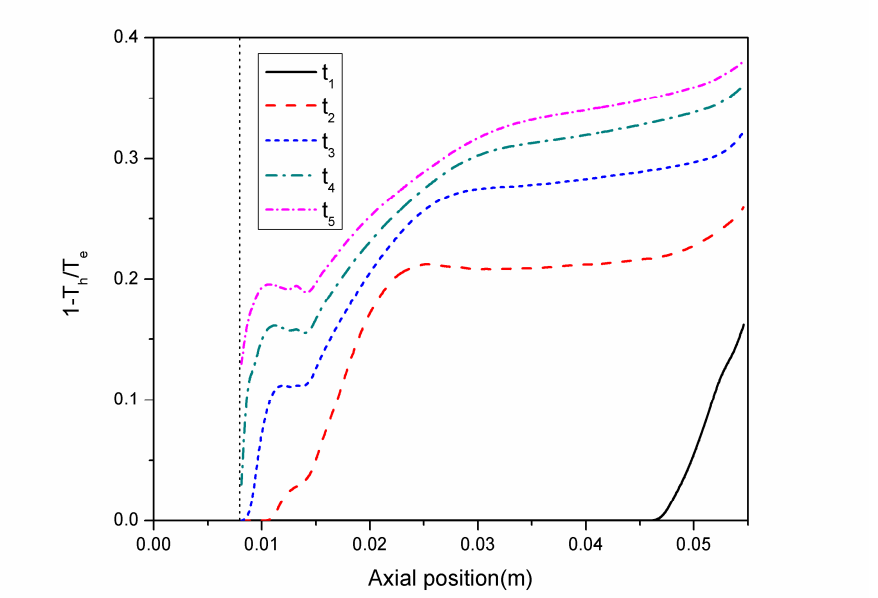

(a)

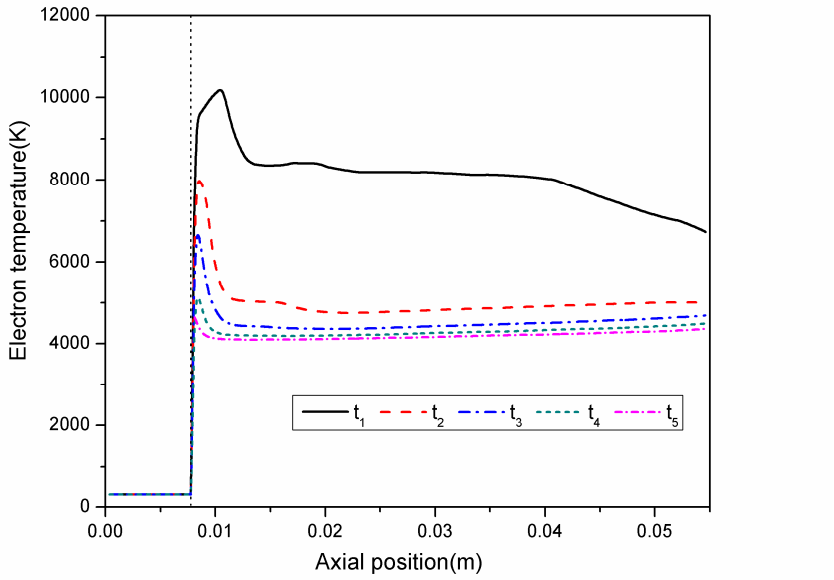

(b)

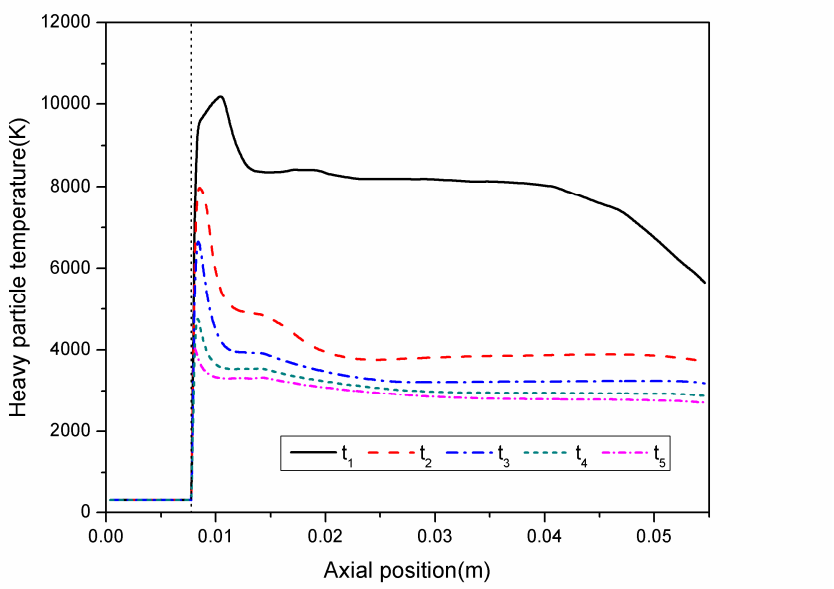

(c)

Figure 5.15 Axial variation of the on-axis values of (a) $(T_e\text{-}T_h)/T_e$, (b) electron temperature, (c) heavy-species temperature at 5 times after current zero. $t_1 = 0$ μs, $t_2 = 5$ μs, $t_3 = 10$ μs, t_4=15 μs, t_5= 20 μs.

Fig.5.15 shows the axial position dependence of the on-axis values of $(T_e - T_h)/T_e$ and electron and heavy-species temperatures during the arc decay; i.e., subsequent to current zero. The decay of electron temperature is most rapid in the first 5 μs, when the temperature along the central axis has a higher value and the residual arc loses its energy by means of radiation and collisional energy exchange, together with the turbulence-enhanced heat transfer. In contrast, the decay of heavy-species temperature is mainly caused by the convective flow. After 5 μs, the elastic collisions play an increasing role in the electron temperature. However, because of the decreasing electron density, the elastic collision frequency decreases with time, leading to an increase in T_e-T_h. As a consequence, departures from thermal equilibrium gradually become larger during the arc extinction after current zero, initially occurring near the exit due to the more rapid temperature decrease, subsequently extending upstream. In the flow circulation region in front of the upstream electrode, the difference between T_e and T_h is relatively smaller than in other regions due to the weak convective flow.

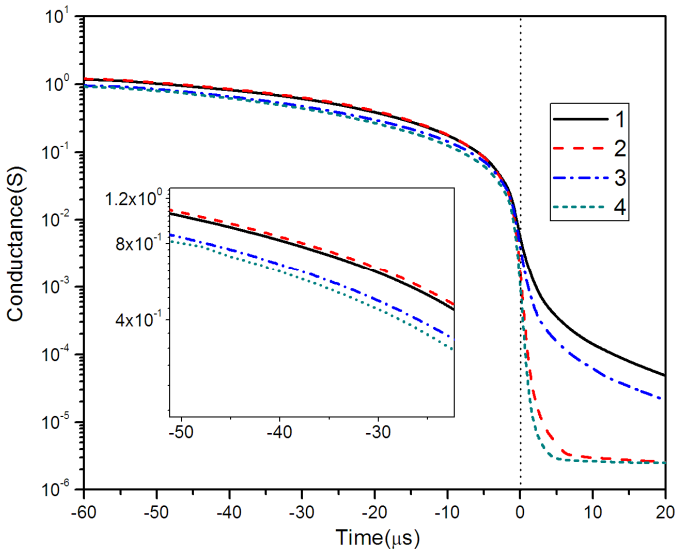

Figure 5.16 Evolution of the discharge channel conductance during the current decay. (1) Two-temperature model with radiation reabsorption, (2) LTE model with radiation reabsorption, (3) Two-temperature model without radiation reabsorption, (4) LTE model without radiation reabsorption.

When interrupting a current, a circuit breaker is effectively required to transform its state from being a conductor to an insulator in the shortest possible time. The gaseous medium between the arcing contacts can be regarded as a nonlinear resistor or conductance with a very short time constant in comparison to the power-frequency sinusoidal current to be interrupted. Hence, the discharge channel conductance, which is often thought as a key parameter reflecting the thermal interruption capability, can be calculated by

$$G = 1/2\pi \int_{z_l}^{z_r} \frac{1}{\int_0^R r\sigma dr} dz \tag{5.20}$$

where σ is the electrical conductivity and R is the arc radius. z_l, z_r are the left and right location of the arc in the axial direction.

In Fig.5.16, the discharge channel conductance obtained using both the two-temperature model and the LTE model with and without the radiation reabsorption near the arc fringe are presented under the free transient-recovery-voltage situation and adopted to study the arc extinction process before and after the current zero. From the start of the

calculation to the time 5 μs before current zero, the conductance obtained from the two-temperature model is slightly lower than that obtained from LTE model and hence a larger arc voltage drop across the electrodes can be obtained. This is because of the higher temperature along the central axis given by LTE model. In the next stage, in which rapid cooling of the discharge region occurs, the two-temperature model shows a relatively slow decay of temperature and large deviation from thermal equilibrium which leads to a smaller arc voltage drop before current zero. As shown in Fig.5.17, the two-temperature model gives a lower heavy-species temperatures and electron temperatures on axis at current zero but a larger arc or discharge cross-section (which is approximately identified as the regions with high electron temperature). Since the electrical conductivity σ increases with the electron density, which is mainly determined by T_e, the conductance is higher for the two-temperature model in the rapid cooling stage. This comparison investigation show that it is important to use a two-temperature model to assess the current zero behaviour of an SF_6 gas blast arc since otherwise the discharge conductance is often underestimated.

For both the LTE and two-temperature models, neglecting radiation reabsorption near the arc edge leads to a faster temperature and hence conductance decay as a result of some energy loss not taken into account in the calculation and this often leads to a overestimation of the current thermal interruption ability

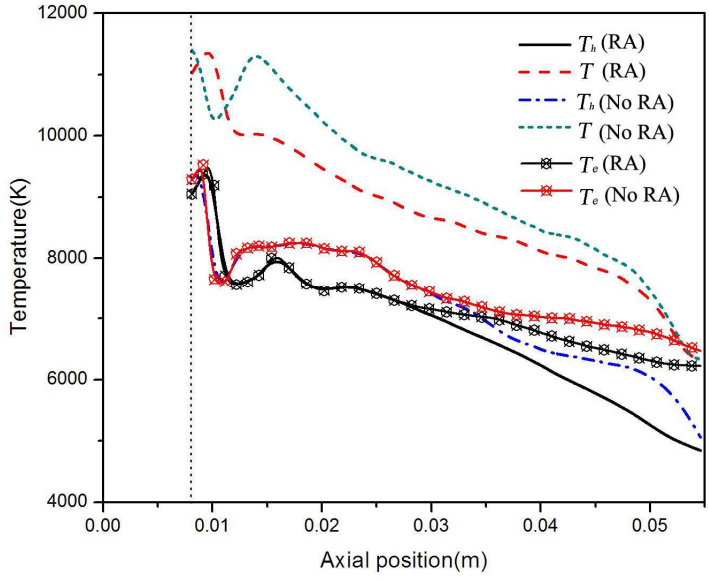

(a)

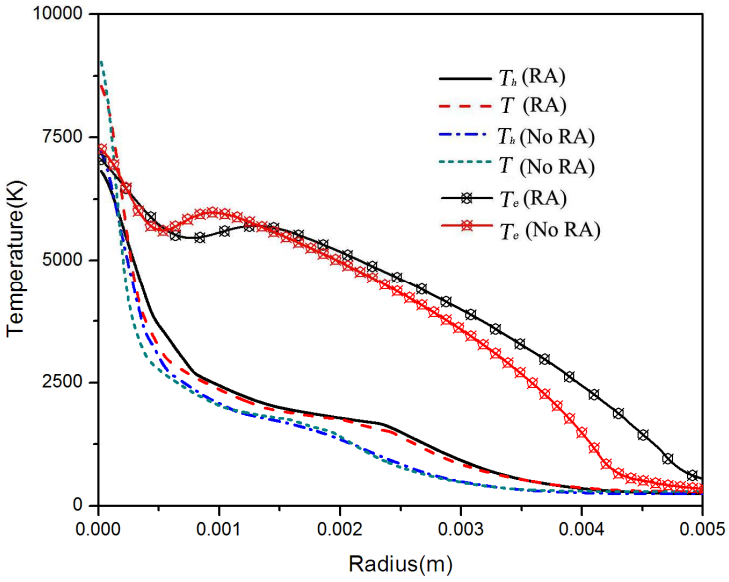

(b)

Figure 5.17 (a) Axial and (b) radial heavy-species temperature profiles and electron temperature profiles, respectively along the axis and at the nozzle throat (z = 33 mm), at current zero. The same symbols as figure 5.4 are used.

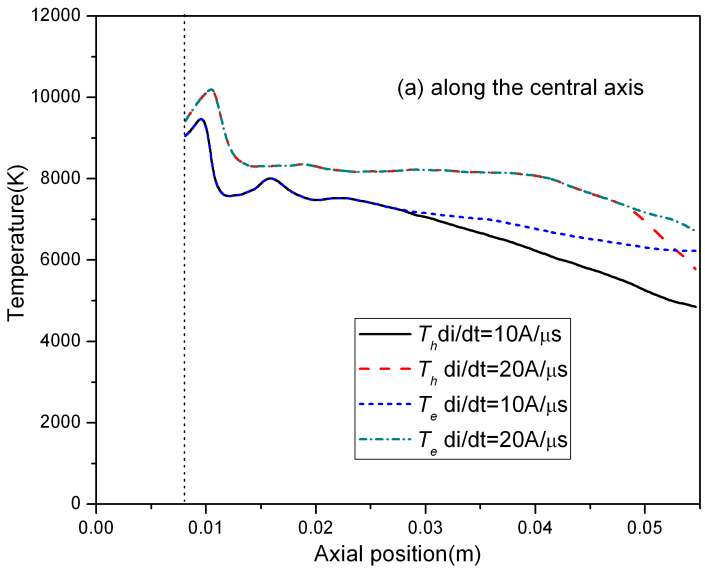

(a)

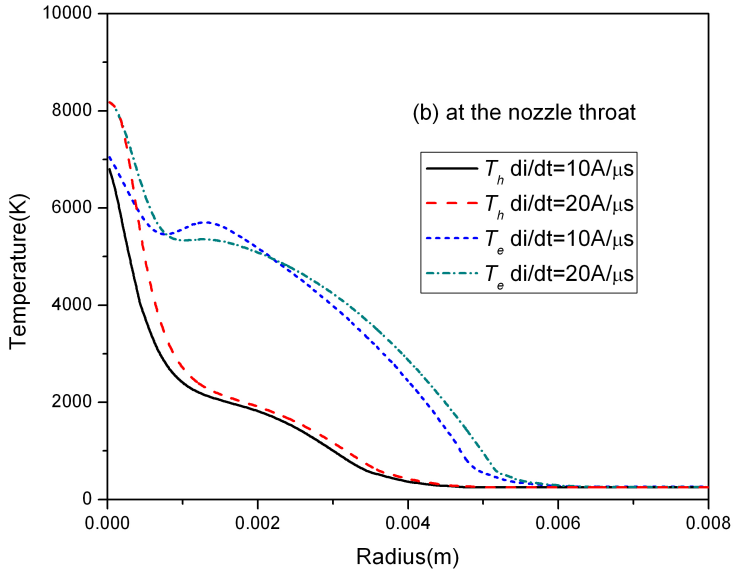

(b)

Figure 5.18 Influence of current damping rate on temperature profile at current zero (a) along the central axis and (b) at the nozzle throat (z = 33 mm).

The influence of the current damping rate on the temperature profile along the central axis and at the nozzle throat at current zero can be seen in Fig.5.18. With a higher current damping rate, the energy generated by the arc cannot be removed effectively and hence lead to a higher temperature value and a smaller departure from thermal equilibrium along the central axis at current zero. For the radial temperature profile, the higher current damping rate leads to a higher value of T_h but possibly lower value of T_e near the arc edge which means a smaller departure from thermal equilibrium. This may be due to the influence of collisional energy exchange between electrons and heavy species. From the results, much stronger cooling actions should be carried out when interrupting a higher value of fault current in order to successfully dissipate the arcing energy in limited interruption time which often means a larger current damping rate.

5.4 Conclusions

In this chapter, a two-temperature model of an SF_6 supersonic arc has been developed, taking departures from thermal equilibrium into account. The main conclusions of this work are summarized as follows:

(1) The reabsorption of arc radiation by cold gas in the arc fringes is an important effect. A modified NEC radiation model that allows for this to be taken into account in a two-temperature model has been developed. The predicted gas temperatures under steady-state conditions show good agreement with experimental values.

(2) One of the originality of the chapter concerns the treatment of cases at high current. For steady-state conditions, differences between the electron and heavy-species temperatures mainly occur near the arc fringe region, where the gas temperature is below 12000 K. The degree of thermal non-equilibrium is largest in the cold boundary layer, and increases as the flow progresses downstream as a result of a reduced collision frequency between electrons and heavy species with decreasing pressure.

(3) As the current decreases, departures from thermal equilibrium become larger, and therefore the differences in the physical quantities obtained from the two-temperature model and an LTE model increase.

(4) The energy exchange mechanism between electrons and heavy species, which links the electron and heavy-species energy equations, has been quantitatively analyzed in terms of the contributions from collision frequency and the difference between electron and heavy-species temperatures. This has allowed, for example, the double peak in the energy exchange as a function of radius to be explained.

(5) For the arc decay phase, the two-temperature model gives a lower cooling rate than the LTE model, and hence a higher conductance of the discharge passage at current zero. Similarly, it is noted that below the value of T_e = 5000 K, the electron temperature decreases slowly comparing with that of heavy species. These conclusions were validated in previous investigation by Gonzalez et al [35] who firstly carried out the investigation on departure from equilibrium on arc decaying behaviour as pioneers. Departures from thermal equilibrium gradually increase during arc extinction, occurring firstly near the exit due to the more rapid cooling in this region, and subsequently spreading upstream and increasing, mainly because of the collisional energy exchange between electrons and heavy species. The occurrence of flow circulation in the region near the electrode decreases the difference between T_e and T_h due to the weak convection and gives more pronounced influence when current decays to zero

and may have adverse effects on dielectric recovery.

(6) When the current damping rate is increased, the arc energy cannot be removed effectively, leading to higher temperatures and smaller departures from thermal equilibrium along the central axis at current zero.

The large departures from thermal equilibrium, particularly at times just before, and after, current zero, demonstrate the importance of using a two-temperature model to accurately predict the current interruption behaviour of SF_6 gas-blast circuit breakers.

5.5 Reference

[1] F. Reichert, J. J. Gonzalez and P. Freton, "Modelling and simulation of radiative energy transfer in high-voltage circuit breakers", J. Phys. D: Appl. Phys., 45, 375201 (2012).

[2] H. Z. Randrianandraina, Y. Cressault and A. Gleizes, "Improvements of radiative transfer calculation for SF_6 thermal plasmas", J. Phys. D: Appl. Phys., 44, 194012 (2011).

[3] C. M. Dixon, J. D. Yan and M.T. C Fang, "A comparison of three radiation models for the calculation of nozzle arcs", J. Phys. D: Appl. Phys., 37, 3309 (2004).

[4] V. Aubrecht and J. J. Lowke, "Calculation of radiation transfer in SF_6 plasmas using the method of partial characteristics", J. Phys. D: Appl. Phys., 27, 2066 (1994).

[5] S. D. Eby, J. Y. Trepanier and X. D. Zhang, "Modeling radiative transfer in SF_6 circuit breaker arcs with the P-1 approximation", J. Phys. D: Appl. Phys., 31, 1578 (1998).

[6] A. A. Iordanidis and C. M. Franck, "Self-consistent radiation-based simulation of electric arcs: II. Application to gas circuit breakers", J. Phys. D: Appl. Phys., 41, 135206 (2008).

[7] J. D. Yan, R. E. Blundel and M. T. C. Fang, "A comparative study of turbulent models for SF_6 arcs in supersonic nozzle", J. Phys. D: Appl. Phys., 32, 1401 (1999).

[8] R. Bini, N. T. Basse, and M. Seeger, "Arc induced turbulent mixing in an SF_6 circuit breaker model", J. Phys. D: Appl. Phys., 44, 25203 (2011).

[9] J. J. Gonzalez, P. Freton, F. Reichert and D. Randrianarivao, "Turbulence and magnetic field calculations in high voltage circuit breakers", IEEE Trans. Plasma Sci., 40, 936 (2012).

[10] M. Seeger, L. Niemeyer, T. Christen, M. Schwinne and R. Dommerque, "An integral arc model for ablation controlled arcs based on CFD simulations", J. Phys. D: Appl. Phys., 39, 2180 (2006).

[11] R. Kozakov, M. Kettlitz, K. Weltmann, A. Steffens and C. M. Franck, "Temperature profiles of an ablation controlled arc in PTFE: I. Spectroscopic measurement", J. Phys. D: Appl. Phys., 40, 2499 (2007).

[12] H. Schneidenbach, D. Uhrlandt, St. Franke and M. Seeger, "Temperature profiles of an ablation controlled arc in PTFE: II. Simulation of side-on radiances", J. Phys. D: Appl. Phys., 40, 7402 (2007).

[13] J. L. Zhang, J. D. Yan, A.B. Murphy, W. Hall and M. T. C. Fang , "Computational investigation of arc behaviour in an auto-expansion circuit breaker contaminated by

ablated nozzle vapor IEEE", Trans. Plasma Sci., 2 ,706 (2002).

[14] K. C. Paul, T. Sakuta, T. Takashima and M. Ishikawa, "The dynamic behaviour of wall-stabilized arcs contaminated by Cu and PTFE vapours", J. Phys. D: Appl. Phys., 30, 103 (1997).

[15] D. Eichhoff, A. Kurz, R. Kozakov, G. Gött, D. Uhrlandt and A. Schnettler, "Study of an ablation-dominated arc in a model circuit breaker", J. Phys. D: Appl. Phys, 45, 305204 (2012).

[16] V. K. Liau, B. Y. Lee, K. D. Song and K. Y. Park, "The influence of contacts erosion on the SF_6 arc ", J. Phys. D: Appl. Phys., 39, 2114 (2006).

[17] J. L. Zhang, J. D. Yan, and M. T. C. Fang, "Electrode Evaporation and Its Effects on Thermal Arc Behaviour", IEEE Trans. Plasma Sci., 3, 1352 (2004).

[18] R. E. Blundel, M. T. C. Fang and A. Vourdas, "Stability of a DC SF_6 arc in an axially accelerating flow", IEEE Trans. Plasma Sci., 25, 852 (1996).

[19] R. E. Blundel and M. T. C. Fang, "The similarity and scaling of radiating arcs burning in a turbulent, axially accelerating gas flow", J. Phys. D: Appl. Phys., 30, 628 (1997).

[20] R. E. Blundel and M. T. C. Fang, "A simplified turbulent arc model for the current-zero period of SF_6 gas-blast circuit-breaker", J. Phys. D: Appl. Phys., 31, 561 (1998).

[21] M. T. C. Fang and Q. Zhuang, "Current zero behaviour of an SF_6, gas blast arc. Part I: laminar flow", J. Phys. D: Appl. Phys., 25, 1197 (1992).

[22] M. T. C. Fang, Q. Zhuang, and X. J. Guo, "Current zero behaviour of an SF_6, gas blast arc. Part II: turbulent flow", J. Phys. D: Appl. Phys., 27, 74 (1994).

[23] R. E. Blundell and M. T. C. Fang, "A simplified turbulent arc model for the current-zero period of a SF_6 gas-blast circuit-breaker", J. Phys. D: Appl. Phys., 31, 561 (1998).

[24] K. D. Song, B. Y. Lee and K.Y. Park, "Analysis of thermal recovery for SF_6 gas-blast arc within Laval nozzle", Japan. J. Appl. Phys., 42, 7073 (2003).

[25] J. B. Belhaouari, J. J. Gonzalez and A. Gleizes, "Simulation of a decaying arc plasma: hydrodynamic and kinetic coupling study", J. Phys. D: Appl. Phys., 31, 1219 (1998).

[26] L. T. Isaac, J. W. Spencer, J. Humphries, G. R. Jones and W. Hall, "Optical-fibre-based investigations of contact travel, gas pressure and particle concentration in SF_6 puffer circuit breakers", IEEE Trans. Plasma Sci., 5, 453 (1999).

[27] Y. Tanaka, Y. Yokomizu, T. Matsumura and Y. Kito, "Transient behaviour of axial temperature distribution in post-arc channel after current zero around nozzle throat in

flat-type SF_6 gas-blast quenching chamber", J. Phys. D: Appl. Phys., 28, 2095 (1995).

[28] Y. Tanaka, Y. Yokomizu, T. Matsumura and Y. Kito, "Transient distribution of metallic vapour concentration in a post-arc channel after current zero along the nozzle axis in a flat-type SF_6 gas-blast quenching chamber", J. Phys. D: Appl. Phys., 29, 1540 (1996).

[29] Y. Tanaka, Y. Yokomizu, T. Matsumura and Y. Kito, "The opening process of thermal plasma contacts in a post-arc channel after current zero in a flat-type gas-blast quenching chamber", J. Phys. D: Appl. Phys., 30, 407 (1998).

[30] D. R. Airey, P. H. Richards, and J. D. Swift, "Time-resolved radial temperature profiles for 10 kA SF_6 arcs", J. Phys. D: Appl. Phys., 8, 1982 (1975).

[31] W. Hermann, U. Kogelschatz, L. Niemeyer, K. Ragaller, and E. Schade, "Investigation on the physical phenomena around current zero in HV gas circuit breakers", IEEE Trans. Power Appl. Syst., 95, 1165 (1976).

[32] D. Leseberg and G. Pietsch, "Optical investigations on a SF_6 switching arc inside a glass nozzle", 7th Int. Conf. on Gas Discharges and Their Applications, pp 9-12 (1982).

[33] S. Vacquié, A. Gleizes, and H. Kafrouni, "Measurement of electron density in a SF_6 arc plasma", J. Phys. D: Appl. Phys., 18, 2193 (1985).

[34] J. P. Trelles, C. Chazelas, A. Vardelle, and J. V. R. Heberlein, "Arc Plasma Torch Modeling ", Journal of Thermal Spray Technology, 18, 728 (2009).

[35] R. Girard, J. J. Gonzalez and A. Gleizes, "Modelling of a two-temperature SF_6 arc plasma during extinction", J. Phys. D: Appl. Phys., 32, 1229 (1999).

[36] J. J. Gonzalez, R. Girard and A. Gleizes, "Decay and post-arc phases of a SF_6 arc plasma: a thermal and chemical non-equilibrium model', J. Phys. D: Appl. Phys., 33, 2759 (2000).

[37] V. Colombo, E. Ghedini, M. Boselli, P. Sanibondi and A. Concetti, "3D static and time-dependent modelling of a dc transferred arc twin torch system', J. Phys. D: Appl. Phys., 44, 194005 (2011).

[38] Hsu K C and Pfender E 1983 Two temperature modeling of the free burning high intensity arc J. Appl. Phys. 54 4359-66.

[39] J. Haidar, "Non-equilibrium modelling of transferred arcs", J. Phys. D: Appl. Phys., 32, 263 (1999).

[40] M. Bouaziz, G. Raynal, M. Razafinimanana and A. Gleizes, "An experimental and theoretical study of the absorption of SF_6 arc plasma radiation by cold SF_6 gas", J. Phys. D: Appl. Phys., 29, 2885 (1996).

[41] R. W. Liebermann and J. J. Lowke, “Radiation emission coefficients for sulphur hexafluoride arc plasmas”, Journal of Quantitative Spectroscopy and Radiative Transfer, 17, 253 (1976).

[42] J. F. Zhang, M. T. C. Fang and D. B. Newland, “Theoretical investigation of a 2 kA arc in a supersonic nozzle”, J. Phys. D: Appl. Phys., 20, 368 (1987).

[43] P. Kovitya and J. J. Lowke, “Two-dimensional analysis of free-burning arcs in argon”, J. Phys. D: Appl. Phys., 18, 53 (1985).

[44] M. Mitchner and C. H. Kruger, Partially Ionized Gases, New York: Wiley, 1973.

[45] A. Gleizes, J. J. Gonzalez and P. Freton, “Thermal plasma modelling”, J. Phys. D: Appl. Phys., 38, R153 (2005).

[46] M. Baeva and D. Uhrlandt, “Non-equilibrium simulation of the spatial and temporal behaviour of a magnetically rotating arc in argon Plasma”, Sources Sci. Technol., 20, 035008 (2011).

[47] A. Gleizes, B. Chervy, and J. J. Gonzales, “Calculation of a two-temperature plasma composition: bases and application to SF6”, J. Phys. D: Appl. Phys. 32, 2060 (1999).

[48] W. Z. Wang, M. Z. Rong, A. B. Murphy, Y. Wu, J. W. Spencer, J. D. Yan and M. T. C. Fang “Thermophysical properties of carbon–argon and carbon–helium plasmas”, J. Phys. D: Appl. Phys., 44, 355207 (2011).

[49] W. Z. Wang, M. Z. Rong, J. D. Yan, A. B. Murphy, and J. W. Spencer, “Thermophysical properties of nitrogen plasmas under thermal equilibrium and non-equilibrium conditions”, Phys. Plasmas, 18, 113502 (2011).

[50] M. C. M. van de Sanden, P. P. J. M Schram, A. G. Peeters, J. A. M.van der Mullen, and G. M. W. Kroesen, “Thermodynamic generalization of the Saha equation for a two-temperature plasma”, Phys. Rev. A 40, 5273 (1989).

[51] D. Leseberg, “Holographische interferometrie und optische spektroskopie an einem SF_6-schaltlichtbogen”, PhD Thesis RWTH Aachen (1982).

[52] D. Leseberg and G. Pietsch, “Interferometrische Unterschungen Von Schaltichtbogen in Stromendem SF_6”, Proc. 4th Int. Symp. On Switching Arc Phenomena (Lodz), pp 236–40 (1981).

[53] J. P. Trelles, J. V. R. Heberlein, and E. Pfender, “Non-equilibrium modelling of arc plasma torches”, J. Phys. D: Appl. Phys., 40, 5937 (2007).

[54] PHOENICS is commercially available from CHAM Ltd., Bakery House, 40 High Street,

Wimbledon Village, London, SW19 5AU, UK

[55] S. V. Patankar, “Numerical Heat Transfer and Fluid Flow”, Hemisphere, New York, 1984.

[56] K. Charraday, G. Zissis, and M. Aubes, “Two-temperature, two-dimensional fluid modelling of mercury plasma in high-pressure lamps”, J. Phys. D: Appl. Phys., 29, 2432 (1996).

[57] S. Ghorui, J. V. R. Heberlein and E. Pfender, “Non-equilibrium modelling of an oxygen-plasma cutting torch”, J. Phys. D: Appl. Phys., 40, 1966 (2007).

CHAPTER 6 KINETIC ANALYSIS OF DECAYING BEHAVIOUR AND CRITICAL DIELECTRIC STRENGTH IN HOT SF_6 DURING CURRENT ZERO PERIOD

6.1 Introduction

For the understanding of the arc behaviour, we often assume they are in the local thermodynamic equilibrium (LTE) state. This assumption is frequently valid in high temperature and high pressure regions of the arcs in a steady/transient state. Actually, the conventional LTE mode predicts the mass, momentum and energy transfer in bulks of arcs. However, more detailed understanding of the distributions of chemical species is necessary for advanced investigation of the arc extinction phenomena during the fault current interruption. In the medium and low temperature region of arcs, which are always present around the high-temperature region, this LTE assumption cannot always be established. It is necessary to account for non-equilibrium effects in this case.

- **Thermally Non-equilibrium Effects**

The electron temperature becomes close to the heavy species temperature if the electron sufficiently transfers its kinetic energy to the heavy species through elastic collision compared to the energy gained by the external electric field. Otherwise, a thermal non-equilibrium condition will be obtained. Generally, the relation between electron temperature and heavy species temperature can be estimated from the simplest equation of a spatially zero-dimensional electron energy conservation.

$$\frac{T_e - T_h}{T_e} = \frac{3\pi}{32}\left(\frac{eE\lambda_e}{1.5kT_e}\right)\frac{m_h}{m_e} \tag{6.1}$$

where e denotes the electronic charge, m_e signifies the electron mass, m_h is the mass of heavy species, λ_e represents the mean free path of the electrons, k means the Boltzmann's constant, E stands for the magnitude of the electric field. According to Eq. (6.1), thermal

equilibrium needs much less electron energy gain $eE\lambda_e$ by an electric field than the thermal energy $1.5kT_e$ of electrons.

- **Chemically Non-equilibrium Effects**

In arcs and thermal plasmas, the species composition depends strongly on its temperature, which is a result of the energy balance between the electrical energy dissipated and the heat losses that occur mainly at the fringes of the plasma. In such a complex mixture, many chemical reactions including dissociation, ionization, recombination and attachment takes place and any reaction requires a certain finite time to reach its chemical equilibrium because the rate coefficients of reactions are also finite. A dynamic equilibrium can be reached when the relaxation time for any reaction is much shorter than the characteristic time of convection and diffusion on the particle composition as well as the transient time of the states.

- **Non-Maxwellian Energy Distribution Function**

The electron energy distribution function (EEDF) cannot be Maxwellian if the electron-electron relaxation time is much longer than the electron acceleration time by an external electric field, Or if the vibrational and rotational excitation cross section is comparable with the momentum transfer cross section by the electron impact. In such cases, the Boltzmann equation should be solved considering such cross sections with an applied electric field. This situation appears in prediction of arc re-ignition phenomena in a circuit breaker.

- **Non-Boltzmann Distribution for a Population of Excited Particles**

In discharges with either high electron density or high gas pressure, it is often believed that an equilibrium Boltzmann distribution among excited particles will be reached due to the presence of strong collisional processes. However, the population of excited particles does not follow the Boltzmann distribution if the population is more influenced by processes such as the radiative de-excitation than by collisional excitation and de-excitation. This concept is important particularly for investigating a physical sate in thermal plasmas from spectroscopic observation results.

In order to interrupt a fault current successfully, a circuit-breaker needs to pass two stages. The first is known as the thermal recovery during which the arc temperature is cooled down rapidly in a few microseconds around an ac current zero. Thermal recovery is determined by energy balance, which determines the arc temperature. The second stage is known as the dielectric recovery which is concerned with the recovery of the dielectric strength of a hot gas between two electrodes left behind by the thermally recovered arc. Dielectric recovery depends on the production and loss of charge particle species.

A thermally non-equilibrium state which is closely connected with the thermal recovery phase appears if the rate of energy transfer between electrons and heavy species is small compared to the energy gain from the electric field. This phenomenon often occurs in the surrounding region of arcs or the current damping process in current-zero period where the electron density is low; then the collision frequency between electrons and heavy species is therefore extremely low, whereas the electric field strength is high. For this situation, the electrons and heavy species have different temperatures determined by separate energy conservation equation. Investigation into the influence of thermally non-equilibrium generally contains the assumption that the arcs are under chemically equilibrium condition. So the species composition and relevant thermophysical properties required by the two-temperature modelling of arc behaviour are computed in advance and tabulated as a function of electron temperature, heavy specie temperature and pressure. However, it is possible that the departure from chemically equilibrium takes place during the arc extinction especially under strong gas blast condition due to the fact that the arc has cooled down to temperatures between 12000 and 4000 K quite swiftly. Detailed analysis of the extinction problems under chemically non-equilibrium condition is difficult because there are still some problems to treat in the determination of species composition and their properties. Additionally, the kinetics of chemical reactions in the quenching medium of circuit breakers is not an isolated phenomenon and it is connected, for example, with the diffusion, flow and transfer of energy. However, a kinetic analysis of decaying SF_6 applied to a homogeneous medium at constant pressure in which the variation of temperature is taken as being known is available to investigate the influence of chemically non-equilibrium on the electrons disappearance. The present study is based on a kinetic model which enables calculation of the changes occurring in particle densities through solution of the rate equations. A large part of this study is built on the work of

Brand and Kopainsky [1] and A Gleizes et.al [2] and realized by FORTRAN code as an initial stage of post arc study with paying more attention to the post-arc phase. Compared with previous literature [3], more species and chemical reactions are taken into account bringing accurate analysis.

In dielectric recovery phase, the electron energy distribution function influenced by the imposed recovery voltage departs from Maxwellian and dielectric recovery depends on the production and loss of charge particle species. The critical breakdown field in residual plasma is expected to deviate from that at room temperature. Electrical breakdown voltages, transport coefficients, and critical electric field strengths at which the production of electrons is exactly balanced by the loss of electrons have been all investigated by both numerical calculations and experiments for various gases at room temperature. However, the systematic investigation on the dielectric properties of hot gases which has great significances on the prediction of fault current interruption capability of high voltage circuit breaker is relatively rare. For example, Eliasson and Schade have reported experimental results for breakdown voltage of hot SF_6 [4]-[5]. Rothhardt et al. have experimentally measured the temperature dependence of breakdown voltage of air, N_2 and SF_6 up to 3500 K [6]-[8]. Uchii et al. reports on an interesting work on the hot gas behaviour in a circuit breaker. Their breakdown voltage measurements using small gaps in two distinct positions in the circuit breaker (at the output of the exhaust tube and near the tank) lead to an estimation of the gas temperature inside the circuit breaker [9]. Yan et al. [10], Cliteur et al. [11] and Yousfi et al. [12]-[13] attempted a numerical investigation for the prediction of the dielectric strength of hot SF_6 gases based on a two-term or multi-term Boltzmann equation solution. Tanaka investigated the dielectric strengths of hot N_2/O_2 mixtures as well as hot air and the influence of copper vapor in the heavy specie temperature range of 300–3500 K [14]-[15]. However, it is noted that the ablated PTFE vapor generated by the nozzle ablation in high current arcing phase often exists in the gaseous mixture after fault current extinction. Detailed investigations on dielectric properties of SF_6 mixed with the PTFE vapor have scarcely been performed concerning electron energy distribution functions (EEDFs) and ionization and electron attachment coefficients in hot gases. Additionally, for the dielectric strength of SF_6, the physical and chemical processes responsible for the breakdown of a hot gas immediately after the thermal extinction of the arc are expected to be very different from those of SF_6 at room temperature. This is because the composition of such a hot gas is complex and is

dependent on the temperature decay rate during thermal recovery. A careful examination of all relevant ionization, recombination and chemical reactions consistent with the time scale for dielectric breakdown is therefore required. Therefore, the influence of departure from equilibrium on dielectric properties which is always ignored in previous study has been taken into account.

6.2 Kinetic Analysis of a Decaying SF_6 Plasma after Current Zero

6.2.1 Basic Principles of the Model

- **Hypotheses**

We assume the energy distribution function of species is Maxwellian. The plasma is homogenous and its temperature is identical. The pressure remains constant during the arc decay. We assume that during plasma decay no recovery voltage is applied. The reaction rates are then taken to be independent of the electric field. Based on the above-mentioned assumptions, the model of kinetics itself, whose solution is the time dependence of the composition of system S for a given time dependence of temperature T under constant pressure P must conform to reality. At least two conditions must be satisfied for its solution. Firstly, the rate constants of chemical reactions considered must contain correct values (obtained by measuring or computing) which start from the familiar definition of the rate of chemical reaction. At an arbitrary constant temperature $T_{0,}$ the species composition of the system must converge to the equilibrium values.

$$\lim_{t\to\infty} T(t) = T_0$$
$$\lim_{t\to\infty} S(T) = S_{eq}(T_0) \tag{6.2}$$

- **Individual Species**

If there exist K kinds of individual species, system S can be described as

$$S = [\chi_1, \chi_2, \ldots, \chi_K] \tag{6.3}$$

If the species in system S are made up by J kinds of basic elements $[E_1, E_2, \ldots, E_J]$, then every species can be understood as a linear combination

$$\chi_i = \sum_{j=1}^{J} a_{i,j} E_{i,j} \tag{6.4}$$

where $a_{i,j}$ gives the number of atoms of the jth element in the particle of the ith species.

If the number density for the ith species is n_i, the species concentration for the whole system can be described by a non-empty ordered set

$$n = [n_1, n_2, \ldots, n_K] \tag{6.5}$$

If the system S does not exchange substances with the environment, an arbitrary composition n must thus satisfy the mass balance conditions

$$b_j = \sum_{j=1}^{K} a_{j,i} n_j \qquad \text{j=1, 2, } \ldots, K \tag{6.6}$$

where b_j is the total amount of substance of element E_j in the system S.

Over the temperature range studied, compared with previous work, we investigate a more wide variety of 28 species including heavy species S, S^-, S^+, S_2, S_2^+, F_2, F, F^+, F^-, F_2^+, SF, SF^+, SF^-, SF_2, SF_3, SF_4, SF_5, SF_6, SF_2^+, SF_2^-, SF_3^+, SF_3^-, SF_4^+, SF_4^-, SF_5^+, SF_5^-, SF_6^- as well as electrons and hence can bring more accurate analysis.

- **Chemical Reactions**

A global model including 183 chemical reactions from literature are taken into account in present study which is tabulated in table 6.1.

Table 6.1 Chemical reaction scheme

Number	Chemical reactions	References	Number	Chemical reactions	References
1	$F + e \leftrightarrow F^+ + e + e$	[16]	2	$S_2^+ + F^- + F \leftrightarrow SF + SF$	[1]
3	$S + e \leftrightarrow S^+ + e + e$	[1]	4	$F_2^+ + F^- \leftrightarrow F + F + F$	[24]
5	$SF^+ + e \leftrightarrow S + F$	[1]	6	$F^+ + F^- + F \leftrightarrow F + F + F$	[24]
7	$S_2^+ + e \leftrightarrow S + S$	[1]	8	$F^+ + S^- + F \leftrightarrow SF + F$	[1]
9	$F_2^+ + e \leftrightarrow F + F$	[1]	10	$SF_6 + SF_2 \leftrightarrow SF_4 + SF_4$	[22]
11	$F^- + F \leftrightarrow F + e + F$	[1]	12	$SF + SF \leftrightarrow S_2 + F_2$	[21]
13	$S^- + F \leftrightarrow S + e + F$	[1]	14	$F + SF \leftrightarrow F_2 + S$	[22]
15	$F + e + e \leftrightarrow F^- + e$	[1]	16	$F + SF \leftrightarrow SF_2$	[21]
17	$F + e \rightarrow F^- + hv$	[17]	18	$S + F_2 \leftrightarrow SF_2$	[21]
19	$S + e \rightarrow S^- + hv$	[18]	20	$SF + F_2 \leftrightarrow SF_2 + F$	[22]
21	$F^+ + e \rightarrow F + hv$	[19]	22	$SF + SF \leftrightarrow SF_2 + S$	[22]
23	$S^+ + e \rightarrow S + hv$	[1]	24	$S_2 + F_2 \leftrightarrow SF_2 + S$	[22]
25	$F^- + F \leftrightarrow F_2 + e$	[1]	26	$SF_2 + F \leftrightarrow SF_3$	[22]
27	$S^- + F \leftrightarrow SF + e$	[1]	28	$SF_2 + F_2 \leftrightarrow SF_3 + F$	[22]
29	$SF^- + F \leftrightarrow F^- + S + F$	[1]	30	$SF + F_2 \leftrightarrow SF_3$	[22]
31	$SF^- + F \leftrightarrow S^- + F + F$	[1]	32	$SF_2 + SF_2 \leftrightarrow SF_3 + SF$	[22]
33	$S_2^+ + F \leftrightarrow S^+ + S + F$	[1]	34	$F + SF_3 \leftrightarrow SF_4$	[22]
35	$SF^+ + F \leftrightarrow S^+ + F + F$	[1]	36	$SF_2 + F_2 \leftrightarrow SF_2$	[22]
37	$SF^+ + F \leftrightarrow F^+ + S + F$	[20]	38	$SF_3 + SF_3 \leftrightarrow SF_2 + SF_4$	[22]
39	$F_2^+ + F \leftrightarrow F^+ + F + F$	[1]	40	$SF_2 + SF_2 \leftrightarrow S + SF_4$	[22]
41	$F + F + F \leftrightarrow F_2 + F$	[1]	42	$F + F \rightarrow F_2 + hv$	[25]
43	$S + F + F \leftrightarrow SF + F$	[1]	44	$SF_3 + F_2 \leftrightarrow SF_5$	[22]
45	$S + S + F \leftrightarrow S_2 + F$	[1]	46	$SF^+ + SF^- \leftrightarrow SF + SF$	[21]
47	$SF_4 + F_2 \leftrightarrow SF_6$	[21]	48	$F^+ + F^- \leftrightarrow F + F$	[21]
49	$F_2 \leftrightarrow F + F$	[22]	50	$S_2^+ + F \leftrightarrow S + F^+ + S$	[20]
51	$SF_5 + F_2 \leftrightarrow SF_6 + F$	[22]	52	$SF^+ + F^- + F \leftrightarrow SF + F + F$	[26]
53	$S_2 \leftrightarrow S + S$	[22]	54	$S_2^+ + SF^- + F \leftrightarrow SF + S_2 + F$	[26]
55	$SF_4 + F \leftrightarrow SF_3 + F_2$	[22]	56	$SF^+ + F^- + F \leftrightarrow SF + F_2$	[27]
57	$SF_4 + F_2 \leftrightarrow SF_5 + F$	[22]	58	$SF^+ + F^- + F \leftrightarrow SF_2 + F_2$	[22]

59	$SF_4 + F \leftrightarrow SF_5$	[22]	60	$e + SF_6 \leftrightarrow SF_5^+ + F + 2e$	[28]
61	$SF_5 + F \leftrightarrow SF_6$	[22]	62	$e + SF_6 \leftrightarrow SF_4^+ + 2F + 2e$	[28]
63	$SF_5 + SF_5 \leftrightarrow SF_6 + SF_4$	[22]	64	$e + SF_6 \leftrightarrow SF_3^+ + 3F + 2e$	[28]
65	$S^+ + SF \leftrightarrow S_2^+ + F$	[22]	66	$e + SF_6 \leftrightarrow SF_2^+ + F_2 + 2F + 2e$	[28]
67	$S^+ + F_2 \leftrightarrow SF^+ + F$	[22]	68	$e + SF_6 \leftrightarrow SF^+ + 3F + F_2 + 2e$	[28]
69	$F_2 + e \leftrightarrow F + F + e$	[1]	70	$e + SF_6 \leftrightarrow S^+ + F_2 + 4F + 2e$	[28]
71	$S^- + SF \leftrightarrow S + SF^-$	[1]	72	$e + SF_6 \leftrightarrow F^+ + SF_4 + F + 2e$	[28]
73	$S^+ + S_2 \leftrightarrow S_2^+ + S$	[1]	74	$e + SF_5 \leftrightarrow SF_5^+ + 2e$	[28]
75	$S^+ + SF \leftrightarrow SF^+ + S$	[1]	76	$e + SF_5 \leftrightarrow SF_4^+ + F + 2e$	[28]
77	$F^+ + S_2 \leftrightarrow S_2^+ + F$	[19]	78	$e + SF_3 \leftrightarrow SF_3^+ + 2e$	[28]
79	$F^+ + SF \leftrightarrow SF^+ + F$	[23]	80	$e + SF_6 \leftrightarrow SF_6^-$	[28]
81	$F^+ + F_2 \leftrightarrow F_2^+ + F$	[1]	82	$e + SF_6 \leftrightarrow SF_5^- + F$	[28]
83	$S^+ + S^- + F \leftrightarrow S_2 + F$	[1]	84	$e + SF_6 \leftrightarrow SF_4^- + 2F$	[28]
85	$S^+ + F^- + F \leftrightarrow SF + F$	[1]	86	$e + SF_6 \leftrightarrow SF_3^- + 3F$	[28]
87	$S_2^+ + F^- + F \leftrightarrow S_2 + F + F$	[1]	88	$e + SF_6 \leftrightarrow SF_2^- + 4F$	[28]
89	$S_2^+ + F^- + F \leftrightarrow SF + S + F$	[1]	90	$e + SF_6 \leftrightarrow F^- + SF_4 + F$	[28]
91	$S_2^+ + F^- + F \leftrightarrow S_2 + F_2$	[1]	92	$SF_5^+ + SF_6 \leftrightarrow SF_3^+ + SF_6 + F_2$	[28]
93-144	$X^- + M \leftrightarrow X + M + e$ $X = SF_6, SF_5, SF_4, SF_3, SF_2, F$ $M = SF_6, SF_5, SF_4, SF_3, SF_2, SF, S, F, F_2$	[28],[29]	145-183	$X^- + Y^+ \leftrightarrow X + Y$ $X = SF_6, SF_5, SF_4, SF_3, SF_2, F$ $Y = SF_6, SF_5, SF_4, SF_3, SF_2, SF, S, F, F_2$	[28],[29]

In the chemical reactions studied, only a single state is considered for each species, namely the ground state. Moreover, the radiative processes (except those involved in electron-atomic ion recombination) are irreversible. In general, for the reversible chemical reactions, results from the literature were used to determine the cross sections or rate constants of the direct reaction. The rates of reverse reactions were calculated by microreversibility (Detailed Balancing Law). For this law, take the following reversible reaction as an example.

$$A + B \underset{k_r}{\overset{k_d}{\rightleftarrows}} C + D \tag{6.7}$$

The chemical equilibrium can be expressed with Eq. (6.8)

$$k_d n_{A,eq} n_{B,eq} = k_r n_{C,eq} n_{D,eq} \tag{6.8}$$

where $n_{i,eq}$ means the equilibrium concentration of the *i*th species involved in the reaction.

If the forward reaction rate is known, the reversible reaction rate can be determined by relation (6.8) by means of the equilibrium species concentrations which are determined by Guldberg–Waage and Saha laws respectively for dissociation reactions and the ionization and electron-third-body recombination reactions.

Consider elementary reversible (or irreversible) reactions involving *K* chemical species that can be represented in the general form

$$\sum_{k=1}^{K} \nu'_{ki} \chi_k \Leftrightarrow \sum_{k=1}^{K} \nu''_{ki} \chi_k \qquad i = 1, 2, 3.....I \tag{6.9}$$

The stoichiometric coefficients ν_{ki} are integer numbers and χ_k is the chemical symbol for the *k*th species. The superscript ' indicates forward stoichiometric coefficients, while the superscript " indicates reverse stoichiometric coefficients. Normally, an elementary reaction involves only three or four species; hence the ν_{ki} matrix is quite sparse for a large set of reactions. For non-elementary reactions, Eq. (6.9) also represents the reaction expression, but the stoichiometric coefficients may be non-integers.

The production rate ω of the *k*th species can be written as a summation of the rate-of-progress variables for all reactions involving the *k*th species:

$$\omega_k = \sum_{i=1}^{I} \nu_{ki} q_i \qquad k = 1, 2, 3.....K \tag{6.10}$$

where $\nu_{ki} = \nu_{ki}^{ii} - \nu_{ki}^{i}$

The rate of progress variable q_i for the *i*th reaction is given by the difference of the forward and reverse rates as

$$q_i = k_{f_i} \prod_{k=1}^{K} (n_k)^{v'_{ki}} - k_{r_i} \prod_{k=1}^{K} (n_k)^{v''_{ki}} \tag{6.11}$$

where n_k is the concentration of the *k*th species and k_{fi} and k_{ri} are the forward and reverse rate constants of the *i*th reaction.

- **Formulation of the Equations**

$$\frac{\partial Y_i}{\partial t} = \omega_i(t) * M_i / \rho(t) \tag{6.12}$$

where Y_i, ω_i and M_i are the mass fraction, molar production rate and molar weight of specie *i* respectively.

The variation of temperature with time *T*(t) is known beforehand as:

$$\frac{\partial T(t)}{\partial t} = f(t) \tag{6.13}$$

Along with the governing equation describing species creation and disappearance rates, additional three relationships exist to link the particle densities: the perfect gas law, electric neutrality and the stoichiometric equilibrium.

Table 6.2 Conditions of cooling rate

Time range t	Temperature range T(t)	Temperature decaying rate dT/dt
0.0s – 1×10^{-5}s	12000 K – 7000 K	5×10^{8} K/s
1×10^{-5}s – 3×10^{-5}s	7000 K –5000 K	1×10^{8} K/s
3×10^{-5}s – 2.3×10^{-4}s	5000 K – 3000 K	1×10^{7} K/s
2.3×10^{-4}s – 0.02023s	3000 K – 1000 K	1×10^{5} K/s
0.02023s – 70.20523s	1000 K – 298.5 K	10

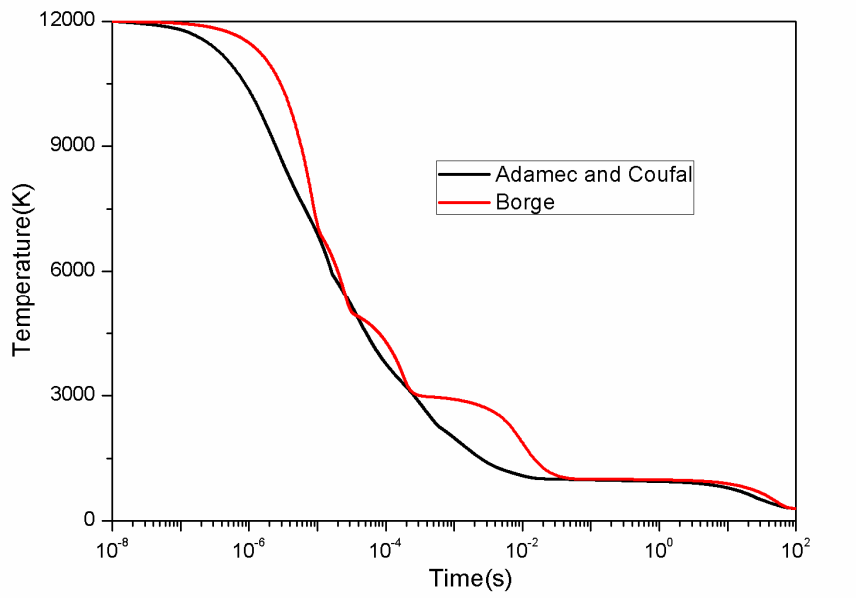

Figure 6.1 Time dependence of temperature variation used in current work

We used more realistic temperature variations in our kinetic model to study the changes in species concentration. The first temperature evolution is that given by a smooth approximation of the dependence given by Borge in [22]. According to [22], T(t) is obtained from theoretical results and is linear between the points given in table 6.2. The second time variation function is given by Adamec and Coufal [3] as described in Eq. (6.13). Both temperature functions are presented in Fig. 6.1.

$$T(t) = T_1(t) + T_2(t) \qquad t \in [0, \infty)$$

$$T_1(t) = \begin{cases} A + B(\dfrac{t_0 - t}{t_0})\alpha & t \in [0, t_0) \\ A & t \in [t_0, \infty) \end{cases}$$

$$T_2(t) = \begin{cases} C(\ln \dfrac{t_0 + dz}{t + dz})^{D/(t+de)} & t \in [0, t_r) \\ G\exp(-Ht) & t \in [t_r, \infty) \end{cases} \tag{6.14}$$

where: A= 298.15 K; B=673 K; C= 0.013690707 K; d_z= 1.145×10−6 s; d_e= 0.07 s; D =0.32980614 s; G= 255.928882543018 K; H =107.15561936024 s^{-1}; t_0 =70 s; t_r= 0.02023 s; α= 2.

6.2.2 Solution Methods

The control equations are solved by LSDOE solver which is available for numerical solution of the initial value problem for stiff and non-stiff systems of ordinary differential equations (ODE's) [30]. LSDOE, the Livermore Solver for Ordinary Differential Equations, is a package of FORTRAN subroutines designed for the numerical solution of the initial value problem for a system of ordinary differential equations. It is particularly well suited for "stiff" differential systems, for which the backward differentiation formula method of orders 1 to 5 is provided. The code includes the Adams-Moulton method of orders 1 to 12; so it can be used for non-stiff problems as well [31]. In addition, the user can easily switch methods to increase computational efficiency for problems that change character. For both methods a variety of corrector iteration techniques is included in the code. Also, to minimize computational work, both the step size and method order are varied dynamically.

6.2.3 Computation Results

6.2.3.1 Plasma Composition

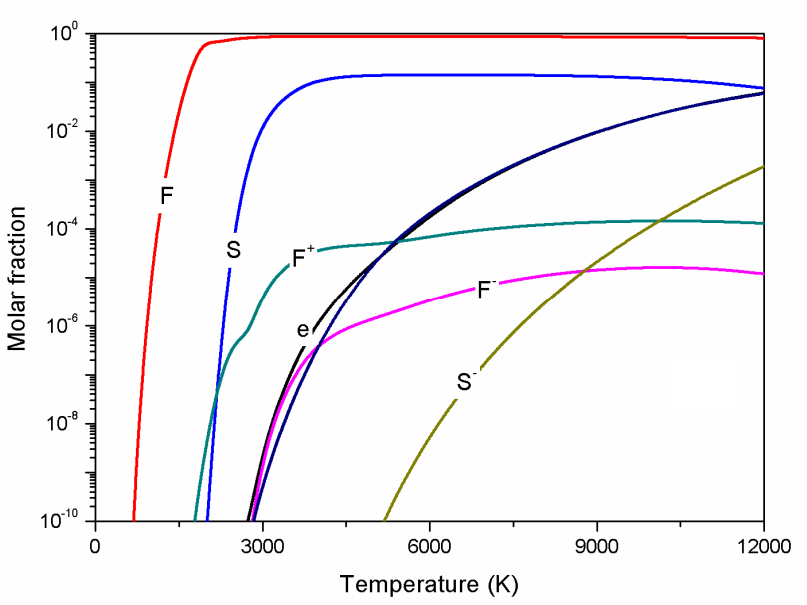

(a)

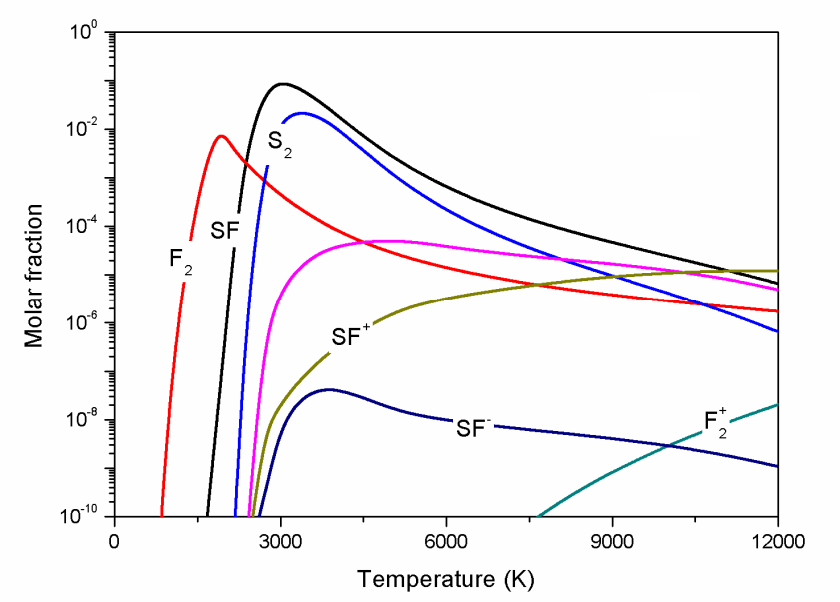

(b)

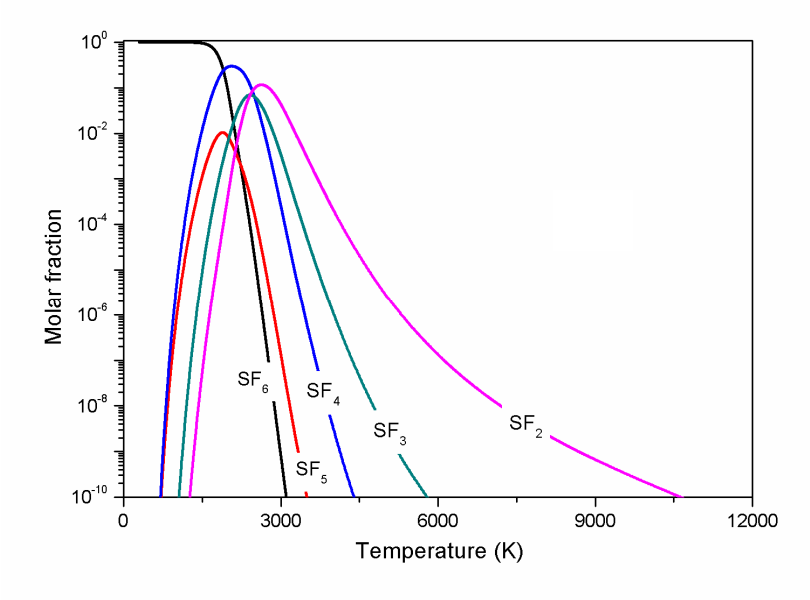

(c)

Figure 6.2 Equilibrium molar fraction: atomic species (a); diatomic molecule species (b); polyatomic molecule (c) at a pressure of 0.6MPa.

Figure 6.2 give the equilibrium molar fraction of atomic species, diatomic molecule species and polyatomic molecule species as a function of temperature at a pressure of 6 atm. In previous investigation, the plasma composition departs from equilibrium at around 12000K and we use the equilibrium molar fractions of species at 12000K as the starting point of our computation. The variations of equilibrium were used as a reference for the values calculated in

the transient state. The decay of species composition at a pressure of 0.60MPa with the cooling rate given by Adamec and Coufal is indicated in Fig. 6.3.

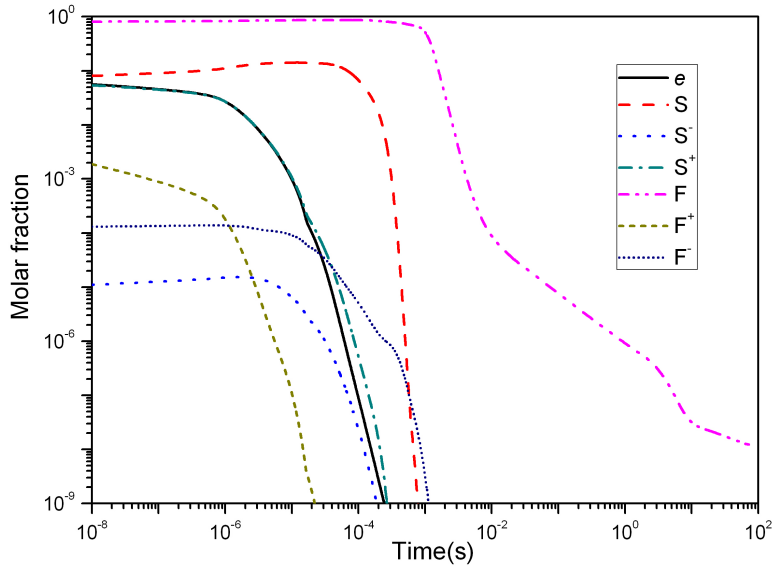

(a)

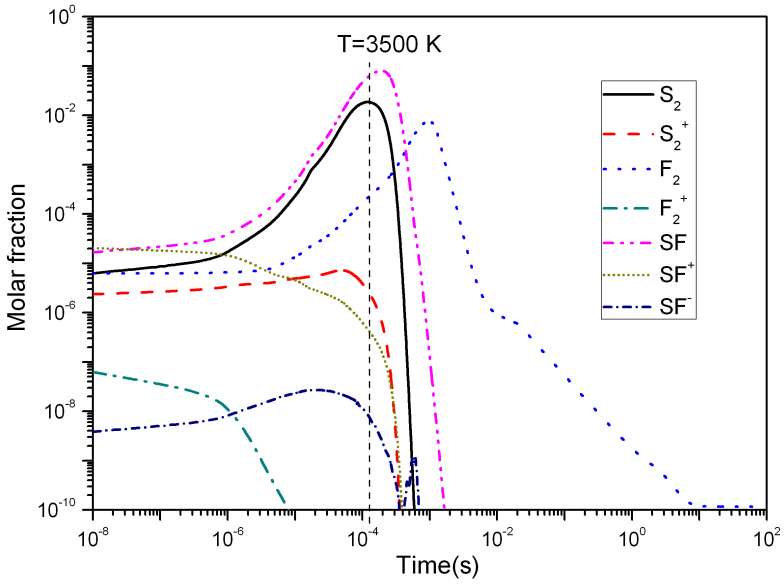

(b)

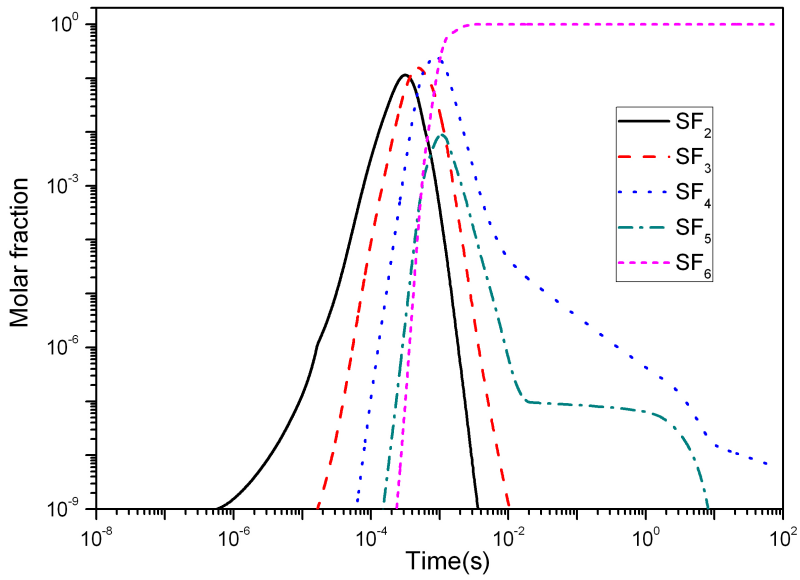

(c)

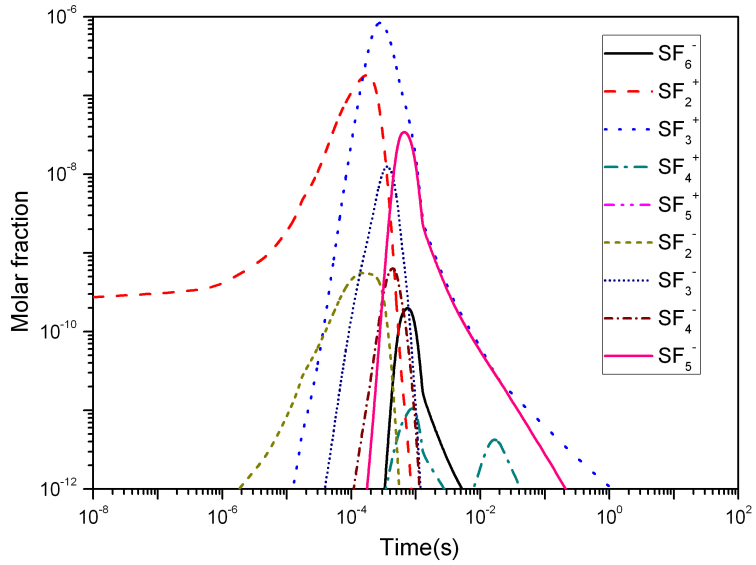

(d)

Figure 6.3 Evolution of species molar faction during SF_6 arc decay as a function of temperature at a pressure of 0.60MPa with a cooling rate given by Adamec and Coufal.

With a cooling rate given by Adamec and Coufal, the evolution of species molar fraction is identified in Fig. 6.3. Certain departure from equilibrium is identified in Fig. 6.3 even though the variations of overalls specie molar fraction with temperature remain the same. The main departure from equilibrium occurs for diatomic species because these species are not rapidly produced and the molar fraction of these diatomic species remains smaller than the equilibrium

value. For example, the molar of S_2 molecule is 0.0186 which is lower than the equilibrium value of 0.2062 at 3500K. The dominant polyatomic charged species are SF_3^+, SF_2^+, SF_5^- and SF_3^- which occurs mainly in lower temperature than 3000 K.

6.2.3.2 Decaying Behaviour of Electrons

To study the impact of departures from equilibrium on the plasma composition, we investigate the species disappearance relaxation time which is the inverse of the disappearance frequency. For the typical chemical reaction in Eq. (6.7), the disappearance frequency of specie *A* in the reaction can be obtained by

$$v_{A,i} = k_d n_A \tag{6.15}$$

The relaxation time for the disappearance of specie *A* can be defined as

$$\tau_{A,i} = 1 / v_{A,i} \tag{6.16}$$

$\tau_{A,i}$ is very similar to the time required for the density of particles *A* to tend to return to the equilibrium value through the chemical reaction in Eq.(6.7). If several reactions exist, all leading to the disappearance of species *A*, each with its relaxation time, $\tau_{A,i}$ an overall disappearance frequencies can be obtained by the summation of all *P* relevant reactions.

$$v_A = \sum_{i=1}^{P} v_{i,A} \tag{6.17}$$

The overall reaction time can be expressed as

$$\tau_A = 1 / v_A \tag{6.18}$$

From the reaction rates and the species densities, the relaxation times of the different mechanisms governing the variation of the electron density can be calculated. Fig. 6.4 shows

the electron relaxation times for the main mechanisms for electron-molecular ion recombination, electron-molecule attachment, electron-atom attachment, electron-atomic ion recombination, dissociative attachment, and dissociative recombination.

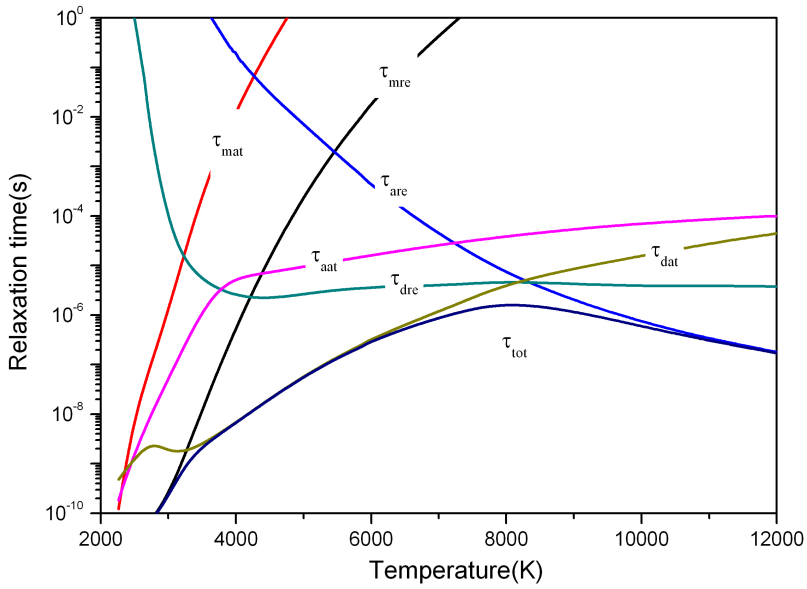

Figure 6.4 Electron relaxation times for the main mechanisms at a pressure of 0.60MPa: τ_{mre}, τ_{mat}, τ_{aat}, τ_{are}, τ_{dat}, τ_{dre} and τ_{tot} are the relaxation times respectively for electron-molecular ion recombination, electron-molecule attachment, electron-atom attachment, electron-atomic ion recombination, dissociative attachment, dissociative recombination and the total relaxation time.

The results show that above the temperature 9000K, the electron–atomic ion recombination contributes to the disappearance of electrons. In the intermediate temperature range from 3500K to 7500K, the dominant mechanism is the dissociative attachment. In the temperature lower than 3500K, the influence of electron-molecular ion becomes increased. Lastly, the dissociative recombination essentially for diatomic molecular ion is predominant around the temperature 8000K.

6.2.3.3 Influence of Temperature Cooling Rate

The influence of temperature cooling rate on the electron density variation can be found in Fig. 6.5. With a high temperature cooling rate, the system cannot adjust to arrive at the steady equilibrium state in finite time period and have a higher electron concentration than that of

equilibrium case at the same temperature because the reaction rate is also finite. The decrease of cooling rate leads to a lower electron number density at the same temperature. The electron density has longer time to reach closely the equilibrium number density of electrons and hence a reduction of the departures from equilibrium. Additionally, it reveals that under the conditions with the temperature cooling rate lower than 5.0E7 K/s, the electrons density evolution shows equilibrium characteristics as the time changes. It should note that any departures from equilibrium obtained in the present work correspond to an electron overpopulation which tends to enhance the electrical conductivity of the plasma and thus decrease the thermal interruption capability of SF_6 obtained by the local thermodynamic equilibrium model.

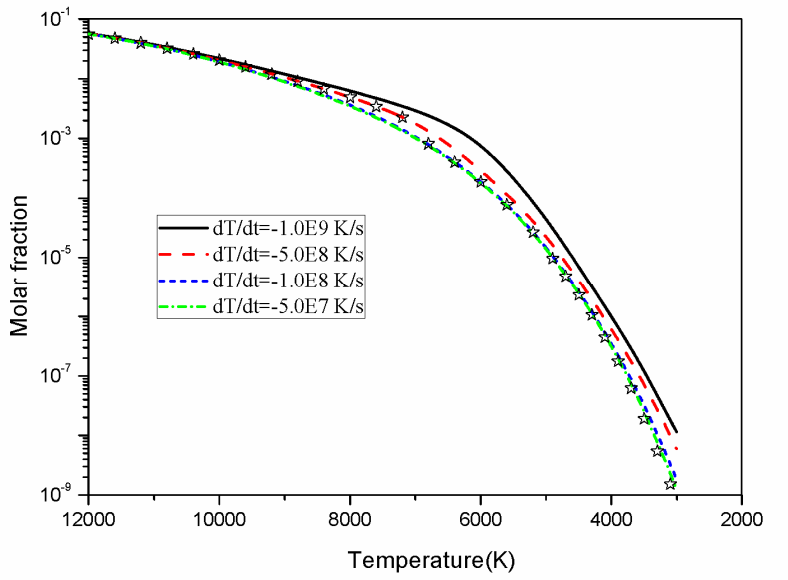

Figure 6.5 Evolution of electron molar faction during SF_6 arc decay as a function of temperature at a pressure of 0.60MPa with different cooling rates. The result obtained using Borge's temperature variation function is also presented by hollow star symbol for comparison.

Fig. 6.6 shows the influence of temperature cooling rate on overall relaxation time for electrons disappearance during SF_6 arc decay. The deviation of electron disappearance relaxation time under different temperature cooling rates mainly occurs in the intermediate temperature range from 4000K to 9000K where the dissociative recombination and dissociative attachment mechanisms especially involving diatomic molecular species are predominant. A larger temperature cooling rate leads to a higher value of electron disappearance relaxation time showing that a larger degree of departure from equilibrium occurs and a longer time is needed

to reach the equilibrium state.

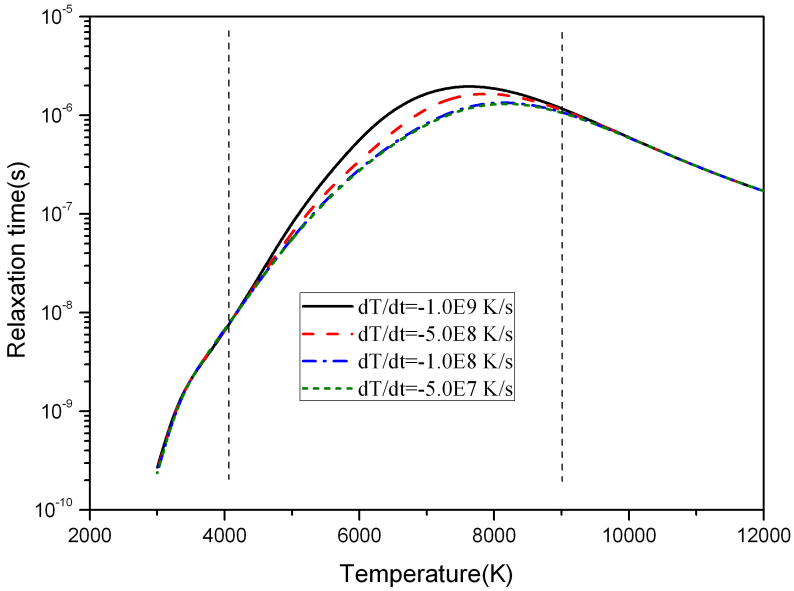

Figure 6.6 Evolution of overall relaxation time for electrons disappearance during SF_6 arc decay as a function of temperature at a pressure of 0.60MPa with different cooling rates.

6.2.3.4 Influence of Different Pressures

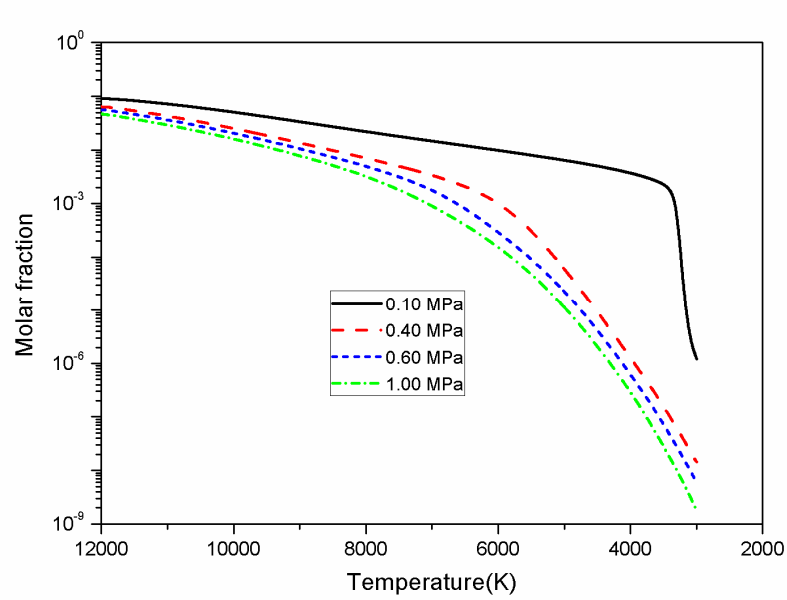

Figure 6.7 Evolution of electron molar faction during SF_6 arc decay as a function of temperature at different pressures with a cooling rate of dT/dt =-5.0E8 K/s.

As presented in Fig. 6.7, at the temperature cooling rate of 5.0E8 K/s, an increase of pressure brings a smaller molar fraction of electrons at the same temperature as a result of suppressed chemical reactions. Hence, the electrical conductivity can be reduced to enhance the thermal interruption capability of SF_6 before current zero by increasing the gas pressure in the circuit breaker tank.

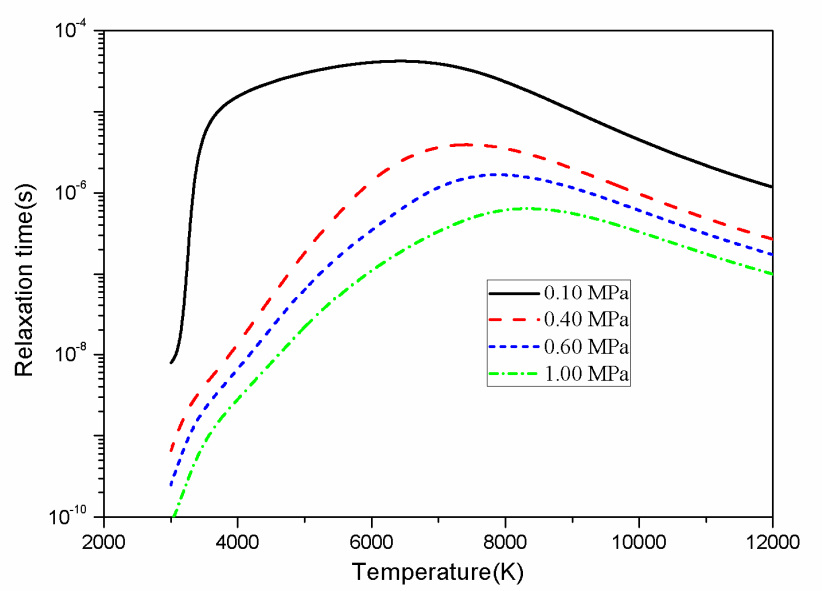

Figure 6.8 Evolution of overall relaxation time for electrons disappearance during SF_6 arc decay as a function of temperature at different pressures with a cooling rate of dT/dt =-5.0E8 K/s

The relaxation times are inversely proportional to the species number densities. Therefore, it is necessary to take account of the species' pressure-dependent density variations. Because the number densities of species increases at the same temperature as the pressure increases, the overall relaxation time for electrons disappearance during SF_6 arc decay decreases. Moreover, the peak value occurs at a higher temperature as a result of suppressed reactions.

6.3 Kinetic Analysis of Dielectric Properties of Hot SF_6 Contaminated by PTFE

6.3.1 Calculation Method to Determine the Dielectric Properties

The dielectric properties, i.e. critical breakdown filed for hot gases are different from that at room temperature as a result of decreased species number density, the varied energy exchange rate between electrons and heavy species and the changed species composition due to the chemical reactions occurring in the system with elevated temperatures. A general computation procedure to determine the dielectric properties of hot gases mainly includes three steps described as follows:

- **Determination of Species Composition in the Hot Gases.**

Successful thermal recovery requires the temperature of the arc in circuit breaker to be cooled down from high temperature to a relatively low temperature of 3500 K after current zero. As the temperature increases, the gas begins to dissociate into other species which can effectively influence the electron energy distribution functions (EEDFs) as well as the chemical kinetics, reflected in the corresponding collision cross sections. Under the condition of local thermal equilibrium, the species composition is determined by adoption of minimum Gibbs energy [32] Because of the rapid cooling rate especially under axial gas flow, the composition of the hot gas possibly departs from that of local thermal equilibrium. Under this condition, a kinetic model which takes into account the reaction kinetics should be used. However, the equilibrium species composition is adopted in current work because the reaction rates between electrons and heavy species interactions affected by the arc electric field distribution can vary with each other for different cases and brings a different species composition of hot gases after the departure from equilibrium takes place before current zero. Additionally, the electrons often have higher temperature than heavy species due to the ineffective energy exchange between them. A subject of debate has long existed for the determination of non-equilibrium species composition [33]. Therefore, we adopt the equilibrium species composition as a simple case and the influence of departure from equilibrium on dielectric properties is discussed later in this chapter.

- **Determination of the Electron Energy Distribution Functions (EEDFs).**

The critical electric field is the field corresponding to a balance between the processes of electron generation and loss. Therefore, all the relevant processes of electron kinetics with regard to the electrons loss and generation including the electron elastic collision, the vibrational and electronic excitation, electron collision ionization and attachment should be taken into account. The transport coefficients and reaction rates of these processes are derived from the electron energy distribution functions (***EEDFs***) which needs a priori knowledge of the collision cross section sets corresponding to the whole species present in the dissociated hot gas and is obtained from a two-term numerical solutions of the Boltzmann transport equation.

- **Determination of the Critical Electrical Breakdown Field for Hot Gas.**

The breakdown of hot gas depends on whether an electron avalanche can be formed for a given electrical field. The formation of electron avalanche is determined by the production and loss processes of electrons. In a residual plasmas after current interruption, electron impact ionization and detachment mainly contribute to the production of electrons. In contrast, electron attachment and recombination with heavy species contribute to the loss of electrons. When both these two processes reach a balance and the critical electrical breakdown field can be evaluated. Compared with ionization processes associated with heavy ions, electron impact ionization is far more efficient. The ion kinetics such as electron detachment from negative ions, Electron-positive ion recombination, mainly involves the dominant ions presenting at higher gas temperature above around 3000K. Their basic processes in the case of SF_6 mixed with fluorine-containing compounds such as PTFE vapor are quite complex .The recombination and detachment reaction channel are not clearly identified and their reaction rates are poorly known. Therefore, if not pointed out especially, and their role on the breakdown are not discussed in the framework of the present work.

6.3.2 Species Composition of Hot Gases

The chemical equilibrium composition of pure SF_6 and its mixture with PTFE vapor was calculated as a function of temperature and pressure based on the method of minimizing the Gibbs energy of a system as described in previous chapter. Taking into account that the

dielectric recovery phase mainly occurs below a temperature value of 5000K, therefore, only the species composition below 5000K is presented in spite that we can compute the species composition in a wide temperature range.

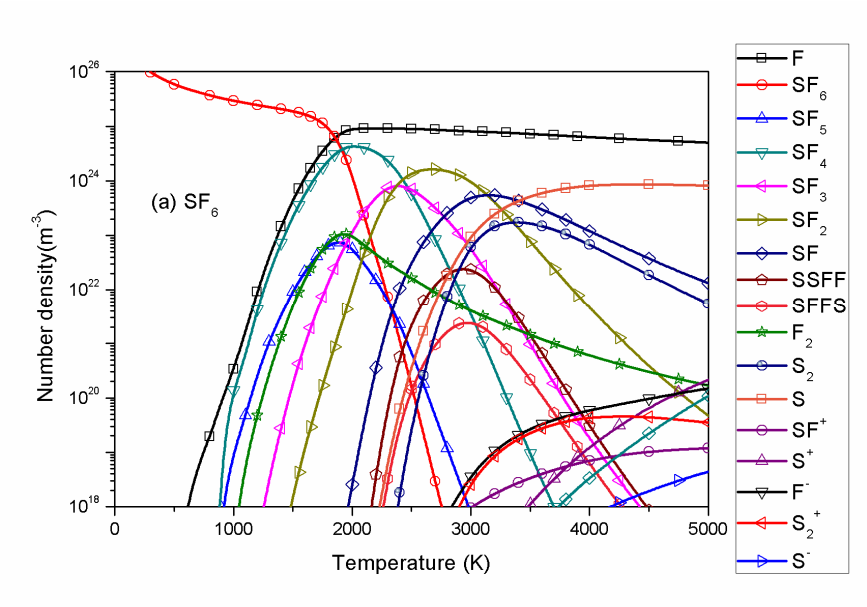

(a)

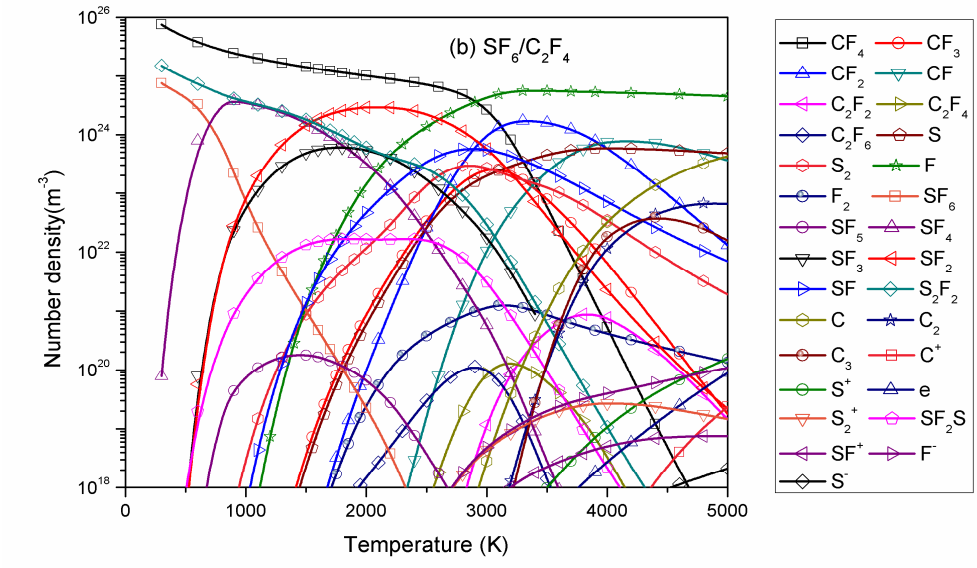

(b)

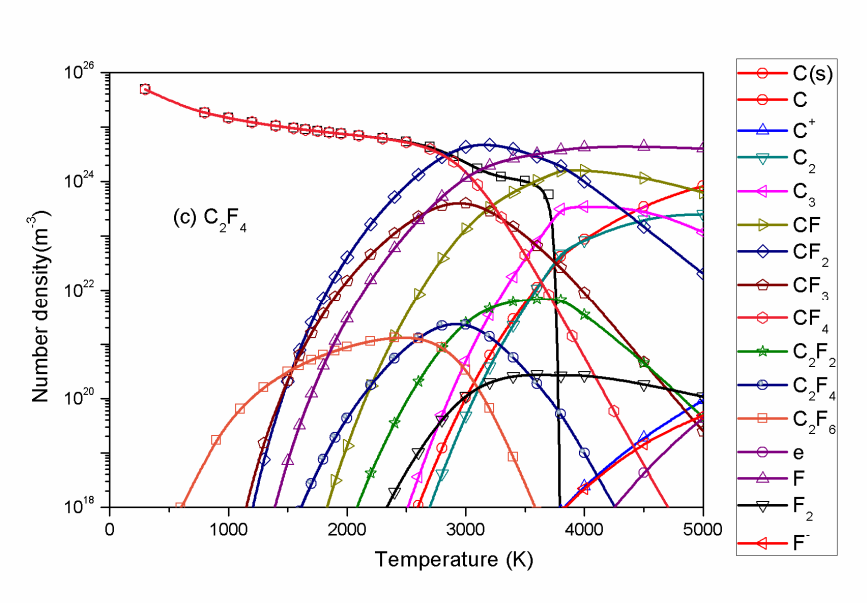

(c)

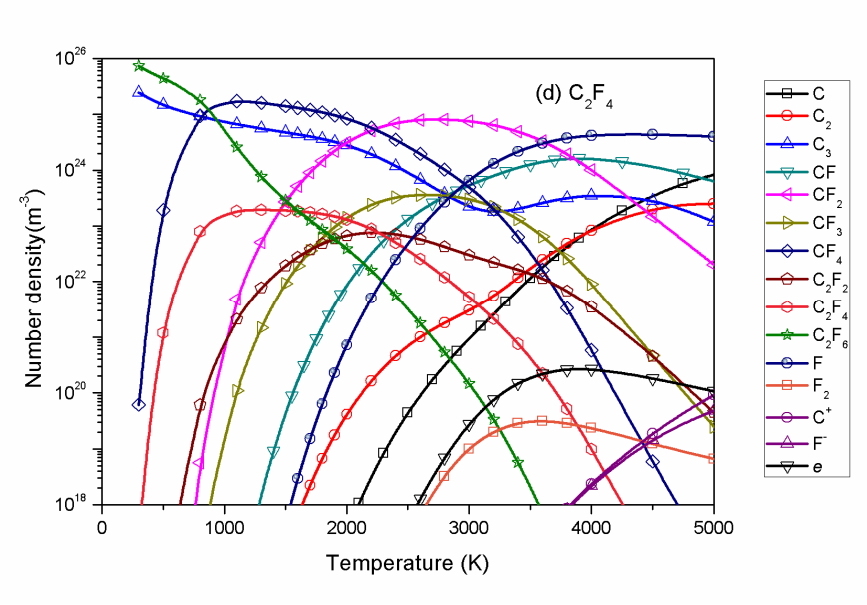

(d)

Figure 6.9 Species composition of pure SF_6 (a), 1:1 SF_6/C_2F_4 mixture (b) and pure C_2F_4 with (c) and without (d) solid carbon in the temperature range from 300K to 5000K at a pressure of 0.40MPa.

Fig. 6.9 shows a typical gas composition of SF_6, SF_6/C_2F_4 and C_2F_4 mixtures with a mixed molar fraction ratio of 1:1 as a function of the temperature in the temperature range from 300K to 5000K at a pressure of 0.40MPa. No solid carbon is observed in the 1:1 SF_6/C_2F_4 mixture. This phenomenon was verified by the observation on an arc jet formed by ablated PTFE vapor injected by a cold SF_6 [36]. However, for pure C_2F_4 gas, it is possible that solid

carbon can generate under arcing atmosphere. With and without considering carbon formation, it is noted that the molar fraction of C_2F_4 at room temperature is quite low and this suggests that once C_2F_4 decomposes to other molecules or atoms at a higher temperature during the arcing phase, the decomposed molecules and atoms no longer recombine to C_2F_4 at temperatures around 300 K after arc extinction. Similarly, it is interesting to note that the composition of 1:1 SF_6/C_2F_4 mixture at room temperature is quite different from that of the two pure gases. In particular, the concentration of many of the polyatomic molecules that are present in large amounts at low temperature in the pure gases, such as SF_6, SF_4, SF_3, and C_2F_6, is greatly reduced in the mixture. These molecules are replaced in the mixture by CF_4, S, and SSFF. We can also find that there is no solid carbon formation in the 1:1 SF_6/C_2F_4 mixture regardless that we indeed takes into account the possibility of its formation in our computation.

6.3.3 Electron Energy Distribution Functions (EEDFs) in Hot Gas under the Electrical Field

6.3.3.1 Cross Section Data

The determination of critical electrical breakdown filed necessarily includes calculations of the electron impact ionization and attachment coefficients and hence the electron energy distribution functions (EEDFs) which are usually based on compilations of cross sections from different sources. For pure SF_6 and its mixture with fluorocarbon compounds of PTFE vapour, the interaction between electrons and 22 neutral heavy species of SF_6、SF_5、SF_4、SF_3、SF_2、SF、F_2、S_2、S、F、SSFF、FSSF、CF、CF_2、CF_3、CF_4、C_2F_6、C_2F_4、C_2F_2、C、C_2、C_3 are taken into account. The other interactions, because the concentrations of these heavy species are low, are not taken into account in current work. Not all needed cross section data is available in the literature. For SF_6, the collision cross sections are rather well known only for electron/SF_6, electron/F_2, electron/F and electron/S systems. However, there are other cross section data available in the literature for the other systems not taken into account in previous investigation. These cross section data are updated in current work and the unknown elastic and inelastic collision cross sections are completed from proper prediction. The influence of predicted cross sections on critical dielectric properties is limited in the temperature range from 1500K to 2000K where related species exist with low molar

fraction but not bring a large shift in the result. For e/SF_2 and e/SF, the electron impact excitation cross sections obtained by the R-matrix method were adopted [34]-[35].

For e/S_2, the momentum-transfer, excitation, and ionization cross sections using the R-matrix method is taken into account [37]-[38]. The total ionization cross section for SF, SF_2, SF_3, SF_4, and SF_5 calculated by the recently developed binary-encounter-Bethe (BEB) model were used for their consistence [39]. For the sets of collision cross sections for electron/SF_6, electron/F_2, electron/S and electron/F, the basic data used for the compilation are from Cliteur et al. [11], Yousfi et al. [12], Itoh et al.[40], Miller et al. [41], Hayashi et al. [42], Morgan [43] and the references given therein these papers. The electron/F and electron/S sets are then completed by adding the attachment cross sections corresponding to radiative attachment (i.e. e + F or S → F- or S-+ *hv*) calculated using the principle of detailed balancing and fitted using the corresponding reaction rates [44]-[45]. For the interaction between electrons and C_2F_6, the cross section sets are based on the compilation of Hayashi et al. [46]-[47]. For electron interaction with CF_4 and its radials CF_x (x=1, 2, 3), the cross section sets are from Bordage et al. [48]-[49] and Rozum et al. [50] supplemented by the momentum transfer cross section data by theoretical study on electron-CF_2 collisions [51]and the experimental ionization cross section [52]. For e/ C_2F_4, the cross section data are from the compilation of Yoshida et al. [53]. In the case of e/SSFF, e/FSSF and e/C_2F_2, their cross section data which are poorly known in the literature are assumed to be respectively similar to the electron-SF_4 for e/SSFF and e/FSSF and the electron-F_2 for e/C_2F_2 for as suggested by previous literatures [11]-[12]. The cross section set of electron/atomic carbon interaction is from [54]. For e/C_2 and e/C_3, the cross section data are obtained by a compilation of recent study of electron impact interaction with molecules of C_2 [55]-[57] and C_3 [57]-[58]. The relevant elastic and inelastic cross sections sources for different interactions can be found in table 6.3.

Table 6.3 Electron impact cross sections data source

Interactions	Data source	Interactions	Data source
e-SF_6	[40]	*e-SF_5*	[11][12][39]
e-SF_4	[11][12][39][41]	*e-SF_3*	[11][12][39]
e-SF_2	[11][12] [35] [39]	*e-SF*	[11][12][34] [39]
e-S_2	[11][12][37][38]	*e-F_2*	[11][12][42][43]

e-S	[11] [44][45]	*e-F*	[11] [44]
e-CF_4	[48][49]	*e-CF_3*	[50][52]
e-CF_2	[50][51][52]	*e-CF*	[50][52]
e-C_2F_2	[11]	*e-C_2F_4*	[53]
e-C_2F_6	[46][47]	*e-C*	[54]
e-C_2	[55][56][57]	*e-C_3*	[57][58]

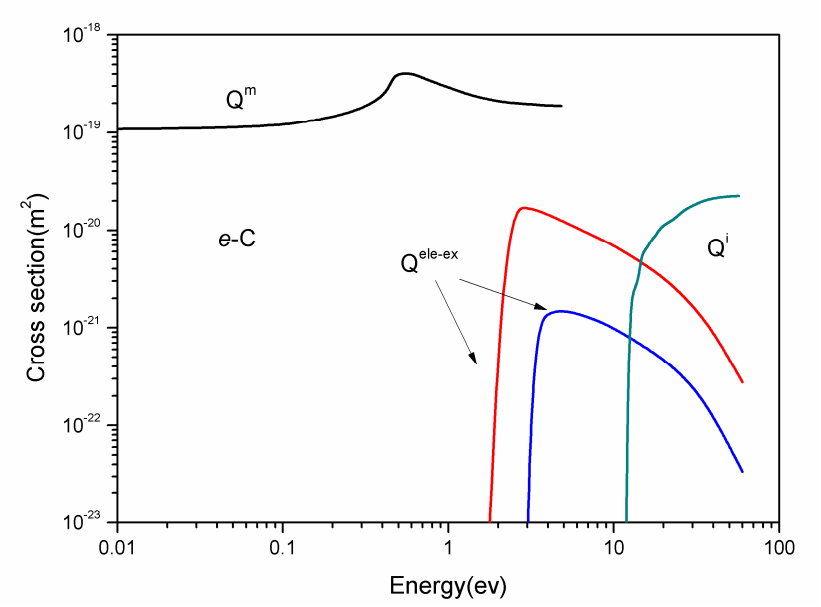

(a)

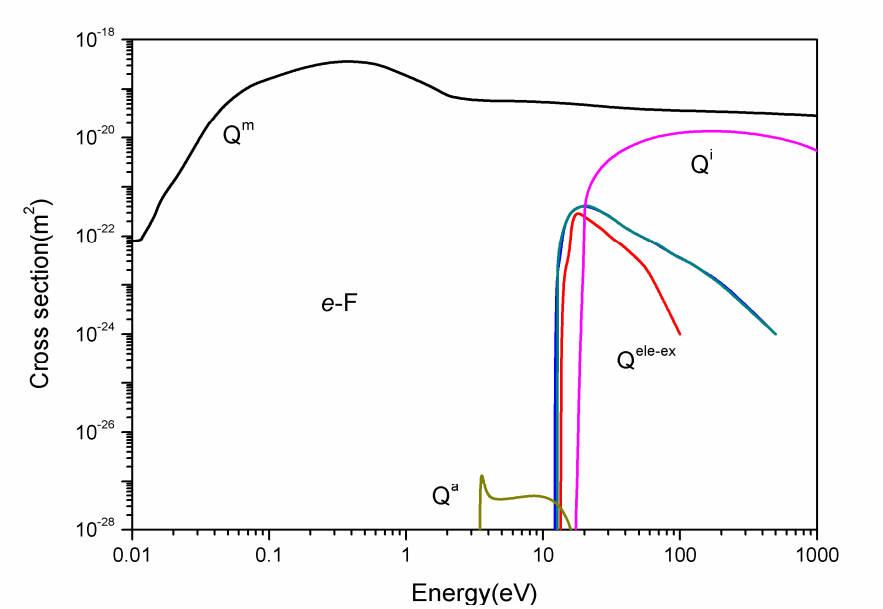

(b)

Figure 6.10 Electron impact cross section with atomic carbon and fluorine.

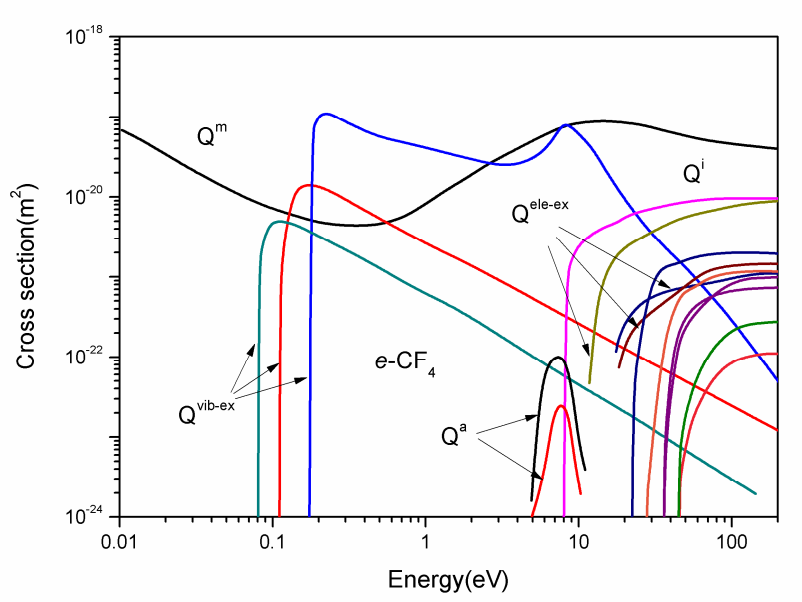

(a)

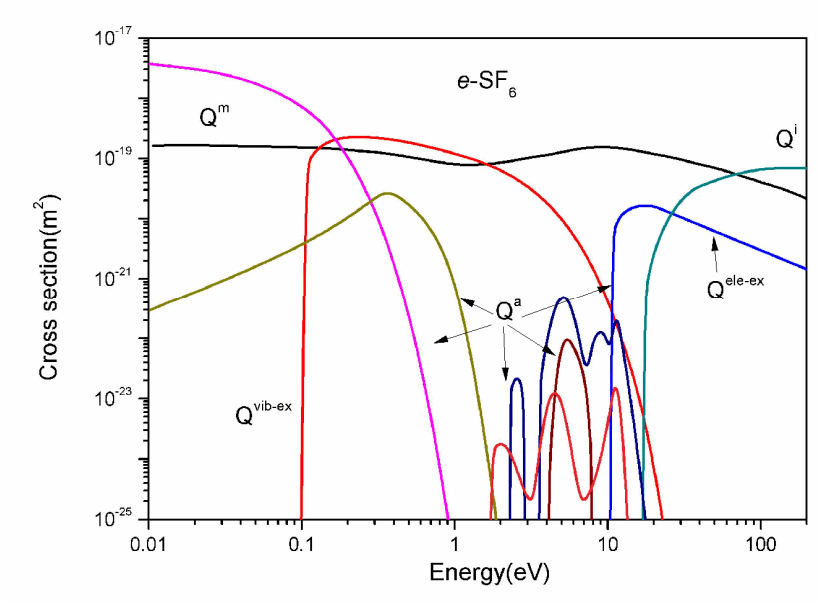

(b)

Figure 6.11 Electron impact cross section with CF_4 and SF_6.

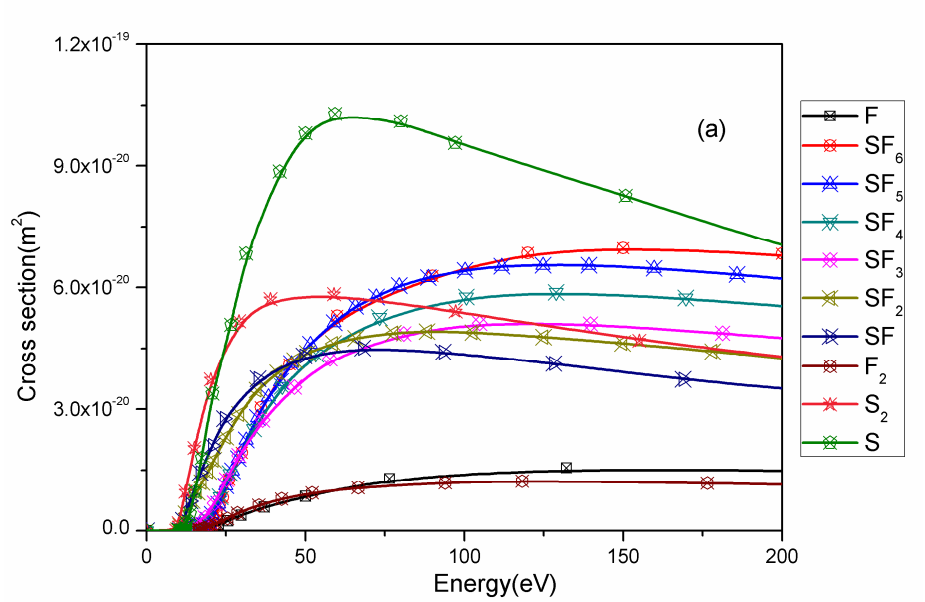

(a)

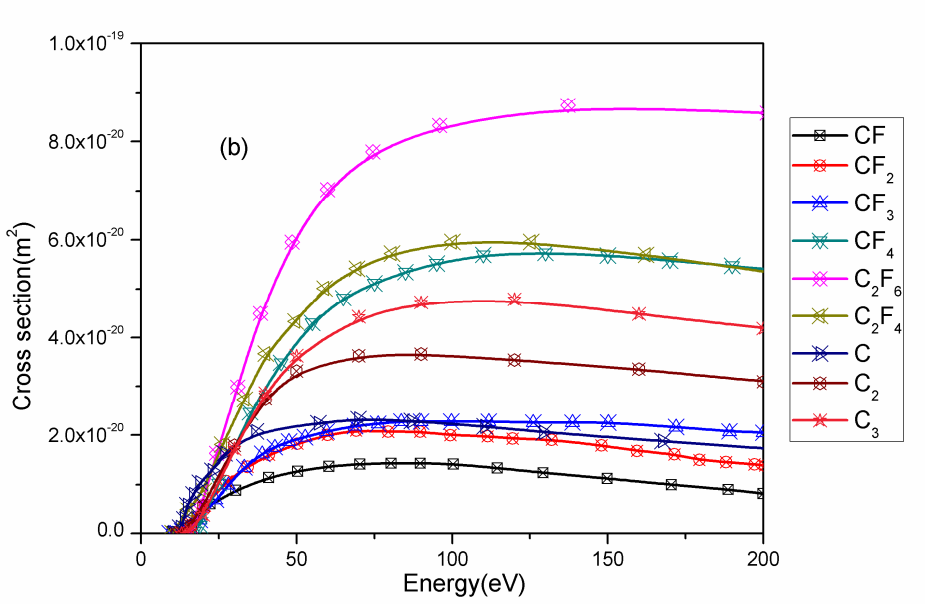

(b)

Figure 6.12 Ionization cross sections by electron impacts on SF_6/ CF_4 and their dissociation products

Figs. 6.10-6.11 respectively give the cross section sets by electron impacts on atomic species of carbon and fluorine and neutral molecular species of SF_6 together with CF_4. All the relevant electron interaction processes are taken into account. For example, the sets of cross sections between electron and SF_6 interactions includes one elastic momentum transfer cross section, one vibrational cross section, one electronic cross section, one ionization cross section along with five attachment cross sections. For CF_4, the elastic momentum transfer cross section,

three vibrational cross sections, three electronic excitation dissociation cross sections and seven ionization cross sections together with two dissociative electron attachment cross sections are adopted. Fig. 6.12 shows the ionization collision cross sections by electron impacts on the different molecules and atoms considered in this work. The different molecules present in the dissociated hot gas can exist also on their vibration states. The population of such vibration states can, for certain gas temperature, be larger than the population of the corresponding fundamental states. As is known, the collision cross sections between an electron and a vibrational molecule are generally larger with a lower threshold occurrence for the inelastic case in comparison to the corresponding fundamental state. This means that for more rigorous critical breakdown field calculations, both the interactions with the fundamental states and the interactions between electrons and molecular species must be taken into account for elastic as well as inelastic collisions. However, the associative cross section data are also poorly known and particularly in the present case of SF_6 and its dissociation products. In the present solving of the Boltzmann equation, effects of collisions with vibrationally excited molecules were neglected for simplicity.

6.3.3.2 Numerical Solution of Electron Energy Distribution Functions

The EEDF is obtained by a solution of the Boltzmann transport equation solved for a uniform, zero-dimensional space with *ELENDIF* code [59] The code utilizes the two-term spherical harmonic approximation and accounts for the spatial gradients resulting from steady-state growth or decay, due to ionization and attachment. In the present calculation, all particles were assumed to be in their ground states for simplicity. The influence of collisions with vibrationally excited molecules is not taken into account because the relevant interactions are not available in the literature. Additionally, it is known that the two-term expansion technique can lead to erroneous results whenever we deal with a high ratio of elastic and inelastic collision cross sections [60]. Fortunately, this is not a problem since the search for the critical electric field strength is done in the range of high values and the applied local field approach neglects thermalization of the electrons with their temperature immediately established by the balance between electronic collisions and the instantaneous electric field when the electrons seek a higher level at which they can balance the energy gained from the electric field, and lose during collisions with heavy species [11]. Hence this can guarantee the computation accuracy using

current method. A detailed description of the solution technique can be found in the work [59] [61]-[62] and simply described as follows [14]-[15]. In the numerical solution of the Boltzmann equation, the energy range was fixed to 0–50 eV, and the energy increment was set with a bin size of 0.020 eV in order to consider the sharp electron impact vibrational excitations of molecules. Time dependent computation was performed with a time step of 10^{-10}s until convergence to derive the steady state solution of EEDF.

$$\frac{\partial n(\varepsilon)}{\partial t} = -\frac{\partial J_f}{\partial \varepsilon} - \frac{\partial J_{el}}{\partial \varepsilon} + \frac{\partial J_{inel}}{\partial \varepsilon} + \frac{\partial J_{ion}}{\partial \varepsilon} + I_{att} + (\frac{\partial n}{\partial t})_{e-e} \tag{6.19}$$

where $n(\varepsilon)d\varepsilon$ is the electron number density with the energy from ε to $\varepsilon + d\varepsilon$, J_f, J_{el}, J_{inel}, and J_{ion} are respectively energy loss rate in elastic collisions with heavy species, energy gain by electrons from the electric field, energy loss in excitation collisions with heavy species and energy loss in ionization collisions with heavy species; I_{att} is energy loss rate in electron attachment processes per unit energy. The last term on the right hand side indicates collision term between electron and electron.

$$J_f = \frac{2Ne^2(E/N)^2\varepsilon}{3m_e\sqrt{(2\varepsilon/m_e)}\sum_s x_s\sigma_s^m(\varepsilon)}(\frac{n(\varepsilon)}{2\varepsilon} - \frac{\partial n(\varepsilon)}{\partial \varepsilon}) \tag{6.20}$$

where N, e, m_e, E, x_s, and σ_s^m are respectively the total number density, the electron charge, electric field, the molar fraction and electron impact momentum transfer cross section for species *s*.

$$J_{el} = -N\sqrt{(\frac{2\varepsilon}{m_e})}\sum_s x_s \frac{2m_e}{M_s}\sigma_s^m(\varepsilon)[n(\frac{kT_h}{2} - \varepsilon) - kT_h\varepsilon\frac{\partial n(\varepsilon)}{\partial \varepsilon}] \tag{6.21}$$

where M_s and T_h are respectively the molar weight for species *s* and heavy specie temperature.

$$J_{inel} = \sqrt{\frac{2}{m_e}} \sum_s \sum_j N_s^0 x_s \frac{2m_e}{M_s} \int_{\varepsilon}^{\varepsilon+\varepsilon_{s,j}^{ex}} \varepsilon^{1/2} \sigma_{s,j}^{ex}(\varepsilon) n(\varepsilon) d\varepsilon \tag{6.22}$$

where N_s^0 $\sigma_{s,j}^{ex}$ and $\varepsilon_{s,j}^{ex}$ are the number density for species *s* in the ground state, electron impact excitation cross section for the *j*-th state and energy threshold for the *j*-th state of species *s*.

$$J_{ion} = \sqrt{\frac{2}{m_e}} \sum_s N_s^0 \int_{\varepsilon}^{\varepsilon+\varepsilon_s^i} \varepsilon^{1/2} \sigma_s^j(\varepsilon) n(\varepsilon) d\varepsilon \tag{6.23}$$

where ε_s^i and $\sigma_s^j(\varepsilon)$ are energy threshold for ionization state and electron impact ionization cross section and for species *s*.

$$I_{att} = -\sqrt{\frac{2}{m_e}} \sum_s N_s^0 \varepsilon^{1/2} \sigma_s^a(\varepsilon) n(\varepsilon) \tag{6.24}$$

where σ_s^a is electron impact ionization cross section for species *s*.

$$(\frac{\partial n}{\partial t})_{e-e} = \frac{2}{3}\pi e^4 (\frac{2}{m}) \frac{1}{2} \ln[\frac{3kT_e}{2e^2}\sqrt{\frac{kT_e}{4\pi n_e e^2}}][\frac{3}{\varepsilon^{1/2}} n(\varepsilon)^2 - 2\varepsilon^{3/2} \frac{\partial \varphi}{\partial \varepsilon} \frac{\partial \beta}{\partial \varepsilon} - \frac{\varphi}{\varepsilon^{1/2}} \beta] \tag{6.25}$$

where T_e is the electron temperature.

$$\varphi = 3\int_0^{\varepsilon} n(\varepsilon') d\varepsilon' - \frac{1}{\varepsilon}\int_0^{\varepsilon} \varepsilon' n(\varepsilon') d\varepsilon' + 2\varepsilon^{1/2} \int_{\varepsilon}^{\infty} \frac{n(\varepsilon')}{\varepsilon'^{1/2}} d\varepsilon' \tag{6.26}$$

$$\beta = \frac{n(\varepsilon)}{2\varepsilon} - \frac{\partial n(\varepsilon)}{\partial \varepsilon} \tag{6.27}$$

$$T_e = \frac{2}{3k}\int_0^{\infty} f_0(\varepsilon) \varepsilon^{3/2} d\varepsilon \tag{6.28}$$

where k and f_0 are respectively the Boltzmann's constant and electron energy distribution

function.

$$n(\varepsilon) = n_e f_0(\varepsilon)\varepsilon^{1/2} \tag{6.29}$$

$$\int_0^\infty f_0(\varepsilon)\varepsilon^{1/2} d\varepsilon = 1 \tag{6.30}$$

6.3.3.3 Numerical Determination of Effective Ionization Coefficients

The effective ionization coefficients $\bar{\alpha}$ which determine the critical breakdown field are influenced by the electron attachment coefficient η and electron impact ionization coefficient α.

$$\bar{\alpha} = \alpha - \eta \tag{6.31}$$

$$\alpha = \frac{1}{v_d}\sum_s \sqrt{\frac{2e}{m_e}} \int_0^\infty x_s \sigma_s^i(\varepsilon)\varepsilon f_0(\varepsilon) d\varepsilon \tag{6.32}$$

$$\eta = \frac{1}{v_d}\sum_s \sqrt{\frac{2e}{m_e}} \int_0^\infty x_s \sigma_s^a(\varepsilon)\varepsilon f_0(\varepsilon) d\varepsilon \tag{6.33}$$

$$v_d = -\sqrt{\frac{2e}{m_e}} \left(\frac{E}{3N}\right) \int_0^\infty \frac{1}{\sum_s x_s \sigma_s^m(\varepsilon)} \frac{df_0(\varepsilon)}{d\varepsilon} \varepsilon d\varepsilon \tag{6.34}$$

where v_d is the drift velocity of electrons.

6.3.4 Computation Results

6.3.4.1 Critical Breakdown Field of Hot SF_6

The calculated values of EEDF for pure SF_6 can be found in Fig. 6.13. The gas temperature increase brings the equilibrium composition changes and causes a different value of EEDF.

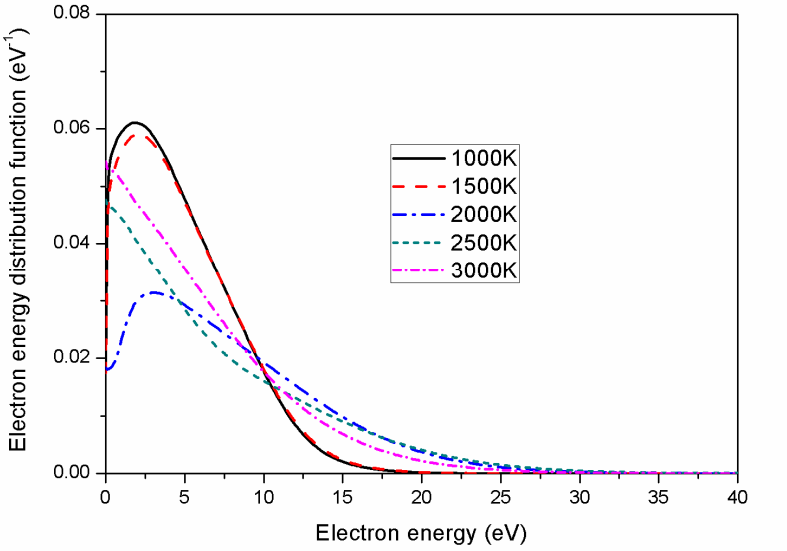

Figure 6.13 Calculated values of electron energy distribution function at different temperatures at a reduced electric field strength E/N of 150 Td with a pressure of 0.4MPa.

Fig. 6.14 shows the variation of ionization and attachment coefficients at a pressure of 0.4MPa for different gas temperatures. For a given temperature, the critical field E_{cr}/N corresponds to the E/N value for which ionization and attachment coefficients are equal, i.e. the crossing point of the corresponding curves. Thus, for a given pressure when the successive values of E_{cr}/N are determined for the whole range of the considered gas temperature we therefore obtain the E_{cr}/N variation with the gas temperature.

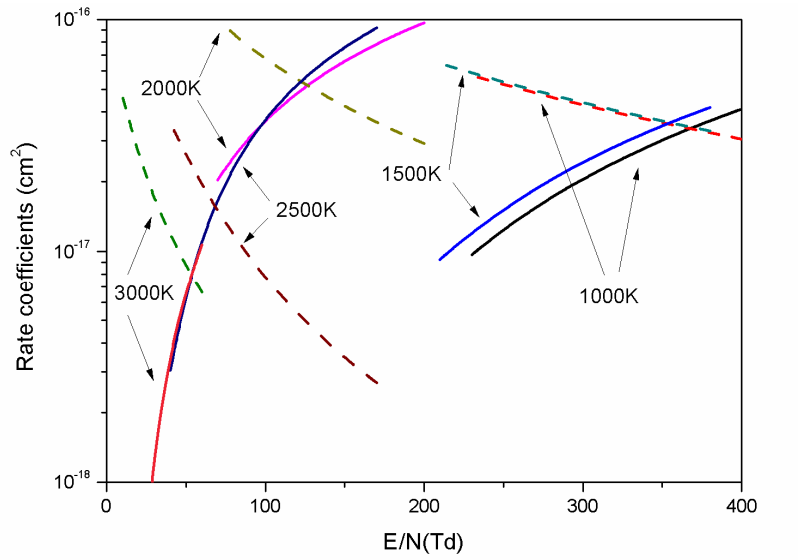

Figure 6.14 Ionization and attachment coefficients as a function of E/N for different gas temperatures at a pressure of 0.4MPa.

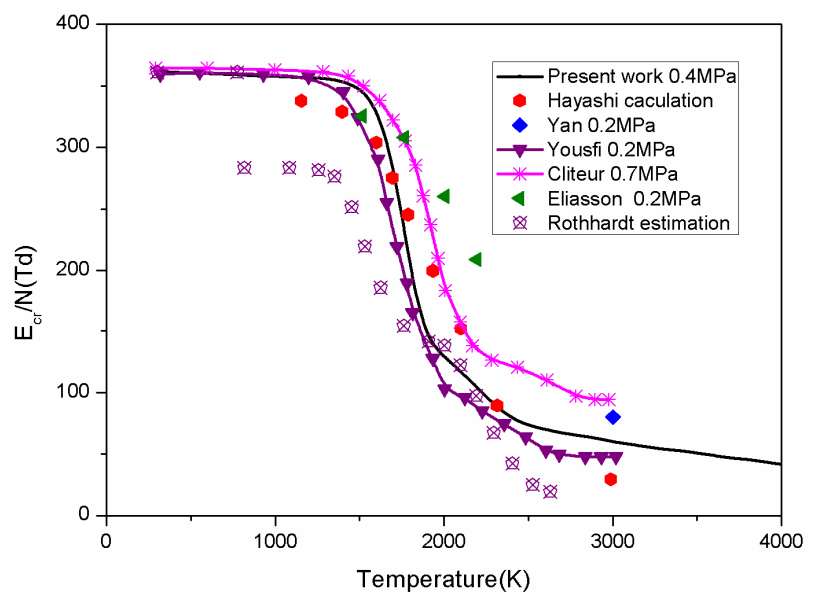

Figure 6.15 Calculated values of critical reduced electric fields with comparison to several literature data.

Fig. 6.15 presents the critical electric field calculated from collision cross sections of hot SF_6 and compared to several data taken from the literatures. (i.e., Eliasson and E. Schade [4], Cliteur et al. [11], Yousfi et al. [12]-[13], Hayashi from Schade [5], Rothhardt et al. [7], Yan et al. [10].). With increasing gas temperature, the critical breakdown field slightly decreases at the low temperature range where the dissociation of SF_6 does not take place due to the reduced species number density and elevated energy exchange rate between electrons and heavy species. When the dissociation occurs, the critical breakdown filed gradually decreases as the temperature increase. Present calculations are coherent with the measurement at the room temperature ([40]), quite close to Hayashi calculation as soon as the population of F atom becomes dominant, in a qualitative agreement with Cliteur results, close to Eliasson measurements between 1500 K up to 2000 K and in agreement with the Rotthardt estimation between 1900K up to 2300 K. Our result presents a good agreement with Yousfi et al.'s calculation. The slight discrepancy is mainly attributed to the deviation of equilibrium species composition together with the different electron impact cross section data source. It is noted that some data used in Yousfi et al.'s calculation have been updated in our current work and this should provide more reliable result. In fact, as already shown by Cliteur et al. [10], the collision cross section sets are complete in the literature only for electron-SF_6, electron-F_2, electron-F and electron-S systems even though we have updated the cross section set for other

species using most recent data.

6.3.4.2 Influence of Different Pressures

Fig. 6.16 shows calculated value of Ecr/N for a quite large gas temperature and gas pressure ranges (i.e. 300 K up to 4000 K and 0.1 atmosphere up to 10 atmospheres). In this temperature range the reduced critical electric field depends on the temperature rather weakly and is independent of pressure. According to Le Chatelier's law, the increase of the pressure opposes changes to the original state of equilibrium so that chemical reactions are suppressed, and the temperature at which these reactions occur is increased. Therefore, in the temperature range where the dissociation takes place, a higher pressure leads to a higher dielectric property of hot SF_6. Therefore, we can enhance the fault current interruption capability by means of the increased pressure in the circuit breaker tank.

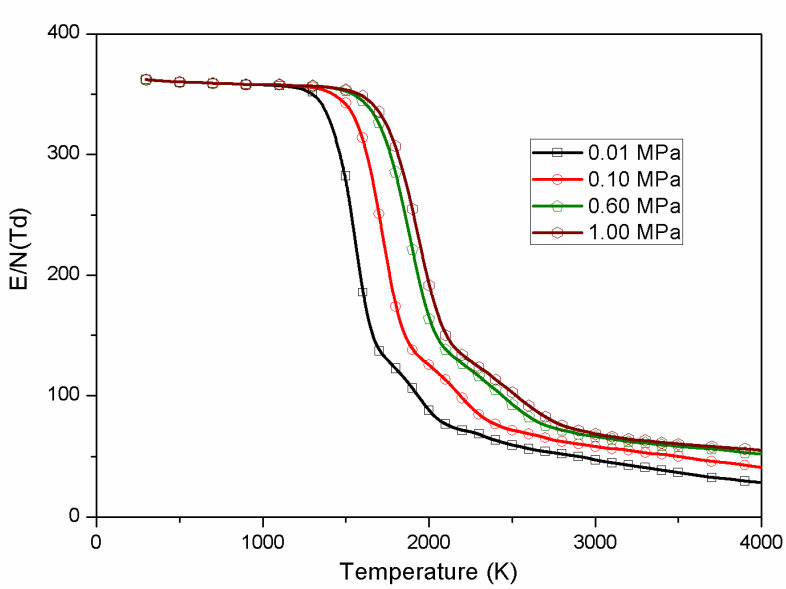

Figure 6.16 Calculated values of critical reduced electric field for different gas pressures.

6.3.4.3 Influence of PTFE Vapor Ablation on Hot Gas Breakdown

After extinction of the arc at current zero, the transient recovery voltage develops at the contacts and successful interruption occurs only if the dielectric strength is sufficiently high. During the arcing period in the fault current interruption, the arc could burn and ablate the

nozzle materials (mostly PTFE vapor, $(C_2F_4)_n$) injected into SF_6 gas and the filling gas is in a SF_6 and PTFE vapor mixture or pure PTFE vapor depending on the design of the interrupter, contact movement, and the arcing history. Nozzle ablation affects the performance of a circuit breaker in two ways. First, the ablated PTFE vapor, which is generated by strong arc radiation, adds mass, momentum, and energy to the system and consequently modifies the arcing environment. This brings changes to the arc characteristics, thus electrical power input. As a result, the arc conditions at current zero, which determine the thermal interruption capacity of the breaker, depend critically on nozzle ablation. Second, nozzle ablation may have a significant influence on the composition of the gas or residual plasma left between the contacts after the thermal extinction of the arc, thus affecting the dielectric strength. It is quite possible that the resulting gas mixture, consisting of SF_6 and PTFE vapor, is used to extinguish the arc. In practice, it is of great interest to investigate the influence of PTFE vapor injected into SF_6 on the dielectric properties after arcing.

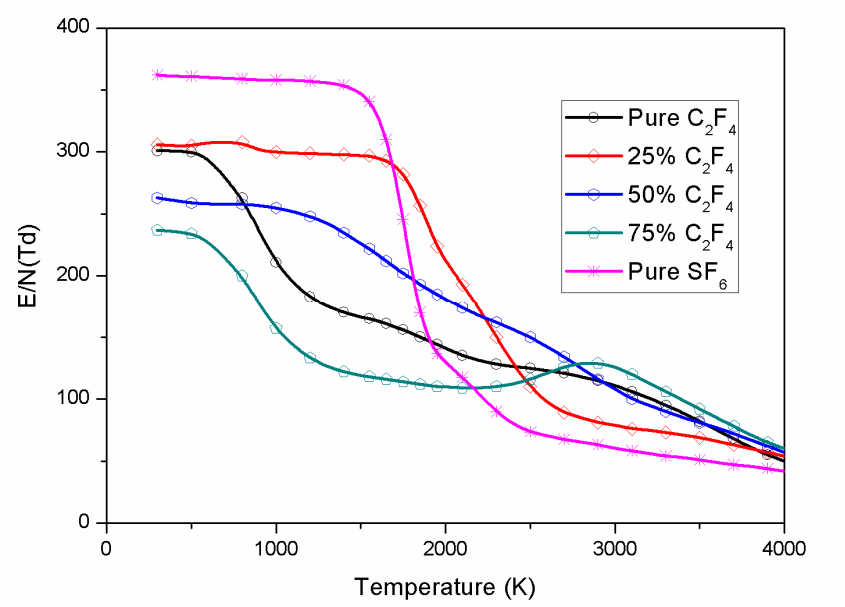

Figure 6.17 Calculated values of critical reduced electric field for SF_6/C_2F_4 mixture with different mixing fraction at a pressure of 0.40MPa. The species composition is computed without considering the formation of solid carbon.

Fig. 6.17 gives the calculated values of critical reduced electric field for SF_6/C_2F_4 mixture with different mixing fractions at a pressure of 0.40MPa. The species composition is obtained without considering solid carbon formation. For the molar fraction of C_2F_4 from zero

to 75%, the addition of C_2F_4 leads to a reduced value of critical breakdown electric field in the lower temperature T<1700K, however, a much richer molar fraction of C_2F_4 brings an increased dielectric strength. No matter what the molar fraction of C_2F_4 in the mixture is, the addition of C_2F_4 always causes the decreased dielectric strength than that of pure SF_6 in the temperature range T<1700K. Above the temperature of 2500K, the addition of C_2F_4 leads to a higher critical breakdown field. The variation of reduced critical breakdown field is mainly caused by the species composition which is strongly dependent on C_2F_4 molar fraction.

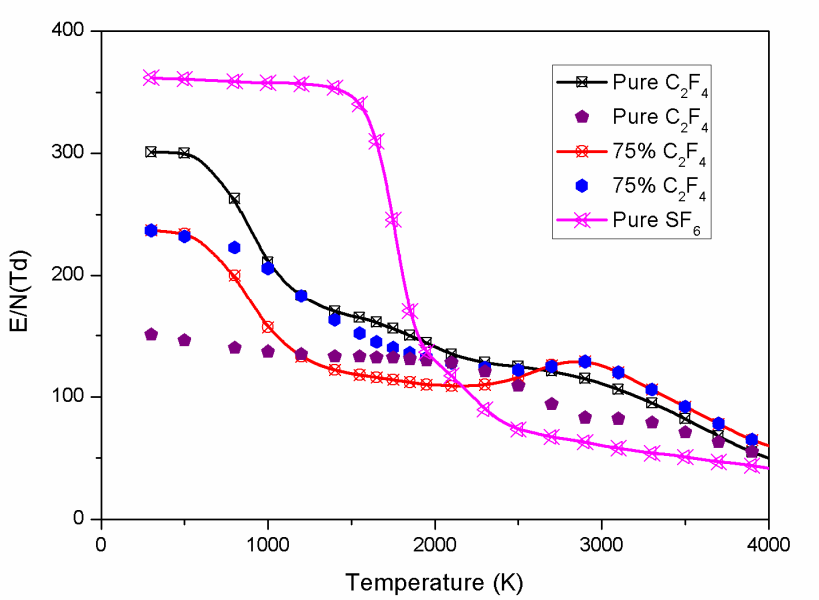

Figure 6.18 Calculated values of critical reduced electric field for SF_6/C_2F_4 mixture at a pressure 0.40MPa. The species composition is computed without (solid line& symbols) and with (symbols) considering the formation of solid carbon.

It is presented that there is no solid carbon formation for SF_6/C_2F_4 mixture with identical mixed fraction. However, with the further addition of C_2F_4, solid formation can possibly occur. The critical breakdown fields considering the solid carbon formation which usually takes place in the arcing phase are quite different from those without considering the solid carbon as indicated in Fig. 6.18. These deviations are due to the apparently different species composition obtained under both conditions. Take pure C_2F_4 as an example, the solid carbon formation makes pure CF_4 gas exist in the gaseous phase at room temperature. However, C_2F_6 is predominant in the gas mixture if there is no solid carbon formation. As a result of lower dielectric strength of CF_4 than that of C_2F_6 at room temperature, the case without solid carbon

formation has a higher critical reduced breakdown field at room temperature. When solid carbon disappears in the system as the temperature increases, both cases have completely identical results because of the same species composition.

6.3.4.4 Influence of Departure From Equilibrium on Hot Gas Breakdown

The reduced critical breakdown filed calculated above is based on the equilibrium species composition. However, as discussed in the section two, if the temperature cooling rate is quite large, the system has no sufficient time to reach equilibrium state and departure from chemical equilibrium occurs. In practice, it is necessary to investigate the influence of departure from equilibrium on hot gas dielectric strength. Moreover, the consideration of electron kinetics is not sufficient to obtain reliable data on critical electric field as soon as the role of ions becomes significant. In fact, the critical field is sensitive to the size of the electron avalanche. It must be high when the size of the electron avalanche is lowered by the processes removing electrons. The critical field must be low when this avalanche size is enhanced. The reactions which contribute to enhance the electron avalanche are ionization for electron kinetics and detachment for ion kinetics while those decreases of the electron avalanche are attachment for electron kinetics and recombination (negative ion-positive ion recombination or electron-positive ion recombination.) for ion kinetics. Therefore, the ion kinetics which mainly involves the dominant ions present at higher gas temperature such as negative ions F^-, S^- and also certain diatomic and atomic positive ions such as SF^+ and S^+ should be taken into account as well.

We use the kinetic method utilized in section two to obtain the species composition. We assume the temperature cooling rate from 12000 K to 5000K is 5E8K/s and at the starting point, the equilibrium species composition is used. From 5000K, we perform the kinetic analysis of species composition under different temperature cooling rates 2E8K/s, 1E8K/s, 5E7K/s and 1E7K/s. Finally the critical electron field is obtained from the solution of the following ordinary differential equation of the electron density evolution giving the balance between the electron generation and loss processes:

$$\frac{\partial n_e(t)}{\partial t} = -\sum n_e n_{M_j} K_{recom-eM_j} - \sum n_e n_{M_j} K_{attach-eM_j} + \sum n_e n_{M_j} K_{ion-eM_j} + \sum n_{N_j} n_{M_j} K_{\det ach-N_jM_j} \quad (6.35)$$

where $K_{recom-eM_j}$, $K_{attach-eM_j}$, $K_{ion-N_jM_j}$ and $K_{\det ach-N_jM_j}$ are respectively the electron-molecular ion recombination rate, the electron- neutral molecular specie attachment rate, the electron-neutral molecular specie ionization rate and detachment rate. The determination of the critical reduced breakdown field is obtained by setting the net production rate as zero.

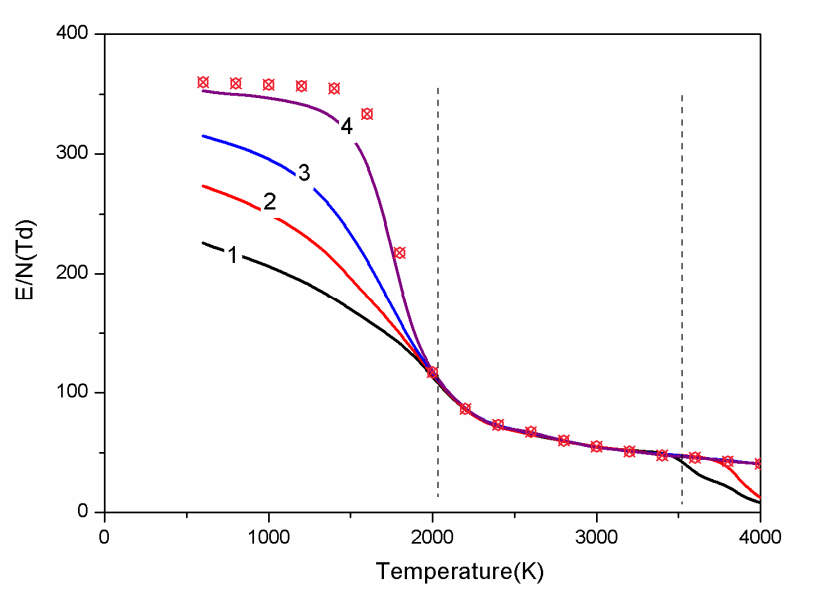

Figure 6.19 Calculated critical reduced electric field for hot SF_6 at a pressure of 1MPa. 1, *dT/dt*=-2E8 K/s; 2, *dT/dt*=-1E8 K/s; 3, *dT/dt*=-5E7 K/s; 4, *dT/dt*=-1E7 K/s. The data for equilibrium species composition is also given for comparison.

As the increase of the temperature cooling rate, the degree of departure from equilibrium increases. As found in figure 6.19, the critical breakdown field is reduced in the higher temperature range T>3500 K. This is partly attributed to the contribution of increased electrons number density which can greatly increase the electron-electron collision and hence affect the electron energy distribution function. Meanwhile, regardless of the abundance of atomic fluorine, it contributes little to the dielectric strength at elevated temperatures; in contrast, the neutral diatomic and polyatomic molecular species such as SF_2, SF which own a larger dielectric strength than that of the neutral atomic species have a relatively higher concentration under the slower cooling process at the same temperature. This can increase the critical reduced breakdown field as well. In the temperature range from 2000K to 3500K, the influence of electrons collision together with the deviation of the neutral diatomic molecular species' concentration is small under current temperature cooling rates; the discrepancy of

dielectric strength is negligible as well. With the further decrease of the temperature, the simple species including atomic and diatomic species in the system has no sufficient time to compose into large molecular species. Therefore, an increase of the temperature cooling rate causes a significant reduction of the critical dielectric properties at the same gas temperature.

6.4 Conclusion

This chapter investigates the decaying behaviour of SF_6 indicating that any departures from equilibrium obtained in the present work correspond to an electron overpopulation due to the finite reaction rate which tends to enhance the electrical conductivity of the plasma and thus to decrease the thermal interruption capability of SF_6 obtained by the local thermodynamic equilibrium model.

The main mechanisms of electrons elimination above the temperature 9000K is mainly the electron–atomic ion recombination. In the intermediate temperature range from 3500K to 7500K, the dominant mechanism is the dissociative attachment. In the temperature lower than 3500K, the influence of electron-molecular ion becomes increased. Moreover, the dissociative recombination essentially for diatomic molecular ion is predominant around the temperature 8000K.

The deviation of electron disappearance relaxation time under different temperature cooling rates mainly occurs in the intermediate temperature range from 4000K to 9000K where the dissociative recombination and dissociative attachment mechanisms especially involving diatomic molecular species are predominant. A larger temperature cooling rate leads to a higher value of electron disappearance relaxation time showing that a larger degree of departure from equilibrium occurs and a longer time is needed to reach the equilibrium state.

The presence of polyatomic charged species which were not taken into account have been included in current work indicating that the dominant polyatomic charged species are SF_3^+, SF_2^+, SF_5^- and SF_3^- in the order of substance concentrations which occurs mainly in lower temperature than 3000 K.

The critical reduced breakdown field for pure SF_6 is updated using most recent electron impact cross sections and gives excellent agreement with previous calculation estimation and experimental test. It was expected and has been shown that atomic fluorine, although abundant, contributes little to the dielectric strength at these temperatures. The influence of PTFE vapor injected into the SF_6 on dielectric strength of hot gas mixture has been studied with and without considering solid carbon formation. Both cases shows that the addition of PTFE vapor always causes a decreased dielectric strength compared with that of pure SF_6 in the temperature range $T<1700K$ where the dissociation of SF_6 does not occur. Above the temperature of 2500K, the addition of PTFE vapor leads to a higher critical breakdown field which is an important result for practical applications.

When departure from chemical equilibrium takes place, the critical breakdown field is reduced in the higher temperature range $T>3500$ K. This is attributed to the common contribution of the increased electron-electron collision and the reduced concentration of SF_2, SF which own higher dielectric strength under higher temperature cooling rate. There exists an intermediate temperature range from 2000K to 3500K in which the species composition is almost identical, the system has similar dielectric properties. With the further decrease of the temperature, the simple species including atomic and diatomic species in the system has no sufficient time to compose into large molecular species. Therefore, an increase of the temperature cooling rate causes a significant reduction of the critical dielectric properties.

6.5 Reference

[1] K. P. Brand and J. Kopainsky, "Particle Densities in a Decaying SF_6 Plasma", Appl. Phys., 16, 425 (1978).

[2] A. Gleizes, F. Mbolidi and A.A.M. Habibt, "Kinetic model of a decaying SF_6 plasma over the temperature range 12000 K to 3000 K", Plasma Sources Sci. Technoi. 2, 173 (1993).

[3] L. Adamec and O. Coufal, "On kinetics of reactions in HV circuit breakers after current zero", J. Phys. D: Appl. Phys., 32, 1702 (1999).

[4] B. Eliasson and E. Schade, "Electrical breakdown of SF_6 at high temperatures (<2300 K)", 1977, Proc. 13th Int. Conf. Phenomena in Ionized Gases (Berlin) pp. 409–10.

[5] E. Schade, "Recovery of switching arcs", Proc. 17th Int. Conf. Phenomena in Ionized Gases , Budapest, pp. 277–97 (1985).

[6] L. Rothhardt, J. Mastovsky and J. Blaha, "Dielectric strength of SF_6 at elevated temperatures", J. Phys. D: Appl. Phys., 14, L215 (1981).

[7] L. Rothhardt, J. Mastovsky and J. Blaha, "Breakdown experiments in diluted SF_6 at elevated temperatures", J. Phys. D: Appl. Phys., 18, L155 (1985).

[8] L. Rothhardt, J. Mastovsky, G. Jahn and J. Blaha, "Breakdown experiments in air and nitrogen above 1500K", J. Phys. D: Appl. Phys., 14, 715 (1981).

[9] T. Uchii, K. Iwata, H. Kawano, T. Nakamoto, and K. Suzuki, "Behaviour in Inhomogeneous High-temperature SF_6 Gas in a Gas Circuit Breaker", IEEE Power-Eng. Society Winter Meeting Conference Proc. Vol. 1, pp. 289-94, 2001.

[10] J. D. Yan, M. T. C. Fang and Q. S. Liu, "Dielectric breakdown of a residual SF_6 plasma at 3000K under diatomic equilibrium", IEEE T DIELECT EL IN, 4, 114 (1997).

[11] G. J. Cliteur, Y. Hayashi, E. Haginomori and K. Suzuki, "Calculation of the uniform breakdown field strength of SF_6 gas", IEEE T DIELECT EL IN, 5 843 (1998).

[12] M. Yousfi, Ph. Robin-Jouan, Z. Kanzari, "Breakdown Electric Field Calculations of Hot SF_6 for High Voltage Circuit Breaker Applications", IEEE T DIELECT EL IN, 12, 1192 (2004).

[13] Ph. Robin-Jouan, M. Yousfi, "New Breakdown Electric Field Calculation for SF_6 High Voltage Circuit Breaker Applications," *Plasma* Sci. Technol., 9, 690 (2007).

[14] Y. Tanaka, "Prediction of dielectric properties of N_2/O_2 mixtures in the temperature range of 300–3500K", J. Phys. D: Appl. Phys., 37, 851 (2004).

[15] Y. Tanaka, “Influence of copper vapor contamination on dielectric properties of hot air at 300-3500 K in atmospheric pressure”, IEEE T DIELECT EL IN, 12, 504 (2005).

[16] W. C. Lewis, A System of Physical Chemistry vol 1, London: Longmans, 1920.

[17] S. Vacqui´e, A. Gleizes, and M.Sabsabi, “Measurements of the photodetachment cross section of the negative ion fluorine”, Phys. Rev. A, 35, 1615 (1987).

[18] E. J. Robinson and G. Geltman, “Single- and double-quantum photodetachment of negative ions”, Phys. Rev., 153 4 (1967).

[19] S. Glastone, Textbook of Physical Chemistry 2nd edn, New York: Van Nostrand, 1946.

[20] J. C. Jungers, J. C. Balaceanu, F. Coussemant, F. Eschard, A. Giraud, M. Hellin, P. Leprince, and G. E. Limido, “Cin´etique Chimique Appliqu´ee”, Paris: Soci´et´e des Editions Techniques, 1958.

[21] G. Cliteur, K. Suzuki, H. Ikeda and S. Yanabu, “A collisional-radiative SF_6 arc plasma model using Boltzmann analysis”, IEEE Trans. Plasma Sci., 25, 996 (1997).

[22] E. Borge, “Mod´elisation de la cin´etique chimique d’un plasma d’arc d’hexafluorure de soufre (SF_6) en presence d’impuret´es”, PhD Thesis Paul Sabatier University, Toulouse, 1995.

[23] V. N. Kondrat’ev, “Kinetics of Chemical Gaseous Reactions”, Moscow: Academy of Sciences, in Russian, 1958.

[24] J. W. Wilson and A. Shapiro, “Nuclear-induced excimer fluorescence”, J. Appl. Phys., 51, 2387 (1980).

[25] R. Girard, J. B. Belhaouari, J. J. Gonzalez, and A. Gleizes, “A two-temperature kinetic model of SF_6 plasma”, J. Phys. D: Appl. Phys., 32, 2890 (1999).

[26] L. Adamec and O. Coufal, “Comments on the computation of the composition of quenching media in HV circuit breakers after current zero”, J. Phys. D: Appl. Phys., 30, 1646 (1997).

[27] L. Adamec, “Kinetical systems—local analysis Application of Mathematics”, 43, 111 (1998).

[28] L. Lallement, A. Rhallabi, C. Cardinaud, M. C. Peignon-Fernandez, and L. L. Alves, “Global model and diagnostic of a low-pressure SF_6/Ar inductively coupled plasma”, Plasma Sources Sci. Technol. 18, 025001 (2009).

[29] G. Kokkoris, A. Panagiotopoulos, A. Goodyear, M. Cooke, and E. Gogolides, “A global model for SF_6 plasmas coupling reaction kinetics in the gas phase and on the surface of the

reactor walls", J. Phys. D: Appl. Phys., 42, 055209 (2009).

[30] R. Krishnan, A.C. Hindmarsh, Description and Use of LSODE, the Livermore Solver for Ordinary Differential Equations, NASA-RP-1327 UCRL-ID-113855, E-5843, 1993.

[31] J. C. Butcher, Numerical Methods for Ordinary Differential Equations, John Wiley, ISBN 978-0-471-96758-3, 2003.

[32] S. Gordon and B. J. McBride, "Computer program for calculation of complex chemical equilibrium composition, rocket performance, incident and reflected shocks, and chapman jouguet detonations", NASA publication SP-273, 1971.

[33] V. Rat, A. B. Murphy, J. Aubreton, M. F. Elchinger, and P. Fauchais, Treatment of non-equilibrium phenomena in thermal plasma flows, J. Phys. D: Appl. Phys., 41, 183001 (2008).

[34] K. L. Baluja and J. A. Tossell, "Electron scattering by the sulfur fluoride radical using the R-matrix method", J. Phys. B: At. Mol. Opt. Phys., 36, 19 (2003).

[35] K. L. Baluja and J. A. Tossell, "Electron collisions with the SF_2 radical using the R-matrix method", J. Phys. B: At. Mol. Opt. Phys., 37, 609 (2004).

[36] Speckhofer G et al, "A consistent set of thermodynamic properties and transport coefficients for high temperature plasmas", 14th Int. Symp. On Plasma Chemistry, Prague, Czech Republic, 1999.

[37] M. Tashiro, "Electron impact excitations of S_2 molecules", Chem. Phys. Lett., 453, 145 (2008).

[38] J. S. Rajvanshi and K. L. Baluja, "Electron-impact study of the S_2 molecule using the R-matrix method", Physical Review A, 84, 042711 (2011).

[39] M. A. Ali, K. K. Irikura, Y. K. Kim, "Electron-impact total ionization cross sections of SF_x (x=1–5)", Int. J. Mass Spectrom., 201, 187 (2000).

[40] H. Itoh, Y. Miura, N. Ikuta, Y. Nakao and H. Tagashira, "Electron swarm development in SF_6. I. Boltzmann equation analysis", J. Phys. D: Appl. Phys., 21, 922 (1988).

[41] T. M. Miller, A. E. S. Miller and J. F. Paulson, "Thermal Electron Attachment to SF_4 and SF_6", J. Chem. Phys., 100, 8841 (1994).

[42] M. Hayashi and T. Nimura, "Calculation of Electron Swarm Parameters in Fluorine", J. Appl. Phys., 54, 4679 (1983).

[43] W. L. Morgan, A Humid Air Chemistry Kinema Research& Software, http://www.kinema.com/, 2003.

[44] M. Yousfi, Ph. Robin-Jouan, Z. Kanzari, "Electron-molecule collision cross sections needed for breakdown electric field calculations of hot dissociated SF_6", Journal of Physics: Conference Series, 115, 01201 (2008).

[45] S. Vacquie, A. Gleizes, and M. Sabsabi, "Measurement of the Photodetachment Cross Section of the Negative Ion of Fluorine", Phys. Rev. A, 35, 1615 (1987).

[46] M. Hayashi and A. Niwa, in Gaseous dielectrics V, Proceedings of the 5th international symposium on gaseous dielectrics, 1987.

[47] H. Okumo and Y. Nakamura, "Electron transport coefficients in C_2F_6-Ar mixtures and inelastic cross sections for the C_2F_6 molecule", Proceedings of International Conference on Atomic and Molecular Data and Their Applications, Gaithersburg, Maryland, ETATS-UNIS, 1999.

[48] M. C. Bordage, P. Segur, and A. Chouki, "Determination of a set of electron impact cross sections in tetrafluoromethane consistent with experimental determination of swarm parameters", J. Appl. Phys., 80, 1325 (1996).

[49] M. C. Bordage, P. Segur, L. G. Christophorou and J. K .Olthoff, "Boltzmann analysis of electron swarm parameters in CF_4 using independently assessed electron-collision cross sections", J. Appl. Phys., 86, 3558 (1999).

[50] I. Rozum, P. Limao-Vieira, S. Eden, J. Tennyson, and N. J. Mason, "Electron interaction cross sections for CF_3I, C_2F_4 and CFx(x=1-3) radicals", J. Phys. Chem. Ref. Data, 35, 267 (2006).

[51] M. T. Lee, I. Iga, L. E. Machado, L. M. Brescansin, E. A. y. Castro, G. L.C. de Souza, "Theoretical study of electron collisions with the CF_2 radical", Physical Review A, 74, 052716 (2006).

[52] W. M. Huo, V. Tarnovsky, and K. H. Becker, "Total electron-impact ionization cross-section of CF_x and NF_x(x=1-3)", Chem. Phys. Lett., 358, 328 (2002).

[53] K. Yoshida, S. Goto, H. Tagashira, C. Winstead, B. V. Mckoy, W. L. Morgan, "Electron transport properties and collision cross sections in C_2F_4", J. Appl. Phys. ,91, 2637 (2002).

[54] Morgan database, http://www.lxcat.laplace.univ-tlse.fr

[55] S. E. Michelin, H. L. Oliveira, L. S. S. Soares, E. Veiteinheimer, C. A. R. Luz, K. T .Mazon, M. M. Fujimoto, and M. T. Lee, "Cross sections for electron–C_2 collisions", Chemical Physics, 309, 177 (2005).

[56] G. Halmov´a, J. D. Gorfinkiel and J. Tennyson, “Low-energy electron collisions with C_2 using the R-matrix method”, J. Phys. B: At. Mol. Opt. Phys., 39, 2849 (2006).

[57] R. Naghma and B. Antony, “Electron impact ionization cross-section of C_2, C_3, Si_2, Si_3, SiC, SiC_2 and Si_2C”, Molecular Physics, 111, 267 (2012).

[58] H. Munjal and K. L .Baluja, “Elastic and excitation processes of electron impact on C_3 using the R-matrix method”, J. Phys. B: At. Mol. Opt. Phys., 39, 3185 (2006).

[59] W. L. Morgan and B. M. Penetrante, “ELENDIF: A Time Dependent Boltzmann Solver for Partially Ionized Plasmas”, Computer Phys. Commun., 58, 127 (1990).

[60] L. C. Pitchford, S. V. ONeil and Jr. J. R. Rumble, “Extended Boltzmann Analysis of Electron Swarm Experiments”, Phys. Rev. A, 23, 294 (1981).

[61] S. D. Rockwood, “Elastic and inelastic cross sections for electron-Hg scattering from Hg transport data”, Phys. Rev. A, 8, 2348 (1973).

[62] C. J. Elliott and A. E. Greene, “Electron energy distributions in e-beam generated Xe and Ar plasmas”, J. Appl. Phys., 47, 2946 (1976).

CHAPTER 7 EXPERIMENTAL INVESTIGATION OF DYNAMIC CHARACTERISTICS AND DECAYING BEHAVIOUR OF SF_6 ARCS IN A SUPERSONIC NOZZLE

7.1 Introduction

Current interruption is closely associated with the electric arc physical phenomena. During circuit breaker operation, the arc discharge between the electrodes gap changes rapidly from a conductive plasma to an insulating gas. The electrical arc performance during this short period of time is dependent on the energy balance in the plasma column. To operate successfully, the circuit breaker must be capable of interrupting this current in a short period of time, around current zero. In order to assess circuit breaker capability during current interruption, many arc physical models are suggested and much theoretical work is performed as reviewed in chapter 1. It should be noted that despite the many computer aided design options available today [1]-[2], it is still not possible to neglect the experimental test to inform the modelling. These extremely time-consuming and cost-intensive experimental investigations return the maximum amount of information and knowledge which, in turn, makes the development more assured faster and thorough.

Numerous experimental investigations have been carried out to measure macroscopic parameters such as the voltage across the electrode gap and the current passing through the arc discharge channel from which we can obtain the arc resistance evolution characteristics and provide the opportunity to study the dynamic arc behaviour in detail [3]-[8]. Based on this experimental work several arc models have been proposed, many of them focused on fitting measured data and model results. Additionally, recent investigation has been gradually focused on the physical information related to the arc itself such as the pressure, electron density, temperature, and species composition as well as more detailed information related to arc quenching process which has been presented in [9]-[18]

For high-voltage circuit-breakers, SF_6 gas is exclusively used because of its high insulation strength and its high fault-current interruption capability. However, it is known that

this artificial gas has an extremely high global warming potential (GWP) of 23 900 over 100 years and is regarded as a greenhouse effect gas in the 3rd Conference of the Parties to the United Nations Framework Convention on Climate Change (COP3). This means that SF_6 can absorb and reradiate some of the earth's natural infrared radiation back to earth and results in an elevation of the average surface temperature. Additionally, its lifecycle management is a challenge for utility and industrial users and the cost of handling it in a compliant manner can also be substantial, particularly when decommissioning aging substations. Therefore, a comparative investigation of arc and decaying characteristics between SF_6 and the pure gases of CO_2 (lower GWP) and N_2 (environment-friendly gas) is also desirable.

Based on what has been mentioned above, this research utilized the experiments to investigate the dynamic characteristics and decaying behaviour of SF_6 arcs in a supersonic nozzle. To accomplish this, a representation of a circuit breaker was used in which an arc could be drawn between the electrodes. The arc behaviour was studied by means of voltage and current measurements, optical spectrometer, displacement and pressure monitoring. This chapter is organized as follows: the experimental apparatus and diagnostic apparatus are respectively described in section 2 and section 3. The diagnostic results and analysis are presented in section 4. The typical characteristics of decaying SF_6 arcs in a supersonic nozzle under different interruption currents with and without gas flow are reported. The variation of electrode movement, gas pressure, and arc resistance together with arc radiation has been obtained. Additionally, a comparative investigation of arc interruption capability of SF_6 and pure gases of CO_2 (lower GWP) and N_2 (environment-friendly gas) has been preformed and discussed. The possible species occurring in the arcing phase in which PTFE nozzle ablation usually takes place has been investigated by an optical emission spectroscopy. Finally, conclusions are drawn in Section 5. It is believed that these studies may contribute much to the future circuit breaker development

7.2 Experimental Apparatus

7.2.1 Main Test Chamber

The test chamber comprised of a steel cylinder with four cylindrical ports se 90^o from each

other that contained windows made of 18mm thick toughened class which allowed monitoring of the arc. The ports could also be fitted with special brackets to allow the fitting of other apparatus, such as optical fibre points. The lid of the chamber was steel and secured using sixteen 15mm diameter bolts and sealed with a rubber o-ring allowing pressurization of the vessel with gases. This can prevent the leakage of potentially harmful arc by products. The lid of the chamber contained a central mounting for the initiation electrode mechanism and radial screw mounts for internal sensor accouchement. The main external features of the test chamber are shown in Fig.7.1.

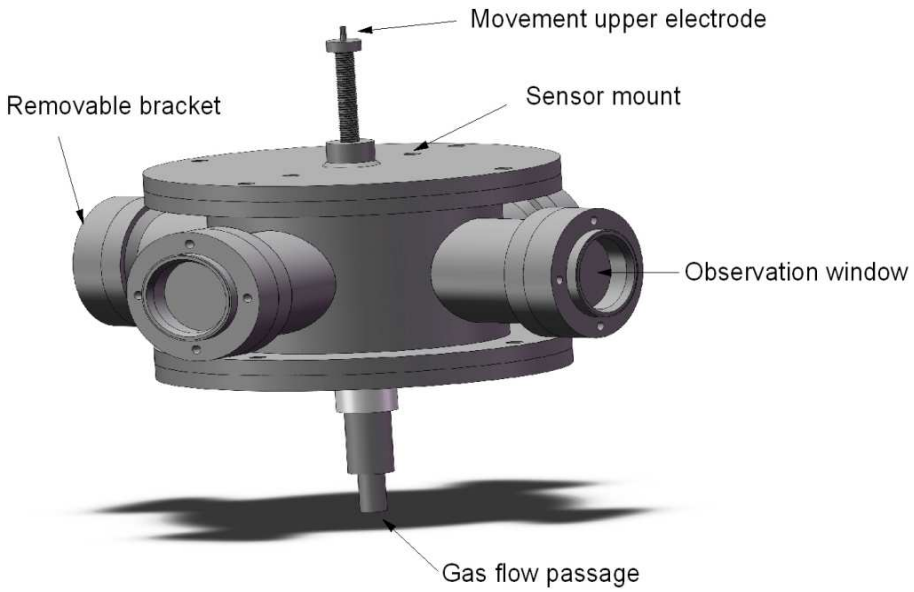

Figure 7.1 Main external features of experiment chamber

The design of this apparatus was such that it provided a realistic environment but still allowed easy access for diagnostic apparatus and faster experiment turnaround time than would be experienced with a full scale circuit breaker. The total volume, including the central chamber and observation arms, was $0.017m^3$, which was large enough to minimize pressurization effects.

The electrodes were copper and cylindrical in shape with a length of 50mm and diameter 10mm, mounted centrally in the chamber and spaced 60mm apart. The anode was the lower electrode and was fed via a high voltage cable connected to a capacitor bank; ground and experimental earth were connected to the body of the chamber and the second

electrode, which also contained the arc initiation mechanism. The cathode was the upper electrode with the same dimensions as a copper-tungsten initiation electrode retracted. The anode was mounted centrally in a steel cylindrical bracket which was insulated by PTFE materials from the body of the chamber and the lower plate. There are six holes from which the blast gas can flow into the chamber. The cathode and initiation electrode mechanism were directly connected to the chamber and therefore earthed.

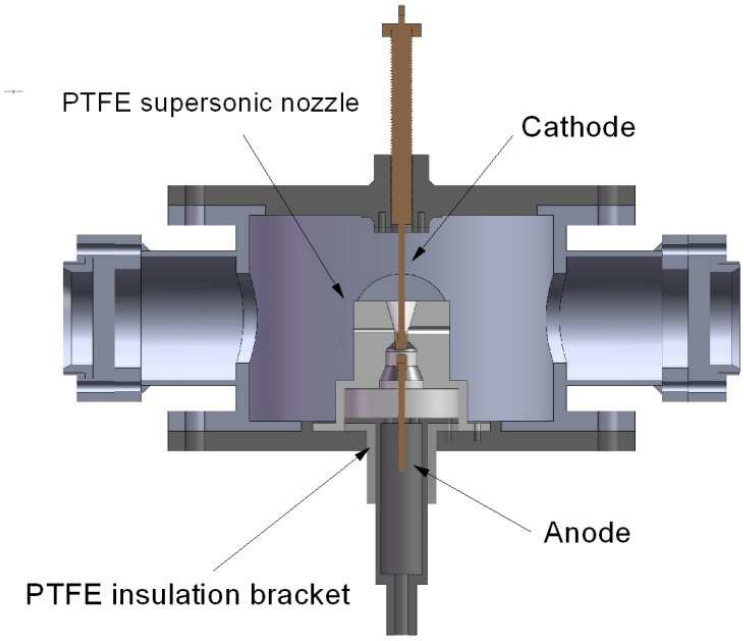

Figure 7.2 Internal features of experiment chamber

A supersonic nozzle made of PTFE was mounted centrally on the lower plate. The internal features of the test chamber were shown in Fig.7.2. Both electrodes were screw mounted into the chamber allowing easy replacement when worn. The formation of the arc centrally in the chamber meant its characteristic could be observed more easily by optical access.

7.2.2 Capacitor Bank Circuit

Arcs are formed by supplied energy from a capacitor bank to the test chamber electrodes via a series electric resistance and inductor. The simultaneous application of this energy with the separation of the test chamber electrodes was sufficient to cause ionization and dielectric breakdown that developed into an arc discharge between the anode and cathode.

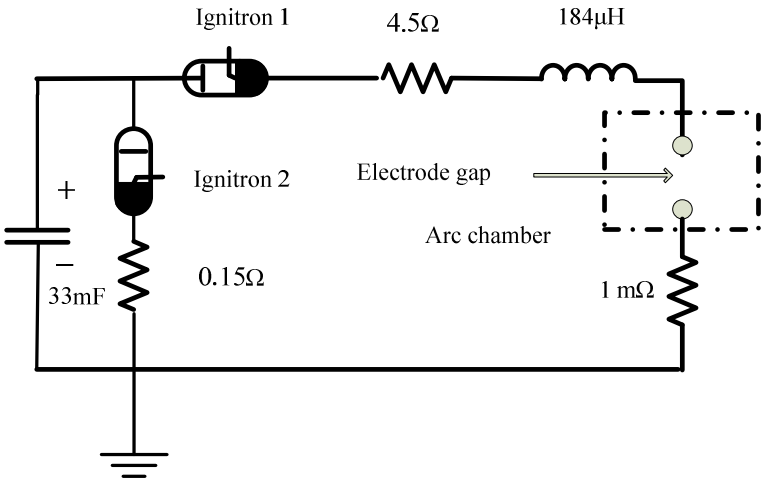

Figure 7.3 Capacitor bank discharge circuit diagram

The capacitor bank consisted of a 33mF bank and an ignitron based control circuit. The ignitrons were used as switching devices in order to control the discharge of the capacitor bank into the test chamber and its deactivation at end of each experiment in accordance with the control signals. The experimental circuit consisted of an 184μH inductor in series with a 0.15Ω electric resistance; a 1mΩ current shunt was in series. Schematic diagram of the capacitor bank connection is shown in Fig.7.3.

In each experiment the capacitor bank was charged, subsequently the first ignitron was triggered in synchronism with the activation of the initiation electrode and triggering of other apparatus, discharging the capacitor bank via the electric resistance and inductor circuit and forming the arc. The apparatus was configured to form a pseudo-dc arc in initiation for a maximum duration of 220ms.

Configuration of the timing and control unit determined when the second ignitron was activated to discharge the remaining capacitor bank energy to earth and extinguished the arc (if it had not already been extinguished by the interruption medium). In all tests the maximum time period was set to the 220ms in order to enable a stable arc to be formed between the electrodes to allow experimental consistency; allow the blast-gas injection into the plasma, and to permit the interaction to be monitored in detail.

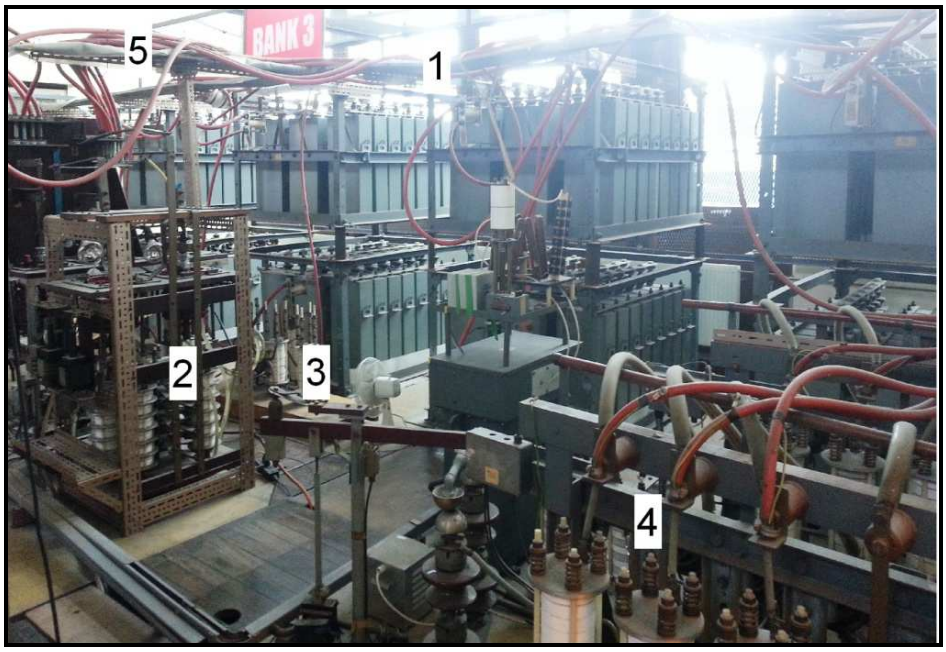

Figure 7.4 Full configuration of capacitor bank and associated circuit. 1, Capacitor bank; 2, Ignitrons and control signals interface; 3, Electric resistance stack; 4, Discharge mechanism; 5, Bank output cabling.

7.2.3 Arc Initiation and Timing Control

The arc formation mechanism consisted of a cylindrical copper-tungsten imitation electrode 300mm long and 6mm in diameter that retracted into the cathode, driven by a solenoid which was powered by an 115V/5A DC power supply supplemented by booster capacitors of total capacitance 2.94mF. The initiation electrode was driven by the solenoid and reaches its full length between electrodes after activation. At the start of the experiment, the initiation electrode was in contact with the anode. The solenoid was triggered by the timing and control system to move in synchronism with the discharge of the capacitor bank energy, drawing an arc between the anode and the initiation electrode. When the initiation electrode was fully retracted the arc was established between the anode and cathode and was at full length. A cut away view of the initiation apparatus is shown in Fig.7.5. The correct synchronization between the capacitor bank discharge and movement of the initiation electrode was important to ensure arc formation. The timing and control unit needed to be configured to account for the mechanical delay due to inertia in the solenoid movement so as to discharge the capacitor bank simultaneous to when the initiation electrode began to move.

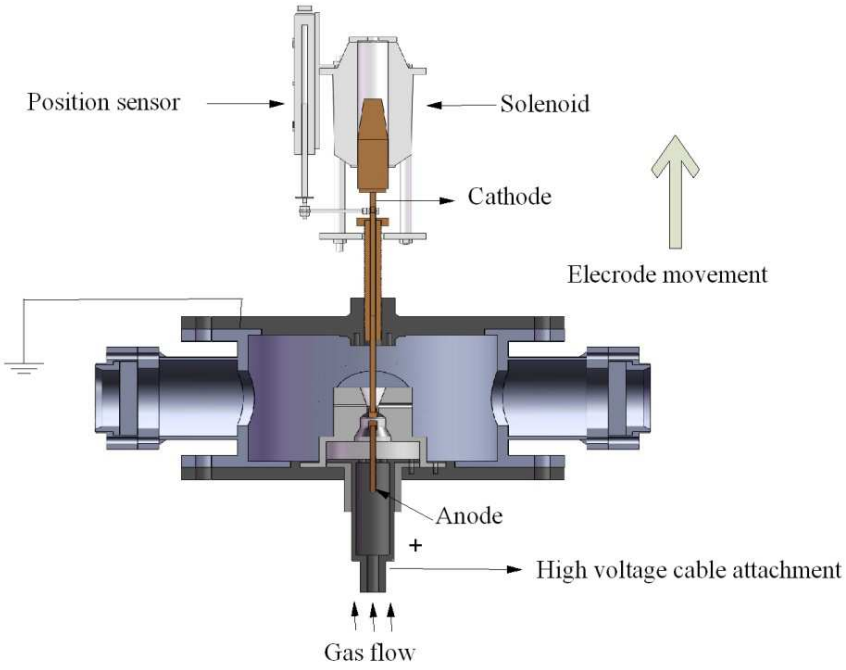

Figure 7.5 Cut-away view of initiation electrode solenoid mechanism

Trigger signals for all of the apparatus and diagnostic equipment emanated from a central control unit. In the first instance the control unit was used to charge capacitor bank via a manually operated variac. The trigger signals for all of the apparatus consisted of 200V/μs pulses that emanated from the control unit; the sequence of each trigger was adjusted based on the results of calibration tests performed initially in the absence of an arc. This was necessary in order to ensure that the arc initiation apparatus and diagnostic equipment activation occurred in the correct sequence.

The delay between the solenoid trigger and the movement of the initiation electrode was found to be 20ms; as a result of this the capacitor bank was not triggered until 20ms after the solenoid trigger. The second ignitron, used to end the experiment by discharging the remaining capacitor bank energy to earth through a resistor of 0.15Ω, was triggered last and configured to cause a maximum arc duration of 220ms. If gas blast is used, it is initiated before the capacitor bank trigger.

7.2.4 Gas Handling Apparatus

A gas handling plant was used to both add different gases to the chamber and also, importantly, flush out potentially harmful arcing by products. In cases where only a gas was used, such as with SF_6, the chamber was reduced to a vacuum before being re-filled with the test gas to 101kPa. After each test, the chamber was twice reduced to a vacuum and flushed with N_2 in order to remove any gaseous by-products of the reaction and prevent contamination of later tests.

The flow of gas into the chamber was controlled by a 500kPa regulator attached to the source compressed gas cylinder. Gasses N_2, CO_2, and SF_6 were used in the course of the project provided by 11m^3, 230bar gas cylinders. When the test chamber was at the desired pressure, valve was closed before the experiment commenced. The chamber could be refilled with atmospheric air following cleaning or flushing by opening valve. Following a test, an electric 0.16kW Edwards 5 two stage rotary vacuum pump was used to pump the gas from the chamber. In order to remove harmful species, two filters were used, a carbon pellet type prior to the gas entering the pump and a liquid sodium variety before the gases were emitted after disposed. To ensure the removal of harmful gasses or contaminants that could after the accuracy of test results the chamber was flushed with N_2 following the gas extraction.

When SF_6 gas was used, a Dilo Type B048R01 SF_6 recovery system was utilized attached via a filter to replace the pump and atmospheric outlet system. This prevented the environmentally damaging gas escaping into the atmosphere after it was used.

7.3 Diagnostic Apparatus

7.3.1 Current and Voltage Measurement

The changes in electrical characteristics of the arcs were studied to determine the arc quenching efficiency and mechanisms that occurred. A high voltage probe was an ISO9001 compliant Tektronix P6015A passive high voltage probe and corresponding compensation box with 7-49pF range. The probe had a 1000Xattenuation effect such that the voltage displayed

on the oscilloscope was understated by a factor of 1000. Current was measured by use of a Tomas type current shunt, using a 1mΩ manganin electric resistance with 1000:1 ratio connected via a coaxial cable to the oscilloscope. The shunt was considered to have an accuracy of 0.5% with a derating factor of 66% for continuous use, defined as being greater than 2mins, so was not a factor in any of these tests. The current shunt was mounted on experimental earth. This is a common configuration in power application in order to eliminate any common mode voltage that could damage the oscilloscope measuring device. The voltage and current probes were to a Tektronix 2230 100MHz two-channel oscilloscope, which in turn was connected to a data-logging computer running the Tektronix WaveStar software. The oscilloscope was triggered externally by a signal from the timing and control unit via a 2kV/2μs isolation pulse transformer.

7.3.2 Pressure Measurement

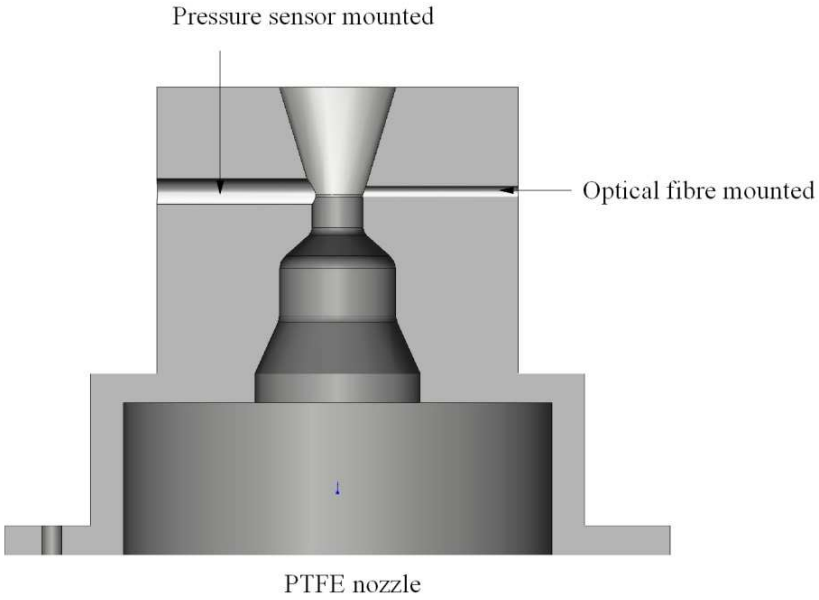

Figure 7.6 Mounted pressure senor and optical fibre

Gas blast is often used in circuit breaker to intense gas flow that in turn increases convective cooling of the arc. Any pressure increase were studied by pressure sensing apparatus consisted of a Kistler type pressure sensor. The sensor utilized the piezoelectric effect via a quartz crystal with the pressure measured during arcing through a diaphragm pressure measurement and rapid changes expected in arcing experiments. A charge amplifier converted the small

charge from the sensor crystal into a proportional voltage that could be monitored and stored via a Tektronix 2230 oscilloscope. It consisted of an inverting voltage amplifier with a high open loop gain and extremely high input impedance, being such that the capacitance of the sensor and cable could be neglected.

The pressure monitoring oscilloscope was triggered directly from the timing and control unit via a 2kV/2μs isolation pulse transformer. Voltage calibration of the pressure sensor was achieved by use of a Druck digital pressure indicator and compressed N_2, allowing the voltage displayed on the oscilloscope to be directly attributed to a value of pressure. The location of mounted pressure sensor and optical fibre can be found in Fig.7.6.

7.3.3 Optical Measurement

Optical emission spectroscopy is a common plasma diagnostic technique and provides many clues as to how the arc is changed by the application gases and so can aid in the understanding of the reaction and quenching mechanisms observed. A Stellarnet EPP 2000-LT14-VIS-10 optical spectrometer was used and interfaced with the Spectraviz software. The device used a CCD detector with a 1000:1 signal to noise ratio and pixel size 14mm×200mm. The dynamic range of the system was 2000:1. The software integration time was adjusted in order to maximize the detector output whist avoiding saturation and maximizing signal to noise ratio. The Spectrawiz software was configured with smoothing and averaging switched off in order to allow more accurate determination of low intensity spectral features with respect to the dominant copper emission lines formed from evaporated electrode materials. It should be noted that the integration time of the spectrometer means that the spectra is an average measurement during the integration time. It was normally set 4ms but changed according to the specified experimental condition from 4ms to 40ms.

The input of the spectrometer was connected to an SMA905 0.22na optical fibre that was clamped facing into the observation access mounted in the supersonic nozzle and pointing at the center of the electrode gap. The spectrometer was factory calibrated but was tested for wavelength and intensity by analysis of the main features of a test spectrum and reference to published spectra data. The spectrometer was found to be accurate to ±0.28nm

for wavelength and ±13.5% for relatively intensity. The larger error in intensity is due to an inherent difficulty in performing relative intensity calibration because published data is less accurate due to different scales being used in different publications. In terms of both wavelength and intensity the spectrometer was considered sufficiently accurate to be used for related comparisons.

Beside the spectrometer, the optical fibre is also directly connected to the oscilloscope by means of multi-channel photon detector amplifier system. The nozzle carried a 3 mm width slot located downstream of the nozzle throat to provide optical access for monitoring the arc plasma at a location believed to critically control arc extinction during current interruption. The introduction of such a sealed slot has been shown not to affect the circuit breaker performance.

7.3.4 Electrode Movement Measurement

During the test, the displacement of moving electrode is monitored by a Honeywell linear displacement sensor which transforms the mechanical linear displacement signal to the electric signal. The sensing element of a linear potentiometer is a conductive track. A wiper, attached to the operating shaft, contacts the track. As the shaft is moved, the resistance between one end of the track and the wiper changes in a linear manner.

Typically, a constant voltage is supplied across the ends of the conductive track and the potentiometer is used as a voltage divider. When used in this way, the voltage at the wiper is proportional to the shaft position. The sensing element consists of a stable, precision wire base track with a high resistivity conductive plastic bonded to it. The wiper contacts the plastic part of the track. This arrangement gives stability over a wide range of temperature and humidity as most of the current flows through the precision wire base element. This reduces the effect of wear compared to an all plastic construction. The bodies of the linear potentiometers are anodized aluminum and the shafts are stainless steel. The sensors are sealed to keep out dirt and dust but the seals are not intended to prevent the ingress of fluids under pressure. The shaft is captive and cannot be removed from the body. The full arc formation and diagnostic apparatus configuration can be found in Fig.7.7.

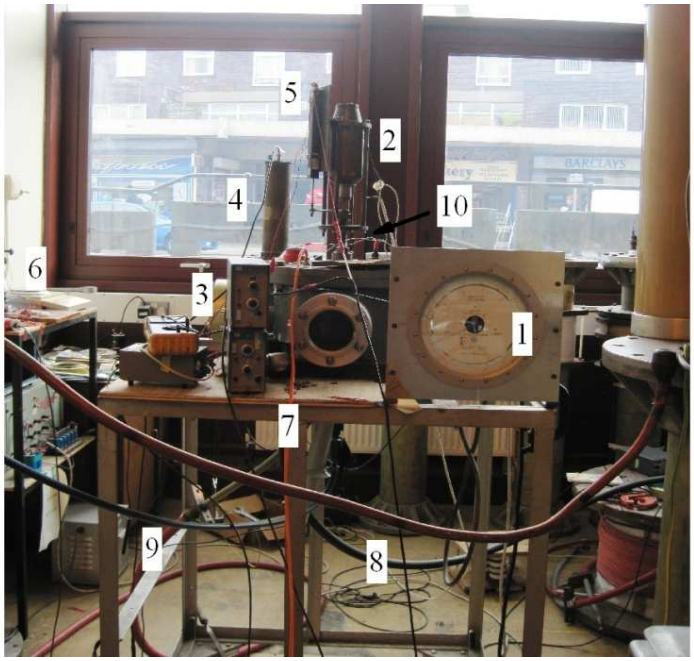

Figure 7.7 Full arc formation and diagnostic apparatus configuration. 1. Pressure gauge; 2, Solenoid; 3, Charge amplifier; 4, Current shunt; 5, Position sensor; 6, Time control circuit; 7, Optical fibre; 8, Gas flow pipe; 9, Power supply input; 10, pressure sensor cable.

7.4 Diagnostic Results and Analysis

7.4.1 Dynamic Characteristics of an SF_6 Arc without Gas Flow

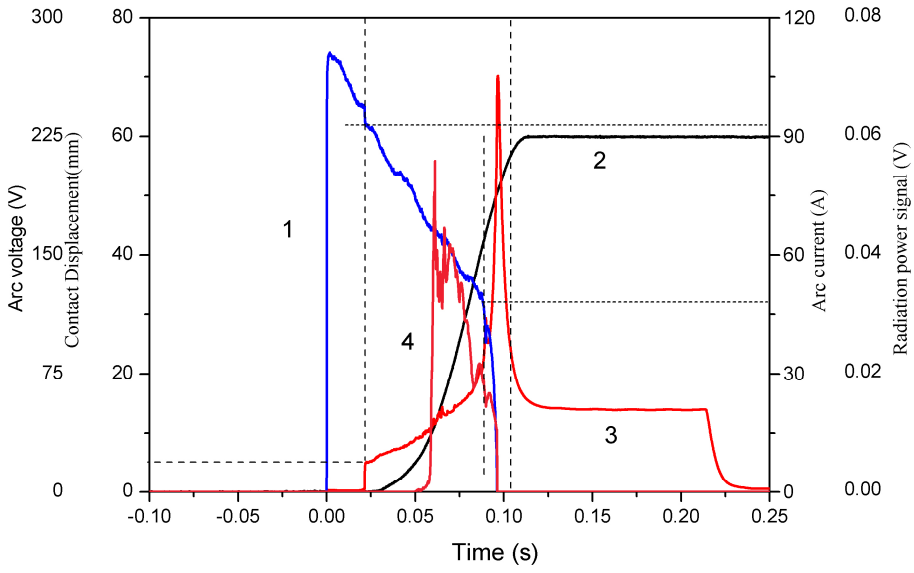

Figure 7.8 Experimental (1), arc current, (2) electrode displacement, (3) arc voltage, and (4) radiation power signal.

Fig.7.8 gives the typical results of the arc voltage, arc current, and electrode movement displacement together with the radiation power signal in the current interruption. At the time instant of 0s, the capacitor begins to discharge and there exists a current in the test circuit which gradually deceases due to the loss of energy from the capacitor bank. At the time instant of 0.023s, the solenoid is activated to drag the upper electrode to move upwards. At the beginning of the electrode separation, the current value is 92A together with a voltage jump of 19 V which is mainly attributed to the contribution of the sheath voltage drop in order to keep a balance of electrons and ions passing through the sheath in equal numbers. As the distance between the separated electrodes increases, the arc voltage drop across the electrode gap gradually increases by the rising gap electric resistance. The fault current decreases almost with a linear rate until the time instant of 0.08s at which a current value of 47A is reached. After that, the current rapidly reduces to zero meanwhile the arc voltage produces an extinction peak of 264 V. There is still a positive voltage across the electrode gap after the arc extinction until the system is dumped at the time instant of 0.22s. From what is indicated in Fig.7.8, the electrode separation can successfully interrupt the fault current in this case without gas flow.

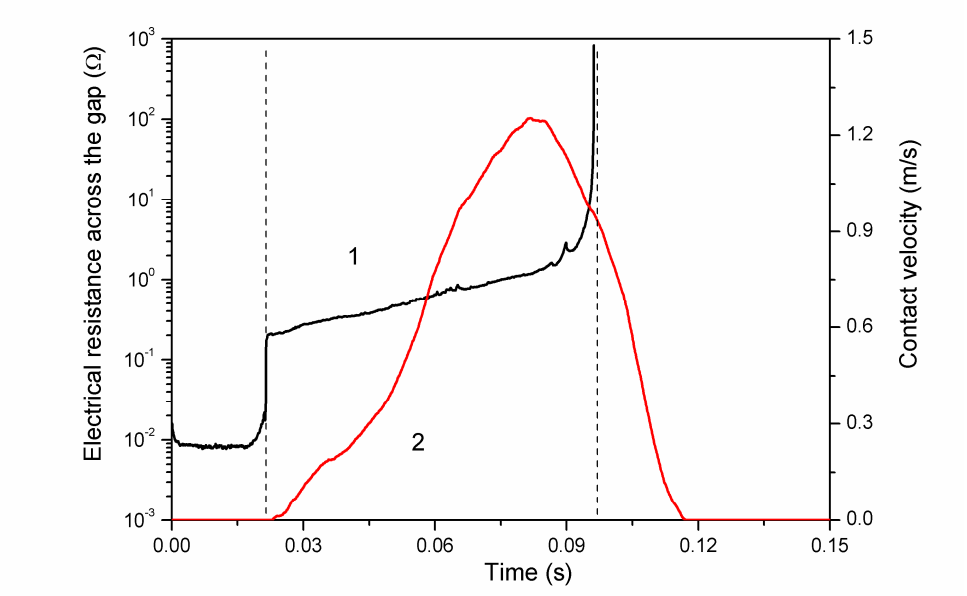

Figure 7.9 Calculated arc electrical resistance and electrode movement velocity according to the experimental results. (1), electrical resistance across the electrical gap; (2), contact velocity.

Fig.7.9 presents the calculated electric resistance across the electrode gap and the

electrode movement velocity by means of the signal obtained in Fig.7.8. The electrical resistance is 0.01Ω before the electrode separation. This is due to the contact electric resistance. With the further separation of electrodes, the arc electric resistance increases. During current zero period, the arc electric resistance increases quite rapidly showing that the temperature and hence the electrical conductivity of the arc discharge passage goes down rapidly. The upper electrode's velocity firstly increases until a peak value is reached at the time instant of 0.08s. After that, the velocity decreases before the contacts are fully open.

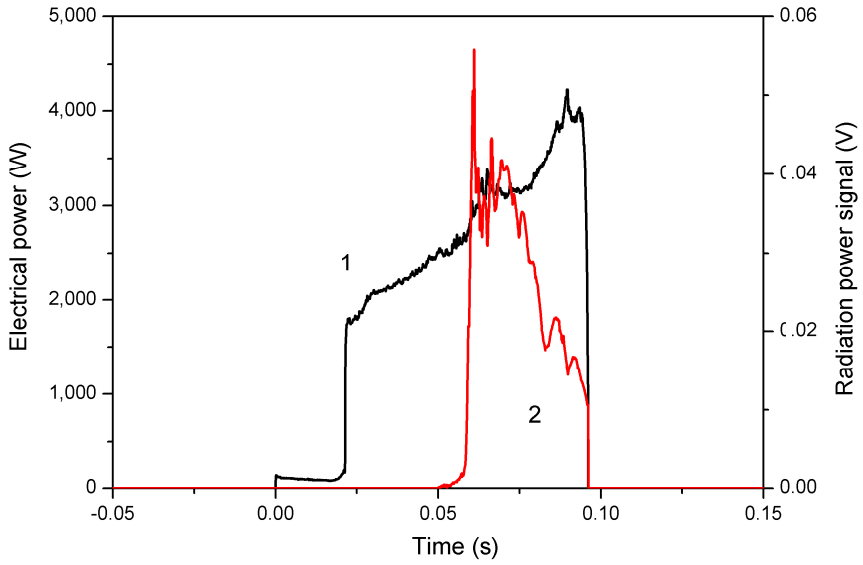

Figure 7.10 Calculated electric power across the electrode gap and radiation power signal by means of photon detector transformation. (1), electric power; (2), radiation power signal.

Fig.7.10 gives the electric power across the electrode gap and the radiation power signal recorded by photon detector system at the slot located downstream of the nozzle throat is also presented for comparison. The electric power shows a general increasing trend regardless of the reducing current which causes a reduction in the radial radiation power loss.

7.4.2 Influence of Different Interruption Currents

The dynamic characteristics of SF_6 arcs under two different interruption currents of 440 A and 165 A have been investigated. Fig.7.11 gives the voltage drop and arc current curves across the electrode gap. The sheath voltage drops at the beginning of electrodes separation under

both cases have almost identical value. In the time range of 220ms, system fails to break the fault current with an initial current amplitude of 440A until the end of the experiment by discharging the remaining capacitor bank energy to earth. The voltage drop in the first time period of 75ms is independent on the current amplitude indicating the dominant contribution of the voltage increase comes from the elongation of electrode gap. When the moving electrode reaches its full range at the time instant of 120ms, the voltage drop shows typical characteristics of fluctuation related to arc root movement with little dependence on the damping current.

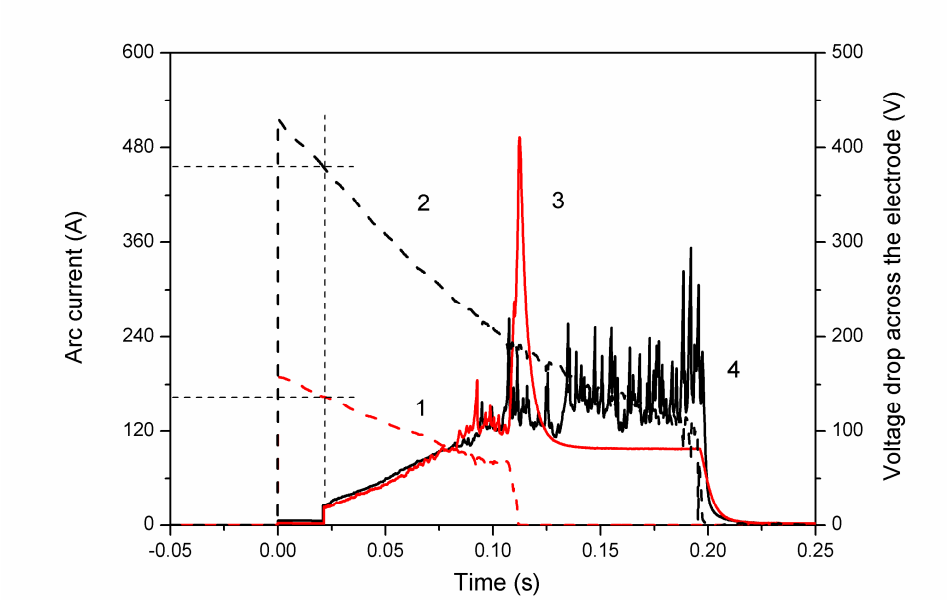

Figure 7.11 Experimental arc voltage and arc current under different interruption currents. (1), arc current, 160A; (2), arc current, 440A; (3), voltage drop across electrode gap, 160A; (4), voltage drop across electrode gap, 440A.

Fig.7.12 shows the calculated electric resistances across the electrode gap according to the experimental results. For the same value of electrode gap, a higher arc current produces lower arc electric resistance due to a larger conducting cross section area. During the current-zero period, the gap resistance shows an extremely rapid rise due to arc extinction which can be found in Fig.7.13.

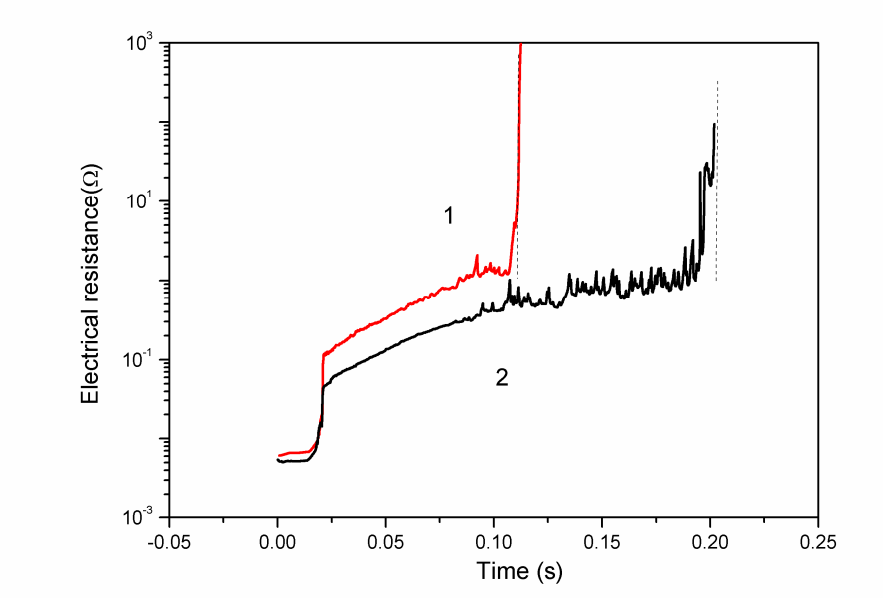

Figure 7.12 Calculated electric resistances across the electrode gap under different interruption currents according to the experimental results. (1), 160A; (2), 440A.

The power input across the gap at first increases due to the elongation of the arc. This is caused by an increase of arc resistance as presented in Fig.7.12 which outweighs the influence of the damping current.

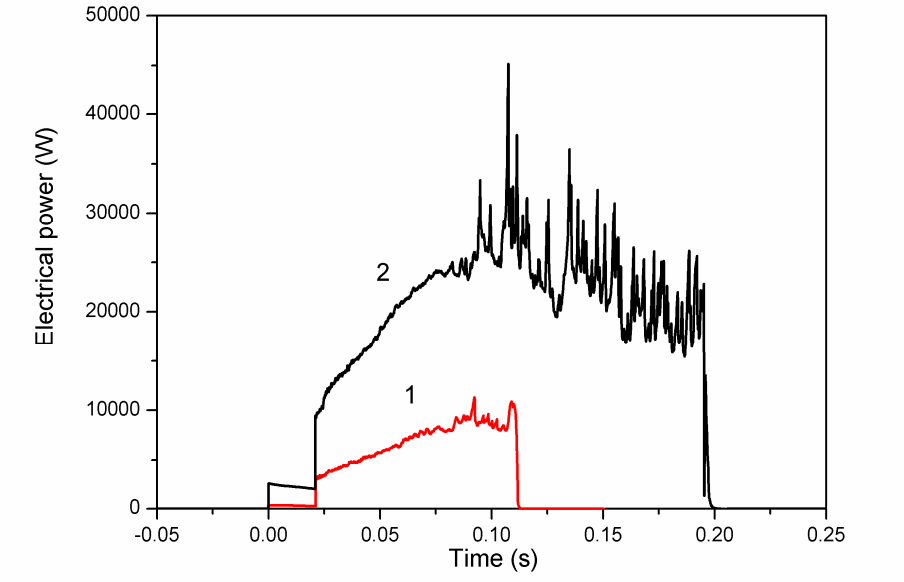

Figure 7.13 Calculated electric power across the electrode gap. (1), 160A; (2), 440A.

The electric power under the case with an initial interruption current of 440 A reaches

its maximum value at the time instant of 100ms and then gradually decreases. When the moving electrode reaches its full range, the energy input power across the electrode gap in this case with an initial interruption current of 440 A shows fluctuation behaviour which is caused by the voltage fluctuation in this period due to arc root movement.

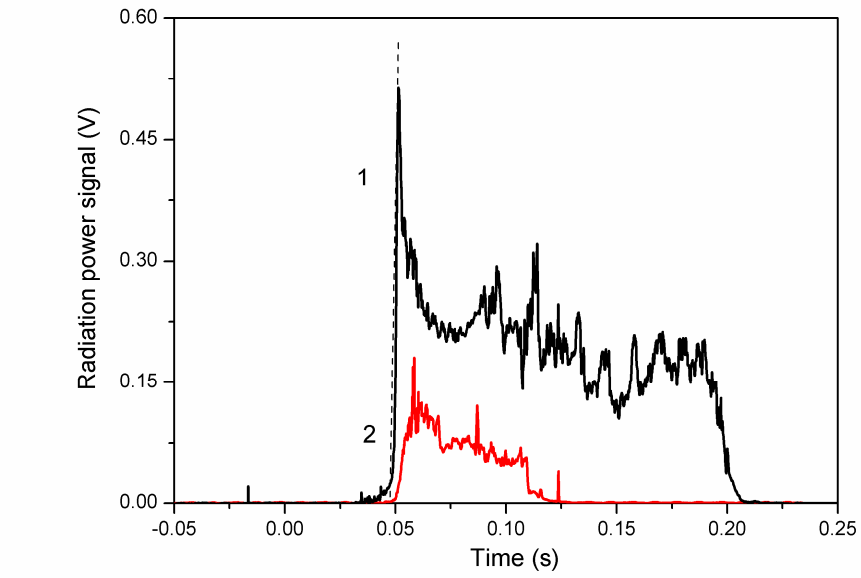

Figure 7.14 Radiation power signal by means of photon detector transformation. (1), 160A; (2), 440A.

Fig.7.14 shows the real time variation of radiation power with the arc current. For the same time instant, the radiation power transformation signal shows a higher value with a higher arc current.

7.4.3 Dynamic Characteristics of an SF_6 Arc with Gas Flow

With the gas flow, the mechanical characteristics of moving electrode can be influenced as indicated in Fig.7.15. The gas blast into the supersonic nozzle can help push the moving electrode upwards so that it reach its full range earlier and therefore it has a larger mean velocity compared with the case without gas flow.

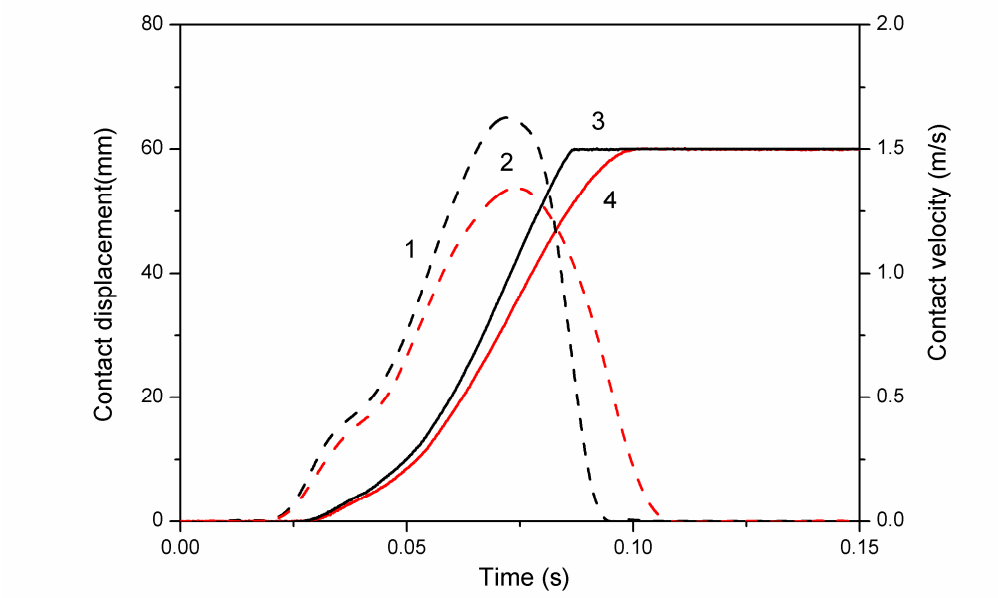

Figure 7.15 Variation of electrode gap length and electrode movement velocity as a function of time with and without gas flow. (1), contact velocity with gas flow; (2), contact velocity without gas flow;. (3), contact displacement with gas flow; (4), contact displacement without gas flow.

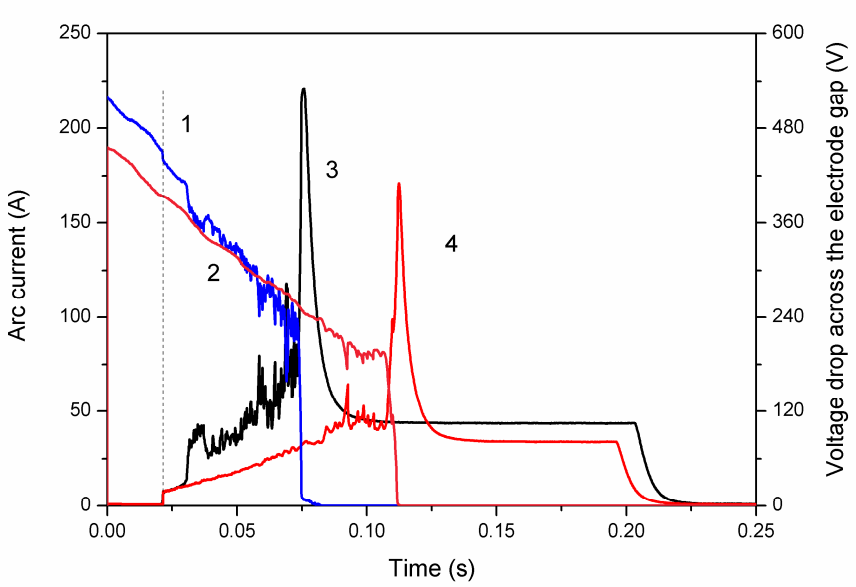

Figure 7.16 Experimental voltage drop across the electrode gap and arc current with and without gas flow. (1), arc current with gas flow; (2) arc current without gas flow; (3), voltage drop across the electrode gap with gas flow; (4), voltage drop across the electrode gap without gas flow.

;

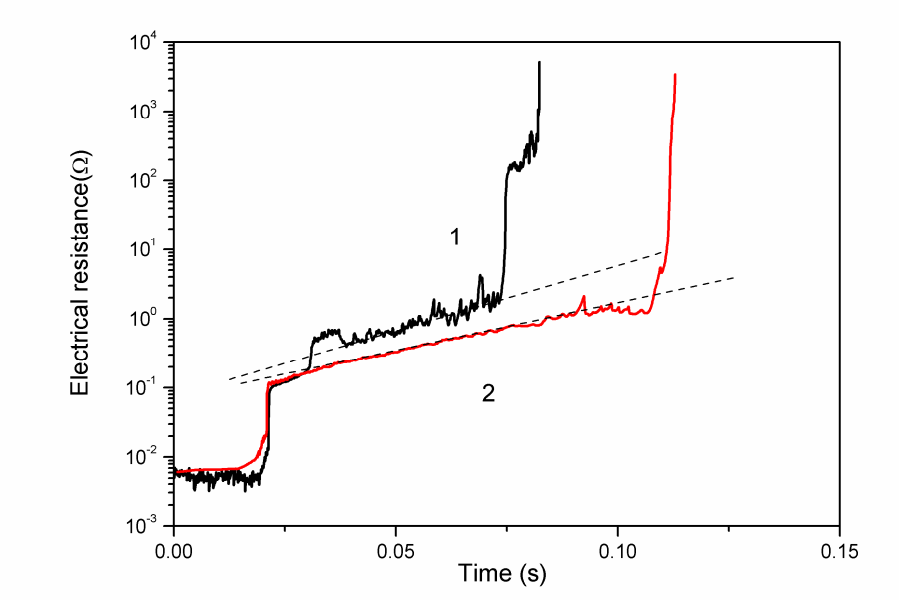

Figure 7.17 Calculated electric resistances across the electrode gap under different interruption currents according to the experimental results. (1), with gas flow; (2), without gas flow.

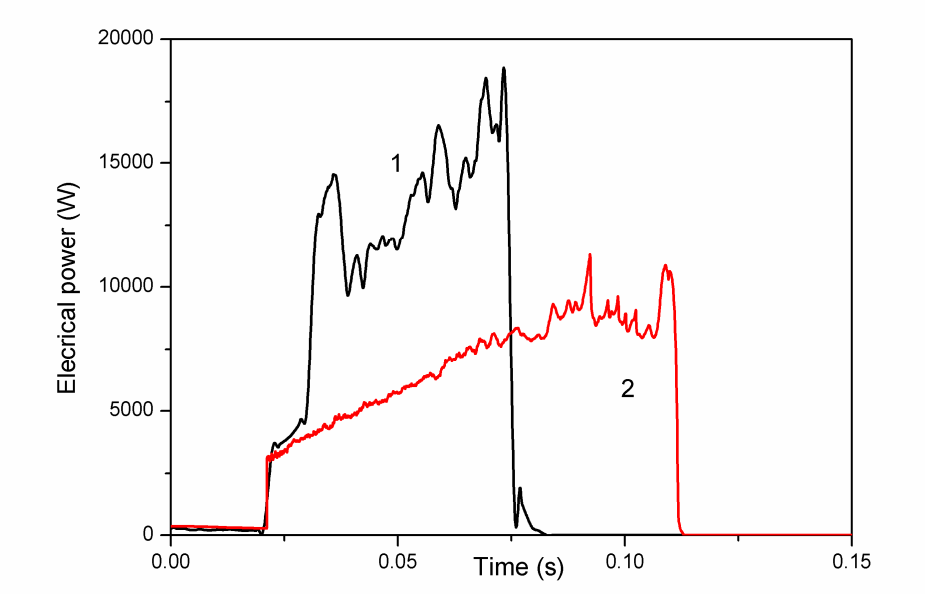

Figure 7.18 Calculated electric power across the electrode gap. (1), with gas flow; (2), without gas flow.

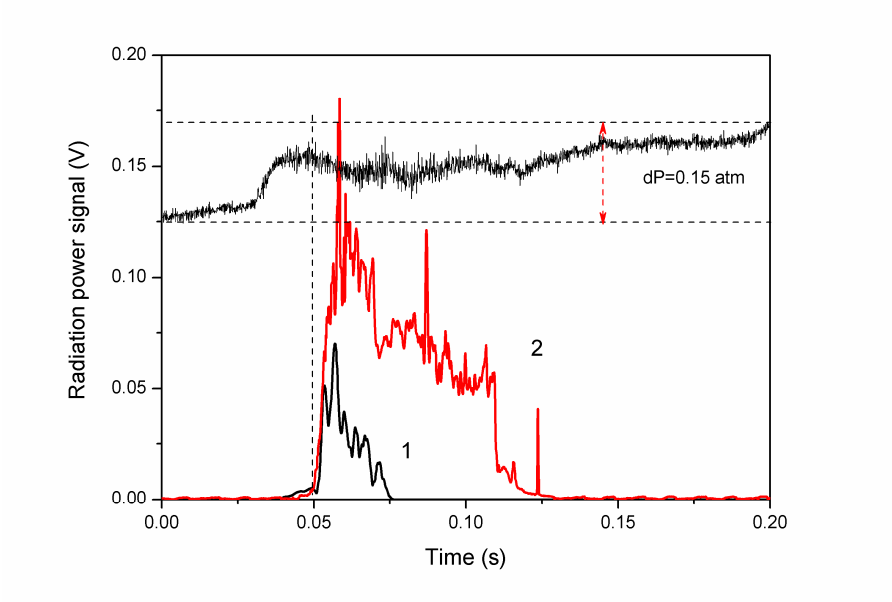

Figure 7.19 Radiation power signal by means of photon detector transformation. (1), with gas flow; (2), without gas flow. The experimental pressure data are also given.

The influence of the gas flow on electric characteristics of switching arcs can be found in Figs.7.16-7.19. Gas blast flow can enhance the energy removal by convection and turbulent cooling. Therefore, in spite of similar fault current, under the condition with gas flow, the system can break the current in a shorter time duration. At the first stage of the electrode separation, the short arc between the electrodes can hardly be affected by the gas flow. Therefore, at the same time instant, the voltage drop is nearly the same with and without gas flow. With the further separation of the electrodes, the influence of gas flow on arcing is gradually increasing and the cooling function of gas flow can bring a rise of the electric resistance as presented in Fig.7.17. The voltage drop also increases as well. Additionally, with gas flow, the voltage drop across the electrode gap fluctuates more heavily and has a much higher extinction peak during the arc extinction. As we can see in Fig.7.17, with gas flow, the electric resistance in the stage of the separation elongation shows a larger higher rate regardless of almost identical current value.

The influence of gas flow on energy variation can be found in Figs.7.18-7.19. With gas flow, the stored energy in the capacitor can be dissipated much more quickly than that without gas flow. This is due to the larger arc resistance at the same time instant. Moreover, as a result of the gas flow cooling, the mean arc temperature is relatively lower and hence brings

a lower radiation power.

In Fig.7.19, the pressure variation at the slot located downstream of the nozzle throat is also given. There exists a pressure increase of about 10kPa in the arcing period. The pressure at monitoring point arrives at a maximum value when the cylindrical nozzle throat is being evacuated by the solid contact. After the electrode leaves the nozzle throat, a reduction of the pressure can be found as a result of the pressurized gas out of the nozzle into the diverged nozzle downstream. After the arc extinction, more gas flows into the test chamber and lead to a slight pressurization.

7.4.4 Influence of Different Arcing Gases

We investigated the arc current interruption behaviour of CO_2 and N_2 which are usually considered as a replacement of electronegative gas SF_6 under certain conditions.

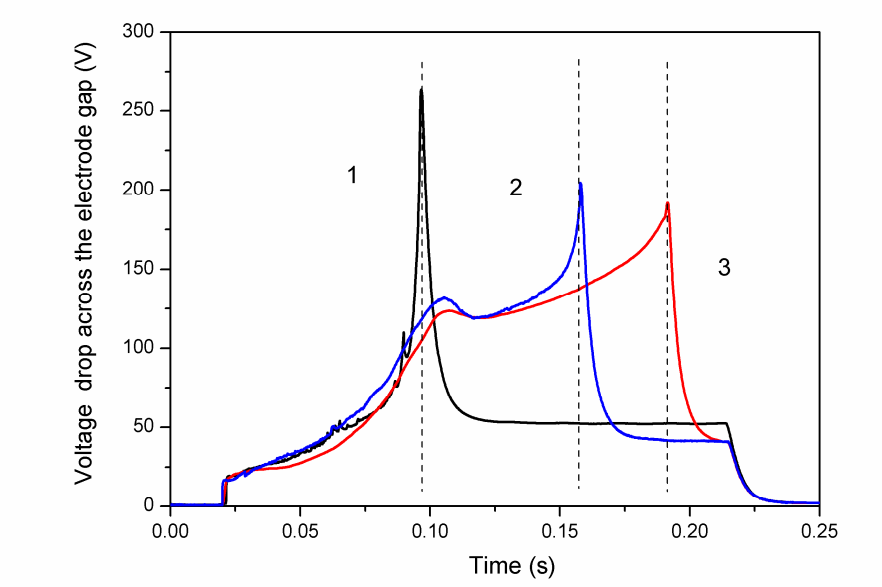

Figure 7.20 Experimental arc voltages without gas flow (chamber filled with (1), SF_6; (2), CO_2; (3), N_2).

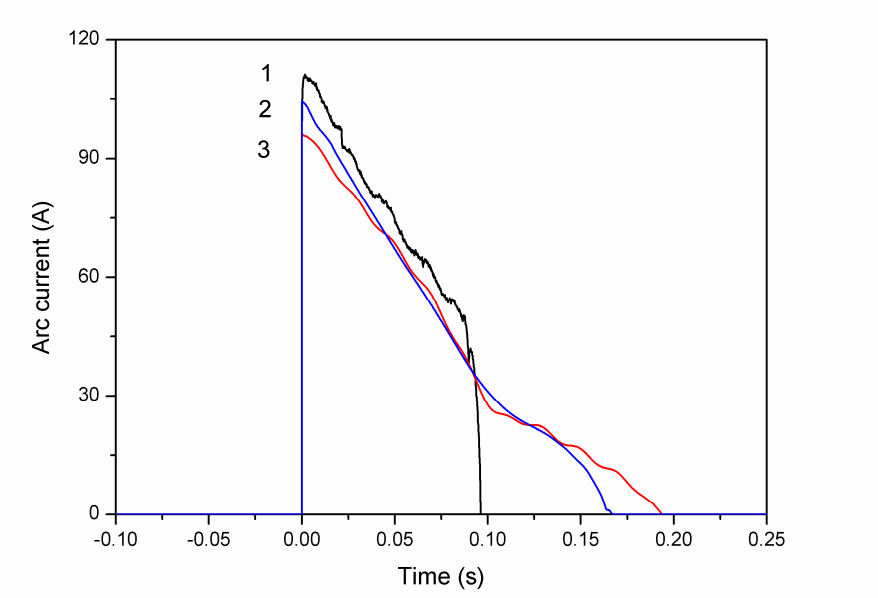

Figure 7.21 Experimental arc current without gas flow (chamber filled with (1), SF_6; (2), CO_2; (3), N_2.)

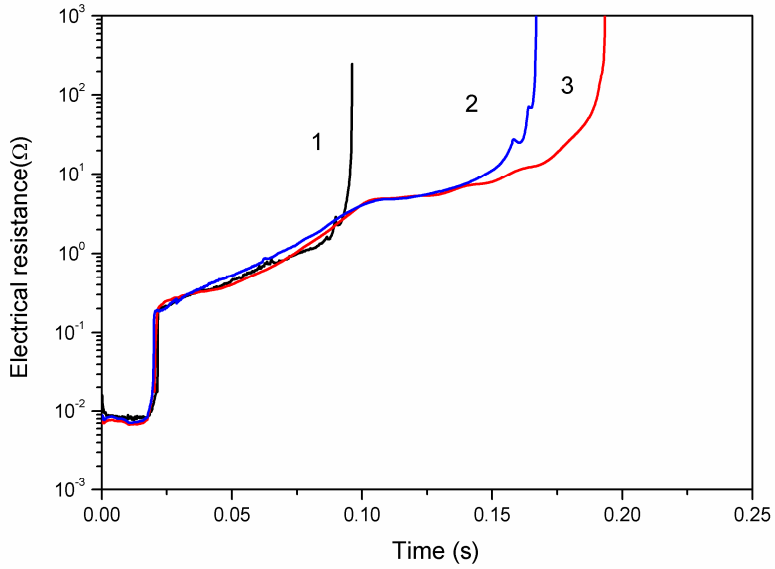

Figure 7.22 Calculated electric resistances across the electrode gap (chamber filled with (1), SF_6; (2), CO_2; (3), N_2.)

Compared with SF_6, CO_2 and N_2 have poorer current interruption behaviour. For almost identical initial arcing current, it takes much more time to break the current using CO_2 and N_2 than that of SF_6 indicating the strong arc quenching ability of SF_6. The voltage extinction peak of SF_6 is much higher than that of CO_2 and N_2 as well and this can be

attributable to the fast rising arc resistance in the current-zero period as we can see in Fig.7.22.

The electric resistance across the electrode gap shows slight deviation in the gap elongation period showing that the gas properties can influence the arcing behaviour in these cases. The value of electric resistance is dominantly determined by the changing arc length. During the extinction process, the electric conductance of SF_6 owns the highest decaying rate as we can see that its slope of electric resistance which is inversely proportional to the electric conductance is largest. In contrast, N_2 gas has the lowest decaying rate of electric conductance although it has similar electric characteristics in the time period from 0.10s to 0.13s when the electrode arrives at its full range.

Figs.7.23-7.27 give the theoretical calculation results of typical thermodynamic properties and transport coefficients as well as net radiation coefficients at atmospheric pressure.

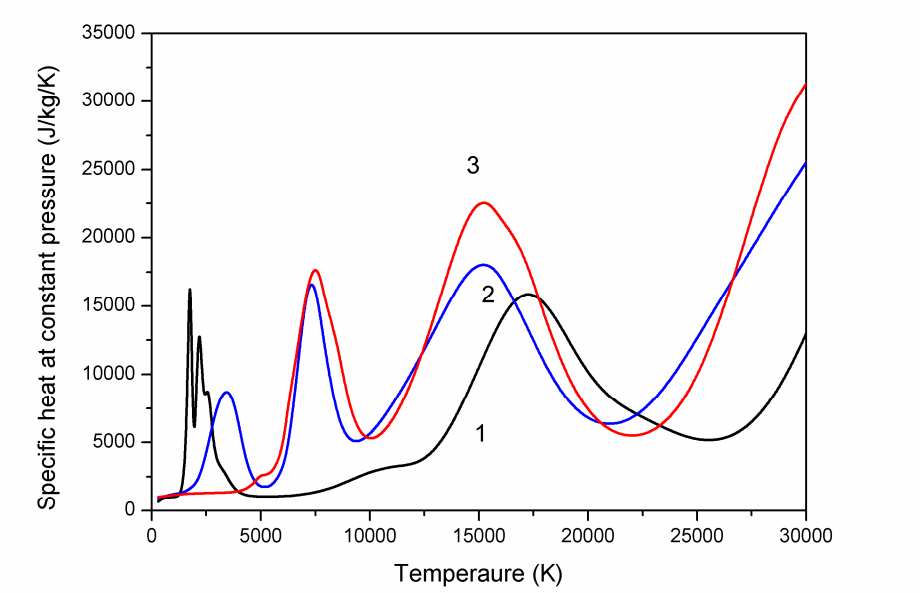

Figure 7.23 Calculated specific heat at constant pressure at atmospheric pressure. (1), SF_6; (2), CO_2; (3), N_2.

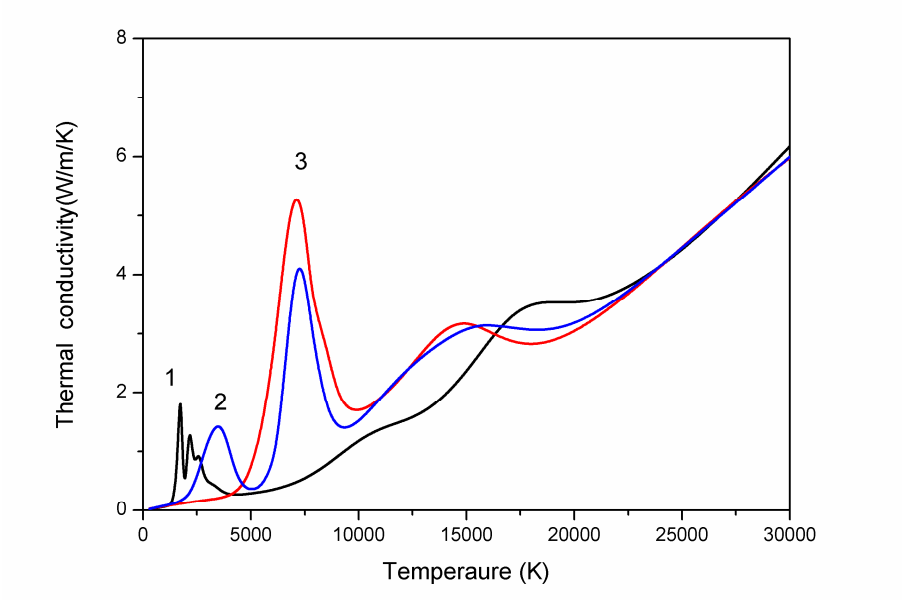

Figure 7.24 Calculated thermal conductivity at atmospheric pressure. (1), SF_6; (2), CO_2; (3), N_2.

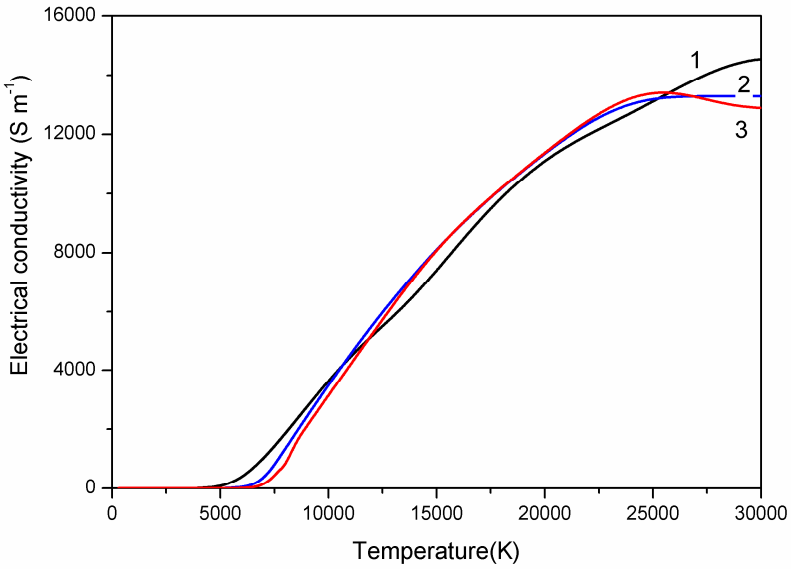

Figure 7.25 Calculated electrical conductivity at atmospheric pressure. (1), SF_6; (2), CO_2; (3), N_2.

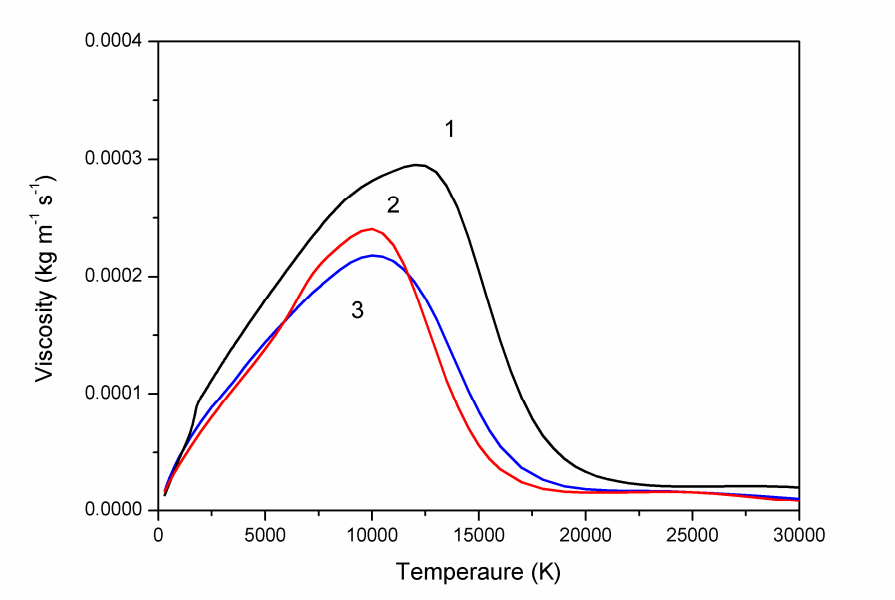

Figure 7.26 Calculated viscosity at atmospheric pressure. (1), SF_6; (2), CO_2; (3), N_2.

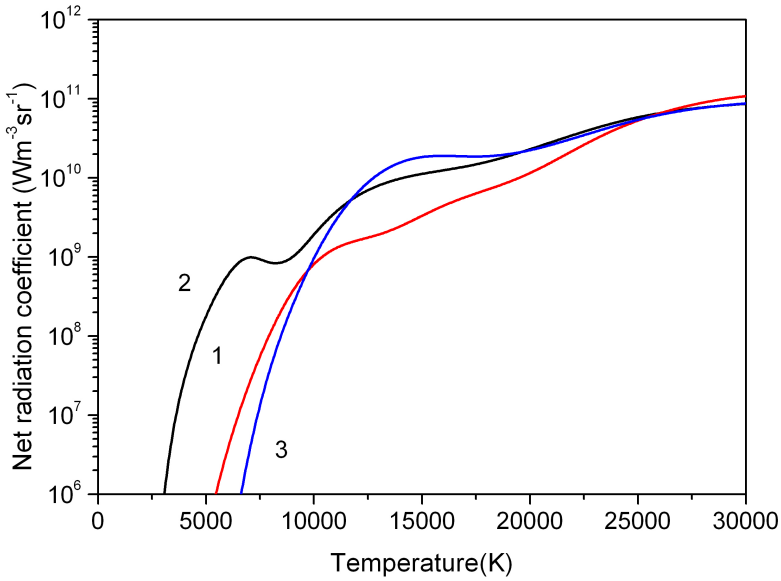

Figure 7.27 Calculated net radiation coefficient with arc radius of R=0 at atmospheric pressure. (1), SF_6; (2), CO_2; (3), N_2.

The arc quenching behaviour of gases is closely linked with their internal properties especially under the lower temperature range. SF_6 dissociates in the temperature range of lower than 5000K and leads to a higher specific heat at constant and thermal conductivity. Therefore, the energy produced by Joule heating can be removed by different energy dissipated actions such as radiation and convective and will not bring too higher temperature

increase in spite of higher electrical conductivity and viscosity at the same temperature. In the lower temperature range of lower than 10000K, CO_2 has a much higher net radiation coefficient than that of SF_6 but a lower current interruption indicating that there should other microscopic properties to determine the arc quenching behaviour. In contrast, N_2 dissociates at a higher temperature around 7000K and owns lower specific heat and thermal conductivity in the temperature of lower than 5000K. The cooling function of heated gases is less effective than that of CO_2 regardless of almost similar characteristics of electrical conductivity and viscosity.

Figs.7.28-7.29 give the electrical and radiation power variation in the current interruption process. We can find that in spite of different arcing time duration, N_2 and CO_2 have almost identical Joule heating energy consummation in whole arcing phase. That is why we can see in Fig.7.29 that N_2 and CO_2 arrive at the same residual voltage after arc extinction. The difference of radiation power between gases is apparent. In general, N_2 has a larger radiation emission power than that of CO_2 under the same Joule heating power from 0.11s to 0.14s.

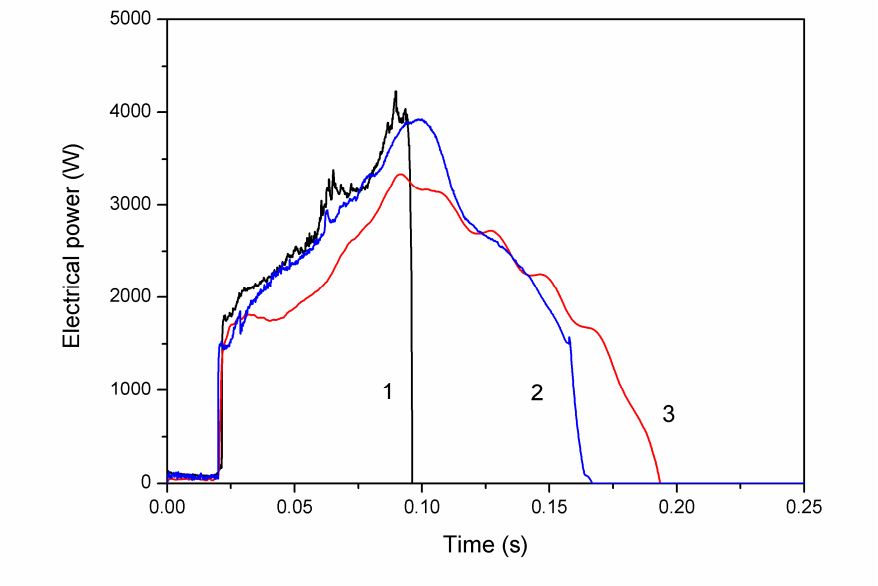

Figure 7.28 Calculated electrical power across the electrode gap (chamber filled with SF_6, CO_2, N_2).

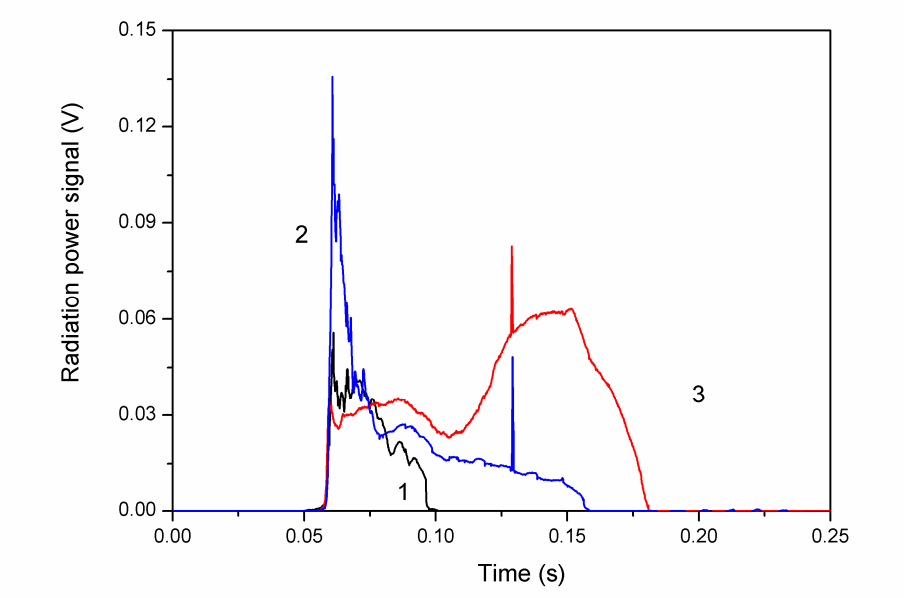

Figure 7.29 Radiation power signal recorded by photon detector system(chamber filled with SF_6, CO_2, N_2).

7.4.5 Emission Spectroscopy Diagnostic of Arcing SF_6 in Current Interruption

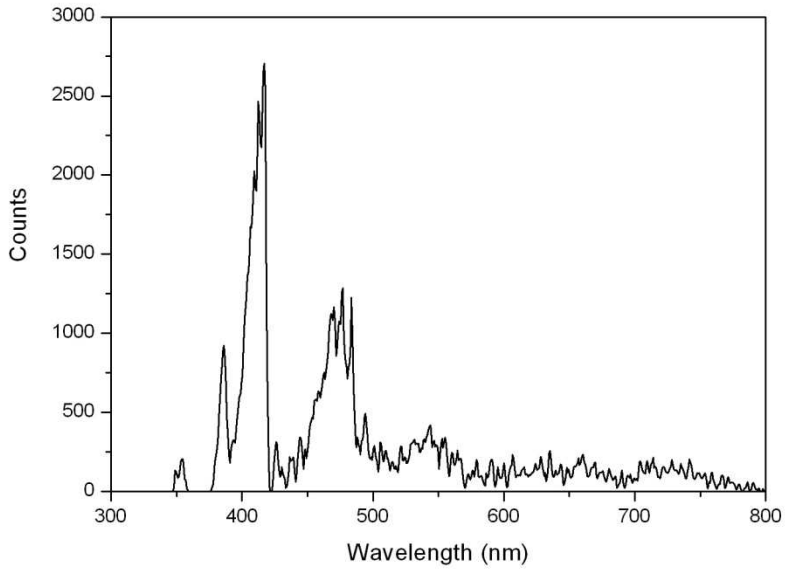

Figure 7.30 Emission Spectral lines of the arcing SF_6 in current interruption. The initial interruption current is 100A without gas flow. Integration time: 40ms.

The emission spectrum of a chemical element or chemical compound is the spectrum of frequencies of electromagnetic radiation emitted due to an atom's electrons making a

transition from a high energy state to a lower energy state. The energy of the emitted photon is equal to the energy difference between the two states. There are many possible electron transitions for each atom, and each transition has a specific energy difference. These collections of different transitions, leading to different radiated wavelengths, make up an emission spectrum. Each element's emission spectrum is unique. Therefore, spectroscopy can be used to identify the elements in matter of unknown composition. Similarly, the emission spectra of molecules can be used in chemical analysis of substances.

The analysis of the overview spectra obtained in our experiments in fig.7.30 showed the presence of atomic carbon C I and ionized carbon C II lines indicating that the PTFE nozzle ablation occurs. After arc current interruption, the solid graphite deposition can be observed as presented in Fig.7.31. This can further verify the existence of PTFE nozzle ablation caused by arc radiation.

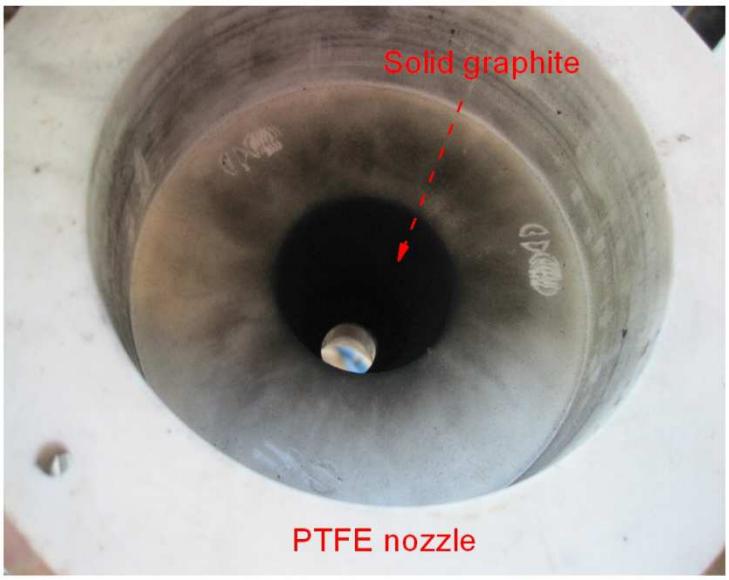

Figure 7.31 A photo of solid graphite deposition after arc interruption.

For the measurement of detailed spectra a region around 630 nm and 650 nm was chosen containing two fluorine lines at 634.851 nm and 623.965 nm and a doublet of ionized carbon at 657.805/658.288 nm. Also some measurements were performed in the region of 420 nm where a CII triplet 426.700/426.718/426.726 nm can be found. Moreover, the spectra lines of S II around 416.266 nm, a doublet 542.867/543.2815 nm, 545.383 nm, 560.615 nm

together with 563.997 nm were also found. For atomic copper, the persistent lines 510.554 nm, 515.324 nm, 521.820 nm along with 529.252 nm were found showing that the cooper vapor generated by electrode erosion entrains into the arcing plasma phase and can greatly influence the arcing behaviour and the dielectric phase after arc extinction. The ionized fluorine and copper can be found as well. For example, a triplet FII can be found at a region around 385nm respectively centered at 384.707 nm, 384.999 nm, and 385.1669 nm. The ionized copper Cu II at 600.120 nm and a doublet of lines at around 615.038 nm and 615.422 nm were found.

7.5 Conclusion

With a model SF_6 gas blast interrupter, dynamic characteristics and decaying behaviour of SF_6 arcs were experimentally investigated. The voltage and current wave forms were compared under different test-sets such as different interruption currents with and without gas flows. The arcing behaviour and interruption capability of CO_2 and N_2 is compared with SF_6. An emission spectroscopy diagnostic of arcing is used to identify the elements existing in the arc plasma. Some fundamental conclusions are summarized as follows.

(1) From the arc voltage characteristics, the voltage drop across the electrode gap is proportional to the gap length in the electrode gap elongation stage regardless of the interruption currents. When the moving electrode reaches its full range, the voltage drop shows little dependence on the damping current with typical characteristics of fluctuation due to arc root movement until the extinction phase in which an extremely high extinction voltage peak occurs. It is noted that the extinction voltage, which decreases with increase in the interrupting current, is related to the conductance decay during current zero period and can be considered as a macroscopic evaluation of interruption capability.

(2) The arc resistance decreases as the interruption current increases. It rises rapidly near current zero. Gas blast flow can enhance the energy removal by convection and turbulent cooling. Therefore, in spite of similar fault current, under the condition with gas flow, the system can break the current in a shorter time duration.

(3) The power input across the gap firstly increase with the continuous elongation of

the arc. This is connected with the increase of arc resistance which outweighs the influence of the arc current. At the same time instant, the radiation power transformation signal shows a higher value with a higher arc current. With gas flow, the stored energy in the capacitor can be dissipated much more quickly than that without gas flow. This is due to the larger arc resistance at the same time instant. Moreover, as a result of the gas flow cooling, the mean arc temperature is relatively lower and hence brings a lower radiation power.

(4) SF_6 has a much better interruption capability of current than that of CO_2 and N_2. The performance deviation is mainly attributed to their internal properties. SF_6 dissociates at a lower temperature than 5000K and leads to a higher specific heat at constant and thermal conductivity. Therefore, the energy produced by Joule heating can be removal by different cooling actions such as radiation and convective and will not bring too higher temperature increase.

(5) The emission spectroscopy diagnostic shows that even a low current amplitude of 100A without gas flow occurs the PTFE nozzle ablation and copper electrode erosion. Relevant chemical species such as atomic copper and carbon, ionized copper and carbon have been found in the emission spectral lines. These species can be entrained into the SF_6 and influence the decaying behaviour and dielectric properties after the arc extinction. Their influence should be further investigated in future.

7.6 Reference

[1] J.D. Yan, M.T.C. Fang, and W. Hall, "The Development of PC Based CAD Tools for Auto-Expansion Circuit Breaker Design", IEEE Transactions on Power Delivery, 14,176 (1999).

[2] J. D. Yan and M. T. C. Fang, "Visualization of Arcing Process in an Auto-Expansion Circuit Breaker", IEEE Trans. Plasma Sci., 27, 40 (1999).

[3] H. Nishikawa, A. Kobayashi, T. Okazaki and S. Yamashita, "Arc Extinction Performance of SF_6 Gas Blast Interrupter", IEEE Transactions on Power Apparatus and Systems, PAS-95, 1834 (1976).

[4] P. H. Schavemaker and L. van der Sluis, "An improved Mayr-type Arc model based on current-zero measurements," IEEE Tran. Power Delivery, 15, 580 (2000).

[5] A. M. Cassie, "Theorie Nouvelle des Arcs de Rupture et de la Rigidité des Circuits," Cigre Report 102, 1939.

[6] K. J. Tseng, Y.Wang, and D. M.Vilathgamuwa, "An experimentally verified hybrid Cassie-Mayr electric arc model for power electronics simulations," IEEE Trans. Power Electron., 12,429 (1997).

[7] L. S. Frost, "Dynamic arc analysis of short-line fault test for accurate circuit breaker performance specifications," IEEE Trans. Power App. Syst., 478 (1978).

[8] J. L. Guardado, S. G. Maximov, E. Melgoza, J. L. Naredo, and P. Moreno, "An Improved Arc Model Before Current Zero Based on the Combined Mayr and Cassie Arc Models", IEEE Tran. Power Delivery, 20, 138 (2005).

[9] E. Lewis, N. Y. Shammas and G. R. Jones, "The current zero SF_6 blast arc at high *di/dt*", in Proc.8th Int. Conf. on Gas Discharges and Their Applications, 1985, pp.35-38.

[10] E. Lewis, A. N. Prasad and G. R. Jones, "Current zero spectroscopy of a high power SF_6 circuit breaker arc", in Proc.8^{th} Int. Conf. on Gas Discharges and Their Applications, 1985, pp.31-34.

[11] Y. Tanaka, Y. Yokomizu, T. Matsumura and Y. Kito, "Transient behaviour of axial temperature distribution in post-arc channel after current zero around nozzle throat in flat-type SF_6 gas-blast quenching chamber", J. Phys. D: Appl. Phys., 28, 2095 (1995).

[12] Y. Tanaka, Y. Yokomizu, T. Matsumura and Y. Kito, "Transient distribution of metallic vapour concentration in a post-arc channel after current zero along the nozzle axis in a

flat-type SF_6 gas-blast quenching chamber", J. Phys. D: Appl. Phys., 29, 1540 (1996).

[13] G. R. Jones, W. Hu and S. M. Ei-Kholy, "A spectroscopic investigation of electrode material entrained into the extinguished arc of an SF_6 circuit breaker", J. Phys. D: Appl. Phys., 21, 1414 (1988).

[14] R. Kozakov, M. Kettlitz, K. Weltmann, A. Steffens and C. M. Franck, "Temperature profiles of an ablation controlled arc in PTFE: I. Spectroscopic measurement", J. Phys. D: Appl. Phys., 40, 2499 (2007).

[15] M. Seeger, M. Schwinne, R. Bini, N. Mahdizadeh, T. Votteler, "Dielectric recovery in a high-voltage circuit breaker in SF_6", J. Phys. D: Appl. Phys., 45, 395204 (2012).

[16] T. Mori, H. Ohashi, H. Mizoguchi, K. Suzuki, "Investigation of technology for developing large capacity and compact size GCB", IEEE Transactions on Power Delivery, 12 ,747 (1997).

[17] R. Bini, N.T. Basse, and M. Seeger, "Arc induced turbulent mixing in an SF_6 circuit breaker model", J. Phys. D: Appl. Phys., 44, 25203 (2011).

[18] J. J. Gonzalez, P. Freton, F. Reichert and D. Randrianarivao, "Turbulence and magnetic field calculations in high voltage circuit breakers", IEEE Trans. Plasma Sci., 40, 936 (2012).

CHAPTER 8 CONCLUSIONS AND FUTURE WORK

8.1 Conclusions

The dynamic characteristics and decaying behaviour of gas blast arcs are often vital in fault current interruption. Achieving an effective utilization and exploitation of the interruption capability of SF_6 requires a thorough understanding of the plasma properties and its physical process. Therefore, the dynamic characteristics and decaying behaviour of sulphur hexafluoride arcs in current interruption has been investigated in this thesis.

The species composition, thermodynamic properties and transport coefficients of SF_6 under local thermodynamic equilibrium state were computed firstly in chapter 2. The chemical equilibrium composition is determined as a function of temperature and pressure by finding the composition that minimizes the Gibbs free energy, which is a standard technique in equilibrium chemistry. The thermodynamic properties of gaseous mixtures, such as mass density, molar weight, enthalpy and specific heat at constant pressure were determined using the standard formulas based on obtained species composition. Transport properties, namely diffusion coefficients, electrical conductivity, thermal conductivities and viscosity, are calculated approximately using the classical Chapman–Enskog method with a much higher order approximation, i.e. third-order approximation for transport properties except viscosity, for which the second-order approximation is considered. The transport cross sections are evaluated with updated interaction potentials including a most recent phenomenological description of elastic cross section. From the computation, properties especially transport coefficients became sensitive to the choice of Debye length definition partly due to the differences in plasma composition as a consequence of the altered internal partition functions, but predominantly due to the different collision integrals for interactions between charged species, which are affected by the different screening distance used in evaluating the Coulomb potential. Pressures can also influence thermophysical properties. This can be explained by Le Chatelier's law as well as the modified species composition. Validation of the transport coefficients determined using these collision integrals was carried out by comparing with available theoretical and experimental data in the literature. The results presented here are

expected to have high accuracy, and are reliable reference data for numerical modelling of SF_6 switch arc behavior.

There is increasing evidence that deviations from kinetic equilibrium in thermal arc plasmas are rather common. Since thermodynamic properties and transport coefficients are a pre-requisite for arc modelling, there is a growing need for calculating non-equilibrium properties of SF_6 arc plasmas. In our computation in chapter 3, the electrons and heavy particles are treated as two different gases with Maxwell-Boltzmann distribution but with different temperatures. The plasma species composition is obtained by solving a system of simultaneous nonlinear equations derived from a generalized mass action laws, the gas state law and the condition for charge neutrality using Newton-Raphson iterative method. The two-temperature transport coefficients of electrons and heavy particles are computed independently under different non-equilibrium degrees of electrons and heavy particles temperature ratio utilizing modified Chapman-Enskog approach. It is noted that the species composition, thermodynamic properties as well as transport coefficients of non-equilibrium plasmas are quite different from those under LTE state. The two-temperature properties can reduce to the LTE properties once the electrons and heavy particles have identical temperature. We can also note that the adopted forms of mass action law, i.e. Guldberg-Waage and Saha equations can modify the species composition, thermodynamic properties and transport coefficients but can reduce to the same expression under LTE state. Moreover, the choice of reaction excitation temperature for molecular ionization can influence the species composition and hence the properties mainly in the moderate temperature range when the molecular species are present and the ionization degree is low.

In chapter 4, considerable effort has been devoted to arc-shock interaction and its influence on steady and dynamic characteristics of SF_6 arcs in a supersonic nozzle with hollow contact, which is representative of switching arcs in a gas blast high voltage circuit breaker. The physical parameters, such as the arc radius, the flow field, the temperature, and the electric field strength before and after current-zero have been obtained. The significant quantity in determining the thermal interruption capability of a circuit breaker, i.e. the critical rate of rise of recovery voltage (RRRV), was predicted and compared with available test results. It is found that the high pressure penetration into the thermal layer along with the

downstream electrode's blocking effect can both contribute to a low flow entrainment into the arc core to form shocks and hence a broadening effect of the arc column. Moreover, the velocity deceleration caused by the shocks and the enhanced turbulent cooling brought by the sucked gas and arc interaction as two completive factors both pay a significant role in the determination of thermal interruption capability. Additionally, different nozzle exit pressures can greatly influence arc behavior between electrodes and hence the thermal interruption capability. Thus, the design of a supersonic nozzle interrupter should ensure that the pressure ratio must be guaranteed at the last current zero of the circuit breaker operation to decrease the deterioration caused by shocks and enhance the turbulent heat cooling.

The behaviour of a decaying SF_6 arc, which is representative of the approach to the final current zero state of switching arcs in a high voltage circuit breaker, is theoretically investigated in chapter 5 by a two-temperature hydrodynamic model, taking into account the possible departure of the plasma state from local thermodynamic equilibrium (LTE). The model is then applied to a two-dimensional axisymmetric SF_6 arc burning in a supersonic nozzle under well-controlled conditions; for this configuration, experimental results are available for comparison. The effect of turbulence is considered using the Prandtl mixing length model. The edge absorption of the radiation emitted by the arc core is taken into account by a modified net emission coefficient approach. It is found that the reabsorption of arc radiation by cold gas in the arc fringes is an important effect. With our modified net emission coefficient approach, the predicted gas temperatures under steady-state conditions show good agreement with experimental values. For steady-state conditions, differences between the electron and heavy-species temperatures mainly occur near the arc fringe region, where the gas temperature is below 12000 K. The degree of thermal non-equilibrium is largest in the cold boundary layer, and increases as the flow progresses downstream as a result of a reduced collision frequency between electrons and heavy species with decreasing pressure. As the current decreases, departures from thermal equilibrium become larger, and therefore the differences in the physical quantities obtained from the two-temperature model and an LTE model increase. The energy exchange mechanism between electrons and heavy species, which links the electron and heavy-species energy equations, has been quantitatively analyzed in terms of the contributions from collision frequency and the difference between electron and heavy-species temperatures. This has allowed, for example, the double peak in

the energy exchange as a function of radius to be explained. For the arc decay phase, the two-temperature model gives a lower cooling rate than the LTE model, and hence a higher conductance of the discharge passage at current zero. Departures from thermal equilibrium gradually increase during arc extinction, occurring firstly near the exit due to the more rapid cooling in this region, and subsequently spreading upstream and increasing, mainly because of the collisional energy exchange between electrons and heavy species. When the current damping rate is increased, the arc energy cannot be removed effectively, leading to higher temperatures and smaller departures from thermal equilibrium along the central axis at current zero. The large departures from thermal equilibrium, particularly at times just before, and after, current zero, demonstrate the importance of using a two-temperature model to accurately predict the current interruption behaviour of SF_6 gas-blast circuit breakers.

Beside the thermally non-equilibrium effects, further investigation of some categories of non-equilibrium effects were taken into account for understanding the decaying process of high temperature SF_6 gases and arcs. The influence of chemically non-equilibrium on post-arc in circuit breaker operation under free recovery condition and the dielectric properties of high temperature SF_6 gases and residue plasma with an applied field determined by non-Maxwellian energy distribution function are discussed by using a method of kinetic analysis. Firstly, considering the effects of chemically non-equilibrium, a kinetic model is presented for the decay of an SF_6 arc plasma, concerning the period when the electrons disappear in post-arc phase. It is found that any departures from equilibrium obtained correspond to an electron overpopulation which tends to enhance the electrical conductivity of the plasma and thus to decrease the thermal interruption capability of SF_6 obtained by the LTE model. We note that the main mechanisms of electrons elimination are the electron–atomic ion recombination above 9000K, the dissociative recombination around 8000K, the dissociative attachment from 3500K to 7500K, electron-molecular ion in the temperature lower than 3500K. The deviation of electron disappearance relaxation time under different temperature cooling rates mainly occurs in the intermediate temperature range from 4000K to 9000K where the dissociative recombination and dissociative attachment mechanisms especially involving diatomic molecular species are predominant. A larger temperature cooling rate leads to a higher value of electron disappearance relaxation time showing that a larger degree of departure from equilibrium occurs and a longer time is needed to reach the equilibrium state.

The critical reduced electric field strengths of hot SF_6 and its mixture with ablated PTFE vapor corresponding to the dielectric recovery phase are calculated from the temperature of 4000 K. The influence of departure from equilibrium on dielectric properties is investigated. It was expected and has been shown that atomic fluorine, although abundant, contributes little to the dielectric strength at these temperatures. We have found that the addition of PTFE vapor causes a decreased dielectric strength in the temperature range where the dissociation does not occur. Above 2500K, the addition of PTFE vapor leads to a higher dielectric strength. When departure from chemical equilibrium takes place, the critical breakdown field is reduced in the higher temperature range T>3500 K. This is attributed to the joint contribution of the increased electron-electron collision and the larger concentration of SF_2, SF which own higher dielectric strength. There exists an intermediate temperature range from 2000K to 3500K in which the species composition is almost identical, the system has similar dielectric properties. With the further decrease of the temperature, the simple species including atomic and diatomic species in the system has no sufficient time to compose into large molecular species. Therefore, an increase of the temperature cooling rate causes a significant reduction of the critical dielectric properties. The obtained critical electric fields show a reasonable agreement with the available theoretical and experimental data.

Finally, with a model SF_6 gas blast interrupter, transient and decaying behavior of SF_6 arcs was experimentally investigated using various diagnostic actions such as voltage & current waveforms, pressure sensor, optical access together with displacement sensor. The voltage and current wave forms, radiation power signal transformed by photon detector were compared under different test-sets such as different interruption currents with and without gas flows. The arcing behavior and interruption capability of carbon dioxide and nitrogen is compared with sulfur hexafluoride in order to obtain the dominant properties influencing arc quenching. An emission spectroscopy diagnostic of arcing is used to identify the elements existing in the arc plasma. We have noted that the arc voltage is almost constant in the electrode gap elongation stage regardless of the interruption currents. When the movement electrode reaches its full range, the voltage drop shows typical characteristics of fluctuation with little dependence on the damping current until the extinction phase in which an extremely high extinction voltage peak occurs. It is noted that the extinction voltage, which decreases with increase in the interrupting current, is related to the conductance decay during

current zero period and can be considered as an evaluation of interruption capability. Gas blast flow can enhance the energy removal by convection and turbulent cooling. Therefore, in spite of similar fault current, under the condition with gas flow, the system can break the current in a shorter time duration with a much more rapid variation of arc resistance before its extinction. The light radiation energy generally shows a decreasing trend as current damps. Sulfur hexafluoride has a much better interruption capability of current than that of carbon dioxide and nitrogen with a much higher extinction voltage peak and cut-off current possibly due to its high thermal conductivity and specific heat. The emission spectroscopy diagnostic shows that even a lower current amplitude of 100A without gas flow can lead to the PTFE nozzle ablation and copper electrode erosion. Relevant chemical species such as atomic copper and carbon, ionized copper and carbon have been found in the emission spectral lines. These species can entrain into the SF_6 and influence the decaying behavior and dielectric properties after the arc extinction.

8.2 Future Work

In computer modelling of the transient and decaying behavior of gas last SF_6 arcs, we aimed at comparing the effects of departures from thermal equilibrium on the arc decaying behavior during the current zero period in the fault current interruption. Many works are needed for improving the switch arcs modelling especially the interruption capability prediction and some of the developments we anticipate will greatly improve the predictive power of switch arcs simulations are described considering its involvement of many sophisticated processes. Firstly, it is possible that chemical non-equilibrium and electron diffusion, which will be introduced as a future development in the model, will have a non-negligible effect on the predicted discharge properties. Secondly, turbulence is expected to play a relevant role in determining the gas mixing, enhancing the effective transport of energy and momentum and dissipating the arc energy when current decreases towards zero. Its contribution to the arc decaying should be separately treated and analyzed in order to better understand their mechanism especially when non-equilibrium takes place. Fundamental work needs to be done in order to devise a suitable turbulence model for arcs in gas flow validated by tests in current interruption especially under shock condition. Thirdly, the influence of solid materials and there interaction with arcs on the arcing decaying process should be taken into account. The

electrodes should be incorporated into the computation area and treated as a coupled system with the arc. The thin non-LTE layer between the electrode and the arc along with its effects should be taken into account in the energy balance at the electrode surface. Moreover, the electrode material erosion evaporation together with the nozzle ablation vapor which possibly exists during the arc decaying process and has a significant effect on current interruption should also be considered in the future in non-equilibrium modelling of switch arcs. Finally, reasonable values of non-equilibrium thermodynamic and transport properties including proper radiation coefficients for different gases and its mixtures with ablated nozzle material and electrode vapor which can provide accurate modelling for two temperature plasmas are required.

In experimental investigation of the arc decaying behavior of gas last SF_6 arcs, we aimed to obtain fundamental information with regard to arc quenching. A further thorough investigation is desirable in future in order to fully reveal the mechanism of arc interruption. The investigation on the transient evolution in physical parameters such as temperature, electrons density and metallic vapor concentration in an SF_6 blast arcs under different condition for pressure, gas flow rate, interruption current and nozzle shape before and after current zero during fault current interruption processes is expected to perform in a practical circuit breaker with a supersonic nozzle. Some effects such as nozzle ablation and non-equilibrium should be taken into account in futural tests to elucidate its influence on arc interruption. We have theoretically investigated the influence of nozzle ablation and departure from equilibrium on dielectric strength after arc extinction. However, reliable experimental diagnosis which can provide rigorous validation of theoretical estimation is expected. Detailed comparison of theoretical results against experimental measurements of arc decaying characteristics is required.

The author believes that the above-mentioned scope for the future research can help to better understand the current interruption phenomena.

LIST OF ACADEMIC PUBLICATIONS

REFEREED ARTICLES PUBLISHED IN ARCHIVAL JOURNALS

[1] **W Z Wang**, J D Yan, M Z Rong, A B Murphy, J W Spencer, Theoretical investigation of the decay of an SF_6 gas-blast arc using a two-temperature hydrodynamic model 2013 *J. Phys. D: Appl. Phys* **46** 065203.

[2] **W Z Wang**, J D Yan, M Z Rong, A B Murphy, Y Wu, J W Spencer, Investigation of SF_6 Arc Characteristics under shock condition in a Supersonic Nozzle with Hollow Contact 2013 *IEEE Trans. Plasma Sci.*, **41**, 915.

[3] **W Z Wang**, M Z Rong, Y Wu, J W Spencer, J D Yan, Investigation on Critical Breakdown Electric Field of Hot SF_6/CF_4 Mixtures for High Voltage Circuit Breaker Applications 2013 *Plasma Sources Sci. Technol.*, under review**.**

[4] **W Z Wang**, M Z Rong, Y Wu, J W Spencer, J D Yan, Influence of Chemically-non Equilibrium on Critical Dielectric Strength of Hot SF_6/N_2 Gas Mixture 2013 *J. Phys. D: Appl. Phys.*, under review**.**

[5] Yi Wu, **W Z Wang**, J D Yan, M Z Rong, J W Spencer, Nonuniqueness of two-temperature Guldberg-Waage and Saha equations: Influence on thermophysical properties of SF_6 plasmas 2013 *J. Appl. Phys*, Corresponding author, under review**.**

[6] **W Z Wang**, M Z Rong, Y Wu , J W Spencer, J D Yan, D H Mei, Thermodynamic and transport properties of two-temperature SF_6 plasmas 2012 *Phys. Plasmas* **19** 083506 .

[7] **W Z Wang**, M Z Rong, A B Murphy, Y Wu, J W Spencer, J D Yan, M T C Fang, Thermophysical properties of carbon–argon and carbon–helium plasmas 2011 *J. Phys. D: Appl. Phys.* **44** 355207.

[8] **W Z Wang**, M Z Rong, J D Yan, A B Murphy, J W Spencer, Thermophysical properties of nitrogen plasmas under thermal equilibrium and non-equilibrium conditions 2011 *Phys. Plasmas* **18** 113502 .

[9] **W Z Wang**, M Z Rong, J D Yan, Y Wu, The Reactive Thermal Conductivity of Thermal Equilibrium and Non equilibrium Plasmas: Application to Nitrogen 2012 *IEEE Trans. Plasma Sci.* **40** 980- 989.

[10]**W Z Wang**, A B Murphy, J D Yan, M Z Rong, J W Spencer, M T C Fang, Thermophysical Properties of High-Temperature Reacting Mixtures of Carbon and Water in the Range 400–30,000 K and 0.1–10 atm. Part 1 Equilibrium Composition and Thermodynamic Properties 2011 *Plasma Chem. Plasma Process.* **32** 75–96.

[11]**W Z Wang**, J D Yan, M Z Rong, A B Murphy, J W Spencer, Thermophysical Properties of High Temperature Reacting Mixtures of Carbon and Water in the Range 400–30,000 K and 0.1–10 atm. Part 2 Transport Coefficients 2012 *Plasma Chem. Plasma Process.* **32** 495-518.

[12]**W Z Wang**, Y Wu, M Z Rong, F Yang, Theoretical computation studies for transport properties of air plasmas 2012 *Acta Phys. Sin.* **61** 105201**.**

[13]**W Z Wang**, Y Wu, M Z Rong, L Éhn, I Černušák, Theoretical computation for thermophysical properties of high temperature high-temperature F_2, CF_4, C_2F_2, C_2F_4, C_2F_6, C_3F_6 and C_3F_8 plasmas 2012 *J. Phys. D: Appl. Phys.* **45** 285201.

[14]F Yang, MZ Rong, Wu Y, A B Murphy, **Wang WZ**, J Guo, Simulation of arc characteristics in miniature circuit breaker 2010 *IEEE Trans. Plasma Sci.* **38** 2306-2311.
[15]Y Wu, M Z Rong, F Yang, XH Wang, Q Ma, **W Z Wang**, Introduction of 6-band P-1 radiation model for numerical analysis of three-dimensional air arc plasma 2008 *Acta Phys. Sin.* **57** 5761-7.
[16]**W Z Wang**, Y Wu, M Z Rong, F Yang, J Guo, J L Gao, Simulation of Electric Arc in Low-Voltage Air Switch(In Chinese) 2009 *Low Voltage Apparatus* **23** 6-9.
[17]J J Yao, **W Z Wang**, Y Wu, X W Li, Simulation Technique on Low Voltage Electrical Apparatus and Its Application (In Chinese) 2009 *Low Voltage Apparatus* **7** 1-3.
[18]**W Z Wang**, M Z Rong, Y Wu, Q Q Zhou, F Yang, Studies on Properties Calculation Models of Equilibrium and Non-equilibrium Plasma (In Chinese) 2010 *High Voltage Apparatus* **46** 41-45.
[19]**W Z Wang**, M Z Rong, Y Wu, F Yang, Q Q Zhou, Simulation Technique of Electric Arc In Air Switch And Its Applications(In Chinese) 2010 *Low Voltage Apparatus* **5** 7-11.
[20]J Guo, Q Ma, F Yang, Z Q Sun, **W Z Wang**, Experimental Research on Arc Movement Characteristics of Different Gas Production Materials (In Chinese) 2009 *Low Voltage Apparatus* **5** 5-7.
[21]**W Z Wang**, M Z Rong, A B Murphy, Y Wu, H B Su, F Yang, Calculation Analysis on Statistic Thermodynamic Properties of Thermal Arc Plasmas Academic (In Chinese) 2011 *Journal of Xi'an Jiaotong University* **45** 86-92.
[22]**W Z Wang**, M Z Rong, A B Murphy, Y Wu, H B Su, F Yang, Computation Analysis on Properties of High Temperature Nitrogen Arc Plasmas (In Chinese) 2011 *High Voltage Engineering* **11** 2777-2784.
[23]**W Z Wang**, J D Yan, M Z Rong, and J W Spencer, Two-temperature modelling of SF_6 arc behaviour in a supersonic nozzle 2012 *High Voltage Engineering Special Issue on Gas Discharge and Its Application* **38** 198-201.
[24]**W Z Wang**, J D Yan, M Z Rong, and J W Spencer, Two-temperature thermodynamic and transport properties of SF_6 plasmas 2012 *High Voltage Engineering Special Issue on Gas Discharge and Its Application* **38** 812-815.

REFEREED ARTICLES PUBLISHED IN CONFERENCE PROCEEDINGS

[1] **W Z Wang**, J D Yan, A B Murphy, J W Spencer, M Z Rong, and M T C Fang, Composition and thermodynamic properties of high temperature mixtures of carbon and water vapour **(Poster).** *In: eds. Proceedings of XIXth Symposium on Physics of Switching Arc*. Brno, Czech Republic, 2011, pp.343-346.
[2] **W Z Wang**, M Z Rong, A B Murphy, Y Wu, J W Spencer, J D Yan, and M T C Fang, Transport properties of carbon /argon and carbon/ helium plasmas **(Topical Lecture).** *In: eds. Proceedings of XIXth Symposium on Physics of Switching Arc.* Brno, Czech Republic, 2011, pp.335-338.
[3] **W Z Wang**, J D Yan, A B Murphy, J W Spencer, M Z Rong, and M T C Fang, Thermophysical Properties of Thermal Equilibrium and Non-Equilibrium Nitrogen Plasmas **(Topical Lecture)**. *In: eds. Proceedings of XIXth Symposium on Physics of*

Switching Arc. Brno, Czech Republic, 2011, pp.339-342

[4] **W Z Wang**, M Z Rong , Y Wu, J W Spencer, and J D Yan, Transport coefficients of High Temperature CF_4, C_2F_6, and C_3F_8 as candidate of SF_6 **(Topical Lecture).** *In: eds. Proceedings of ICEPE-ST: 1st International Conference on Electric Power Equipment-Switching Technology*. Xi'an, China, 2011, pp.621-624.

[5] **W Z Wang**, J D Yan, M Z Rong, and J W Spencer, Two-temperature modelling of SF_6 arc behaviour in a supersonic nozzle **(Topical Lecture).** *In: eds. Proceedings of 19th International Conference on Gas Discharges and Their Applications*. Beijing, China, 2012, pp.198-201.

[6] **W Z Wang**, J D Yan, M Z Rong, and J W Spencer, Two-temperature thermodynamic and transport properties of SF_6 plasmas **(Topical Lecture).** *In: eds. Proceedings of 19th International Conference on Gas Discharges and Their Applications*. Beijing, China, 2012, pp.812-815.

[7] **W Z Wang**, M Z Rong, A B Murphy, Y Wu, and J D Yan, The reactive thermal conductivity of thermal equilibrium and non-equilibrium nitrogen plasmas **(Poster)**. *In: eds. Proceedings of the 15th Asian Conference on Electrical Discharge.* Xi'an, China, 2010, pp.685-688.

[8] F Yang, M Z Rong, Z Q Sun, Y Wu, and **W Z Wang**, A Numerical Study of Arc Splitting Processes with Eddy Current Effects **(Invited Lecture)** *In: eds. Proceedings of XVII International Conference on Gas Discharges and Their Applications.* Cardiff, UK, 2008, pp.309-312.

[9] M Z Rong, Y Wu, F Yang, **W Z Wang**, and X H Wang. The research of electric arc simulation in low voltage switching device **(Topical Lecture).** *In: eds. Proceedings of XVII International Conference on Gas Discharges and Their Applications.* Cardiff, UK, 2008, pp.9-12.

[10]**W Z Wang**, X H Wang, M Z Rong, M Li, A J Yang, X Peng, Study on Mechanical Condition Measurement and Mechanical Fault Prediction Algorithm of Vacuum Circuit Breaker **(Topical Lecture).** *In: eds. Proceedings of the annual Symposium of Distributed Special Committee for Chinese Society for Electrical Engineering.* Changzhou, China, 2009，pp.144-151.

[11]**W Z Wang**, M Z Rong, F Yang, Q Ma, Y Wu, Study on A high-power direct current circuit breaker actuator**(Topical Lecture).** *In: eds. Proceedings of the annual Symposium of High Voltage Engineering Special Committee for Chinese Society for Electrical Engineering.* Shenzhen, China, 2007，pp.933-936.

CHINISE PATENT

F Yang, M Z Rong, Y Wu, **W Z Wang**, X H Wang, Y Y Liu, A Kind of Gas-Blast Circuit breaker Used for Fast Interruption of DC Fault Current, No. CN101789338A.